SYNTHESIS, CHARACTERIZATION AND ENERGY APPLICATIONS OF TRANSITION METAL CHALCOGENIDE NANOSTRUCTURES

Thesis

submitted in partial fulfilment of the requirements for the degree

of

DOCTOR OF PHILOSOPHY

by

KARTHIK S BHAT

DEPARTMENT OF PHYSICS

NATIONAL INSTITUTE OF TECHNOLOGY KARNATAKA

SURATHKAL, INDIA-575 025

November, 2020

DECLARATION

I hereby *declare* that the Research Thesis entitled **Synthesis, Characterization and Energy Applications of Transition Metal Chalcogenide Nanostructures**, which is being submitted to the **National Institute of Technology Karnataka, Surathkal** in partial fulfillment of the requirements for the award of the Degree of **Doctor of Philosophy** in **Physics** is a *bonafide report of the research work carried out by me*. The material contained in this Research Thesis has not been submitted to any University or Institution for the award of any degree.

Karthik S Bhat
(Reg. No.: 155062 PH15F03)
Department of Physics

Place: NITK, Surathkal
Date: 10-11-2020

CERTIFICATE

This is to *certify* that the Research Thesis entitled **Synthesis, Characterization and Energy Applications of Transition Metal Chalcogenide Nanostructures**, submitted by **Karthik S Bhat** (Register No.: **155062 PH15F03**) as the record of the research work carried out by him, is *accepted as the Research Thesis submission* in partial fulfillment of the requirements for the award of degree of **Doctor of Philosophy**.

Dr. H S Nagaraja
Research Guide
Department of Physics
NITK, Surathkal
Date:

Chairman-DRPC

ACKNOWLEDGEMENT

A successful Ph.D. is not just an individual effort but a constant support of many. In this short space, I wish to acknowledge the people who have made it possible, and whose constant guidance and encouragement crown all the efforts with success.

Role of a research supervisor in shaping the Ph.D. is of paramount importance and therefore I dedicate my sincere thanks to my research supervisor Dr. H S Nagaraja, Associate Professor at the Department of physics, NITK for everlasting support and inspiration. I shall always apprize the academic freedom provided to explore and evaluate the ideas under his guidance.

I take this opportunity to thank my RPAC members, Dr. Ravishankar, Department of Metallurgy and materials engineering and Dr. Partha Pratim Das, Department of Physics, for their insightful comments and fruitful discussions throughout the progress of my research work.

I would like to thank Dr. Ajith K M, HOD at the department of physics, Prof. H D Shashikala and Prof. M N Satyanarayan, former HODs of the department of physics, who have extended facility for my Ph.D work. I am also thankful to NTTK Surathkal for providing an opportunity to pursue my research work and other faculty members of the department of physics for their good wishes.

I am thankful to the kind assistance of characterization facilities in the Department of physics-NITK, SAIF-Cochin, DST-PURSE Mangalore university, MNIT Jaipur, BIT-Bangalore for extending their sophisticated experimental and characterization facilities.

My deepest gratitude goes to my parents for their everlasting support throughout my thesis work. I am grateful to my parents Krishna Bhat and Shantha Kumari for their love, care and support. I recall the continuous encouragement and moral support from my wife Krithi Amai.

At last, I would like to express my thanks to lab mates and colleagues, Shreyas, Brijesh, Brian, Achyuta, Hegde, Mahendra, Mukesh, Sagar, Sourav, Makesh, Mishra, Amudha, Bindu, Soumalya, Ramesh Reddy and etc. who were the part of fruitful discussions.

Finally, I conclude with an abundance of thanks to all those who have helped me directly or indirectly in making this dissertation a possibility.

Karthik S Bhat

ABSTRACT

The thesis titled "Synthesis, Characterization and Energy Applications of Transition Metal Chalcogenide Nanostructures" encompass the work on transition metal chalcogenide nanostructures for their prospective use as electrode materials for supercapacitors and electrochemical water-splitting. Herein, the hydrothermal method is employed for the synthesis of different transition metal chalcogenide nanostructures, namely cobalt chalcogenides ($CoTe_2$ and $CoSe_2$), nickel chalcogenides ($NiTe_2$, $NiSe_2$ and NiSe), molybdenum chalcogenides (MoS_2, $MoSe_2$ and $MoTe_2$) and copper chalcogenides (Cu_2S and Cu_2S-Ni_3S_2). The synthesis is followed by some of the important physiochemical characterization techniques, such as XRD, SEM, HRTEM, XPS and etc.

$CoTe_2$ and $CoSe_2$ as supercapacitor electrodes delivered the specific capacitances of 360 F g^{-1} and 951 F g^{-1} at 5 mV s^{-1} scan rate. NiTe/$NiTe_2$ nanosheets as HER electrocatalyst required an overpotential of -432 mV to deliver 20 mA cm^{-2} current density. While, it required overpotential of 679 mV for the OER. Further, $NiSe_2$ nanosheets and NiSe nanoflakes required the overpotentials of -198 mV and -217 mV, respectively, to deliver 10 mA cm^{-2} current density for the HER. MoX_2 (X= S, Se, Te) nanostructures as HER electrocatalyst rank their performance in the order: $MoSe_2$>MoS_2>$MoTe_2$. On the other hand, isoelectronic tungsten (W) doping enhanced the specific capacitance of $MoSe_2$ supercapacitor electrodes. Specific capacitance as a function of W-doping indicated 2 M % as an optimum doping amount, delivering the maximum specific capacitance of 147 F g^{-1}. Furthermore, graphene composites of these nanostructures delivered enhanced specific capacitance (248 F g^{-1}) and superior cycle life. Cu_2S micro-hexagons could catalyze the HER in both basic (1 M KOH) and acidic solutions (0.5 M H_2SO_4), corresponding to the extreme pH values of 14 and 0, respectively. On the other hand, Cu_2S enhanced the alkaline water-splitting characteristics of nickel sulfide (Ni_3S_2), requiring the overpotentials of -149 mV and 329 mV to deliver current density of 10 mA cm^{-2} for the HER and OER, respectively. Furthermore, overall-water splitting required the cell-voltage of 1.77 V to deliver 10 mA cm^{-2} and demonstrated ultra-long term stability for 100 h.

Keywords: *cobalt chalcogenides; nickel chalcogenides; molybdenum chalcogenides; copper chalcogenides; supercapacitors; electrochemical water-splitting.*

CONTENTS

LIST OF FIGURES

Page No.

CHAPTER 1

CHAPTER 2

CHAPTER 3

CHAPTER 6

LIST OF TABLES

Page No.

Abbreviations

TMC	Transition metal chalcogenides
XRD	X-ray diffraction
FESEM	Field emission scanning electron microscopy
EDS	Energy dispersive X-ray spectroscopy
TEM	Transmission electron microscopy
HRTEM	High-resolution transmission electron microscopy
SAED	Selected area electron diffraction
XPS	X-ray photoelectron spectroscopy
TGA	Thermogravimetric analysis
BET	Brunauer-Emmett-Teller
BJH	Barrett-Joyner-Halenda
GO	Graphene oxide
rGO/RGO	Reduced graphene oxide
GRE	Graphite rod electrode
NF	Nickel foam
CV	Cyclic voltammograms
LSV	Linear sweep voltammograms
GCD	Galvanostatic charge-discharge
CP	Chronopotentiometry
EIS	Electrochemical impedance spectroscopy
EEC	Electrochemical equivalent circuit
EDLC	Electrical double-layer capacitors
PC	Pseudocapacitors
AC	Alternating current
DC	Direct current

Nomenclature

d	Interplanar spacing
λ	x-ray wavelength
Z	Total impedance
Z'	Real part of impedance
Z"	Imaginary part of impedance
R_S	Solution resistance
R_{CT}	Charge-transfer resistance
Q	Pseudocapacitance
C	Capacitance
C_S	Specific capacitance
η	Overpotential

CHAPTER 1

INTRODUCTION

This chapter outlines the fundamental aspects of transition metal chalcogenides. This chapter also accounts for their electrochemical properties. It is then followed by the literature survey. The scope of the present thesis and objectives are mentioned.

1.1 TRANSITION METAL CHALCOGENIDES

Transition metal chalcogenides (TMCs) have gained wide momentum owing to their unique electronic properties, structural and rich intercalation chemistry, which put this class of compounds at the interface of physics, chemistry and materials science.

TMCs have a long fruitful history. Their structure was first determined by Linus Pauling in 1923 (Dickinson and Pauling 1923). The term "chalcogen" was proposed by Werner Fischer to denote the chemical elements of group 16, while he was working at the University of Hannover in 1930s. The chemical elements of group 16 ranging from oxygen to polonium was collectively referred as the "chaclogens" However, the term "chalcogen" is more commonly reserved for sulfides, selenides, and tellurides, rather than oxides and polonium compounds, due to the strong non-metallic characteristics of oxygen and the strong metallic characteristics of polonium. The family of TMCs is quite huge and diverse, and could be categorized in many different ways. For example, in terms of the chalcogen elements, they could be divided into sulfides, selenides, tellurides, and multi-chalcogen chalcogenides. On the other hand, according to the number of chemical elements present, they could be classified as, binary, ternary, quaternary, and multi-component chalcogenides.

Chalcogens (S, Se and Te) form layered structures especially with transition metals of group 4 to 7B. Their layered structure resembles those of graphite with weak van der Waals interactions between the individual layers. These layered structures are of industrial importance, since they could be employed as dry lubricants to withstand higher temperatures than graphite (Gustavsson et al. 2013). Further, TMCs are characterized by noncovalent bonding between the individual layers and strong in-plane covalent bonding. Therefore, bulk TMCs can be exfoliated into few-layered structures by different approaches such as liquid exfoliation (Nicolosi et al. 2013), adhesive tape

exfoliation (Frindt 1966) and chemical exfoliation via lithium intercalation (Zeng et al. 2012).

TMCs exist in several structural phases, however, the two common structural phases are either trigonal prismatic (2H) or octahedral (1T) coordination of metal atoms. The different structures of TMCs are pictured in Figure 1.1. Further, the most important and common TMCs has either 1:1 or 1:2 stoichiometry. For example; NiSe and MoS_2, respectively.

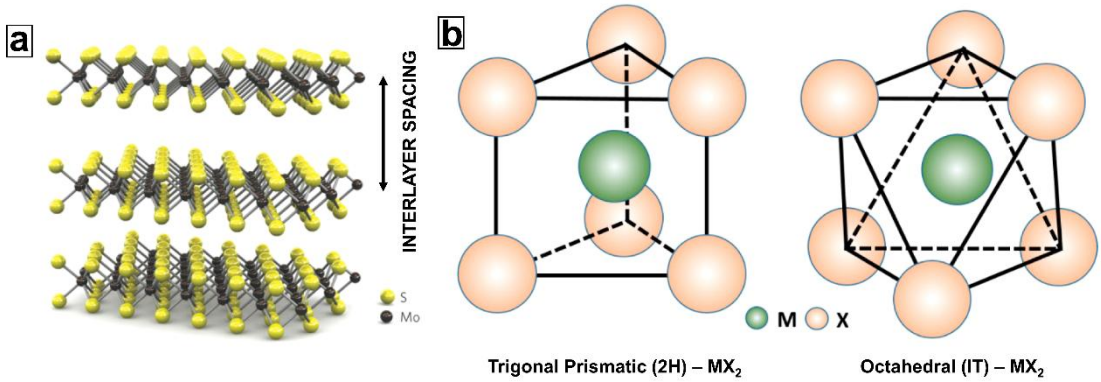

Figure 1.1 Crystal structure of TMCs with a general formula of MX_2. (a) Three-dimensional model of the MX_2, (b) Unit cell structures of 2H-MX_2 and 1T-MX_2.

Owing to the quantum confinement and surface effects, few-layered TMCs exhibit various exciting properties, which is not seen in their bulk counterparts. For example, bulk TMCs possess an indirect bandgap, while few-layer TMCs demonstrate direct bandgaps, which leads to enhanced optical properties (Mak et al. 2010). Furthermore, the electronic properties are also unique (Lv et al. 2015), which range from superconducting ($NbSe_2$, $TaSe_2$), semi-metals (VS_2), semi-conductors (MoS_2) and insulating (HfS_2), which make them unique for a variety of energy applications. In this regard, TMCs have become focal point for a wide range of interesting advanced applications in renewable and alternative energy, owing to their diverse physiochemical properties and also their flexibility in stoichiometry, structure, and morphology.

With this background, the present research work is focused on the hydrothermal synthesis of some of the novel TMCs and their electrochemical applications such as electrodes for supercapacitors and water-splitting (HER, OER and overall water-splitting).

To accomplish this task, the research, characterization and analysis described here will center around four main TMCs and their applications, namely $CoTe_2$, $CoSe_2$, $MoSe_2$, W-doped $MoSe_2$ and W-$MoSe_2$/graphene composites for supercapacitor electrodes. On the other hand, $NiTe_2$, $NiSe_2$, NiSe, MoX_2 (X=S, Se and Te), Cu_2S and Cu_2S-Ni_3S_2 was evaluated towards electrochemical water-splitting. The brief outline on supercapacitors and electrochemical water splitting is provided below.

1.2 ELECTROCHEMICAL APPLICATIONS OF TRANSITION METAL CHALCOGENIDES

1.2.1 Supercapacitors

Supercapacitors are also termed as ultracapacitors are the electrochemical energy storage devices, which offer a higher capacitance value than conventional capacitors. A supercapacitor also delivers high power density and energy density (Jung et al. 2013) than conventional capacitors and batteries, respectively.

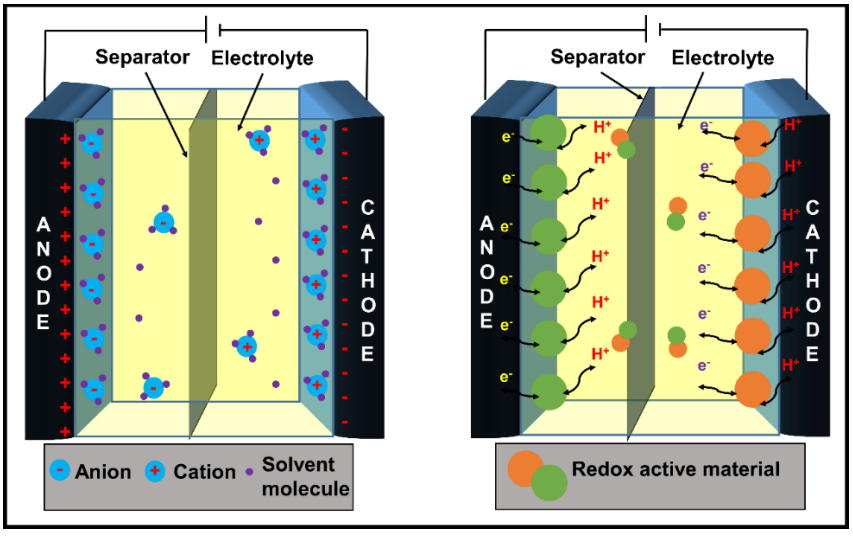

Figure 1.2 Schematic illustrations of different charge-storage mechanisms of supercapacitors.

In this regard, supercapacitors are generally categorized into electrical double-layer capacitors (EDLCs), pseudocapacitors (PC) and hybrid capacitors (Dubal et al. 2015; Sharma and Bhatti 2010). The charge storage mechanism in EDLCs is determined by

the physical adsorption/desorption ions at the electrode surface, while reversible redox reactions administer the energy storage in pseudocapacitors. On the other hand, hybrid capacitors are defined as the combination of EDLC and pseudocapacitor in a single device. The different charge-storage mechanisms of supercapacitors are illustrated in Figure 1.2.

The different components of a supercapacitor are described as follows:

Electrodes: The electrode material plays an important role in the construction of a supercapacitor. The supercapacitor should be able to deliver high specific capacitance, prominent cycle life along with high power density and energy density. All of these metrics are dependent on physiochemical properties of the electrode materials such as specific surface area, porosity, morphology, redox structures and electronic conductivity. Further, plenty of materials such as oxides, hydroxides, chalcogenides, conducting polymers and carbon materials along with their composites are investigated as electrodes for supercapacitors.

Separator: A separator in a supercapacitor acts as an insulator between the two electrodes. The separator should provide a pathway for the diffusion of ions and should be chemically inert and mechanically strong. Polypropylene membrane and filter paper are common separators in supercapacitors. However, the three-electrode system eliminates the use of a separator.

Electrolyte: The performance of a supercapacitor is also dependent on the electrolyte. The commonly used aqueous electrolytes are prepared by dissolving the inorganic salts in deionized water. The performance of a supercapacitor depends upon the electrolyte parameters such as concentration, pH and etc. The most commonly used aqueous electrolytes are KOH, Na_2SO_4 and H_2SO_4. These aqueous electrolytes have a limitation of limited operating voltage window due to electrolysis of water above a certain voltage limit. For this, non-aqueous electrolytes (such as quaternary ammonium salts dispersed in carbonates or acetonitrile) could be used to overcome this disadvantage.

Some of the advantages of supercapacitor are,

- High specific capacitance as compared with conventional capacitors.
- High rate-capability and longer life.
- Reduced size and cost.

On the other hand, some of the disadvantages are,

- Limited operating voltage window (up to 3 V).
- High self-discharge rate.
- Energy density less than Li-ion batteries.
- Non-operational at high-frequency circuits.

An ideal electrode material is required to possess vital parameters such as high specific surface area, good porosity, high electronic conductivity, substantial electroactive sites, high thermal and chemical stability (Zhang et al. 2010). Electrode materials based on various nanoscale metal oxides, carbon allotropes, conducting polymers and metal chalcogenides have been so far investigated for supercapacitor applications. However, the excellent electrochemical activity owing to characteristic attributes such as high specific surface area, active redox structures, high conductivity and multivalent oxidation states together with structural diversity make metal chalcogenides attractive as promising electrode materials for applications in energy storage (Gao et al. 2013).
After the primary research on graphene based supercapacitor electrode materials, the research on graphene-like layered TMCs as supercapacitor electrodes has gained momentum (Kumar et al. 2018). TMCs possesses large interlayer spacing for the ion intercalation, reversible redox reactions, large specific surface and porosity (Chia et al. 2015). Further, the predominant charge storage mechanism is unclear, since, some of the TMCs exhibit EDLC behavior due to non-Faradaic response, while others exhibit pseudocapacitive behavior attributing to the Faradaic response (Conway 1991). In addition, the performance of a supercapacitor electrode depends strongly on a wide variety of experimental conditions, electrolyte and cell configurations (two-electrode or three-electrode) (Bissett et al. 2016).

1.2.2 Electrochemical water-splitting

The splitting of water into hydrogen and oxygen has been an attractive avenue in the alternative energy research owing to the zero-carbon emission, high energy density and efficiencies (Barreto et al. 2003). Among various available methods for water splitting, thermal , electrochemical and photochemical approaches have attained enormous

research owing to the zero-emission, high energy density and conversion efficiencies (Edwards et al. 2008). The schematic illustration of electrochemical water-splitting is provided as Figure 1.3.

Water-splitting via an electrochemical route is governed by two half-cell reactions viz., hydrogen evolution reaction (HER) at the cathode ($2H^+(aq) + 2e^- \rightarrow H_2(g)$) and oxygen evolution reaction (OER) at the anode ($2H_2O(l) \rightarrow O_2(g) + 4H^+(aq) + 4e^-$) (Cheng et al. 2015). However, in practice, the real water electrolysis requires a much larger voltage to overcome unfavorable drawbacks such as high overpotentials and sluggish kinetics, especially for the OER (Walter et al. 2010). In this context, it is essential to use an electrocatalyst to bring down the higher overpotentials and also to improve the energy conversion efficiencies. So far, noble metals such as platinum, ruthenium, indium and their compounds are regarded as the state-of-the-art electrocatalyst for HER (Gomez et al. 1993) and OER (Lee et al. 2012), respectively. However, their scarcity, high-cost and poor stability have restricted the advancement in this field and subsequently prompt explorations for economic and viable alternatives.

Considering transition metals, there are certain reports on the catalytic activity of transition metals alone (Liang et al. 2017) and various surface treatments have been employed to enhance the electrocatalytic activity of the metal surface (Shang et al. 2018). Further, the electronic environments of transition metals could be tuned by alloying with electronegative nonmetal atoms such as O, P, S, Se, Te and C, which in turn it is anticipated to enhance the adsorption/desorption energy to facilitate the catalytic process. In this framework, nanostructured transition metal compounds ranging from oxides, double-hydroxides, phosphides, carbides and chalcogenides are demonstrated with their excellent electrocatalytic activities owing to their high abundance, efficiency and ease of synthesis (Gao et al. 2013).

Among chalcogenide series (sulfides, selenides and tellurides), it is well documented that as the degree of covalency in the metal-chalcogen bond increase, the declination of electronegativity from sulfur to tellurium correlates to the enhancement of metallic features (De Silva et al. 2018). Further, it believed that selenides are said to deliver the best HER catalytic efficiency owing to its low resistivity, small bandgap and a higher degree of covalency in the metal-anion bond (Masud et al. 2016). On the other hand, it has been anticipated that tellurides are the prominent OER electrocatalysts due to their

better band alignment with the water redox levels and lower electronegativity. This hypothesis was proved in nickel chalcogenide series, demonstrating tellurides as prominent OER electrocatalyst due to the pre-oxidation conversion of Ni^{2+} to Ni^{3+}, which influence the coordination environment for decreasing electronegativity. Herein the oxidation peak is shifted towards more cathodic potentials (Levesanos et al. 2017), which make a positive impact in lowering onset potential for the OER and thereby increasing their catalytic efficiencies. On the other hand, the overall water splitting efficiency depends upon the HER and OER kinetics, parity of two-electrodes, electrolyte solution and catalytic stability of the individual electrodes. Thus significant efforts have been made to develop highly efficient HER and OER catalyst in the same electrolyte to demonstrate the overall water splitting characteristics, which is highly demanding and challenging.

With this background, the various characteristic features of TMCs such as high specific surface area, porosity, electroactive sites and high electronic conductivity and chemical stability, make them attractive and favorable materials for applications in energy conversion and storage (Wang et al. 2015; Zhang et al. 2017b). All of these factors make TMCs diverse and are of practical importance for the design and development of earth-abundant-electrocatalysts for water-splitting reactions (Li et al. 2016).

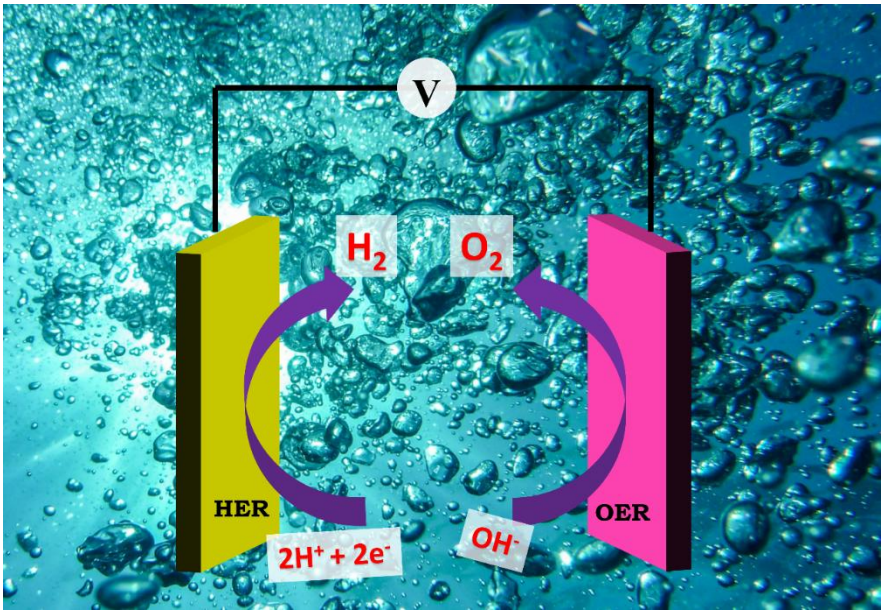

Figure 1.3 Schematic illustration of electrochemical water-splitting.

1.3 LITERATURE SURVEY

TMCs find a variety of applications in the field of an optic, electronic, photonic, piezoelectric, bio-sensing, energy storage and conversion devices (Choi et al. 2017). Among these, electrochemical applications such as water-splitting, supercapacitor and Li-ion battery electrodes are the trending areas of research. In this context, some of the important works on TMCs are highlighted below.

- (Pumera et al. 2014) studied various TMCs (MoS_2, $MoSe_2$, WS_2, WSe_2 etc.) and reported TMCs with 0 to ~2 eV have remarkable electrochemical properties. Also, it was said that the band gaps and electrochemical properties of TMCs can be tuned by exchanging the transition metal or chalcogenide elements. Further, (Mu et al. 2016) reported tube-like hierarchical $MoSe_2/CoSe_2$ microcages by hydrothermal method. It was said that structure of the materials can be easily tuned by varying Mo/Co ratio.

- (Kukunuri et al. 2015) hydrothermally synthesized different morphologies of nickel selenide (NiSe) by the choice of different selenium precursors (selenourea/selenium dioxide/potassium selenocyanate). The morphology of nickel selenides were spheres, wires and hexagons when selenium dioxide, selenourea and selenocyanate used as precursors, respectively. NiSe wires revealed the better HER performance, which was attributed to the high surface area (ECSA) and lower charge transfer resistance as compared with other NiSe morphologies.

- (Ge et al. 2017) calculated the Gibbs free energy ($\Delta G_{ads, H}$) for hydrogen adsorption in nickel chalcogenide series on chalcogenide sites (S, Se, Te) and metallic nickel sites by constructing a 2×2 supercell for (001) surface. Chalcogenide sites portrayed the free energy ($\Delta G_{ads, H}$) of 0.659 eV and 0.773 eV for nickel sulfide and nickel selenide, while it was quite higher (0.9 eV) for nickel telluride.

  On the other hand, the free energy ($\Delta G_{ads, H}$) on the metallic site (Ni) were 0.568 eV, 0.417 eV and 1.246 eV for nickel sulfide, nickel selenide and nickel telluride, respectively. The higher free energy ($\Delta G_{ads, H}$) of layered $NiTe_2$ was attributed to the outmost Te atoms and Ni atoms near (001) surface are saturated by Ni-Te bonds.

Whereas, both pyrite-phase NiS_2 and $NiSe_2$ had dangling bonds due to the formation of the surfaces. In this regard, it was outlined that the Ni sites are significantly influenced by their non-metal ligands and surface structures.

- (Chia et al. 2017) prepared layered $NiTe_2$ via a physical method. $NiTe_2$ required the overpotential of 590 mV to deliver 10 mA cm^{-2} current density and a low Tafel slope of 45 mV dec^{-1} in an acidic solution.

- (Shit et al. 2018) demonstrated CoS_x/Ni_3S_2@NF heterostructure on nickel foam through the hydrothermal approach. Herein the HER performance of CoS_x/Ni_3S_2@NF outperformed pristine CoS_x and Ni_3S_2 counterparts, which was attributed to the formation of nano interface. The nano interface facilitated the charge transfer between Co and Ni via an S-bridge, which in turn facilitated the charge transfer between the electrocatalyst and the electrolyte.

- (De Silva et al. 2018) reported synthesis of nickel telluride (Ni_3Te_2) via two different techniques (electrodeposition and hydrothermal). The better electrocatalytic performance of electrodeposited Ni_3Te_2 was attributed to their binder-free approach.

- (Soon and Loh 2007) reported the synthesis of MoS_2 nanowall films by thermal evaporation. MoS_2 delivered the specific capacitance of 100 F g^{-1} at a scan rate of 1 mV s^{-1}. Herein, the charge storage mechanism was attributed to the both Faradaic and non-Faradaic processes.

- (Ratha and Rout 2013) synthesized layered structure of WS_2/reduced graphene oxide (RGO) hybrids by a facile hydrothermal method for application as supercapacitor electrodes. The WS_2/RGO hybrids exhibited enhanced supercapacitor performance with a specific capacitance of 350 Fg^{-1} at a scan rate of 2 mV s^{-1}. The obtained capacitance values of WS_2/RGO hybrids was about 5 and 2.5 times higher than bare WS_2 and RGO sheets. The excellent performance of the WS_2/RGO hybrids was attributed to the high electrical conductivity of the composite and homogenous coverage of WS_2 sheets over RGO sheets, which

facilitated the rapid transport of the electrolyte ions. This similar trend in enhancement of electrochemical performance was also observed in $MoSe_2$/graphene hybrids as demonstrated by (Balasingam et al. 2016).

- (Huang et al. 2015b) synthesized CuS nanosheets and reported pseudocapacitive characteristics exhibiting a high specific capacitance of 833.3 F g^{-1} at a current density of 1 A g^{-1} and 85.1 % retention for 500 cycles.

- (Arul and Han 2016) reported hexapod-like $NiSe_2$ by a facile hydrothermal method. $NiSe_2$ exhibited a specific capacitance of 75 F g^{-1} with cyclic retention of 94% at a current density of 1 mA cm^{-2} for 5000 charge-discharge cycles.

- (Shen et al. 2016) demonstrated $FeNi_2S_4$–g–$MoSe_2$ supercapacitor electrodes, delivering specific capacitance of 1700 F g^{-1} at 2 A g^{-1} current density. The capacitance retention was 106% after 4000 cycles.

- (Arul and Han 2019) synthesized $NiSe_2$/$Ni(OH)_2$ nanocomposites, which delivered a high specific capacitance of 2212 F g^{-1} than pristine $NiSe_2$ (326 F g^{-1}). The enhanced performance was due to the synergetic effect between $NiSe_2$ and $Ni(OH)_2$, which provided a free diffusion pathway for the fast ion transport.

- (Mao et al. 2019) synthesized nanoflower-shaped $CoTe_2$ through hydrothermal route, which delivered the capacitance of 460 F g^{-1} at 1.5 A g^{-1} current density. The electrode was also complimented with excellent capacitance retention of 91% after 5000 cycles.

The above literature explains TMCs are good candidates for electrochemical applications. Further, we can also understand that the physiochemical properties of these materials can be varied with experimental conditions. In addition, it is also understood that the electrochemical performance could be enhanced by synthesizing a hetero-structure TMCs and/or hybridizing with graphene.

1.4 SCOPE AND OBJECTIVES OF THE PRESENT WORK

With the rapid progress of sustainable energy economy, it is vital to significantly utilize renewable energy more efficiently. In this regard, TMCs are multifunctional materials with unique properties and applications. Nanostructured TMCs plays a prominent role in energy conversion and storage devices ranging from rechargeable batteries, supercapacitors, electrochemical water-splitting, dye-sensitized solar cells and photo-electrochemical devices.

The structural features of TMCs depend upon the synthesis method, precursors used, method of synthesis and also the external parameters such as reaction temperature, pressure, pH, reaction time, etc. Thus, TMCs with unique morphology and properties can be synthesized by varying the above mentioned experimental parameters. Further, hydrothermal method is one of the energy-efficient methods for the synthesis of nanostructured materials. The main advantages of hydrothermal method are fast reaction kinetics, large area uniform production, moderate processing times, phase purity, high crystallinity, low cost, environmental friendliness and use of simple equipment.

In this perspective, with the variation of synthesis conditions, it is anticipated to observe the variation of various physiochemical parameters such as specific surface area, pore size, electronic conductivity and nanostructure morphology, which are the key factors determining the electrochemical applications of these materials. With this background, it would be interesting to synthesize nanostructured TMCs employing the hydrothermal method and to study their various electrochemical properties.

1.4.1 Objectives

The main research objectives are:

1. The synthesis of binary, ternary and doped TMCs using the hydrothermal method.
2. The study of structural and compositional features of prepared materials.
3. The study of electrochemical properties of synthesized TMCs towards applications in supercapacitors.
4. The study of electrochemical properties of synthesized TMCs towards application in HER, OER and overall water-splitting.

1.5 ORGANIZATION OF THE THESIS

The research work presented in this thesis is divided into 7 chapters.

Chapter 1 and its sub-sections provide the background and motivation for the present work. This chapter also outlines the fundamental aspects of TMCs and provides an overview of electrochemical applications, such as supercapacitors and electrochemical water-splitting. It is then followed by the literature survey. The scope of the present thesis work and objectives are mentioned.

Chapter 2 provides the details of the experimental techniques used in the present work. The hydrothermal synthesis of TMCs and different physiochemical characterizations employed for the synthesized samples are briefly explained. The different electrochemical techniques to study supercapacitor and electrocatalytic performances and their evaluation parameters are discussed.

Chapter 3 describes the pseudocapacitive characteristics of cobalt chalcogenide ($CoTe_2$ and $CoSe_2$) nanostructures**.**

Chapter 4 demonstrates the electrocatalytic performance of nickel chalcogenide ($NiTe_2$, $NiSe_2$ and NiSe) nanostructures**.**

Chapter 5 illustrates the electrocatalytic performance of molybdenum chalcogenide MoX_2 (X= S, Se, Te) nanostructures and supercapacitor characteristics of W-doped $MoSe_2$ and W-$MoSe_2$/graphene hybrid nanostructures.

Chapter 6 presents the electrocatalytic performance of copper sulfide (Cu_2S) hexagons at different pH conditions and also the electrocatalytic performance Cu_2S-Ni_3S_2 arrays as a bifunctional electrocatalyst for overall water-splitting.

Chapter 7 summarizes the conclusions drawn from the present work. Next, the scope for further work in this field is mentioned. An appendix followed by a list of references and a brief profile with publications in international journals and conferences is presented at the end of the thesis.

CHAPTER 2

EXPERIMENTAL TECHNIQUES

In this chapter, the theory and methodology of various experimental techniques are illustrated. A brief introduction on the hydrothermal synthesis technique is followed by the discussions on important physiochemical characterization, using techniques such as X-Ray diffraction (XRD), Electron microscopy (SEM and TEM), X-ray photoelectron spectroscopy (XPS), Raman spectroscopy and Thermogravimetric analysis (TGA) measurements. Furthermore, this chapter also presents an outlines for different electrochemical measurements such as, cyclic voltammograms (CV), linear sweep voltammograms (LSV), galvanostatic charge-discharge (GCD), electrochemical impedance spectroscopy (EIS) and constant current chronopotentiometry (CP) measurements towards different electrochemical energy applications. At last, the parameters used to evaluate different electrochemical activities of the prepared samples are discussed.

2.1 SYNTHESIS OF TRANSITION METAL CHALCOGENIDE NANOSTRUCTURES

2.1.1 Hydrothermal method

Since the 1960s, the hydrothermal method has been widely employed for the synthesis of a variety of functional materials with specific shapes, sizes, and phases (Chen and Mao 2007; Lu et al. 2007). In the present work, hydrothermal method is employed for the transition metal chalcogenide nanostructures owing to their main advantages such as fast reaction kinetics, large area uniform production, short processing times, phase purity, high crystallinity, low cost, environmental friendliness and use of simple equipment's (Liang et al. 2012).

The hydrothermal process uses water as the reaction medium in Teflon lined stainless steel autoclaves, which are heated to the required temperature (generally above 100 °C) to promote the reaction. On the other hand, since, solvent possesses properties such as polarity, viscosity and softness, etc., the solvent properties shall influence transport behaviour of the precursors. These transport properties of a solvent will control the reactivity, shapes and sizes of final products. Thus, in this regard, this new method is termed as the solvothermal method. The pressure generated inside the reactor

autoclaves not only depends on the reaction temperature but also relies on the other experimental factors, such as amount of the water/solvent added and dissolved precursors. In this background, a review (Devaraju and Honma 2012) on hydrothermal process explains the fast reaction kinetics, short processing times, phase purity, high crystallinity, low cost and so on. Hydrothermal autoclave systems are available of different volumes ranging from 25 mL to 5000 mL. In the present work, hydrothermal autoclaves of 120 mL capacity were used and the reaction was maintained at a temperature of 180 to 200 °C, depending upon the requirement. A photograph of hydrothermal autoclaves and the heating zone is provided as Figure 2.1.

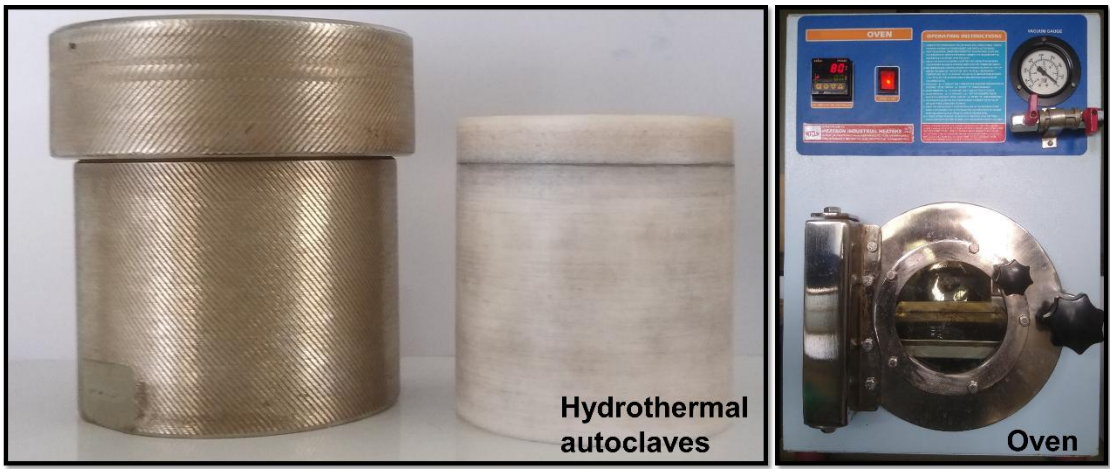

Figure 2.1 Photograph of hydrothermal autoclaves and heating zone (oven).

2.1.2 Hydrothermal anion-exchange method

Hydrothermal anion-exchange of chalcogen ions with pre-synthesized transition metal hydroxides in one of the easy, scalable and controllable method for the synthesis of transition metal chalcogenide nanostructures. In addition, the synthesized transition metal chalcogenides attain the morphology of the precursor hydroxides. Using this method, different transition metal chalcogenide nanostructures were synthesized and their electrochemical properties are reported (Manos et al. 2007; Xu et al. 2013).

In this context, the growth insights of metal chalcogenide (MX_n, X=S, Se, Te) nanostructures via anion-exchange reaction could be as follows (Zhao et al. 2014); the reduction with $NaBH_4$ reducing agent lead to the quick exchange of OH^- from $M(OH)_2$ with chalcogen ions forming thin layer of MX_2 on the surface of $M(OH)_2$ nanostructures. Further, the lattice mismatch between the just formed thin layer of MX_2

and $M(OH)_2$ can cause quick strain release and lead to the formation of pores. Similar strain-induced pores have been observed and theoretically predicted for the cation-exchange reaction of nanocrystals (Yin et al. 2004). Further, the Kirkendall effect leads to the formation of hollow structures (Li et al. 2006). When the anion exchange reaction is prolonged for required hours, the complete transformation of $M(OH)_2$ nanostructures into MX_2 nanostructures are observed. The schematic of probable anion-exchange reaction is illustrated in Figure 2.2.

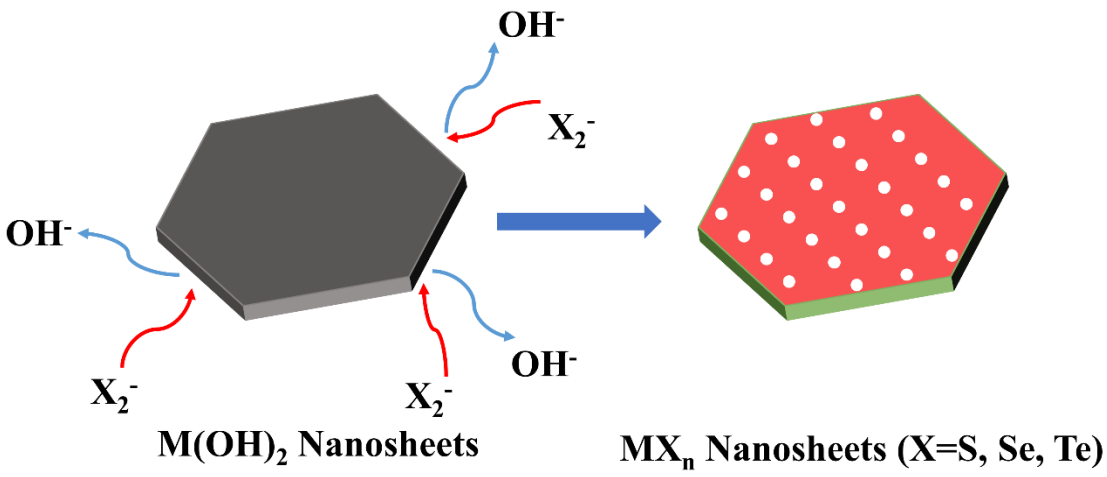

Figure 2.2 Schematic of the anion-exchange reaction of $M(OH)_2$ nanostructures with chalcogen ions to form porous hollow metal chalcogenide nanostructures.

2.1.3 Hydrothermal chalcogenization of the metal substrate

Recently, as an improved method of hydrothermal synthesis, chalcogenization of a metallic substrate (Ni foam, Cu foam) is employed. Researchers have also tried chalcogenization of a metallic substrate using other techniques such as thermal deposition (Sun et al. 2018) and physical vapour deposition (Yu et al. 2018), etc. During hydrothermal chalcogenization, precursor solutions are prepared and metallic substrate is directly introduced into the autoclaves. After the reaction, prepared samples are directly used for electrochemical measurements. The superior performances of these prepared chalcogenides were anticipated owing to predominant conductivity of the metallic substrate and binder-free approach. The use of different binders hinders the charge-transfer and limits active sites for the water-splitting reactions (Deng et al. 2016).

2.2 PHYSIOCHEMICAL ANALYSIS

2.2.1 X-Ray diffraction

X-ray diffraction (XRD) is a scattering phenomenon to investigate the crystallinity of the synthesized materials. This technique began when Von Laue discovered (1912) that crystals diffracted X-rays. Afterwards, it has been applied to chemical analysis, measurements of crystallite sizes and stress/strain measurements. X-rays have wavelength comparable to interatomic spacing, make them successful for the structural investigations of the materials. The diffraction of X-rays is governed by the Bragg's law: $2dsin\theta = n\lambda$ (2.1)

Wherein, d is the distance between the lattice planes, θ is the angle which the X-ray photon makes with the incident plane, λ is the X-ray wavelength and n is the order of reflection. XRD analysis are conducted using Panalytical Rigaku miniflex 600 diffractometer coupled with Copper (Cu) K_α radiation (λ= 1.54 Å) at a scan rate of 1° min^{-1} in the required 2θ range. Further the as obtained data is analyzed and indexed using Panalytical Xpert high score plus 3.0 software to match with the standard Joint Committee for Powder Diffraction Standard (JCPDS) files.

2.2.2 Electron microscopy and Energy Dispersive X-ray spectroscopy (EDS)

SEM and TEM are the two different types of electron microscopes in which electron beam is illuminated on the specimen surface to study the morphology of synthesized materials. These microscopes provides a great combination of magnification (100,000x), greater resolution (few nm), larger depth of view and ease of sample preparation and observation. Herein, the generated electron beam by a cathode is focused over a specimen surface with the help of magnetic lenses. The interaction of electron beam with the specimen leads to several interactions like back-scattering, Auger emission, cathodo-luminescence, secondary electrons and X-rays etc., lead to a variety of imaging techniques and modes to characterize different parameters of the specimen under investigation. Whereas, in TEM, the electron beam passes through the specimen to form a microscopic image. In the present work, morphological images are recorded using a field emission scanning electron microscope (FESEM, ZIESS) fitted

with an EDS and TEM measurements are performed using a JEOL 2100 HRTEM microscope operated at an acceleration voltage of 200 kV.

Further, EDS is a technique used to analyze the elemental composition of the material. EDS measurements are based on the interaction of electron beam with the specimen, thereby producing characteristic X-rays. Each element has a unique atomic structure allows emitted X-rays that are characteristic of an element's atomic structure to be identified uniquely from each other. EDS measurements provide qualitative information of atomic and weight percentages of all the elements present in the sample. Furthermore, elemental mapping analysis indicate the order of distribution of different elements present in the sample.

2.2.3 X-ray photoelectron spectroscopy (XPS)

X-ray photoelectron spectroscopy (XPS) has been a valuable characterization technique since the 1950s, which provides information about the bonding states, elemental and composition of the sample. Different chemical elements within the near surface are identified on the basis of their binding energy (BE). Kinetic energy (KE) and binding energy (BE) are related via the equation: $KE = h\nu - BE - \phi$ (2.2)

Where, $h\nu$ represents the energy of absorbed photon and ϕ is the work function of the spectrometer. In the present work, XPS analysis was carried out using a commercial Omicron EA 125 source with Al-Kα radiation (1486.7 eV).

2.2.4 Brunauer-Emmet-Teller (BET) surface area and (BJH) pore size

The specific surface area and pore size of the samples can be calculated using Brunauer Emmett and Teller (BET) and Barrett Joyner and Halenda (BJH) measurements based on nitrogen adsorption- desorption isotherms, respectively. In the present work, both measurements are performed using ChemStar chemisorption analyzer (Quantachrome Instruments, USA).

2.2.5 Thermogravimetric analysis (TGA)

Thermogravimetric analysis (TGA) is one of the widely used thermal analysis technique to study the property of material as a function of applied temperature. In

TGA, the mass of the sample is measured as a function of temperature or time in a controlled atmosphere. The change in the mass on increasing temperature can be attributed to the physical or chemical changes. TGA helps us to find out the thermal stability, melting point, and transition temperature of a material.

TGA measurements were conducted using a TGA-DSC (DSC SDT Q600) system under nitrogen atmosphere by heating the samples from room temperature to a required temperature.

2.2.6 Raman spectroscopy

Raman spectroscopy is used to observe the various frequency modes and crystalline parameters of the sample under investigation. In the present work, Raman spectra's are recorded using a WITEC ALPHA300 spectrometer by exciting the samples using a ~532 nm laser having a spot size of ~24 µm. Raman shifts are directly related to energy and has the unit inverse of length (Ohsaka et al. 1978). Raman shift is determined using the equation: $\Delta\omega = \lambda_0^{-1} - \lambda_1^{-1}$ (2.3)

Where, $\Delta\omega$, λ_0^{-1}, and λ_1^{-1} are the Raman shift (cm^{-1}), excitation wavelength, and incident wavelength, respectively.

2.3 ELECTROCHEMIAL MEASUREMENTS

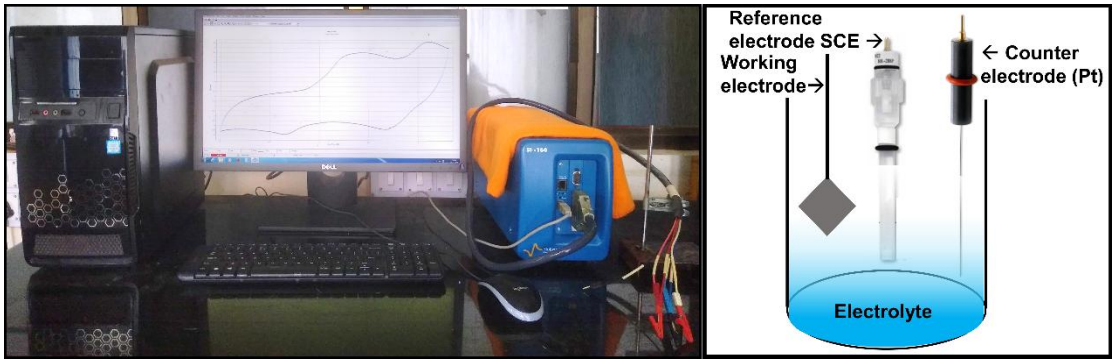

Figure 2.3 Photograph of Biologic SP-150 electrochemical workstation and a schematic of three-electrode arrangements.

The electrochemical performances of the prepared samples are evaluated using Biologic SP-150 electrochemical workstation. A typical photograph of SP-150 setup and a schematic of a three-electrode arrangements is provided above (Figure 2.3).

2.3.1 Cyclic voltammograms and linear sweep voltammograms

Voltammograms or voltammetry is study of current response as a function of the applied potential. Voltammograms could be recorded either by a two-electrode system or a three-electrode system. A typical three-electrode system consist of a working electrode, counter electrode and reference electrode as pictured in Figure 2.3.

Cyclic voltammograms (CV) and linear sweep voltammograms (LSV) are very similar to each other. In CV, the voltage is swept between two values at a fixed scan rate. When the voltage reaches upper limit, the scan is reversed and the voltage is swept back to lower limit. Whereas in LSV, the voltage is swept from a lower limit to an upper limit only. In other words, LSV could be understood as half-cycle of a CV curve.

In CV, the potential of a working electrode ramps linearly in cyclical phases vs. time as shown in Figure 2.4a. The potential between working electrode and reference electrode and the current between working electrode and counter electrode are measured. The rate of change of voltage with time during each phases is known as scan rate (v). The curve of current versus potential is known as cyclic voltammograms (Figure 2.4b). Cyclic voltammetry provides information about the kinetics of the reaction and the redox potential of the electro active species in the system. The important parameters of a CV are peak currents i.e., anodic peak current (I_{pa}) and cathodic peak current (I_{pc}) and peak potentials i.e. anodic peak potential (V_{pa}) and cathodic peak potential (V_{pc}).

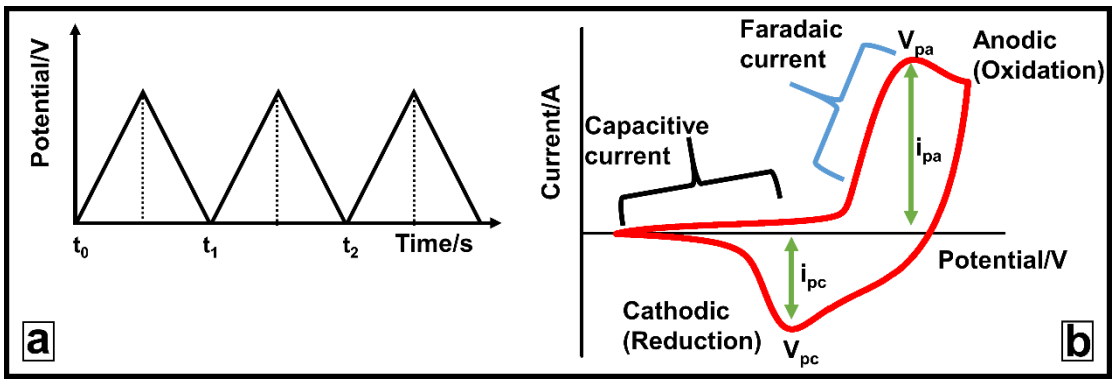

Figure 2.4 Input waveform and cyclic voltammetry technique.

2.3.2 Galvanostatic charge-discharge

Galvanostatic charge-discharge (GCD) is also an electrochemical technique used to study the mechanism and kinetics of an electrochemical reaction. This technique is mainly used to calculate the specific capacitance/specific capacity, stability and Coulomb efficiency of an electrochemical energy storage devices. In this technique, a constant current density is applied to charge a device, and when the device reaches the potential limit, the device will be discharged with a negative current density. A schematic of GCD curve of a supercapacitor is shown in Figure 2.5.

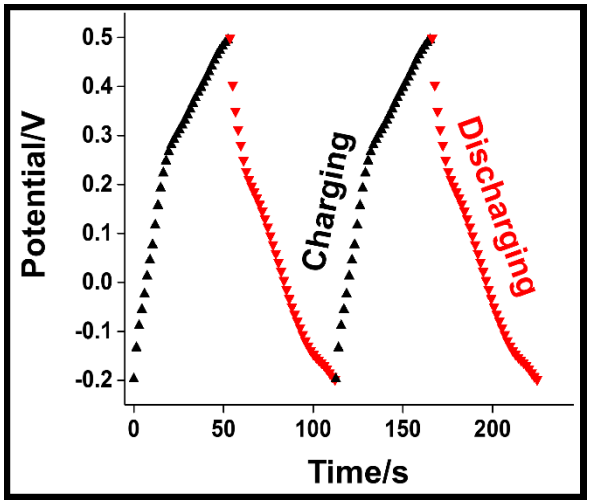

Figure 2.5 Schematic of a GCD curve.

2.3.3 Electrochemical impedance spectroscopy

Impedance spectroscopy is a reliable tool of estimating electrochemical performance of the electrodes in the required frequency region. In this method, an electric field is applied and the impedance of a system with respect to frequency of the applied field is recorded. This method helps us to separate the contributions from different components with known dimensions. Electrochemical impedance is obtained by applying a sinusoidal voltage excitation and by measuring the resulting current. In general, the impedance of a system could be summarized by the following equation:

$$Z = |Z|e^{i\phi} = Z' + iZ'' \quad (2.4)$$

Here, Z' and Z'' are the real imaginary part of the complex impedance, respectively and ϕ is the phase difference. A plot of imaginary impedance versus real impedance is

called as 'Nyquist plot'. Impedance at a frequency on the Nyquist plot can be represented as a vector of length |Z|. The angle between the X-axis and |Z| is known as phase angle (ϕ). The semicircle in a Nyquist plot is the characteristic of a time constant. Impedance graphs often possesses few semicircles, however generally only a portion of a semicircle are seen. The Representation of a Nyquist plot is shown in Figure 2.6. Further, impedance data is generally analyzed by fitting it into an electrochemical equivalent circuit (EEC) model consisting of electrical components. Common electrical components in the most of the models are capacitors, resistors and inductors. The commonly obtained EEC components are solution resistance (R_S), charge transfer resistance (R_{CT}), double layer capacitance (C_{dl}) and pseudocapacitances (Q).

Herein, R_S - the solution resistance, which is the resistance of bulk electrolyte between reference and working electrodes. R_{CT} - this resistance is due to the kinetically-controlled electrochemical reaction. R_{CT} is commonly observed in reactions involving diffusion of ions. C_{dl} - double-layer capacitance at the interface of electrode and electrolyte. Q represents the pseudocapacitance and gives the measure of effective surface area available for the reaction (Najafi Sayar and Bahrololoom 2009).

For all of the Nyquist plots, the EEC fitting is conducted using EC-lab V11.04 software using the Z fit module. The ensure correctness of an EEC fit, the obtained χ^2 /|Z| value was ensured to be at the lowest (example: 5 to 10 E^{-3}). Here, Z represents the total impedance in the circuit.

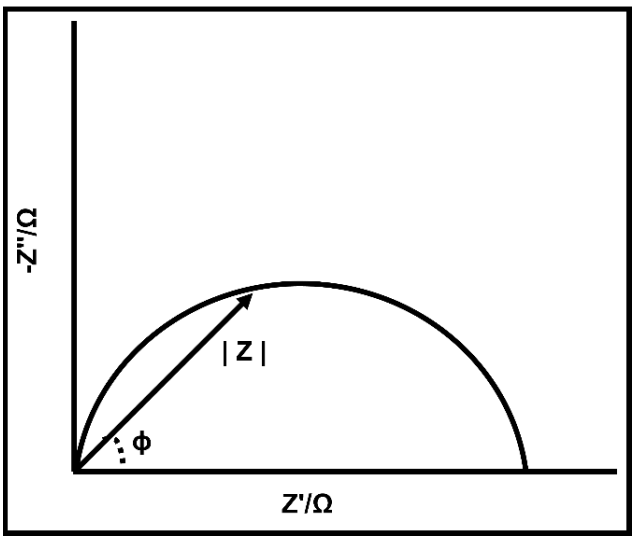

Figure 2.6 Representation of a Nyquist plot.

Additionally, Bode phase angle is also a significant parameter for supercapacitors, which is determined from Nyquist plots of the electrodes. Herein, Ideal capacitors exhibit the phase angle of -90º, while a shallower slope accounts for pseudocapacitive/hybrid charge-storage mechanism of the electrodes (Zhang and Pan 2015).

2.3.4 Constant current chronopotentiometry

In constant current chronopotentiometry, a constant current is applied to the working electrode, which favors the oxidation or reduction of electroactive species in the electrolyte. The potential across the working electrode will be measured as a function of time. This technique is used to study the stability of an electrocatalyst, supercapacitors and also in electrochemical and pH sensors.

2.3.5 Preparation of supercapacitor electrodes

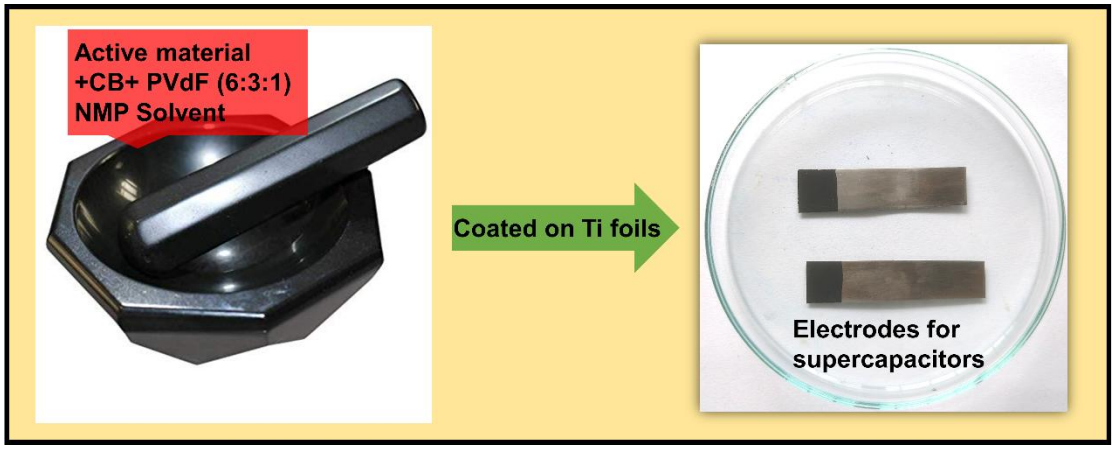

Figure 2.7 Schematic of electrodes preparation for supercapacitors.

The working electrodes for electrochemical measurements are prepared by mixing the active material with conductive carbon black (Acetylene black) and polyvinylidene fluoride (PVdF) in the 6:3:1 ratio, using N-methyl-2-pyrrolidone (NMP) as a solvent. Here, carbon black helps in increasing the electronic conductivity of the electrodes and PVdF serves as a binder. The as formed slurry was uniformly coated on a ~1 cm^2 geometric area of titanium (Ti) foil current collectors (Alfa Aesar, 0.25 mm thickness and dimension 5×1 cm), followed by drying in an oven at 60 °C for 6 h, ensuring the

complete evaporation of solvent. The average mass of active materials was estimated by the weight difference before and after coating, which was found to be in the range of ~2-3 mg. The schematic of electrodes preparation for supercapacitors is provided as Figure 2.7.

2.3.6 Supercapacitor evaluation parameters

The following parameters are widely recognized for evaluating the performance of the supercapacitors.

2.3.6.1 Specific capacitance

The specific capacitance (C_s) is defined as the charge storage ability of supercapacitor material. The C_s is usually expressed as the amount of charge storage per unit mass, which has a unit of Fg^{-1}. Both CV and GCD measurements could be used to evaluate the specific capacitance of the electrode materials using the following equations.

From the CV curves, C_s can be calculated using the equation,

$$C_s = \frac{\int I(V)dV}{vm\Delta V} \ (Fg^{-1}) \quad (2.5)$$

where the integral represents the area of the CV curve, 'C_s' is the specific capacitance in Fg^{-1}, 'm' is the mass of the electroactive material in mg, $'v'$ is the scan rate (mVs^{-1}) and $'\Delta V'$ is the potential window (V).

From the GCD curves, C_s can be calculated using the equation,

$$C_s = \frac{I\Delta t}{m\Delta V} \ (Fg^{-1}) \quad (2.6)$$

Where '$\frac{\Delta t}{\Delta V}$' is the slope of the discharge curve and 'I' is discharge current (mA).

2.3.6.2 Impedance spectroscopy

The characteristics of supercapacitor electrodes are studied through electrochemical impedance spectroscopy analysis (EIS) technique in potentiostatic mode. In general, the impedance curves in the Nyquist plots of a supercapacitor can be divided into three frequency regions (low, middle and high), wherein the electrodes in the low frequency exhibiting a vertical straight line behave as an ideal capacitor. Further, It is well known

that supercapacitors exhibit resistive (blocking) behavior at high frequencies and capacitive behavior at low frequencies (Kötz et al. 2006). The intercept at X-axis of the Nyquist plot (real part of impedance Z´) indicate the electrode resistance (R_S) and a small kinetic arc in the high frequency region depicts charge transfer resistance (R_{CT}) at the electrode–electrolyte interface (Yuan et al. 2009). All of these different parameters are better understood by fitting into an EEC.

2.3.6.3 Cycle life

After evaluating the different parameters of a supercapacitor, it is necessary to evaluate the stability of the prepared electrodes. In this regard, the cycle life or the stability of a supercapacitor could be studied by subjecting it into CV or GCD cycling for a definite number of cycles. Generally, stability tests of a supercapacitor are performed at a higher scan rates (50 to 200 mV s^{-1}) or higher current densities (ranging from 5 to 50 A g^{-1}). The stability tests under these conditions indicate if the material under investigation is suitable for fast charge-discharge applications. Furthermore, ideal energy storage devices should be able to deliver the same energy under any operation conditions (Ranganatha et al. 2017). Thus, it is vital to study the specific capacity retention at a higher current density or higher scan rate.

2.3.6.4 Charge-storage mechanism of electrodes

The electrochemical charge storage mechanism of supercapacitor electrodes could be validated via Dunn's method (Wang et al. 2007). The current response (*i*) at a fixed potential (V) can be described as the combination of two separate mechanisms, namely capacitive ($k_1 v$) and diffusive contribution ($k_2 v^{\frac{1}{2}}$) where 'v' is the scan rate and 'k_1' and 'k_2' are constants. Assuming that the current (*i*) response obeys a power-law relationship $i = av^b$; where 'a' and 'b' are adjustable parameters, with b-values determined from the slope of the linear plot of log *i* vs log *v*. The slope b=1 is indicative of ideal capacitive response, while b=0.5 is representative of a battery-type/diffusion controlled behavior (Kirubasankar et al. 2019).

Further, the percentage of capacitive and diffusive contributions to the total stored charge are evaluated using the equations:

$$i(V) = k_1 v + k_2 v^{\frac{1}{2}} \quad (2.7)$$

$$i(V)/v^{\frac{1}{2}} = k_1 v^{\frac{1}{2}} + k_2 \quad (2.8)$$

Where $k_1 v$ and $k_2 v^{1/2}$ correspond to the current contribution from capacitive controlled process and diffusion/redox processes (Ajay et al. 2015), respectively. Thus, by determining k_1 and k_2 from the plots of $v^{1/2}$ Vs i (V)/$v^{1/2}$, the percentage contributions from these mechanisms could be evaluated.

2.3.7 Preparation of electrodes for electrocatalytic measurements

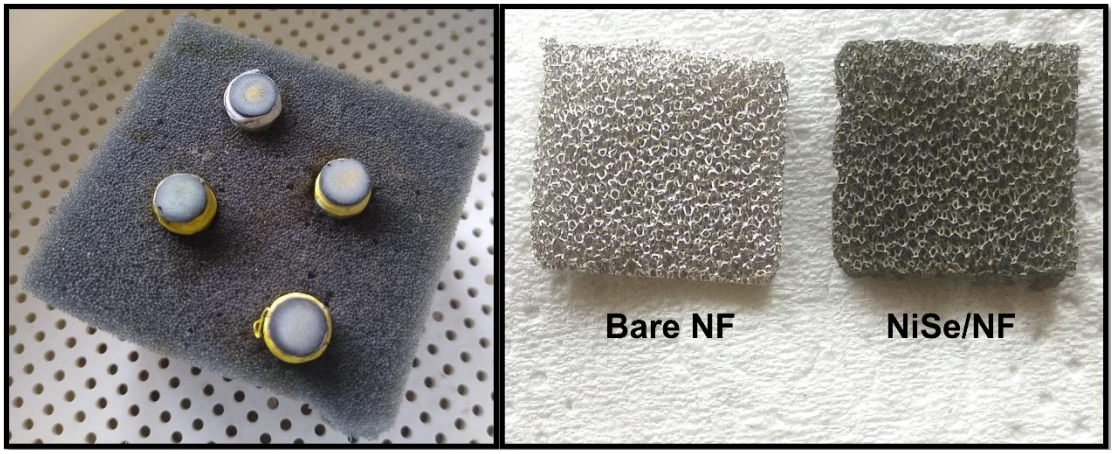

Figure 2.8 Photograph of prepared electrodes for electrocatalytic measurements.

If the synthesized electrocatalysts are in the powder form, the samples are required to be assembled on a substrate for successful electrocatalytic measurements. The powder catalysts were assembled on commercially available graphite rod substrates as follows: Graphite rod of ~10 mm diameter was fine mirror polished using a sand paper, followed by cleaning with acetone, ethanol and DI water through ultra-sonication. About ~4 mg of the synthesized catalyst was added to 1 mL of 3:1 (v/v) water – ethanol solvent containing 40 µL of perforated Nafion resin as a binder. The mixture was ultra-sonicated for 30 min ensuring complete dispersion of catalysts. About 100 µL of dispersed catalyst ink is drop casted onto the surface of graphite rod substrate, followed by drying at room temperature. With the above preparation conditions, the mass loading on graphite rod substrates was about ~0.4 mg cm^{-2}. On the other hand, nanostructures grew directly on metallic substrate (such as nickel foam) can be directly taken for electrochemical measurements. Herein the mass loading on the metallic nickel foam

could be calculated as follows (Tang et al. 2015).

$$\text{In brief, } loading = X\ mg * \frac{M_{NiX_2}}{M_X} \quad (2.9)$$

Where, X is the normalized weight difference for 1 cm^2 area of metallic foam before and after chalcogenization, M_{NiX_2} and M_X are the molar mass of NiX_2 (g/mol) and X (g/mol), respectively. The photograph of prepared electrodes for electrocatalytic measurements is pictured as Figure 2.8.

2.3.8 Evaluation parameters for the electrocatalytic activity

The following parameters are widely recognized for evaluating and comparing the electrocatalytic activities of catalysts.

2.3.8.1 Overpotential (η)

Due to thermodynamic considerations in a real system, an additional driving force in terms of an extra potential is required to proceed with the electrochemical reactions, such potential is known as the overpotential (denoted by the symbol η) (Man et al. 2011). For an electrocatalytic process, there are three sources of overpotential, viz., the activation overpotential, the concentration overpotential, and the overpotential due to the uncompensated solution resistance (R_S), which is the resistance of bulk electrolyte between reference and working electrodes (Zhang et al. 2005). Herein, concentration overpotential is caused by the concentration gradient of the reactants or the products in the bulk electrolyte and on the electrode surface. Further, the overpotential due to solution resistance (R_S) can be removed by carrying out Ohmic drop (iR) compensation, which is now available in the latest electrochemical workstations. However, manually iR compensation may also be carried out by multiplying resultant current density with the obtained value of solution resistance (R_S), followed by subtracting with the experimentally observed potential. The following equations can be used to calculate the iR compensated overpotentials for HER and OER electrocatalysts, respectively.

$$iR\ corr.overpotential\ \eta_{HER} = E_{RHE} - E_{iR} \quad (2.10)$$

$$iR\ corr.overpotential\ \eta_{OER} = E_{RHE} - E_{iR} - 1.229 \quad (2.11)$$

Recently, instead of the onset overpotential, the overpotential required to deliver a fixed current density (j) of 10 mA cm^{-2} (η^{10}) has now widely been accepted as an activity parameter to evaluate the performance of the electrocatalyst (Kibsgaard et al. 2014).

2.3.8.2 Tafel Slope

As discussed earlier, LSV is a half-cycle of the CV curve, which is generally recorded to study the electrocatalytic property of the sample under investigation. LSV measurements are performed in the negative potential window for the HER and in the positive potential window for the OER, at a lowest scan rate (5 mV s^{-1}). Further, LSV curves are iR compensated to obtain the exact overpotentials for the required electrocatalytic processes.

From the LSV curve, Tafel plots for the HER or OER process could be obtained by replotting the iR compensated LSV curve as a plot of log (J) Vs. Overpotential (η) and fit into the equation: $\eta = a + b\ log\ j$ (where b is the Tafel slope and j is the corresponding current density). The schematic of iR compensated LSV curve and Tafel plot is provided as Figure 2.9 below.

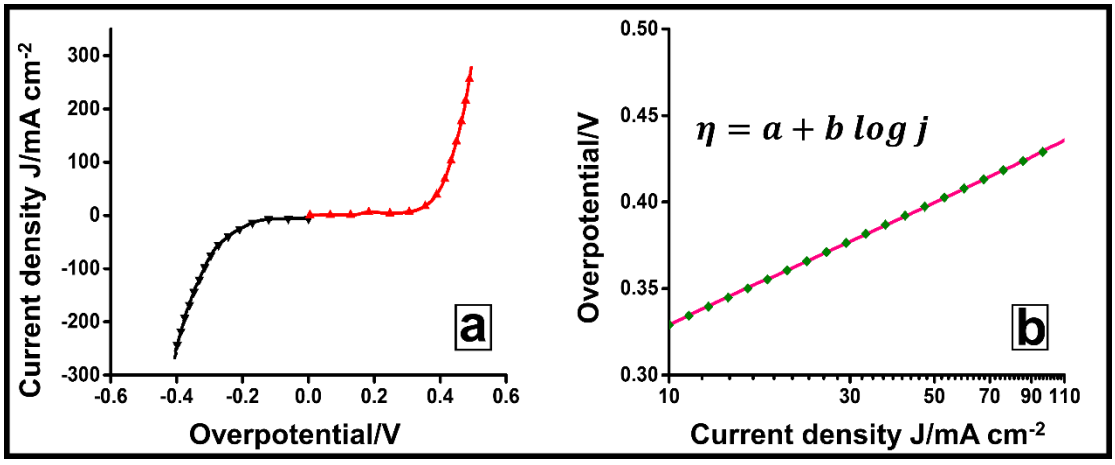

Figure 2.9 (a) Schematic of an iR compensated LSV curve and (b) Tafel plot.

The obtained slope on linear portion of the Tafel plot is termed as a Tafel slope, which could be expressed by the following equation:

$$\frac{d(\log J)}{d\eta} = 2.303RT\ \alpha nF \quad (2.12)$$

Where, α - charge transfer coefficient, R - the ideal gas constant, T - temperature, F - Faraday constant and n - number of electrons transferred (which is equal to 4 for the OER and 2 for the HER). This indicates a catalyst with a high charge-transfer ability should possess a small Tafel slope. This is also the foremost reason for choosing the Tafel slope as a primary activity parameter to determine the electrocatalytic activity.

2.3.8.3 Impedance spectroscopy

The kinetics of electrochemical water splitting characteristics (HER and OER) could be studied through EIS technique. The Nyquist plots (Z' Vs. –Z") of the electrocatalysts at different applied bias voltages are recorded in the required frequency range. Further, the Nyquist plots are extracted into frequency vs. total impedance plots (F vs. Z), from which the declination in total impedance with the variation of applied voltage bias is understood.

Further, the Nyquist plot of the HER/OER are generally semi circles, which are further understood by fitting them into electrochemical equivalent circuit (EEC). Further, EEC for the water-splitting process is usually a simple Randle's circuit, consisting of resistors (R_S – solution resistance, R_{CT} - charge transfer resistance) and capacitive component (constant phase element -Q_{CPE}). The Randle's circuit could be denoted by $R_S(R_{CT}Q_{CPE})$.

As the applied bias voltage is increased, it is believed that adsorption is facilitated and the charge-transfer process dominates. The dominance of the charge transfer process results in decreased resistance values (mainly R_{CT}) and thus the total impedance and Bode phase angle.

Impedance and resistances are related through the following equation:

$$Z(\omega) = R_S + \frac{R_{CT}}{1 + j\omega R_{CT} Q_{CPE}} = Z' + jZ" \quad (2.13)$$

Phase angle and impedance are related through the following equation:

$$\phi = tan^{-1} \frac{Z'}{Z"} \quad (2.14)$$

2.3.8.4 Electrocatalytic stability

The stability of an electrocatalyst can be established by subjecting it into CV cycling for a definite number of cycles or by subjecting the electrocatalyst to hold a fixed current or potential for the duration of several hours. The fixed potential stability test is known as chronoamperometry, while, fixed current density stability test is termed as chronopotentiometry. In the present work, chronopotentiometry is employed to study the stability of the prepared electrocatalysts.

Generally, chronopotentiometry is performed at a fixed current density of 10 mA cm^{-2} for the duration of 10 to 30 hours. While the higher current density stability tests (50 or 100 mA cm^{-2}) validate the robustness of material. Herein, the constant applied current leads to continuous reduction/oxidation of the ions at the electrode surface and thereby the continuous evolution of H_2/O_2. Potential attained by the electrodes in an E-t curve depends on the material, redox couple and may vary with time (Aikens 1983). The potential may also change either due to unavailability or decrease in the concentration of ions in solution or due to instability of the electrode material. On the other hand, if the potential moves close to zero, it may be related to activation of the material or the formation of secondary phases (Ming et al. 2016). Thus, the chronopotentiometric curve establish electrocatalytic stabilities of the material.

2.3.8.5 Electrochemically active surface area (ECSA)

The ECSA represents the internal surface area of the sample under investigation (Gholamvand et al. 2016). The ECSA could be determined through cyclic voltammetry curves at different scan rates, wherein no obvious Faradaic reactions take place.

Further, the slope value of the difference in double-layer charging current densities ($\Delta j = j_a - J_c$)Vs. scan rate (dV) plot represents the double-layer capacitance $2C_{dl}$, which is the ECSA by definition (Young et al. 2013). The double layer capacitances can be calculated using equation:

$$2C_{dl} = d(\Delta j)/dV \quad (2.13)$$

Where Δj is the difference in double layer charging current densities, dV is the scan rate and $d(\Delta j)/dV$ represents the slope of Δj Vs scan rate (dV) plot.

CHAPTER 3

COBALT CHALCOGENIDES FOR SUPERCAPACITOR ELECTRODES

In this chapter, the synthesis of porous cobalt chalcogenide ($CoTe_2$ and $CoSe_2$) nanostructures and their use as active electrodes for supercapacitors are presented. Structural and morphological analysis are conducted using powder X-ray diffraction, scanning electron microscopy and transmission electron microscopy and energy dispersive X-ray spectroscopy. Furthermore, electrochemical investigations as electrodes for supercapacitors were analyzed through cyclic voltammetry, galvanostatic charge-discharge and electrochemical impedance spectroscopy measurements. The superior electrochemical performances of these cobalt chalcogenide electrodes indicate their applicability for high-performance energy storage applications.

3.1 INTRODUCTION

Supercapacitors are one of the effective energy storage and conversion technology that is being actively investigated for being integrated in hybrid power devices and electronic vehicles (Wang et al. 2014). Several metal chalcogenides are synthesized employing different methods through hydrothermal, solvothermal and simple solution processing.

Further, various metal chalcogenides such as, CoSe (Wang et al. 2013b), $NiSe_2$ (Arul and Han 2016), MoS_2 (Huang et al. 2013), WS_2 (Ratha and Rout 2013), SnS (Jayalakshmi et al. 2004), Co_3S_4 (Wang et al. 2012), La_2S_3 (Patil et al. 2014) etc. have been reported as electrodes for supercapacitor applications in the symmetric/asymmetric configuration. Though most metal chalcogenide electrodes reported so far have exhibited good performance, electrodes fabricated using cobalt chalcogenides have attracted much attention owing to their excellent performance with multiple oxidation states and favorable structural diversity enabling redox reactions (Gao et al. 2013). Similarly, it is surprising to note that studies on performance of nanostructured cobalt sulfide (CoS) electrodes have been reported in plenty, while the pseudo-capacitive performance of electrodes based on cobalt telluride ($CoTe_2$) and cobalt selenide ($CoSe_2$) nanostructures have not been intensively investigated.

In this context, the main aim of the present work was to fabricate nanoporous cobalt

chalcogenide ($CoTe_2$ and $CoSe_2$) electrodes and study their pseudo-capacitive performance. For achieving this objective, $CoTe_2$ and $CoSe_2$ nanostructures were synthesized via the anion-exchange reaction between pre-synthesized hollow $Co(OH)_2$ nanosheets and tellurium/selenium ions under hydrothermal conditions. Electrochemical analysis of the electrodes fabricated using the as-transformed products at a scan rate of 5 mV s^{-1} indicated the specific capacitance of 951 F g^{-1} for $CoSe_2$ which was almost three times higher than the value obtained using $CoTe_2$ (360 F g^{-1}). Results indicate that as-transformed nanoporous cobalt chalcogenides can be suitable candidate for the design and development of high-performance supercapacitor electrodes.

3.2 SYNTHESIS OF COBALT CHALCOGENIDES

3.2.1 Synthesis of hexagonal cobalt hydroxide nanosheets

Cobalt hydroxide ($Co(OH)_2$) nanosheets were synthesized by following the procedure reported elsewhere (Zhao et al. 2014). In a typical process, a pink colored solution was formed by adding 0.8728 g (3 mM) of cobalt nitrate hexahydrate ($Co(NO_3)_2.6H_2O$) in 120 mL of DI water at room temperature. Next, 3 mL of triethylamine ($C_6H_{15}N$) was added dropwise to the pink solution which resulted in an immediate color change to dark blue. Final solution was made to reach a total volume of 240 mL by adding 117 mL of excess DI water. Three Teflon-lined stainless-steel autoclaves (100 mL capacity) were added with 80 mL of the final solution, sealed and placed in an oven at 180 °C for 24 h. After the autoclaves cooled down naturally, the black colored precipitates were collected by washing with excess DI water and ethanol under centrifugation, after which they dried were overnight at 60 °C.

3.2.2 Chemical transformation of $Co(OH)_2$ into $CoTe_2$ and $CoSe_2$ nanostructures

The chemical transformation of hexagonal $Co(OH)_2$ into porous $CoTe_2$ and $CoSe_2$ nanosheets was achieved through an anion-exchange-reaction, as described elsewhere (Zhao et al. 2014). Typically, 0.063 g (0.75 mM) of pre-synthesized $Co(OH)_2$ nanosheets were dispersed in 80 mL of DI water to make a homogeneous solution, after which 0.204 g (1.6 mM) of tellurium (Te) powder and 0.181 g (4.8 mM) of sodium

borohydride ($NaBH_4$) reducing agent were added under constant stirring. The finally obtained solution was transferred into a 100 mL Teflon-lined stainless steel autoclave, followed by the hydrothermal reaction at a temperature of 180 °C for 15 h. After the reaction, the autoclave was allowed to cool down naturally and the collected products were washed several times and then dried overnight at 60 °C.

$CoSe_2$ nanosheets were synthesized by following the same procedure as described above just by replacing tellurium (Te) powder with selenium (Se) powder.

3.3 RESULTS AND DISCUSSIONS

3.3.1 Physiochemical analysis

The XRD patterns of the as-synthesized $Co(OH)_2$ and the chemically transformed $CoTe_2$ and $CoSe_2$ products recorded in the 2θ range of 10 to 70º are shown in Figure 3.1. The diffraction peaks in the XRD pattern of $Co(OH)_2$ match well with the hexagonal structure of β-$Co(OH)_2$ with lattice constants a = 3.18 Å and c = 4.65 Å, which are consistent with JCPDS card no. 30-0443.

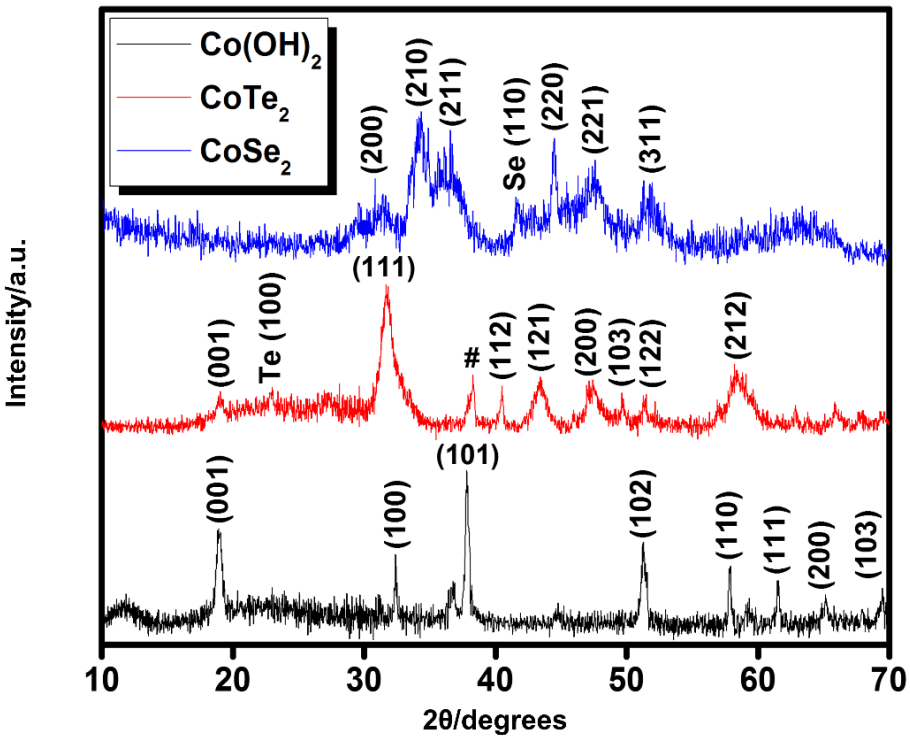

Figure 3.1 XRD pattern of the hexagonal $Co(OH)_2$ precursor and the chemically transformed $CoTe_2$ and $CoSe_2$ nanostructures.

On the other hand, the XRD patterns of $CoTe_2$ and $CoSe_2$ nanostructures after anion-exchange-reaction are quite different from those of $Co(OH)_2$, indicates their formation through chemical transformation under hydrothermal conditions. XRD patterns of $CoTe_2$ can be indexed to the orthorhombic phase (JCPDS card no. 74-0425) with lattice constants a = 3.88 Å, b = 5.3 Å and c = 6.29 Å, while the XRD peaks of $CoSe_2$ can be indexed to its cubic phase with lattice constants $a = b = c$ = 5.85 Å (JCPDS card no. 09-0234). Although phase pure structures of $CoTe_2$ and $CoSe_2$ are formed through anion-exchange-reaction, some additions peaks corresponding to unreacted Te/Se ions and $Co(OH)_2$ appear in the XRD patterns, which can be attributed to the incomplete chemical transformation. Further, the consistent appearance of the broad and low intensity peaks in the XRD pattern of $CoTe_2$ and $CoSe_2$ in comparison to $Co(OH)_2$ reveals their polycrystalline nature and the possibility of a porous hollow structure, which can be revealed through TEM analysis.

FESEM image as shown in Figure 3.2a confirm the hexagonal shape and the two dimensional sheet like morphology of as-synthesized $Co(OH)_2$. Further, FESEM image clearly reveals the uniformly structured $Co(OH)_2$ nanosheets with an average edge thickness of ~15 nm and a mean width of ~150 nm. EDS analysis as shown in Figure 3.2b confirms their purity. As observed from Figure 3.2c the hexagonal morphology of $Co(OH)_2$ were found to be flawed during TEM analysis, which can be attributed to the overlapping of two or more nanosheets on top of each other due to aggregation. However, TEM analysis clearly reveal the nanosheet like morphology of $Co(OH)_2$ and the phase purity of hexagonal β-$Co(OH)_2$ is confirmed from the HRTEM image (Figure 3.2d) with the lattice spacing value of ~2.4 Å corresponding to the prominent (101) plane, which is consistent with XRD results. On the other hand, the spot type SAED pattern (see APPENDIX I) reveals the single crystalline nature of $Co(OH)_2$ nanosheets and further supports the XRD results. The anion-exchange reaction of $Co(OH)_2$ nanosheets with selenium and tellurium ions under hydrothermal conditions lead to the generation of cobalt telluride and cobalt selenide nanostructures as shown in Figure 3.3 and Figure 3.4, respectively. Morphological investigations on the product of the anion-exchange reaction of $Co(OH)_2$ with tellurium ions using FESEM (Figure 3.3a) and TEM (Figure 3.3c) indicate the formation of a mixed morphology of $CoTe_2$ mostly consisting of nanorods along with some nanoparticles.

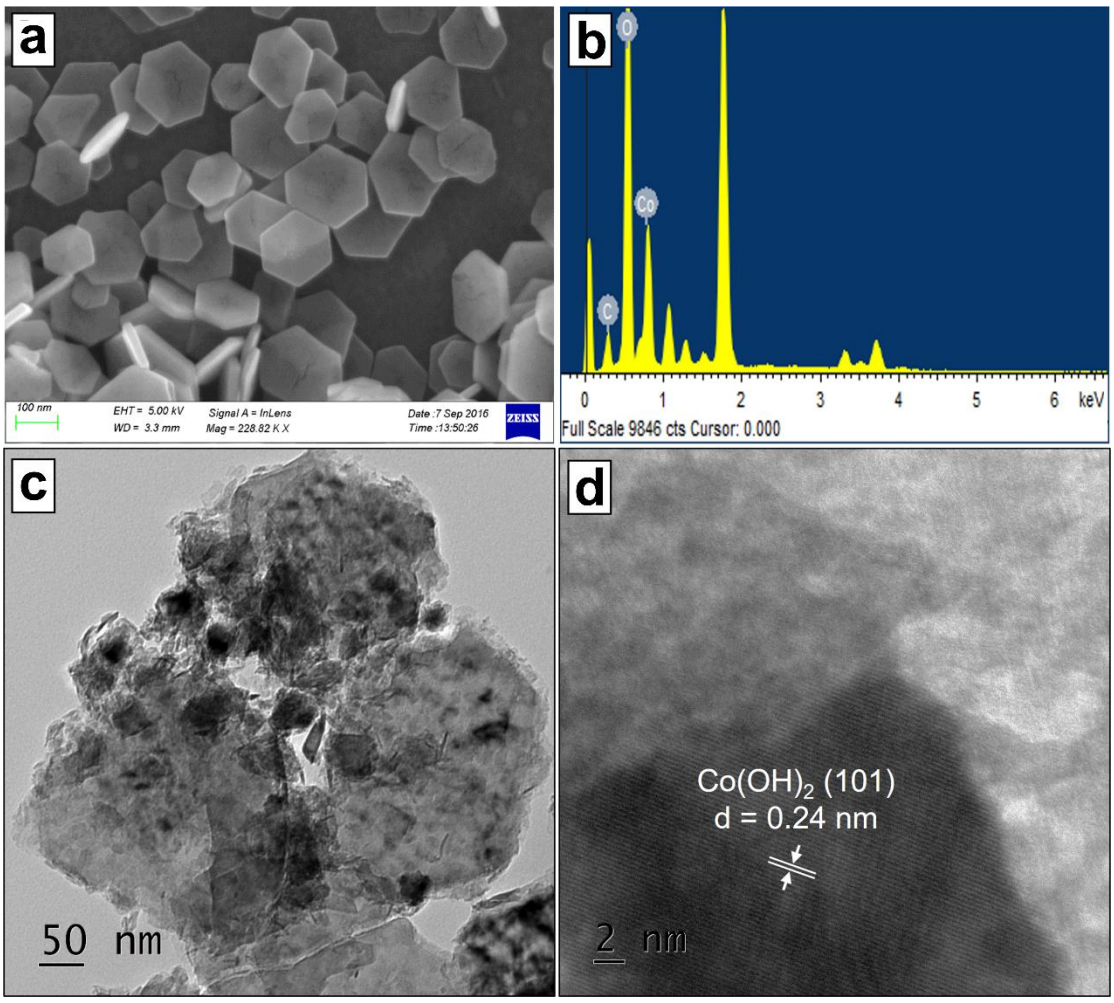

Figure 3.2 (a) FESEM image, (b) EDS spectra, (c) TEM image and (f) HRTEM image showing the fringes of the $Co(OH)_2$ nanosheets.

On the other hand, the FESEM image (Figure 3.4a) and TEM image (Figure 3.4c) analysis on the transformed product via anion-exchange reaction of $Co(OH)_2$ with selenium ions indicate the formation of a $CoSe_2$ nanosheets with a hollow nanoporous structure. Although EDS analysis on $CoTe_2$ (Figure 3.3b) and $CoSe_2$ (Figure 3.4b) reveal the presence of elemental peaks corresponding to cobalt, tellurium and selenium confirm the purity of the as-transformed products, they also indicate the presence of peaks corresponding to elemental oxygen, which can be attributed to the existence of some non-transformed $Co(OH)_2$, as confirmed from XRD analysis. Further, HRTEM analysis was performed to track the transformation of $Co(OH)_2$ nanosheets to $CoTe_2$ and $CoSe_2$.

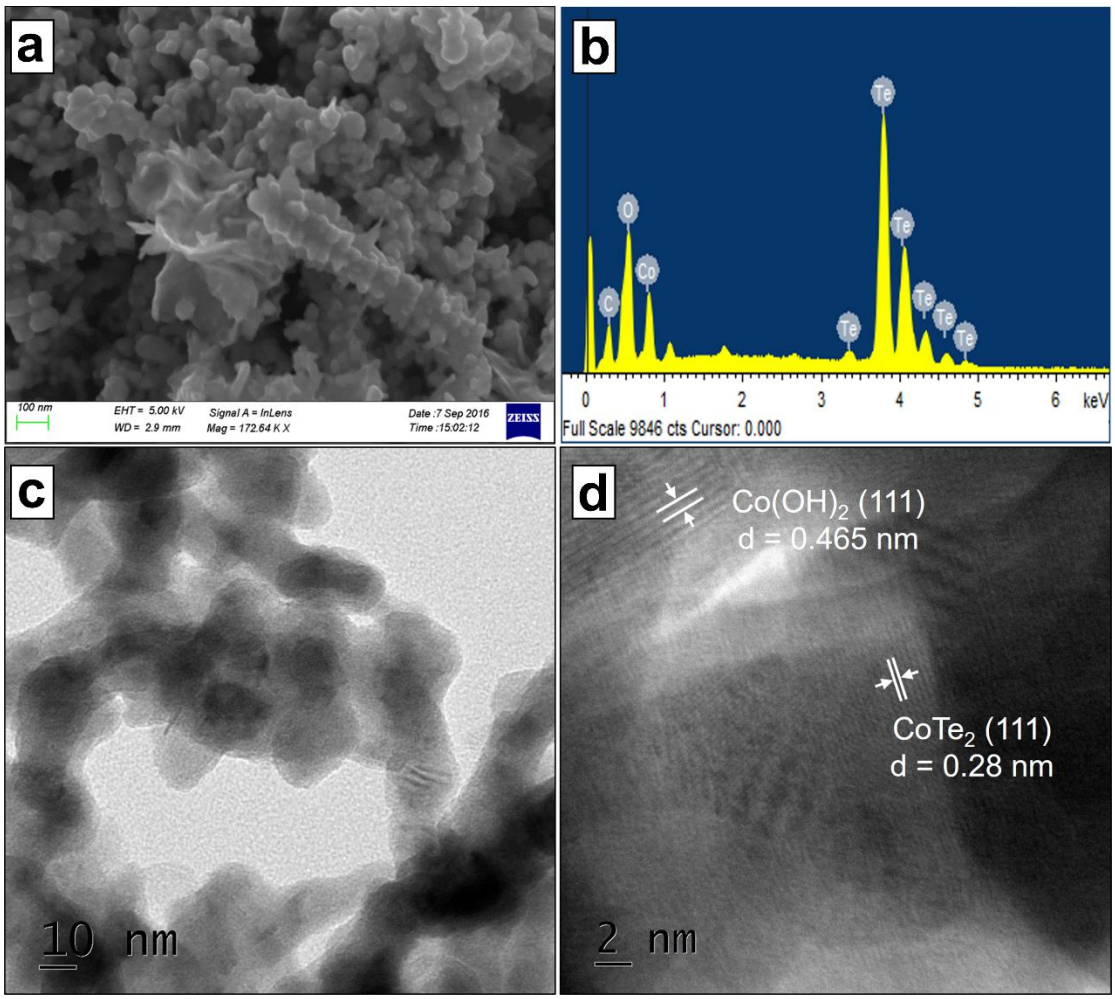

Figure 3.3 (a) FESEM image, (b) EDS spectra, (c) TEM image and (d) HRTEM image showing the fringes of the $CoTe_2$ nanostructures.

As seen from Figure 3.3d, the fringes with a lattice spacing value of ~2.8 Å corresponding to the (111) plane of orthorhombic $CoTe_2$ is analogous to its highly intense XRD peak. Similarly, the fringes with lattice spacing values of ~2.6 Å and ~1.76 Å observed from Figure 3.4d corresponding to the (210) and (311) planes, respectively are also analogous to their highly intense XRD peaks of cubic $CoSe_2$. On the other hand, HRTEM analysis on both $CoTe_2$ (Figure 3.3d) and $CoSe_2$ (Figure 3.4d) interestingly reveals fringes with a lattice spacing value of 4.6 Å that can be attributed to the (111) plane of hexagonal β-$Co(OH)_2$. Results of the HRTEM analysis sheds light on the growth of the nanoporous layer of $CoSe_2$ through the lattice mismatch induced strain release as discussed in detail elsewhere (Zhao et al. 2014). Existence of the hexagonal β-$Co(OH)_2$ phase in both $CoTe_2$ and $CoSe_2$ can be attributed to the

characteristic ability of the (111) plane to exhibit high tensile strength and modulus of elasticity, owing to which it remains intact and un-transformable under hydrothermal conditions. The ring type SAED patterns of both $CoTe_2$ and $CoSe_2$ (see APPENDIX I) indicating the poly-crystalline nature of the as-transformed products are commensurate with the XRD results.

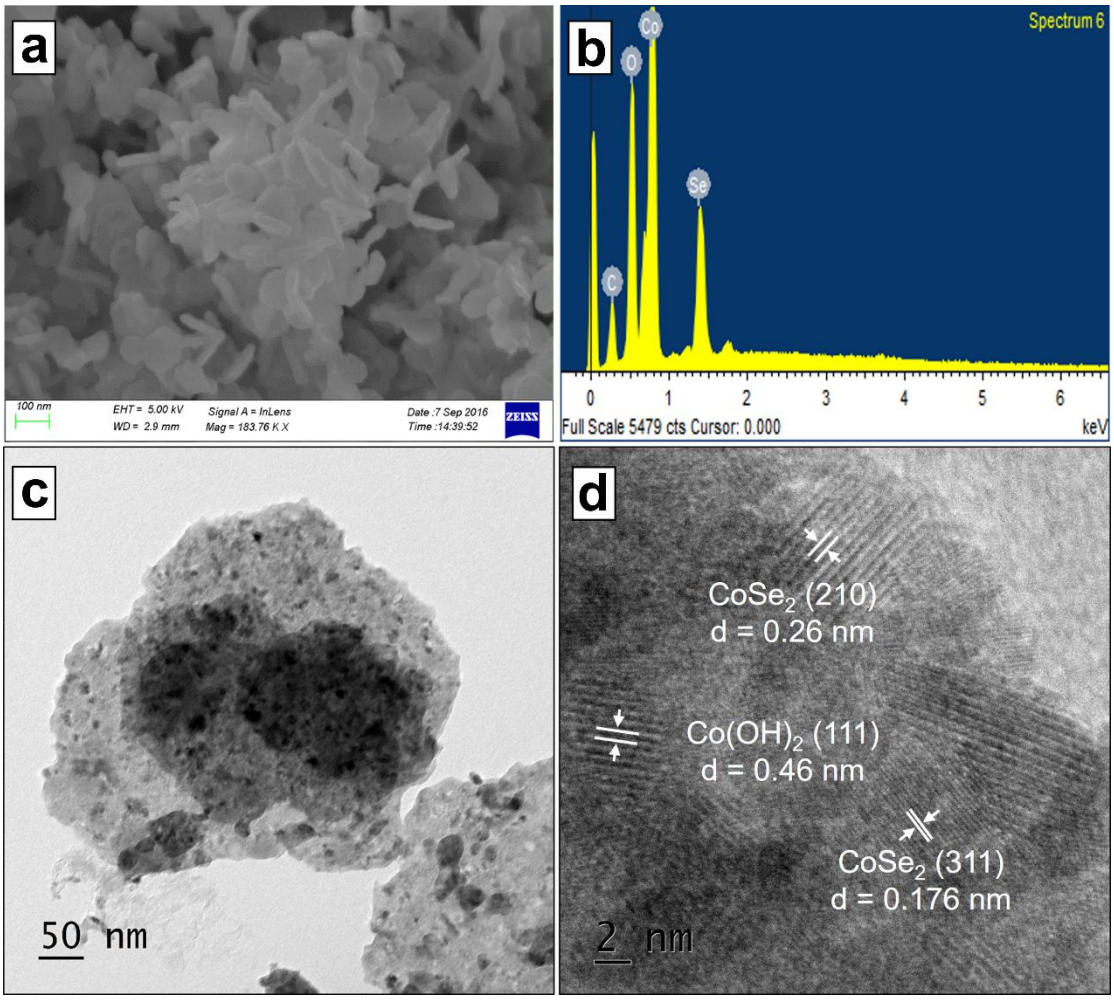

Figure 3.4 (a) FESEM image, (b) EDS spectra, (c) TEM image and (d) HRTEM image showing the fringes of the $CoSe_2$ nanostructures.

3.3.2 Electrochemical measurements for supercapacitor applications

The electrochemical performance of $CoTe_2$ and $CoSe_2$ electrodes are electrochemically characterized through studies conducted using CV, GCD and EIS techniques. Detailed description of electrode preparations for electrochemical measurements are provided in section 2.3.5. Further, all of the electrochemical measurements are performed with 1 M

KOH as the electrolyte. KOH was selected as an electrolyte owing to the smaller hydration sphere volume of K^+ ions, promoting higher mobility for redox reactions and effective interaction of ions with the electrode surface enabling rapid storage of charges (Sankar et al. 2012). Figure 3.5a-b shows the typical CV curves of $CoTe_2$ and $CoSe_2$ electrodes recorded in the potential window range of -0.2 to 0.5 V Vs. SCE at various scan rates (5-100 mV s^{-1}).

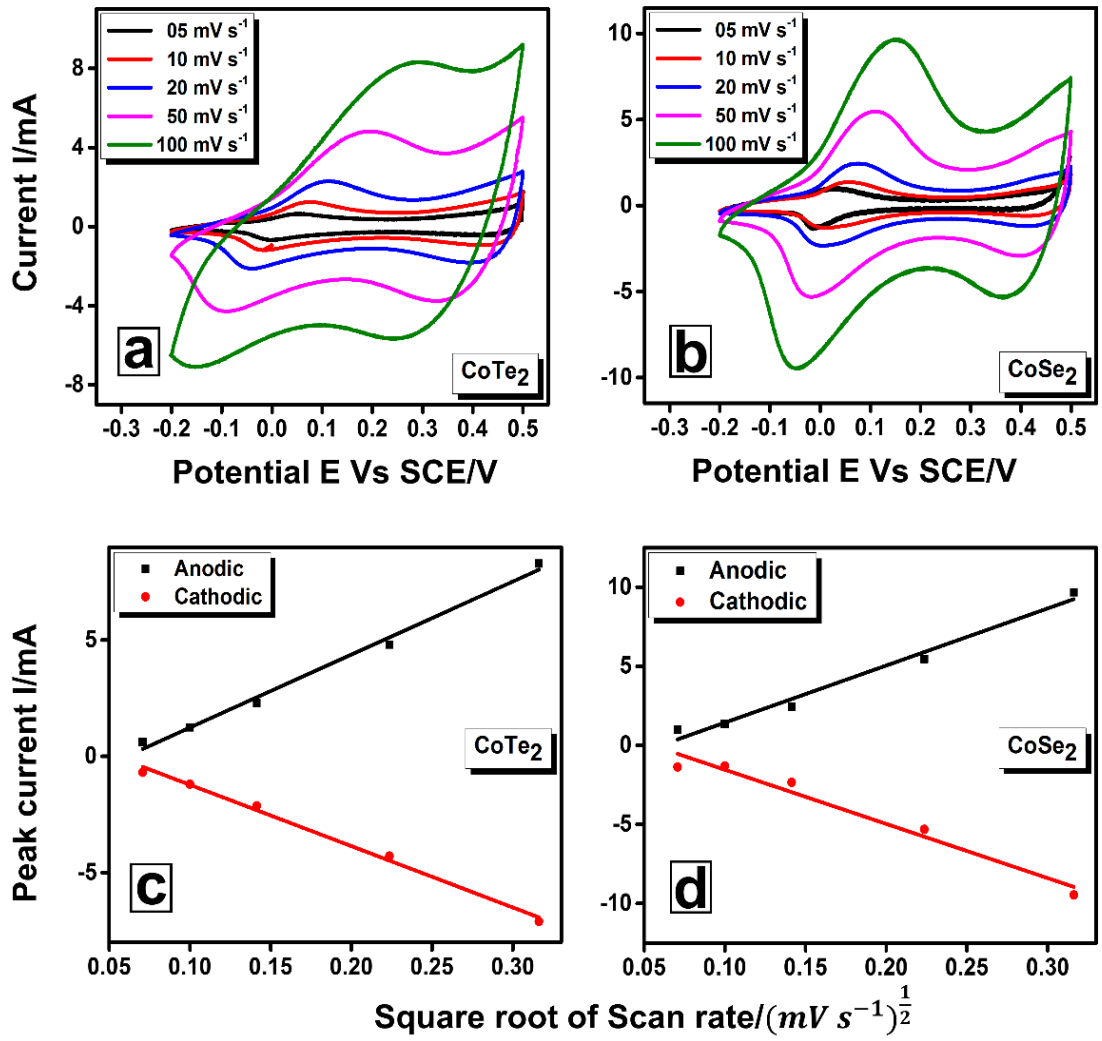

Figure 3.5 Cyclic voltammograms of (a) $CoTe_2$ and (b) $CoSe_2$ electrodes at different scan rates, (c) and (d) represents peak current vs. square root of scan rate plots corresponding to $CoTe_2$ and $CoSe_2$ electrodes for calculating the diffusion coefficients.

The observed cyclic voltammograms for both $CoTe_2$ and $CoSe_2$ electrodes suggest their good reversibility of oxidation and reductions processes, i.e. in other words their

pseudo-capacitive characteristics, which differ from the nearly rectangular CV curves of an electrochemical double-layer capacitor (Bu and Huang 2015). Also, the anodic and cathodic peak potentials exhibiting enhanced shifts in the negative and positive directions with respect to the increase in scan rates indicating increment of the area of the CV curves, suggests the improved charge storage capability of the electrodes. As seen from Figure 3.5b, it is worth noting that $CoSe_2$ electrode in particular exhibited more prominent oxidation-reduction peaks as compared to $CoTe_2$ (Figure 3.5a).

At a scan rate of 5 mV s^{-1}, the calculated value of specific capacitance using equation 2.5 for $CoSe_2$ electrodes are 951 F g^{-1}, which is almost three times higher than those of $CoTe_2$ electrodes (360 F g^{-1}). Such high values of specific capacitances are rarely observed in metal chalcogenides electrodes (Wang et al. 2013a) as shown in Table 3.1, which can essentially be attributed to the nanoporous 2D sheet like structure of the as-transformed $CoSe_2$ product obtained via anion-exchange reaction providing numerous electro-active sites for redox reactions (Zhang et al. 2013). Although, the value of the specific capacitance delivered by $CoTe_2$ electrode is better than those of other metal tellurides such as La_2Te_3 (Patil et al. 2017) , $TaTe_2$ (Chakravarty et al. 2015) and Sm_2Te_3 (Kumbhar et al. 2016) reported in literature, the morphological changes during the anion-exchange reaction leading to shape evolution in the form of nanorods with lesser porosity can be attributed to its poor performance in comparison to the perfectly transformed layered 2D nanoporous $CoSe_2$ electrodes. The large pore diameter of 2D $CoSe_2$ nanosheets (~24.9 nm) in comparison to $CoTe_2$ nanorods (~19.1 nm) revealed through BJH measurements (see APPENDIX II) evidences the superior electrochemical performance of $CoSe_2$ electrodes. On the other hand, the CV curves of $Co(OH)_2$ electrodes displayed the similar oxidation-reduction peaks (see APPENDIX III) like $CoTe_2$ and $CoSe_2$ electrodes, delivering a specific capacitance of 226 F g^{-1} at a scan rate of 100 mV s^{-1}.

Linear relationship was established from the plots between the redox peak currents and the square root of scan rate (Figure 3.5c-d), which indicates the redox reaction kinetics are likely to be diffusion controlled (Wang et al. 2011). Increase in anodic peak current along with the subsequent decrease in the cathodic peak current with respect to the increase in the scan rate, not only indicates the fast-redox reactions at the interface of

electrode and the electrolyte, it also suggests the low resistance of the electrode materials.

The diffusion of ions in the nanopores of the materials can be studied through Randles–Sevcik equation written as, $i_p = (2.69 * 10^5) * n^{\frac{3}{2}} ACD^{\frac{1}{2}} v^{\frac{1}{2}}$ (3.1)

Where i_p is the peak current, n is the number of electrons transferred (n=1), A is the electrode area (cm^2), C is the concentration (mol cm^{-3}) and D is the diffusion coefficient (cm^2 s^{-1}). In another form; where m is the slope, obtained by linearly fitting i_p as a function of $v^{\frac{1}{2}}$. The values of the ion diffusion coefficient calculated from the slope are found to be 4.77×10^{-8} cm^2 s^{-1} for $CoTe_2$ and 1.584×10^{-8} cm^2 s^{-1} for $CoSe_2$.

Table 3.1. Comparison of the specific capacitances of the nanoporous $CoTe_2$ and $CoSe_2$ electrodes with other metal chalcogenide nanostructures reported in literature.

Material	**Specific capacitance**	**Electrolyte**	**Scan rate**	**Reference**
2D $NiSe_2$	75.1 F g^{-1}	1 M KOH	2 mV s^{-1}	(Arul and Han 2016)
WS_2-rGO	350 F g^{-1}	1 M Na_2SO_4	2 mV s^{-1}	(Ratha and Rout 2013)
Co_3S_4/rGO	521.7 F g^{-1}	2 M KOH	5 mV s^{-1}	(Wang et al. 2012)
CoS_2-g	253.1 F g^{-1}	6 M KOH	5 mV s^{-1}	(Wang et al. 2012)
La_2Se_3	363 F g^{-1}	0.8M $LiClO_4$	5 mV s^{-1}	(Patil et al. 2016)
La_2Te_3	194 F g^{-1}	1M $LiClO_4$	5 mV s^{-1}	(Patil et al. 2017)
$CoTe_2$	360 F g^{-1}	1 M KOH	5 mV s^{-1}	Present work
$CoSe_2$	951 F g^{-1}	1 M KOH	5 mV s^{-1}	Present work

At higher scan rates the CV curves exhibit an increase in peak current, which could be due to the over potential for ion transport at the interface between the electrode and electrolyte. Further, as seen from Figure 3.6a, the gradual decrease in the values of specific capacitance for both $CoTe_2$ and $CoSe_2$ could be attributed to the charge resistive behavior of the electrode materials at higher scan rates and also due to the inadequate time for ion diffusion at the electrode surface (Wolfart et al. 2016). The values of specific capacitance (F g^{-1}) of the electrodes at various scan rates are summarized in Table 3.2.

Table 3.2. Specific capacitances (F g^{-1}) of the prepared nanostructured cobalt chalcogenide electrodes at different scan rates (mV s^{-1}).

Scan rate (mV s^{-1})	Specific capacitance (F g^{-1})	
	$CoTe_2$	$CoSe_2$
5	360.1	951.1
10	337.8	609.1
20	302.8	542.7
50	267.6	503.2
100	234.2	469.9

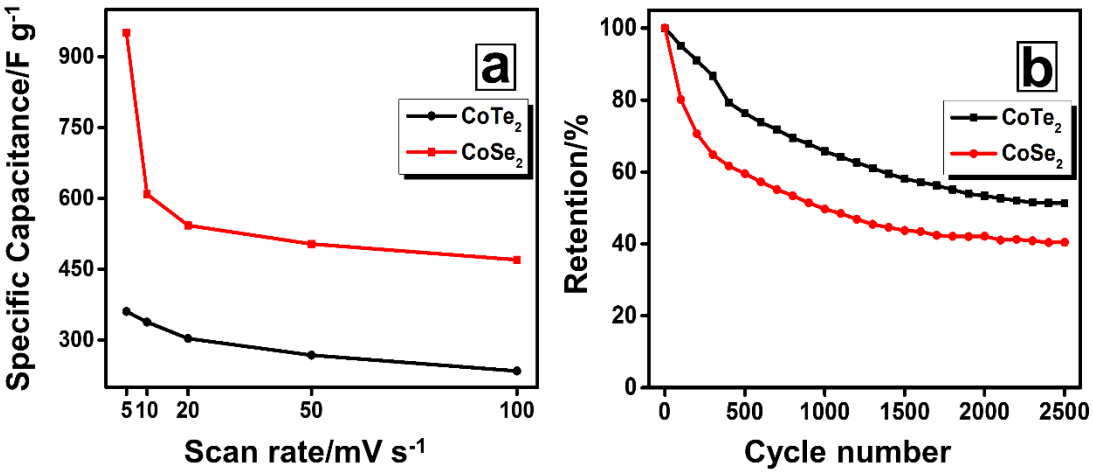

Figure 3.6 (a) The variation of specific capacitance with respect to scan rates and (b) Cycle life of $CoTe_2$ and $CoSe_2$ electrodes at a scan rate of 50 mV s^{-1} for 2500 CV cycles.

The electrochemical cyclic stability of $CoTe_2$ and $CoSe_2$ electrodes was examined through CV measurements at a scan rate of 50 mV s^{-1} for 2500 cycles as shown in Figure 3.6b. Results indicate that $CoTe_2$ retains ~52% of the initial capacitance while $CoSe_2$ shows the retention of ~42% at 2500 cycles. Both $CoTe_2$ and $CoSe_2$ electrodes exhibited reduction in their initial capacitance until ~1500 cycles, which can be attributed to the blocking of the pores inducing lower rate of ion adsorption during the redox processes at a higher scan rate of 50 mV s^{-1} (Perera et al. 2015). However, the loss was comparatively minimal after 1500 CV cycles for both $CoTe_2$ and $CoSe_2$ electrodes which reveals their superior stability and their capability to retain a constant capacitance over longer CV cycles. Whereas, the cyclic stability of $Co(OH)_2$ electrodes

was rationally poor since it could retain only 23% of its initial capacitance after 500 CV cycles (APPENDIX II).

The electrochemical performance of the electrodes were also analyzed through GCD technique to further understand the pseudo-capacitive behavior of the electrodes. The GCD curves obtained in the potential range of -0.2 to 0.5 Vs. SCE in 1 M KOH electrolyte using $CoTe_2$ and $CoSe_2$ electrodes are shown in Figure 3.7a-b, respectively. GCD curves obtained using $CoTe_2$ electrode exhibit a typical saw tooth shape, while $CoSe_2$ exhibited a little deviation from symmetry, indicating its pseudo-capacitive behavior and superior capacitance. The superior performance of the $CoSe_2$ electrode in comparison to $CoTe_2$ can be attributed to its nanoporous 2D sheet like morphology with higher pore size.

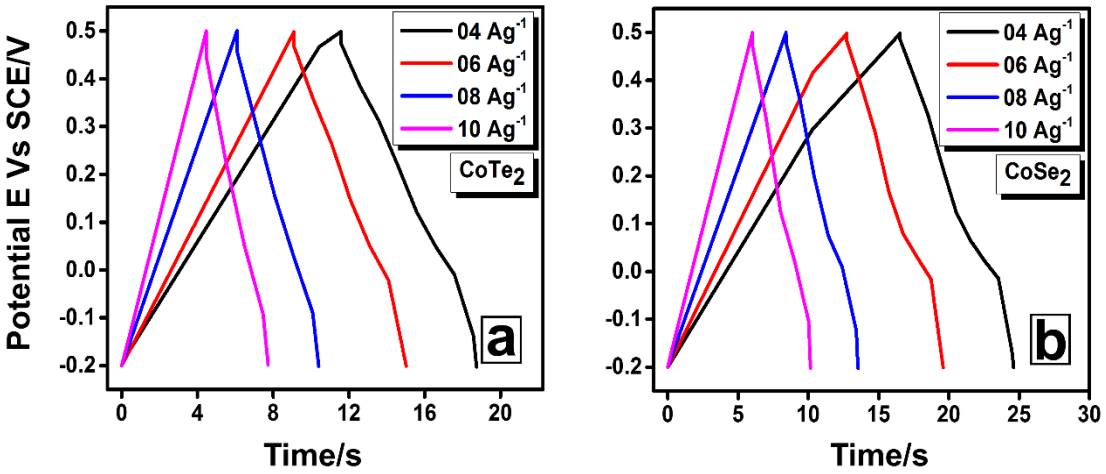

Figure 3.7 Galvanostatic charge-discharge curves of (a) $CoTe_2$ and (b) $CoSe_2$ electrodes at various current densities.

The EIS measurements on $CoTe_2$ and $CoSe_2$ electrodes were performed in the frequency range of 30 kHz to 1 mHz with an applied bias voltage of 10 mV and the Nyquist plots are presented in Figure 3.8a. The values of Rs for $CoTe_2$ and $CoSe_2$ electrodes were estimated to ~1.43 Ω and ~1.41 Ω, respectively. Also, the R_{CT} obtained for $CoTe_2$ electrodes is ~4.1 Ω and ~9.2 Ω for $CoSe_2$ electrodes. Although Rs values are identical for both the electrodes, the R_{CT} is almost double for $CoSe_2$ electrodes. While, the value of Faradaic pseudo-capacitance for $CoSe_2$ electrode is almost three times higher than that of $CoTe_2$, owing to the nanoporous 2D sheet like structure of

$CoSe_2$, enabling improved electrolyte penetration and ion diffusion. Further, Figure 3.8b describes the bode plot of both $CoTe_2$ and $CoSe_2$ electrodes. $CoTe_2$ exhibits phase angle of -66º, while $CoSe_2$ electrodes exhibit phase angle of -41º, confirms the redox type charge storage behavior (Biswal et al. 2013).

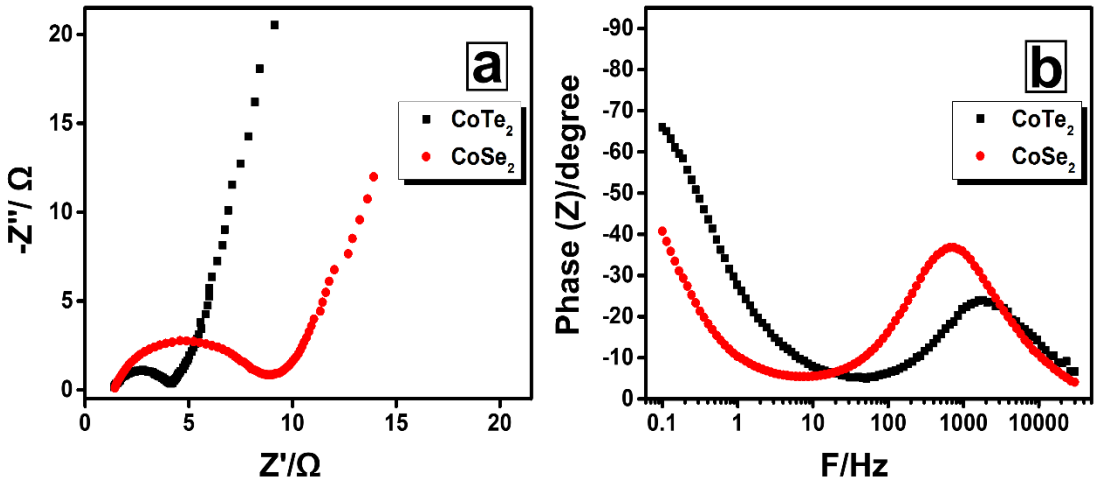

Figure 3.8 (a) Nyquist plots of the electrodes fabricated using $CoTe_2$ and $CoSe_2$ nanosheets and their corresponding Bode phase angle plots (b).

3.4 SUMMARY

$CoTe_2$ and $CoSe_2$ nanostructures were prepared by the transformation of pre-synthesized hexagonal $Co(OH)_2$ nanosheets via anion-exchange reaction with Te/Se ions under hydrothermal conditions. Successful transformation of $Co(OH)_2$ hexagonal nanosheets to $CoTe_2$ and $CoSe_2$ nanostructures through anion-exchange reaction enabled the formation of a nanoporous layer and also strongly enhanced their physiochemical properties, which were realized through CV and GCD studies conducted on the as-fabricated electrodes. Unlike $CoTe_2$ that formed nanorods shaped structures, 2D nanoporous $CoSe_2$ were formed perfectly replicating the layered hexagonal structure of $Co(OH)_2$ under hydrothermal conditions. Synergistic factors such as 2D nanoporous layer formation, good electronic conductivity and shorter diffusion paths for ion exchange enabled the $CoSe_2$ electrode to exhibit an excellent specific capacitance value of 951 F g^{-1}, which was three times higher in comparison to $CoTe_2$ electrode (360 F g^{-1}) at a scan rate of 5 mV s^{-1}. However, both $CoTe_2$ and $CoSe_2$ electrodes exhibited good capacitance retention capability for 2500 CV cycles.

CHAPTER 4

NICKEL CHALCOGENIDES FOR ELECTROCHEMICAL WATER-SPLITTING

In this chapter, the synthesis of nickel chalcogenide ($NiTe/NiTe_2$, $NiSe_2$ and NiSe) nanostructures and their use as electrocatalysts are presented. $NiTe/NiTe_2$ nanosheets are used as electrocatalyst for the HER and OER. Whereas, $NiSe_2$ nanosheets and NiSe nanoflakes were used as electrocatalyst for the HER. Structural and morphological analysis are conducted using powder X-ray diffraction (XRD), X-ray photoelectron spectroscopy, scanning electron microscopy (SEM) and transmission electron microscopy (TEM) and energy dispersive X-ray spectroscopy. Electrochemical measurements as electrocatalyst for HER and OER are performed through linear sweep voltammetry, constant current chronopotentiometry and electrochemical impedance spectroscopy methods. The large current values at small overpotentials and their promising stabilities make them attractive as promising electrocatalysts for water-splitting reactions.

4.1 INTRODUCTION

Advanced materials for water splitting are central for the progress of clean and renewable energy sources. Electrochemical water splitting are governed by two half-cell reactions hydrogen evolution reaction (HER) and oxygen evolution reaction (OER), of which, OER is energetically challenging owing to the sluggish electrode kinetics (Cheng et al. 2015). Present works mainly aim at decreasing the overpotential and improving the energy conversion efficiency of various electrocatalysts used in water splitting reactions.

A variety of nickel based compounds, such as oxides, hydroxides, phosphides and chalcogenides are demonstrated with their excellent electrocatalytic activities owing to their high abundance, efficiency and ease of synthesis. Among nickel chalcogenide series (sulphides, selenides and tellurides), selenides are believed to deliver the best catalytic efficiency owing to its low resistivity, small bandgap, higher degree of covalency and the better band alignment with water redox levels (Masud et al. 2016). In the regard, the present chapter describes the hydrothermal synthesis of nickel

chalcogenide nanostructures, namely nickel telluride and nickel selenide nanosheets via an anion exchange reaction between pre-synthesized nickel hydroxide ($Ni(OH)_2$) nanosheets and chalcogen ions (Te and Se). Furthermore, as an improved method of synthesis, selenization of metallic nickel foam (NF) to form nickel selenide nanoflakes via hydrothermal method are also discussed.

Anion-exchange reaction between $Ni(OH)_2$ nanosheets and Te ions for 15 hours, indicated the formation of mixed phase nickel tellurides ($NiTe/NiTe_2$) consisting on nanosheets. $NiTe/NiTe_2$ as an electrocatalyst for the HER revealed an onset potential of -422 mV and overpotential of -432 mV to deliver 20 mA cm^{-2} current density, with a Tafel slope value of 87.4 mV dec^{-1}. In contrast, $NiTe/NiTe_2$ required an onset overpotential of 679 mV and 745 mV to deliver 10 mA cm^{-2} current density for the OER, with a Tafel slope of 151 mV dec^{-1}.

In the subsequent section, the anion-exchange synthesis of $NiSe_2$ nanosheets and selenization of nickel foam to form NiSe nanoflakes are discussed. $NiSe_2$ nanosheets were derived from $Ni(OH)_2$ via a anion-exchange reaction for 15 hours with Se ions. On the other hand, NiSe nanoflakes were synthesized by the selenization of nickel foam with a reaction time of only 2 hours. Tested as an electrocatalyst for the HER, $NiSe_2$ nanosheets and NiSe nanoflakes could afford a benchmark current density of 10 mA cm^{-2} at an overpotential of 198 mV and 217 mV, respectively. The measured Tafel slope values of NiSe nanoflakes are 28.6 mV dec^{-1}, which is about three times lower as compared with $NiSe_2$ nanosheets (72.1 mV dec^{-1}). These results indicated the HER kinetics of NiSe nanoflakes are at par with state-of-the-art Pt/C catalyst and complimented with short synthesis time of only 2 hours. Further, both nickel selenides exhibit ultra-long term stability for 30 h as evident from constant current chronopotentiometry and electrochemical impedance spectroscopy results.

4.2 SYNTHESIS OF NICKEL CHALCOGENIDES

4.2.1 Synthesis of hexagonal nickel hydroxide ($Ni(OH)_2$) nanosheets

The synthesis of $Ni(OH)_2$ nanosheets were adapted from earlier literature (Zhao et al. 2014), with little modifications as described below. In a typical process, a green colored solution was formed by adding 0.5416 g (3.5 mM) of nickel sulphate ($NiSO_4 \cdot 6H_2O$) in

70 mL of DI water at room temperature. Next 10.5 mL of 2 M ammonia solution (NH_4OH) was added to form an opaque dispersion under stirring for 20 min. After which the solution was transferred into a 120 mL Teflon-lined stainless-steel autoclave, sealed and the hydrothermal process was carried out at a temperature of 180 °C for 24 hours. After the autoclave cooled down naturally, the green colored precipitates were collected by washing with excess of DI water, and then dried overnight at 60 °C.

4.2.2 Synthesis of nickel telluride ($NiTe/NiTe_2$) and nickel selenide ($NiSe_2$) nanosheets

Anion-exchange reaction was employed for the chemical transformation of hexagonal $Ni(OH)_2$ into porous $NiTe/NiTe_2$ nanosheets. Typically, 0.0278 g (0.3 mM) of pre-synthesized $Ni(OH)_2$ nanosheets were dispersed in 80 mL of DI water to obtain a uniform mixture, later 0.0765 g (0.6 mM) of Te powder and 0.068 g (1.8 mM) of sodium borohydride ($NaBH_4$) were added under constant stirring. The finally obtained solution was transferred into a 120 mL Teflon-lined stainless-steel autoclave. The autoclave was sealed and kept in an oven at a temperature of 180 °C for 15 h. After the reaction, the autoclave could cool down naturally; the collected products were washed several times with excess DI water and ethanol, and then dried overnight.

On the other hand, $NiSe_2$ nanosheets were synthesized by following the same procedure as described above by replacing Te powder with Se powder.

4.2.3 Synthesis of nickel selenide (NiSe) nanoflakes by the selenization of nickel surface

Nickel selenide (NiSe) nanoflakes were synthesized by the direct selenization of the nickel surface. In brief, about ~1.8 mg of selenium metal powder were added to 5 mL of hydrazine hydrate ($N_2H_4.2H_2O$), followed by ultra-sonication for 10 min. The sonicated mixture was then transferred to a 50 mL Teflon-lined autoclave containing 35 mL of DI water. Next, two pieces of pre-cleaned Ni foam of dimensions (2.5 cm × 1 cm) were introduced into the autoclave, sealed and the hydrothermal process was carried out for a short interval of 2 h at a temperature of 180 °C. After the reaction, the selenized nickel foams were collected, followed by washing and drying.

4.3 RESULTS AND DISCUSSIONS

4.3.1 Physiochemical analysis of nickel tellurides

The XRD patterns of $Ni(OH)_2$ and anion-exchange product nickel telluride nanosheets were analyzed and indexed as shown in Figure 4.1. The diffraction peaks in the XRD pattern of $Ni(OH)_2$ nanosheets match well with the hexagonal crystal structure with lattice constants a = 2.12 Å and c = 4.60 Å, which are in agreement with the standard JCPDS card no. 014-0117. Further, the XRD pattern of nickel telluride nanosheets indicate their formation in mixed phase viz., NiTe and $NiTe_2$, along with some non-transformed precursor nickel hydroxide (#) and unreacted Te powder (*), owing to the incomplete anion-exchange reaction. The XRD pattern of mixed phase nickel tellurides (NiTe and $NiTe_2$) are indexed to their hexagonal phases with lattice constants a = 3.93 Å and c= 5.35 Å for NiTe, assigning to the standard JCPDS no 017-0502. On the other hand, $NiTe_2$ indicated the lattice constants of a = 3.86 Å and c = 5.3 Å, which is in agreement with standard JCPDS no. 065-3377.

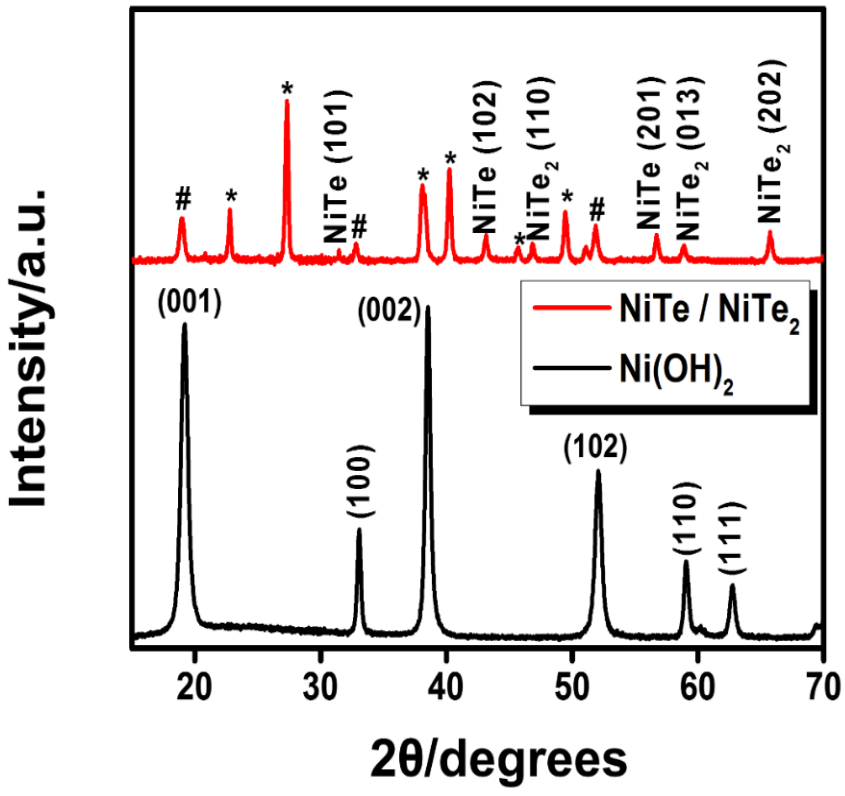

Figure 4.1 XRD patterns of the hexagonal $Ni(OH)_2$ nanosheets precursor and chemically transformed NiTe/$NiTe_2$ nanosheets.

Further, XPS measurements are employed to confirm the chemical states of the as-synthesized NiTe/$NiTe_2$ nanosheets (Figure 4.2). The wide range survey spectra is displayed in Figure 4.2a, while the core level XPS spectra of Ni 2p and Te 3d states are pictured in Figure 4.2b-c, respectively. The core level spectra of Ni 2p state could be resolved into two components (N1 and N2) 2p3/2 and 2p1/2, owing to the spin-orbit coupling. The N1 band centered at ~857 eV is attributed to the nickel-chalcogen bond (Ni-Te) as per the available literature (Ge et al. 2017). Further, the N2 band (satellite peak) with higher binding energy is ascribed to surface oxides of nickel. On the other hand, Te 3d states could be resolved into 3d5/2 and 3d3/2, indicating the presence of Te^{-} and TeO_2 (Anantharaj et al. 2018).

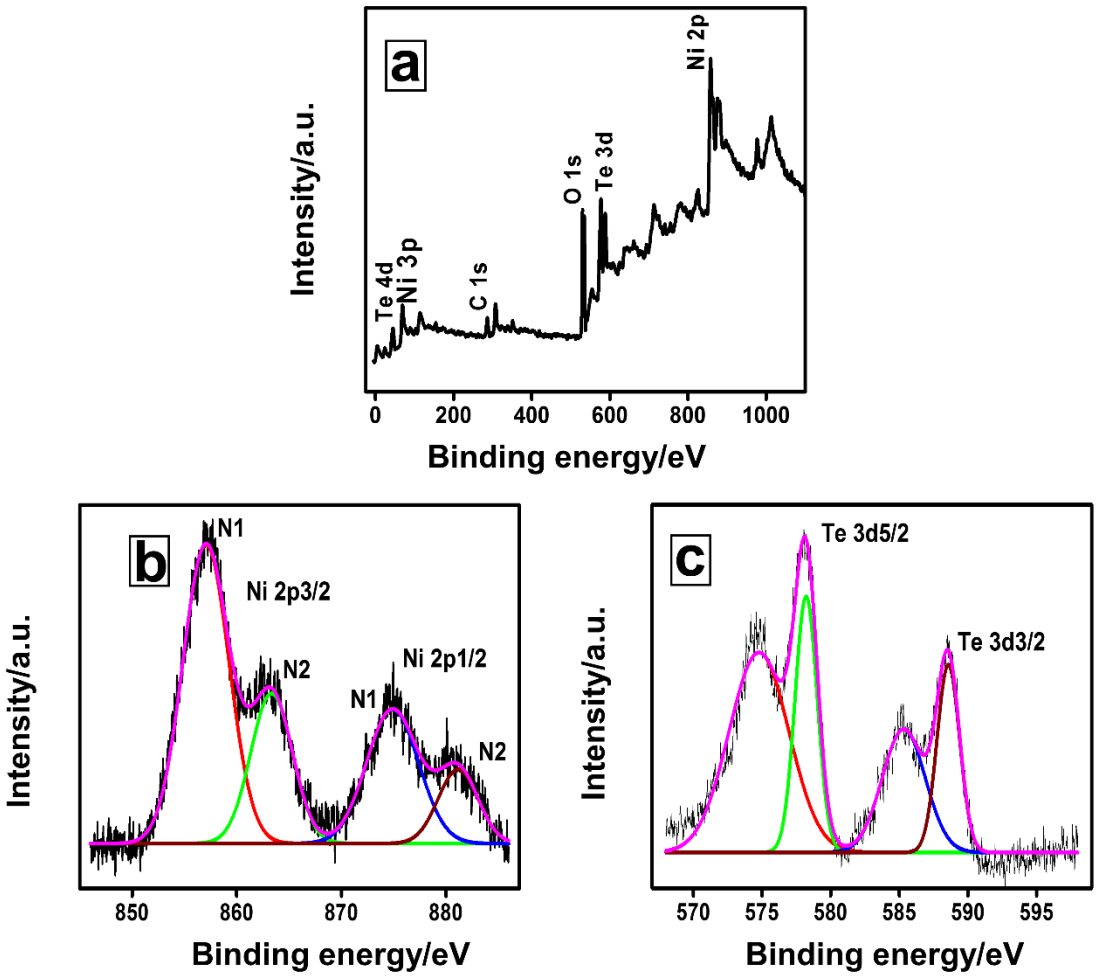

Figure 4.2 XPS survey spectra of as synthesized NiTe/$NiTe_2$ nanosheets (a), (b) Core level spectra of Ni 2p (b) and Te 3d (c).

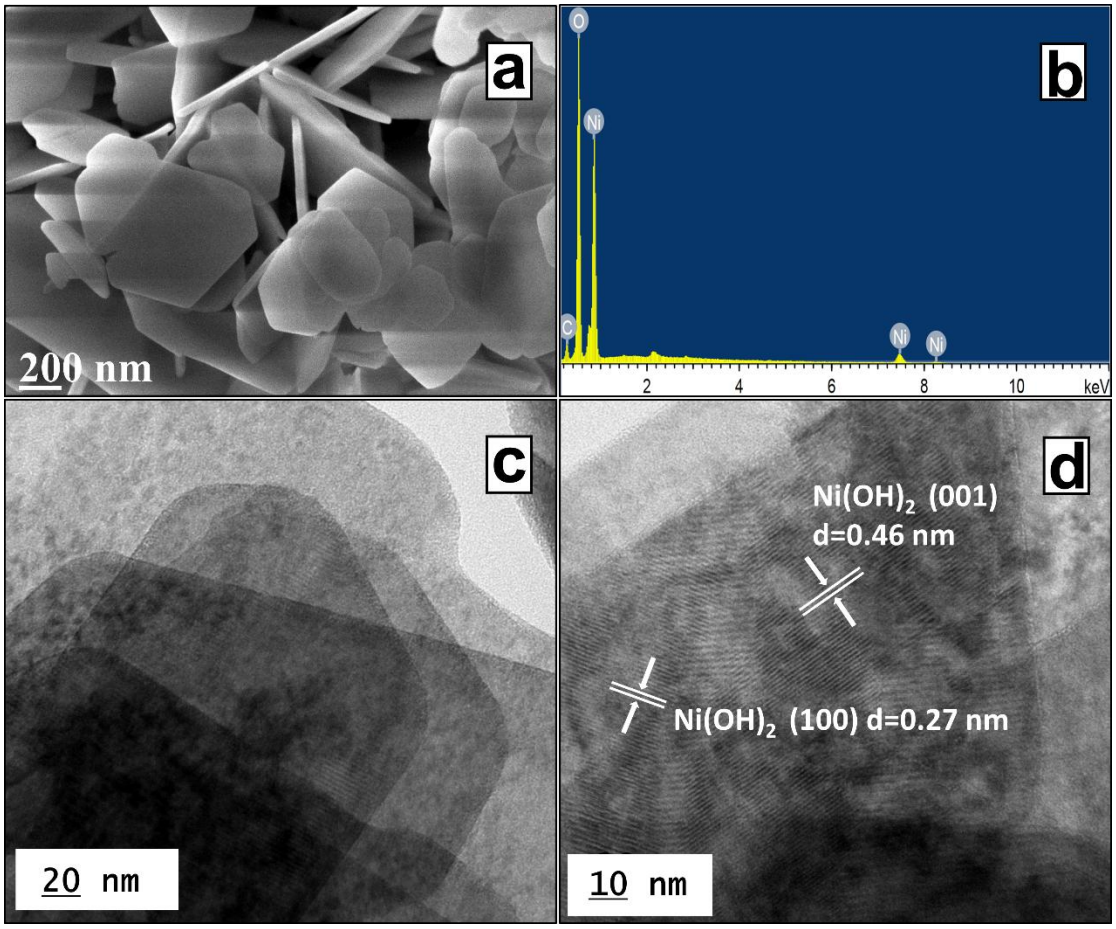

Figure 4.3 (a) FESEM image, (b) EDS spectra, (c) TEM image and (d) HRTEM image of $Ni(OH)_2$ nanosheets.

FESEM image of $Ni(OH)_2$ nanosheets as shown in Figure 4.3a confirm the two-dimensional sheet-like morphology and hexagonal shape, with an average edge thickness of ~55 nm and a mean width of ~350 nm. EDS analysis (Figure 4.3b) of $Ni(OH)_2$ nanosheets as shown in Figure 4.3a, confirms their purity. Further, the hexagonal 2D sheet like morphology of $Ni(OH)_2$ nanosheets are confirmed from TEM image (Figure 4.3c). In addition, the HRTEM fringes as presented in Figure 4.3d indicate lattice spacing values of ~4.6 Å and ~2.7 Å corresponding to prominent (001) and (100) planes of $Ni(OH)_2$, which are consistent with XRD measurements. The anion-exchange reaction of $Ni(OH)_2$ nanosheets with Te ions lead to the generation of $NiTe/NiTe_2$ nanostructures as shown in SEM image (Figure 4.4a) and TEM image (Figure 4.4c), respectively. FESEM and TEM images confirm their hexagonal morphology with an average edge thickness of ~55 nm and a mean width of ~350 nm,

exactly replicating the dimensions of the $Ni(OH)_2$ nanosheets precursor. EDS analysis as shown in Figure 4.4b confirm the purity of $NiTe/NiTe_2$ nanosheets, along with the presence of elemental oxygen. The peaks corresponding to oxygen may be attributed to non-transformed $Ni(OH)_2$ nanosheets, as confirmed from XRD analysis. TEM image (Figure 4.4c) shows the overlapping of two or more nanosheets, also from Figure 4.4c, it could be seen that the edges of the nanosheets are denser as compared to the surface, confirming their hollow structure.

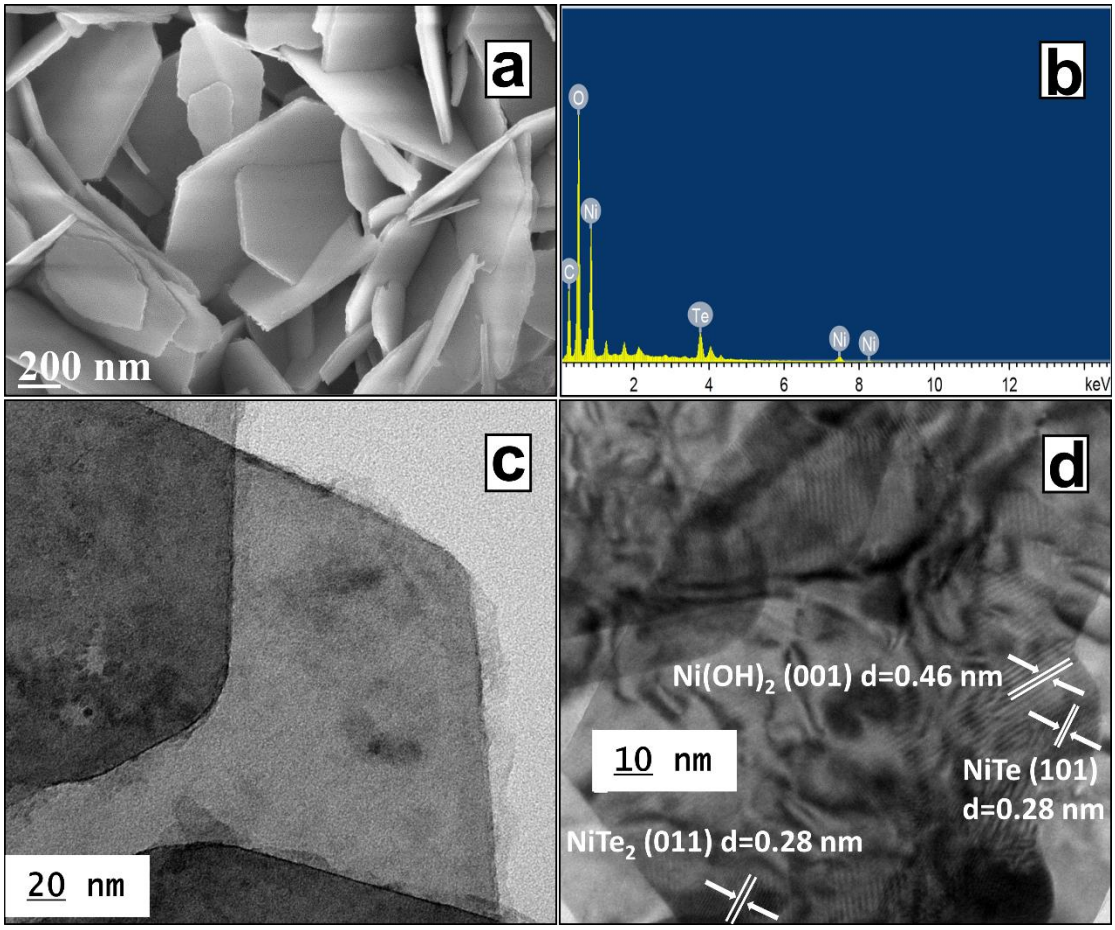

Figure 4.4 (a) FESEM image, (b) EDS spectra, (c) TEM image and (d) HRTEM image of $NiTe/NiTe_2$ nanosheets.

In addition, HRTEM analysis are conducted to track the transformation of $Ni(OH)_2$ nanosheets to $NiTe/NiTe_2$. As seen from Figure 4.4d, the fringes with lattice spacing value of ~2.8 Å is assigned to the (101) plane of hexagonal NiTe phase or (011) planes of $NiTe_2$ phase. In addition, HRTEM analysis also revealed the presence of lattice

spacing value of ~4.6 Å corresponding to (001) plane of $Ni(OH)_2$ nanosheets, which remained intact under hydrothermal conditions as confirmed from XRD analysis. The observed planes from HRTEM measurements are analogous to XRD peaks as seen in Figure 4.1. Further, both $Ni(OH)_2$ and $NiTe/NiTe_2$ nanosheets exhibited SAED patterns with spots (see APPENDIX IV), representing their polycrystallinity. In addition, BJH pore size and BET surface area measurements (see APPENDIX V) indicate $NiTe/NiTe_2$ nanosheets are porous in nature, consisting of nanopores with pore diameter of ~2.65 nm and specific surface area of ~10.20 $m^2 g^{-1}$.

4.3.2 Electrochemical measurements of nickel tellurides

The electrochemical measurements of the synthesized $NiTe/NiTe_2$ nanosheets was evaluated with three-electrode configurations. Herein, $NiTe/NiTe_2$ deposited on graphite rod substrates serves as the working electrode, saturated calomel electrode (SCE) as reference electrode and platinum (Pt) wire as a counter electrode. The resulting data is calibrated to reversible hydrogen electrode (RHE) standards, using the relation of E Vs. RHE = E Vs. SCE + (0.059* pH) +0.244 V.

4.3.2.1 Hydrogen evolution reaction (HER)

The HER performance of $NiTe/NiTe_2$ nanosheets are studied using LSV measurements in the negative potential range using 0.5 M H_2SO_4 solution. Figure 4.5a represents the iR compensated LSV curves of $NiTe/NiTe_2$ nanosheets at a scan rate of 5 mV s^{-1}, revealing the onset overpotential of -422 mV, beyond which a dramatic increase in cathodic current densities with vigorous evolution of hydrogen was observed. Further, LSV curve also indicate an overpotential of -432 mV to deliver the benchmark current density of 20 mA cm^{-2}. Further, Tafel plots derived from iR compensated LSV curves of $NiTe/NiTe_2$ nanosheets as shown in Figure 4.5b, demonstrate the Tafel slope of 87.4 mV dec^{-1}. The graphite rod substrate was catalytically inactive towards the HER in a described potential window range as provided in (see APPENDIX VI). Further, comparison of different nickel telluride nanostructures towards the HER as available in the literature is presented in Table 4.1. Further, electrochemical long-term stability is one of the key parameter for performance evaluation of the electrocatalysts. Some of

the earlier reports describe the instability of nickel-based HER catalysts in acid (He et al. 2014). In the present work, constant current chronopotentiometry was applied to evaluate the stability of NiTe/$NiTe_2$ nanosheets. Figure 4.5c shows the chronopotentiometric curves of NiTe/$NiTe_2$ nanosheets for 6 hours at an applied current of −50 mA (64 mA cm^{-2} current density). Results indicate the continuous evolution of hydrogen with no obvious change in the potential (~23 mV @ 6 h), suggesting promising stability of the electrodes. Stability of NiTe/$NiTe_2$ nanosheets towards HER after 6 hours of chronopotentiometry were also validated using LSV as shown in Figure 4.5d, representing a similar trend before and after chronopotentiometric measurements.

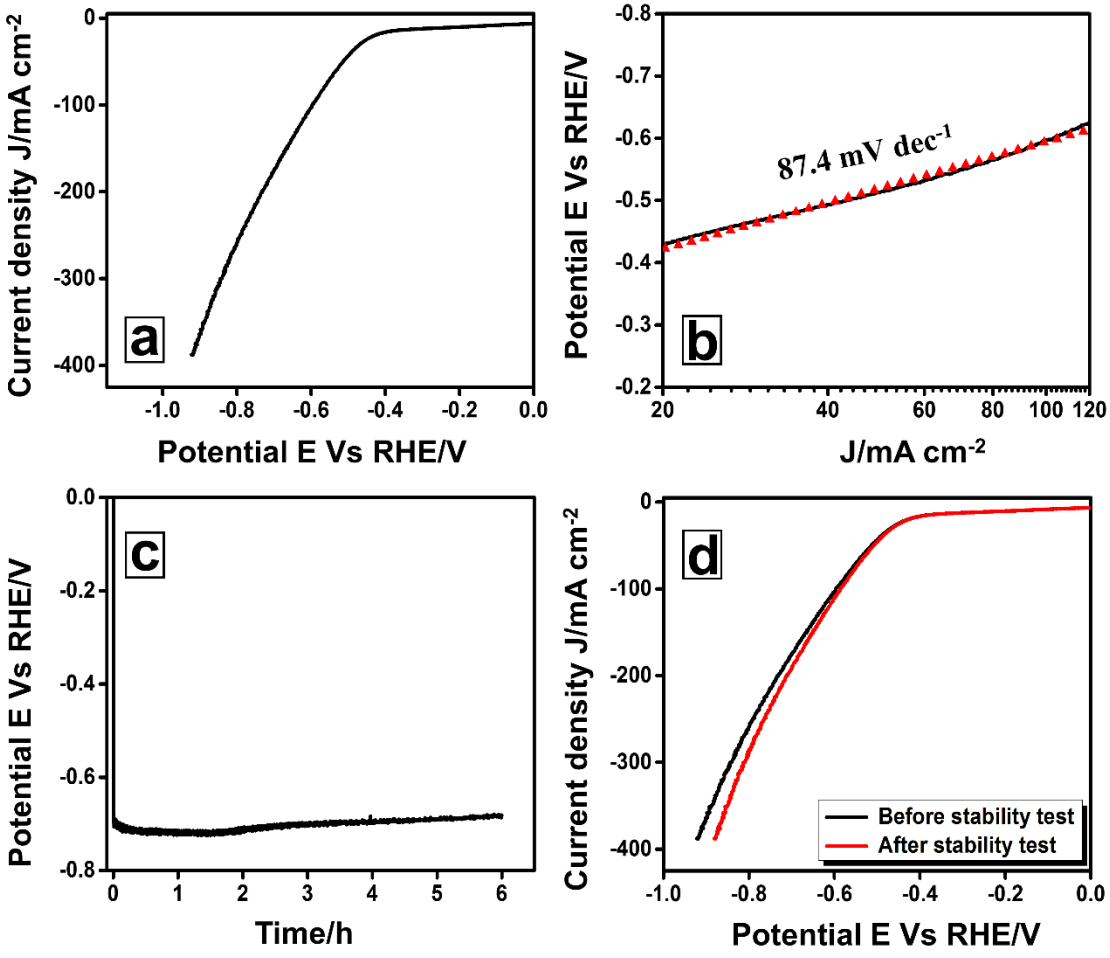

Figure 4.5 (a) iR compensated LSV curves of NiTe/$NiTe_2$ nanosheets towards the HER at 5 mV s^{-1} scan rate, (b) Tafel plots derived from LSV curves, (c) chronopotentiometric stability tests at applied current of -50 mA for 6 hours and (d) LSV curves before and after stability test.

Table 4.1.Comparison of different nickel telluride nanostructures towards the HER as available in the literature.

Material	Potential/mV	Tafel slope	Reference
$NiTe_2$	276@10 mA cm^{-2}	71 mV dec^{-1}	(Ge et al. 2017)
$NiTe_2$	125@10 mA cm^{-2}	36 mV dec^{-1}	(Anantharaj et al. 2018)
$NiTe_2$	590@10 mA cm^{-2}	45 mV dec^{-1}	(Chia et al. 2017)
Ni_3Te_2	167@10 mA cm^{-2}	94.2 mV dec^{-1}	(Silva et al. 2018)
$NiTe/NiTe_2$	432@20 mA cm^{-2}	87.4 mV dec^{-1}	This work

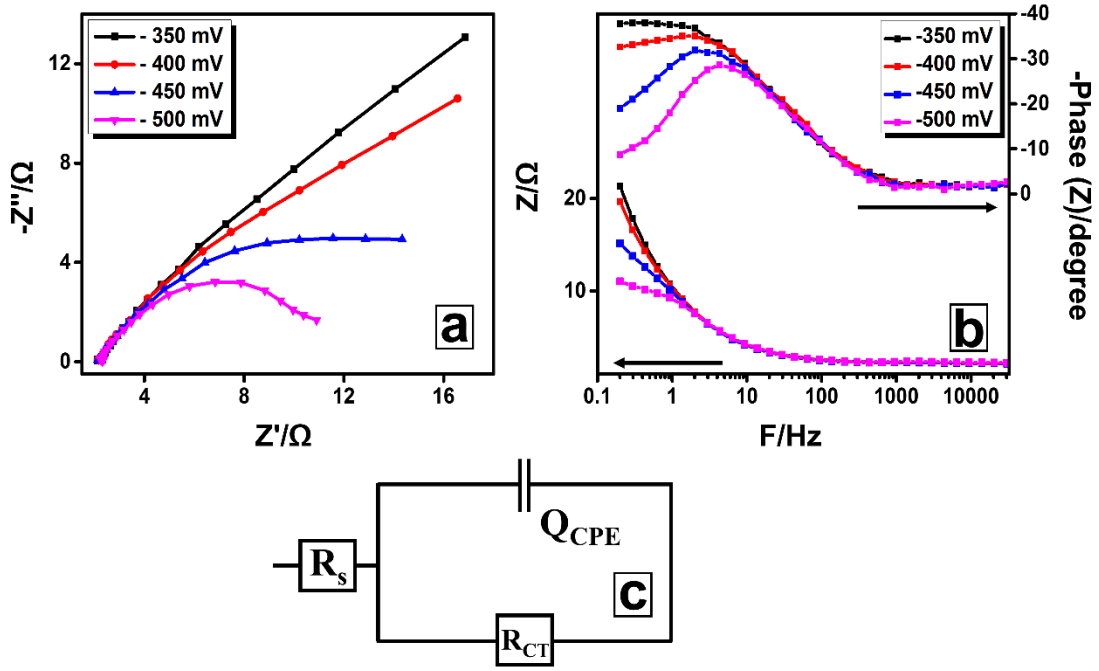

Figure 4.6 (a) Nyquist plots and their corresponding Bode phase angle plots (b) of $NiTe/NiTe_2$ nanosheets towards the HER (c) simulated EEC circuit for Nyquist plots.

Further, the HER kinetics of $NiTe/NiTe_2$ nanosheets are studied using EIS measurements. Using EIS, the Nyquist plots of $NiTe/NiTe_2$ nanosheets were recorded at the vicinity of onset overpotential, viz., -350 mV, -400 mV, -450 mV and -500 mV as displayed in Figure 4.6a. As the overpotential is increased from -350 mV to -500 mV, diameter of the semi-circles decrease, indicating these semicircles are related to the electrode kinetics (Birry and Lasia 2004). It may be noted that the diameter of semicircles decrease considerably as the potential increase, which further supports the

HER as controlled charge transfer process (Shibli and Sebeelamol 2013). Further, Figure 4.6b represents the Bode phase angle plots of NiTe/$NiTe_2$ nanosheets at different applied bias. As the applied bias increase, the phase angle and total impedance decrease, indicating the superior hydrogen evolution (Ojha et al. 2017). Furthermore, EEC was modelled in the form $R_S(Q_{CPE}R_{CT})$ as shown Figure 4.6c, and the corresponding EEC fitting values are tabulated in Table. 4.2. The equivalent circuit was found to be a Randle's circuit, consisting of solution resistance (R_S) in series with a parallel connection of charge-transfer resistance (R_{CT}) and constant phase element (Q_{CPE}). From the EEC fitting parameters, it can be noted that the R_{CT} values decrease with increasing bias, which indicate enhancement of the HER kinetics. Further, Q_{CPE} value provides a measure of effective surface area available for the reaction (Najafi Sayar and Bahrololoom 2009).

Table 4.2. EEC parameters of NiTe/$NiTe_2$ nanosheets towards the HER.

Overpotential (mV)	R_S (Ω)	R_{CT} (Ω)	Q_{CPE} (mF)
-350	2.132	71.50	35.7
-400	2.152	41.51	33.7
-450	2.168	18.08	26.6
-500	2.266	9.739	18.1

4.3.2.2 Oxygen evolution reaction (OER)

The electrocatalytic activity of as-synthesized NiTe/$NiTe_2$ nanosheets towards the OER is studied using LSV measurements in a positive potential range using 1 M KOH solution. Further, iR compensation was applied to the initial data to remove the background current and Ohmic loss. Figure 4.7a represents the iR compensated LSV curve of NiTe/$NiTe_2$ nanosheets towards the OER at a scan rate of 5 mV s^{-1}, revealing an onset overpotential of 679 mV and overpotential of 745 mV to deliver current density of 10 mA cm^{-2}. Further, Tafel plots derived from iR compensated LSV curves (Figure 4.7b) indicate the Tafel slope of 151 mV dec^{-1}. The graphite rod substrate was catalytically inactive towards the OER in a described potential window range as provided in (see APPENDIX VI). The comparison of different nickel telluride

nanostructures towards the OER as available in the literature is presented in Table 4.3.

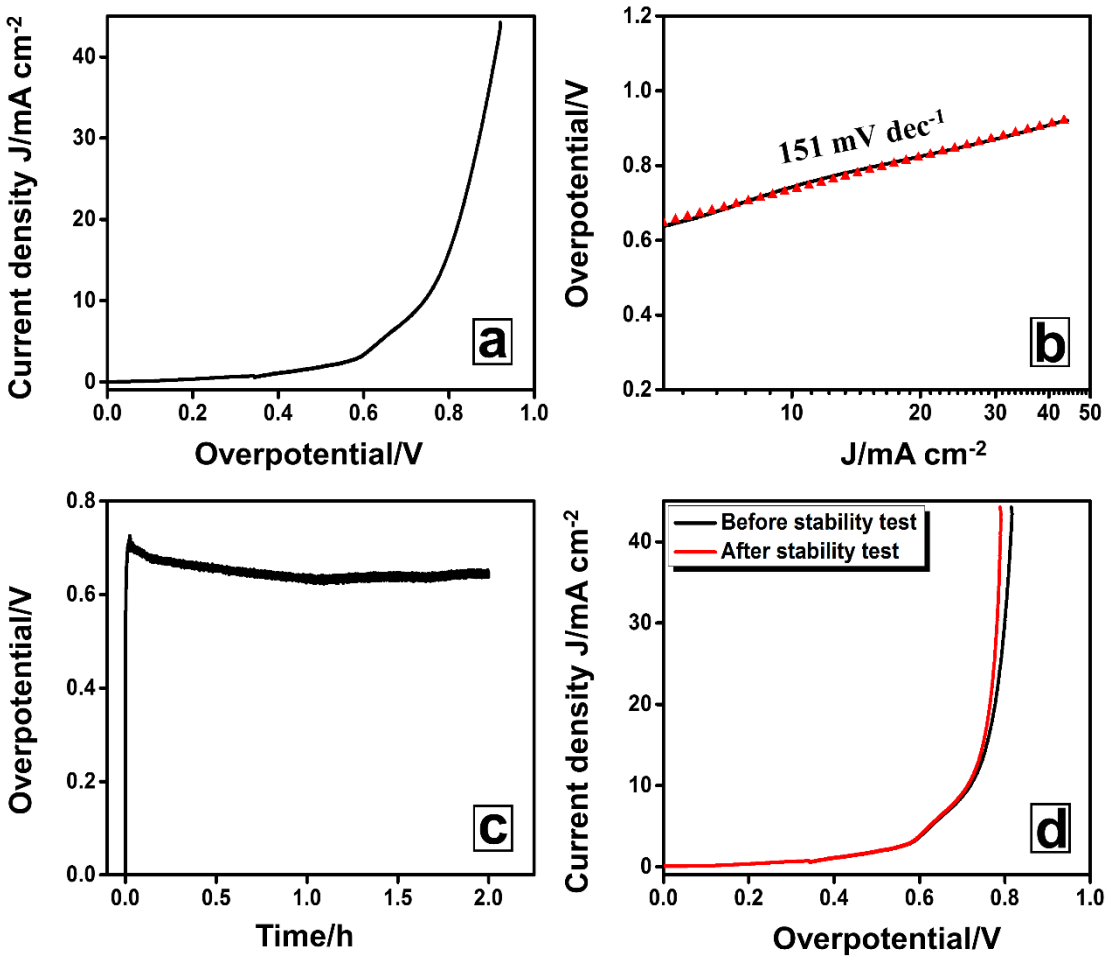

Figure 4.7 (a) iR compensated LSV curve of $NiTe/NiTe_2$ nanosheets towards the OER at 5 mV s^{-1} scan rate, (b) Tafel plots derived from LSV curves, (c) chronopotentiometric stability tests at applied current of +50 mA for 2 hours and (d) LSV curves before and after stability test.

Further, electrocatalytic stability of $NiTe/NiTe_2$ nanosheets towards the OER is studied in a similar way as discussed for the HER at an applied current of +50 mA (64 mA cm^{-2} current density). As the current pulse is applied, a sharp increase in potential was observed until a potential at which OH^- is oxidized to O_2 was reached. The potential was found to be stable when equilibrium is attained between the fresh oxygen bubbles and that escaping from the surface of the electrode (George et al. 2015). Figure 4.7c reveals the chronopotentiometric curves of $NiTe/NiTe_2$ nanosheets towards

the OER for continuous two hours. Results indicate the continuous evolution of oxygen with no obvious potential change, implying the promising stability of electrodes. In addition, no significant change in the LSV curve before and after two hours of chronopotentiometry was observed (Figure 4.7d), implying the promising stability of NiTe/$NiTe_2$ nanosheets.

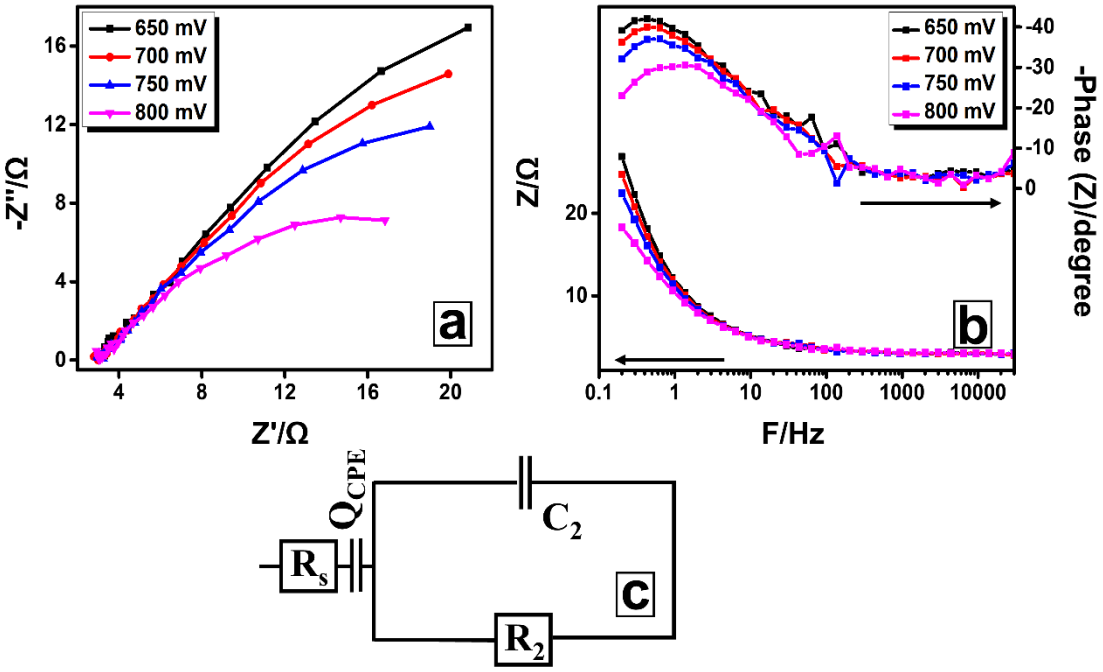

Figure 4.8 (a) Nyquist plots and their corresponding Bode phase angle plots (b) of NiTe/$NiTe_2$ nanosheets towards the OER and (c) simulated EEC circuit for Nyquist plots.

The OER kinetics of NiTe/$NiTe_2$ nanosheets was studied using EIS techniques. The Nyquist and bode phase plots of NiTe/$NiTe_2$ nanosheets were measured at the vicinity of onset potential, viz., 650 mV, 700 mV, 750 mV and 800 mV through EIS as described in Figure 4.8a-b. All the recorded Nyquist plots indicate flattening of the semicircles, representing dispersive capacitance (Gómez-Aguilar et al. 2016). It may also be seen that, at a higher applied bias, diameter of the semicircles considerably decreases indicating lowering of charge-transfer resistances. Further, EEC was modelled in the form LR_SQ_{CPE} (C_2R_2) as shown in Figure 4.8c. The simulated EEC indicate the existence of inductance (L), which is of order of magnitude 10^{-6} H, in

agreement with the inductance value of measuring equipment components (da Silva et al. 1996). The other parameters include solution resistance (R_S), constant phase element (Q_{CPE}), R_2 and C_2 are the resistance and pseudocapacitance associated with redox reactions, possibly due to porosity of the electrode material (Kellenberger et al. 2007). The EEC fitting values are tabulated in Table. 4.4.

Table 4.3. Comparison of different nickel telluride nanostructures towards the OER as available in the literature.

Material	**Potential/mV**	**Tafel slope**	**Reference**
Ni_3Te_2	220@10 mA cm^{-2}	61.5 mV dec^{-1}	(Silva et al. 2018)
$NiTe_2$/NF	262@10 mA cm^{-2}	74 mV dec^{-1}	(Wang and Zhang 2018a)
$NiTe_2$/Ti	315@10 mA cm^{-2}	82 mV dec^{-1}	(Wang and Zhang 2018b)
Ni_3Te_2	180@10 mA cm^{-2}	64.3 mV dec^{-1}	(Silva et al. 2018)
Ni_3Te_2-CoTe/CC	392@100 mA cm^{-2}	68 mV dec^{-1}	(Xu et al. 2019)
Fe-NiTe	280 @10 mA cm^{-2}	80 mV dec^{-1}	(Zhong et al. 2019)
NiTe (Bulk)	388 @10 mA cm^{-2}	117 mV dec^{-1}	(Zhong et al. 2019)
NiTe/$NiTe_2$	679, Onset	151 mV dec^{-1}	This work

Table 4.4. EEC parameters of NiTe/$NiTe_2$ nanosheets towards the OER.

Overpotential (mV)	**R_S (Ω)**	**Q_{CPE} (mF)**	**R_2 (Ω)**	**C_2 (mF)**
650	2.904	45	5.84	105
700	2.908	52	6.15	87
750	2.928	58	4.92	76
800	2.893	81	4.34	46

4.3.3 Physiochemical analysis of nickel selenides

The XRD patterns of synthesized nanostructures were analyzed and indexed as pictured in Figure 4.9.In this regard, Figure 4.9a displays the XRD pattern of $NiSe_2$ nanosheets in comparison with the precursor $Ni(OH)_2$ nanosheets, indicating their cubic crystal structure. The obtained with lattice parameters of $NiSe_2$ are $a = b = c = 5.96$ Å, which is consistent with the standard reference pattern (JCPDS card no. 01-089-7161).

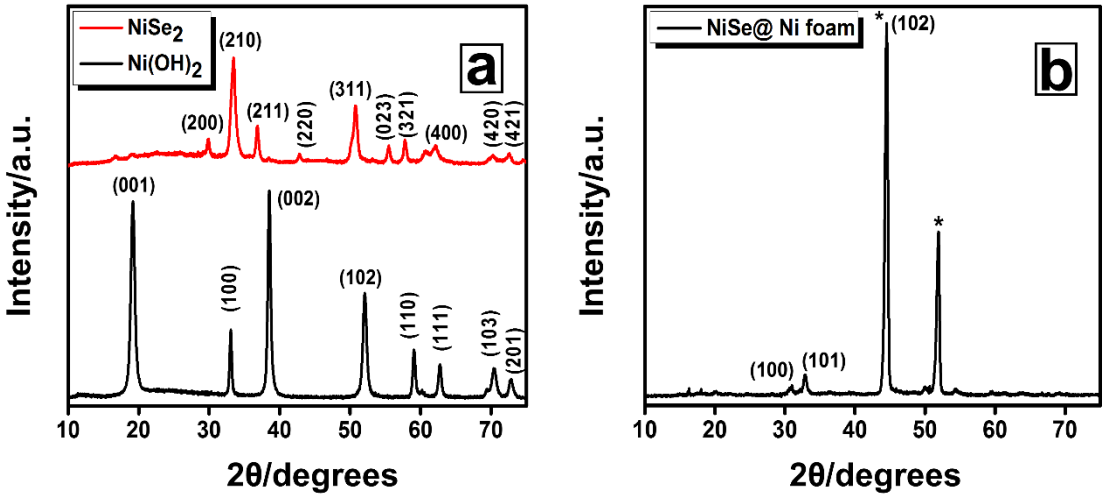

Figure 4.9 (a) XRD patterns of $Ni(OH)_2$ nanosheets and $NiSe_2$ nanosheets and (b) XRD pattern of nickel selenide nanoflakes.

On the other hand, XRD pattern of NiSe nanoflakes obtained by the selenization of nickel foam is represented in Figure 4.9b. The XRD pattern indicate high intense peaks corresponding to metallic nickel (*) and Nickel selenide (NiSe). The existence of metallic nickel can be ascribed to nickel foam substrate and the prominent peaks corresponding to NiSe nanoflakes are at 2θ positions of ~32.79° and ~44.22°, analogous to their (101) and (102) planes. The XRD pattern of NiSe nanoflakes match well with the standard JCPDS card no 03-065-6014, indicating hexagonal crystal structure with lattice parameters of $a = 3.66$ Å and $c = 5.35$ Å. It is interesting to note that the peak emanating at ~44.22° could be assigned to the metallic nickel as well as nickel selenide (NiSe), which indicate the preferential growth of NiSe nanoflakes over metallic nickel foam substrate during the hydrothermal process.

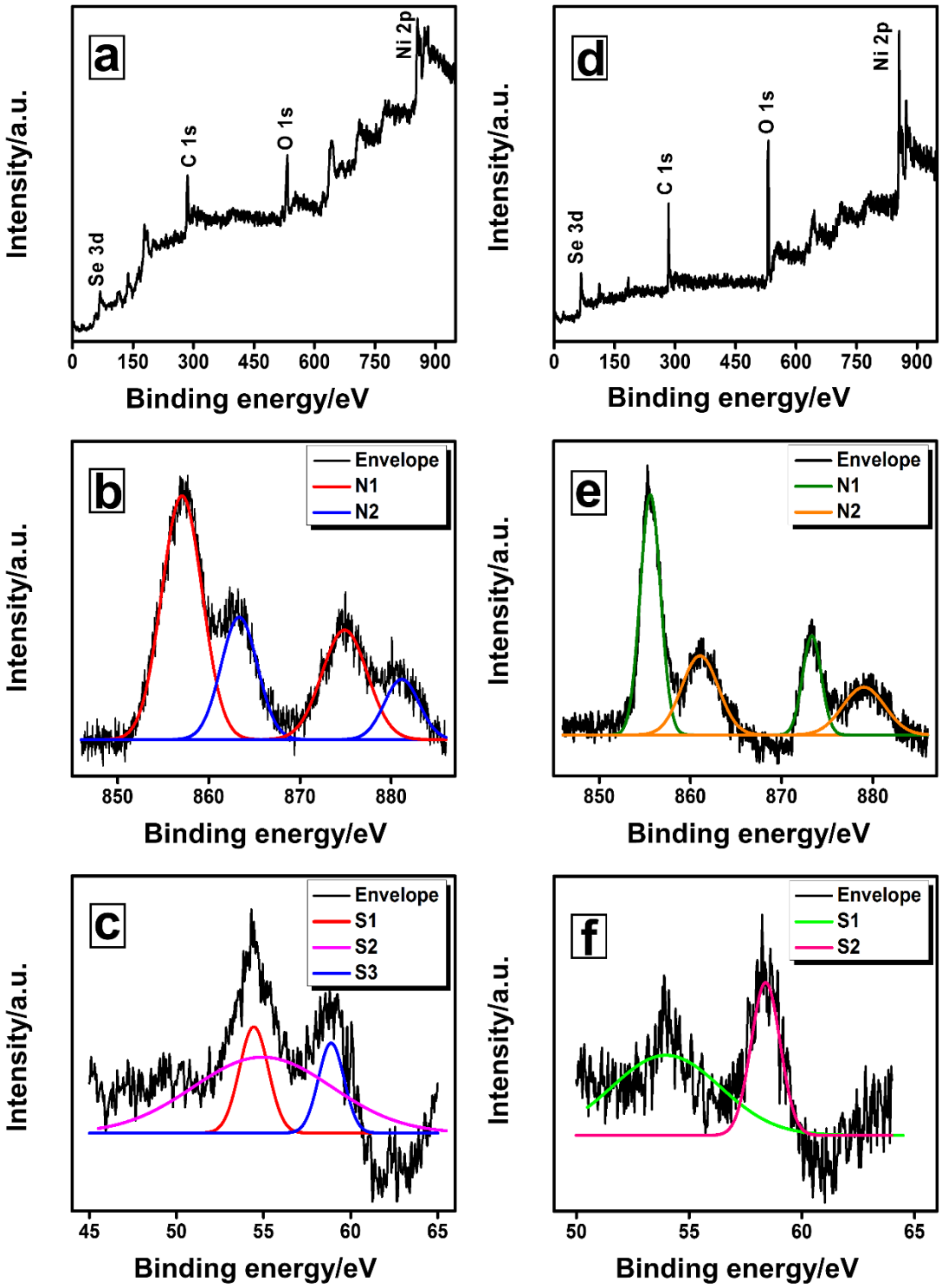

Figure 4.10 XPS survey spectra's of (a) $NiSe_2$ nanosheets and (d) NiSe nanoflakes, Core level spectra of Ni 2p in $NiSe_2$ nanosheets (b) and in NiSe nanoflakes (e), Core level spectra of Se 3d in $NiSe_2$ nanosheets (c) and in NiSe nanoflakes (f).

Further, XPS measurements are employed to confirm the chemical states of elements in the as synthesized products. Figure 4.10a and Figure 4.10d represents the wide range survey spectra of $NiSe_2$ nanosheets and NiSe nanoflakes, respectively. The Ni 2p spectra's of $NiSe_2$ nanosheets (Figure 4.10b) and NiSe nanoflakes (Figure 4.10e) could be resolved into two doublets 2p3/2 and 2p1/2, owing to the spin-orbit coupling. Further, the 2p3/2 peak was resolved into two components N1 and N2. The N1 band is possibly attributed to the nickel-chalcogen (Ni-Se) bond as per the previous findings (Mandale et al. 1984), while the N2 band at higher binding energies could be attributed to the surface oxide of nickel (Grosvenor et al. 2006). The 3d spectra of selenium in $NiSe_2$ nanosheets (Figure 4.10c) are resolved into three components S1, S2 and S3. The S1 and S2 bands could be attributed to the 3d 5/2 and 3d 3/2 owing to spin-orbit coupling and the S3 band can be ascribed to surface oxide structure (Shenasa et al. 1986). On the other hand, the core level spectra of selenium in NiSe nanoflakes (Figure 4.10f) also indicate the bands S1 and S2. The S1 band can be ascribed to Ni-Se bond, while S2 band at higher binding energy can be ascribed to surface selenium oxides (SeO_x) (Sun et al. 2018).

The anion exchange reaction of $Ni(OH)_2$ nanosheets with Se ions resulted in $NiSe_2$ nanosheets as represented in FESEM image (Figure 4.11a) and TEM images (Figure 4.11c), respectively. It is worth noting that, $NiSe_2$ nanosheets exactly replicates the precursor $Ni(OH)_2$ nanosheets in dimensions of thickness and width of ~55 nm and ~350 nm. The morphological features of $Ni(OH)_2$ nanosheets are discussed in previous section 4.3.1. Further, EDS measurements (Figure 4.11b) performed on the area as represented in Figure 4.11a confirms the phase purity of the nanosheets. In addition, the spot type SAED pattern (see APPENDIX IV) confirms the single crystalline nature of $NiSe_2$ nanosheets, which are in par with the results obtained from XRD measurements. Further, HRTEM measurements were conducted on $NiSe_2$ nanosheets as shown in Figure 4.11d to track the selenization of $Ni(OH)_2$ under hydrothermal conditions. From HRTEM images, the measured lattice spacing value of ~2.6 Å is in close agreement with the (210) prominent diffraction plane of $NiSe_2$ nanosheets as confirmed from XRD measurements.

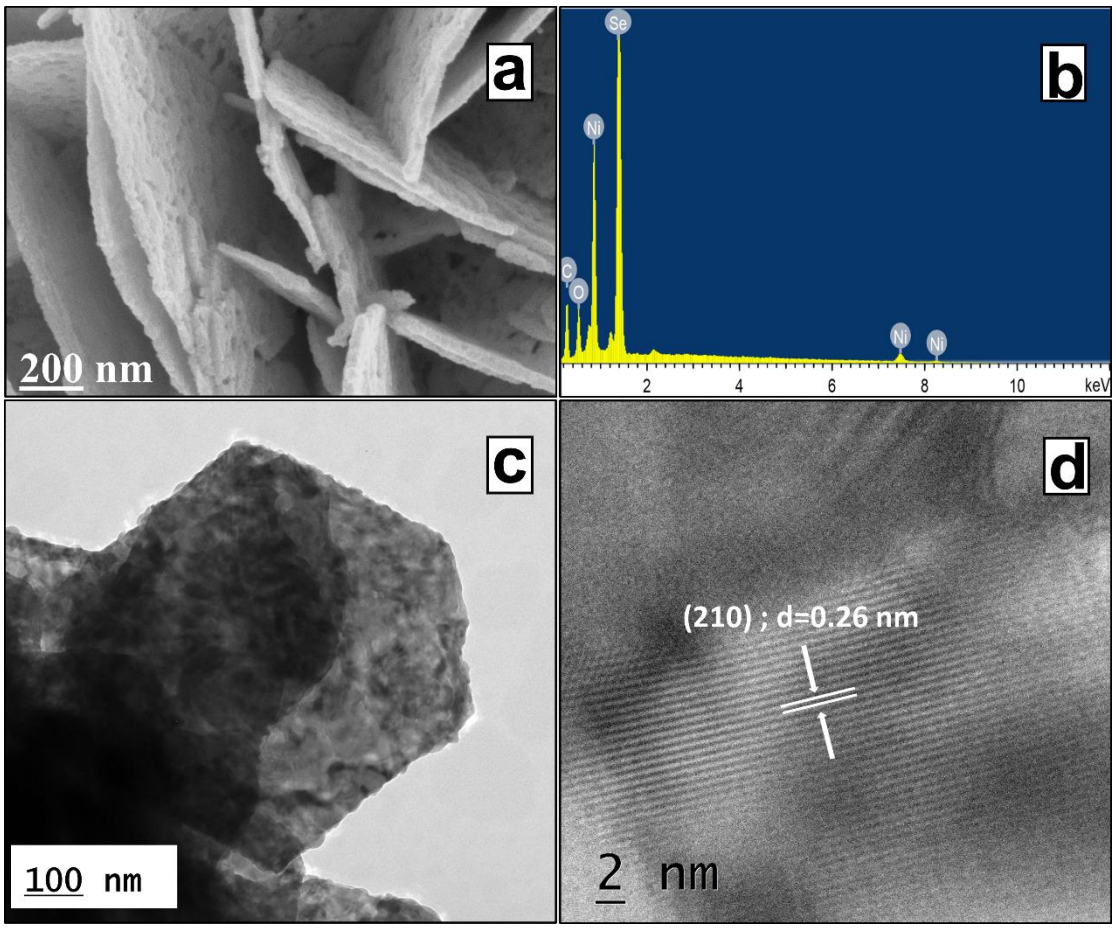

Figure 4.11 (a) FESEM image, (b) EDS spectra, (c) TEM image and (d) HRTEM image of $NiSe_2$ nanosheets.

On the other hand, the morphological analysis of NiSe nanoflakes obtained through the selenization of nickel foam were also conducted using FESEM and TEM measurements. FESEM image as shown in Figure 4.12a indicate the vertically aligned, interconnected flake-like assembly with an estimated average size of ~70 nm. Further, EDS measurements (Figure 4.12b) performed on the area of shown in Figure 4.12a, confirms their purity. In addition, the combination of ring and spot-like SAED pattern (see APPENDIX IV) specify the poly-crystallinity of NiSe nanoflakes. In addition, TEM measurements (Figure 4.12c) confirms the uniform flake-like structures of NiSe. Further, HRTEM sheds light on the growth of NiSe nanoflakes on metallic nickel foam substrate. The lattice spacing value of ~2.7 Å obtained through HRTEM measurements as represented in Figure 4.12d is in contrast with the (101) plane of NiSe nanoflakes as obtained from XRD measurements.

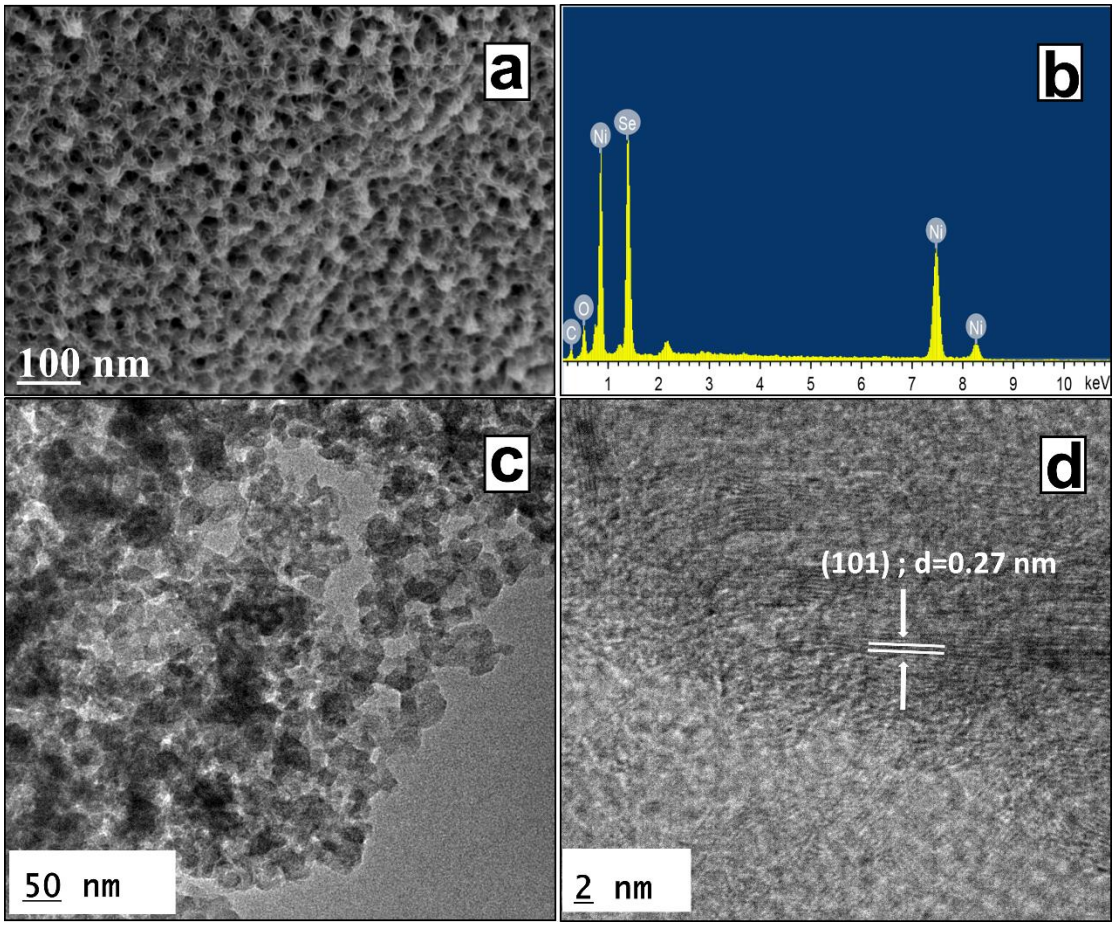

Figure 4.12 (a) FESEM image, (b) EDS spectra, (c) TEM image and (d) HRTEM image of NiSe nanoflakes.

4.3.4 Hydrogen evolution reaction of nickel selenides

The electrochemical measurements of the synthesized $NiSe_2$ nanosheets and NiSe nanoflakes was evaluated with three-electrode configurations. Since the as-synthesized $NiSe_2$ nanosheets was in the powder form, they were assembled on graphite rod substrates as described in section 2.3.7 for successful electrochemical measurements, which resulted in the mass loading of ~0.4 mg cm^{-2}. While NiSe nanoflakes obtained by the selenization of nickel foam was directly taken for electrochemical measurements. Herein, the calculated mass loading of NiSe nanoflakes on nickel foam using equation 2.9 was about ~0.35 mg cm^{-2}. The three-electrode setup consist of $NiSe_2$ deposited on graphite rod substrates or NiSe on nickel foam as a working electrode, saturated calomel electrode (SCE) as reference electrode and platinum (Pt) wire as a counter electrode. Further, the electrocatalytic performance of both nickel selenides

towards the HER was studied with 0.5 M H_2SO_4 solution. The resulting data is calibrated to reversible hydrogen electrode (RHE) standards, using the relation of E Vs. RHE = E Vs. SCE + (0.059* pH) +0.244 V.

The iR compensated LSV curves of $NiSe_2$ nanosheets at a scan rate of 5 mV s^{-1} as seen in Figure 4.13a, reveal the onset potential of -169 mV beyond which a steep increase in the cathodic current density was observed. Further, the overpotentials required for the benchmark current densities of 10, 100 and 200 mA cm^{-2} are -198 mV, -358 mV and -473 mV, respectively. On the other hand, Figure 4.13c represents the iR compensated LSV curve of NiSe nanoflakes, indicate the onset potential of -190 mV. While, the overpotentials required to deliver different current densities of 10, 100 and 200 mA cm^{-2} are -217 mV, -331 mV and -365 mV, respectively. Although the onset potential for NiSe nanoflakes are marginally high as compared with $NiSe_2$ nanosheets, the overpotentials required to deliver different geometric current densities of 10, 100 and 200 mA cm^{-2} are relatively lower. These results demonstrate the superior catalytic behavior of NiSe nanoflakes as compared with $NiSe_2$ nanosheets. Whereas both substrates graphite rod and nickel foam are catalytically inactive in the described potential window range as provided in (see APPENDIX VI).

Furthermore, the Tafel plots derived from iR compensated LSV curves of $NiSe_2$ nanosheets and NiSe nanoflakes are represented in Figure 4.13b-d respectively. The measured Tafel slope values are 72.1 mV dec^{-1} for $NiSe_2$ nanosheets and 28.6 mV dec^{-1} for NiSe nanoflakes. These results indicate the Tafel slope value of NiSe nanoflakes are about three times lower to those of $NiSe_2$ nanosheets and comparable to the reported values of state-of-the-art Pt/C catalyst (Anantharaj et al. 2018) and confirm the HER kinetics of NiSe nanoflakes run parallel to the state-of-the-art Pt/C catalyst. For comparison LSV curve of commercially available 20 wt% Pt/C catalyst is also recorded as provided in (see APPENDIX VI). In addition, the catalytic activity of different nickel selenides towards the HER in contrast to hydrothermal synthesis time as available in the literature are summarized in (see APPENDIX VII).

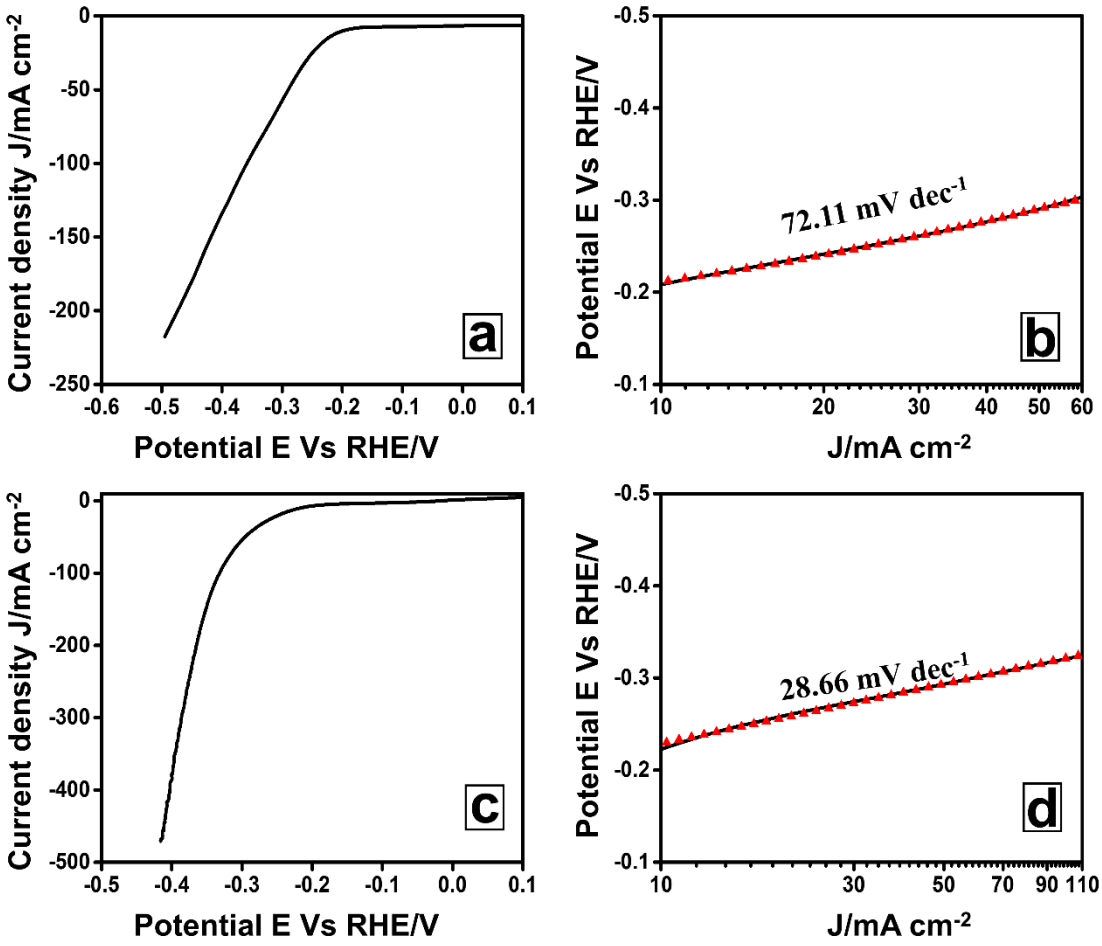

Figure 4.13 iR compensated LSV curves of (a) $NiSe_2$ nanosheets and (c) NiSe nanoflakes at a 5 mV s^{-1} scan rate, Tafel plots of (b) $NiSe_2$ nanosheets and (d) NiSe nanoflakes derived from iR compensated LSV curves.

To gain insight onto superior performance of nickel selenides towards the HER, ECSA was determined. The CV curves of $NiSe_2$ nanosheets and NiSe nanoflakes recorded in the double-layer charging region (see APPENDIX VIII), wherein no obvious redox reaction take place. The double-layer capacitances $2C_{dl}$ are estimated by plotting the difference in double-layer charging current densities $\Delta j = j_a - j_c$ at -0.3 V Vs. SCE for $NiSe_2$ nanosheets and at -0.325 V Vs SCE for NiSe nanoflakes as a function of scan rate (Figure 4.14). The estimated $2C_{dl}$ values are 5 µF cm^{-2} and 8.92 µF cm^{-2} for $NiSe_2$ nanosheets and NiSe nanoflakes respectively. These $2C_{dl}$ values indicate NiSe nanoflakes geometry provides higher electrocatalytic surfaces for the HER and also confirms superior electrocatalytic activity as confirmed from LSV and Tafel plots.

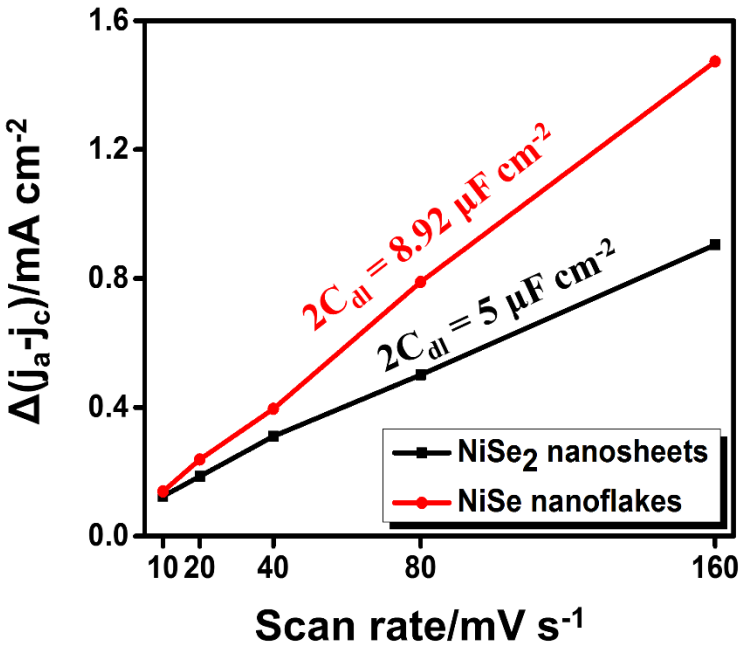

Figure 4.14 Plots of difference in double layer charging current densities Vs. scan rate for $NiSe_2$ nanosheets and NiSe nanoflakes.

The HER kinetics of both $NiSe_2$ nanosheets and NiSe nanoflakes are studied through EIS technique in the frequency range of 0.2 Hz to 100 kHz with a sinusoidal AC amplitude of V_{AC} = 10 mV. The Nyquist plots of $NiSe_2$ nanosheets and NiSe nanoflakes at different applied bias voltages are represented in Figure 4.15a and Figure 4.15c, respectively. Both nickel selenides reveal the Nyquist plots in the form of semi-circle, indicating the charge-transfer resistances. Further, as the bias voltage is varied from -155 mV to -255 mV in steps of 25 mV, the diameter of the semicircles are considerably decreased, indicating these semicircles are related to electrode kinetics (Shibli and Sebeelamol 2013). Figure 4.15b and Figure 4.15d depicts the Bode phase angle plot at different applied bias for $NiSe_2$ nanosheets and NiSe nanoflakes, respectively, indicating the total impedance and phase angle as a function of frequency. The total impedance and phase angle becomes negligible at higher applied bias, indicating the superior hydrogen evolution (Ojha et al. 2017). It is worth noting that the total impedance of NiSe nanoflakes are about four-times lower as compared to $NiSe_2$ nanosheets, complimenting the prominent catalytic activity as confirmed from LSV and Tafel plots.

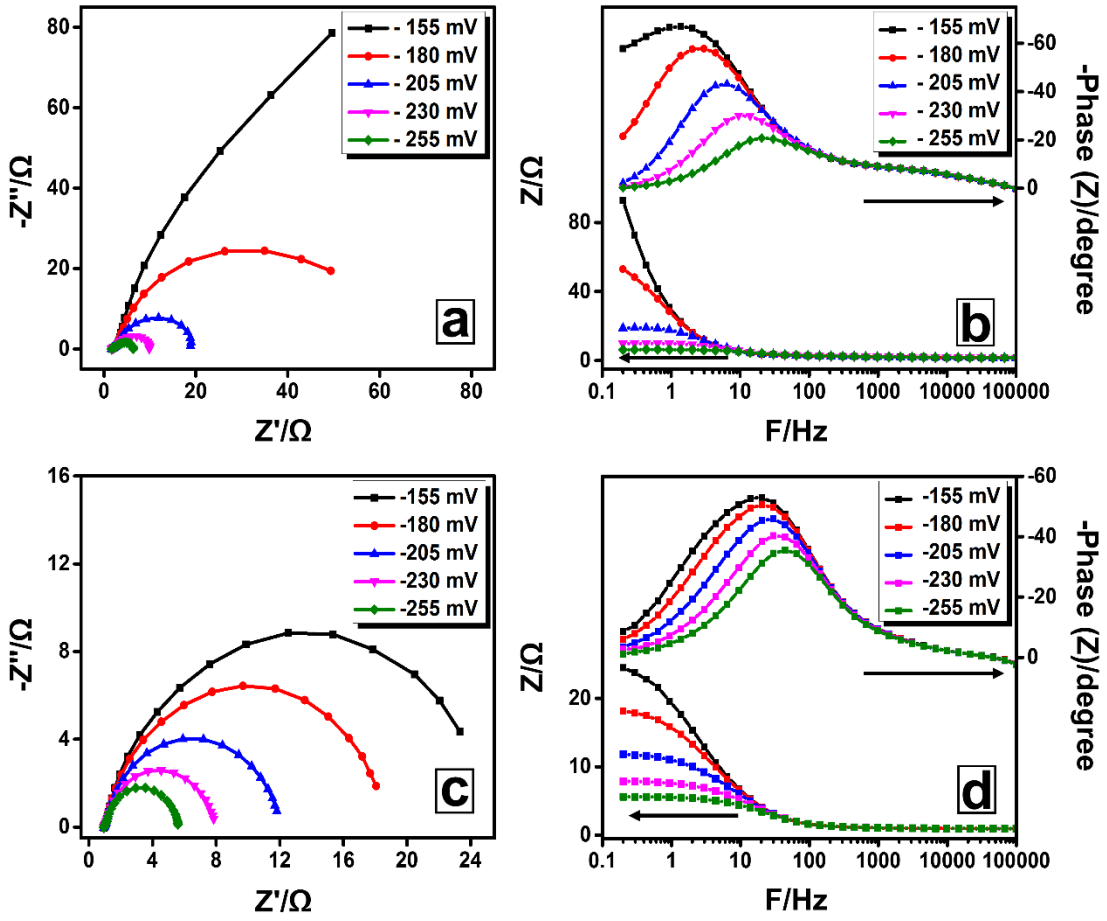

Figure 4.15 (a) Nyquist plots and their corresponding Bode phase plot $NiSe_2$ nanosheets (a-b), and NiSe nanoflakes (c-d).

Further, EEC for the Nyquist plots was modelled and fit into two CPE model (Miousse et al. 1995). Both nickel selenides could fit into the same EEC model as displayed in Figure 4.16. The EEC is represented by $R_S(Q_{CPE1}R_{CT1})(Q_{CPE2}R_{CT2})$, where R_S being the solution resistance, Q_{CPE} and R_{CT} are pseudo capacitances and charge transfer resistances, respectively. The first $Q_{CPE1}R_{CT1}$ component is associated with the porosity of the electrodes and relatively potential independent (Chen and Lasia 1991), while the second $Q_{CPE2}R_{CT2}$ component is strongly dependent on the overpotential (Fournier et al. 1999). The EEC fitting parameters are tabulated in Table 4.5 and Table 4.6 for $NiSe_2$ nanosheets and NiSe nanoflakes, respectively.

From the EEC fitting parameters, the value of solution resistances R_S is ~1.6 Ω for $NiSe_2$ nanosheets and ~0.92 Ω for NiSe nanoflakes, the lower value of R_S indicates

better contact of the catalyst with electrolyte. Further, the charge-transfer resistances R_{CT2} near the vicinity of onset potential (-180 mV) of NiSe nanoflakes are about three-times lower as compared with NiSe nanosheets. While, the charge-transfer resistances R_{CT2} at higher bias (-255 mV) are as low as ~7.55 Ω and ~4.72 Ω for $NiSe_2$ nanosheets and NiSe nanoflakes, respectively, indicating the superior HER at higher applied bias.

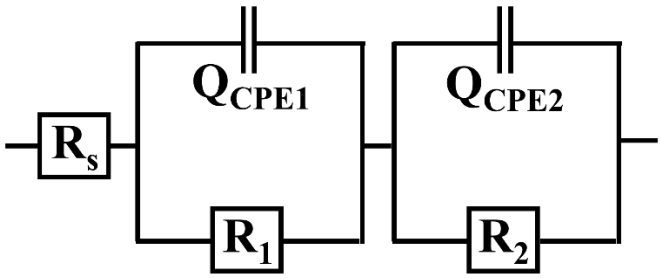

Figure 4.16 EEC circuit for the Nyquist plots.

Table 4.5. EEC fitting parameters of $NiSe_2$ nanosheets towards the HER.

Overpotential (mV)	R_S (Ω)	Q_{CPE1} (F)	R_{CT1} (Ω)	Q_{CPE2} (mF)	R_{CT2} (Ω)
-155	1.47	48.6	2.13	7.17	253
-180	1.58	18.4	1.72	6.16	56.7
-205	1.56	21.6	1.86	5.22	16.2
-230	1.58	16.9	1.70	5.44	9.83
-255	1.60	8.11	1.29	5.73	7.55

Table 4.6. EEC fitting parameters of NiSe nanoflakes towards the HER.

Overpotential (mV)	R_S (Ω)	Q_{CPE1} (F)	R_{CT1} (Ω)	Q_{CPE2} (mF)	R_{CT2} (Ω)
-155	0.92	3.08	0.06	5.49	24.3
-180	0.91	2.56	0.04	5.12	17.0
-205	0.93	1.19	0.05	4.88	11.1
-230	0.93	0.20	0.02	4.37	5.85
-255	0.94	0.11	0.02	4.06	4.72

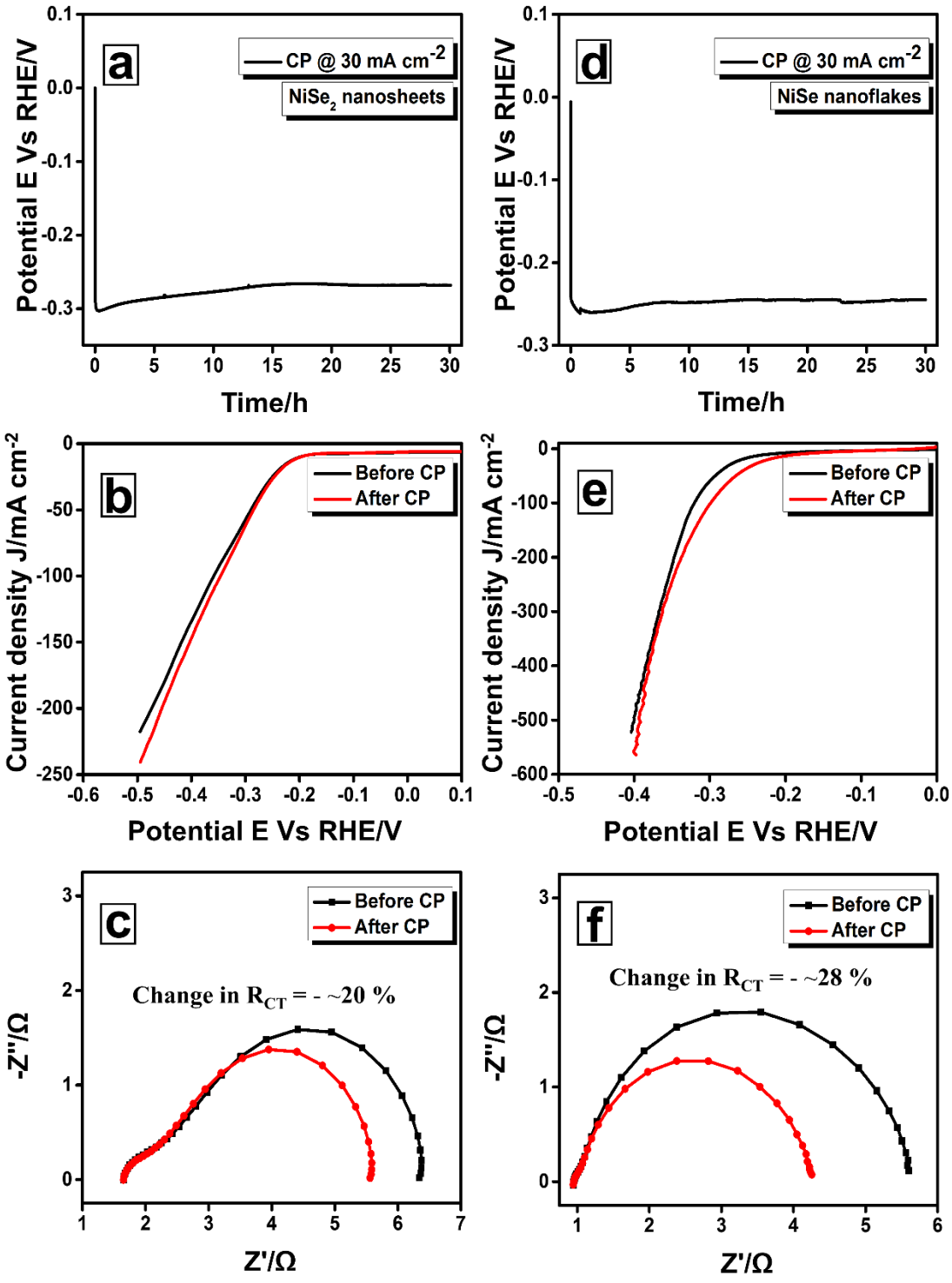

Figure 4.17 Chronopotentiometric stability test of (a) $NiSe_2$ nanosheets and (d) NiSe nanoflakes at an applied current density of -30 mA cm^{-2} for 30 h, LSV curves recorded at a scan rate of 5 mV s^{-1} before and after chronopotentiometric stability test of $NiSe_2$ nanosheets (b) and NiSe nanoflakes (e) and Nyquist plot before and after stability test at the applied bias of -255 mV of $NiSe_2$ nanosheets (c) and NiSe nanoflakes (f).

The catalytic stabilities of both nickel selenides were evaluated through constant current potentiometric methods. Figure 4.17a represents the chronopotentiometry of $NiSe_2$ nanosheets for 30 h at an applied current density of 30 mA cm^{-2}. Results indicate the continuous evolution of hydrogen with a small deviation in the potential, indicating the promising stability of the electrodes. The LSV curve recorded before and after chronopotentiometry as shown in Figure 4.17b, indicate marginal enhancement in the catalytic activity. The Nyquist plots (at -255 mV bias) recorded after the chronopotentiometry test for 30 hours as shown in Figure 4.17c also validated these results. The percentage decrease in charge-transfer resistance (R_{CT2}) is -20 % indicates the activation of catalytic sites and no degradation of the catalyst and catalytic activity of $NiSe_2$ nanosheets as confirmed from LSV curves.

On the other hand, Figure 4.17d represents the chronopotentiometric E-t curve of NiSe nanoflakes for 30 h at an applied current density of 30 mA cm^{-2}. Results indicate the continuous evolution of hydrogen with a small downward shift in the potential. The LSV curves recorded after chronopotentiometry of 30 h indicate the slightly enhanced catalytic activity of NiSe nanoflakes as depicted in Figure 4.17e. The enhanced catalytic activity of NiSe nanoflakes could be attributed to the activation of catalytic sites during long-term stability test. In order to support this claim, the Nyquist plot (Figure 4.17f) recorded after 30 h chronopotentiometric test indicate the decrease in charge-transfer resistance by ~28%. Thus, these results successfully establish the ultra-long term catalytic stability of both $NiSe_2$ nanosheets and NiSe nanoflakes.

4.3.5 Reverse material characterization

Since 3d-group electrocatalysts are susceptible to corrosion in acidic conditions, $NiSe_2$ nanosheets and NiSe nanoflakes were subjected to morphological and elemental analysis through FESEM and EDS measurements as represented in Figure 4.18a-b and Figure 4.18c-d, respectively. $NiSe_2$ nanosheets could retain the sheet-like geometry after stability test, while the hexagonal shape was partially lost. On the other hand, NiSe nanoflakes could retain the vertically aligned flake-like assembly even after chronopotentiometric stability test of 30 h in acidic conditions. Thus, these results

indicate both nickel selenides are morphologically stable under long-term operations. Further, EDS measurements performed on $NiSe_2$ nanosheets and NiSe nanoflakes indicate the peaks corresponding to nickel and selenium. Surprisingly, EDS measurements also signify the incorporation of sulphur in trace quantities. The presence of sulphur moieties may be attributed to long-term chronopotentiometric stability tests performed in sulfuric acid. The marginal increase in the catalytic activity of $NiSe_2$ nanosheets and NiSe nanoflakes after long-term stability test may also be attributed to the incorporation of sulphur. The incorporation of sulphur enhanced the HER activity in molybdenum sulphoselenides as reported by other group (Kiran et al. 2014). The comparison of atomic and weight percentages obtained from EDS measurements before and after chronopotentiometric stability tests of $NiSe_2$ nanosheets and NiSe nanoflakes are provided as Table 4.7.

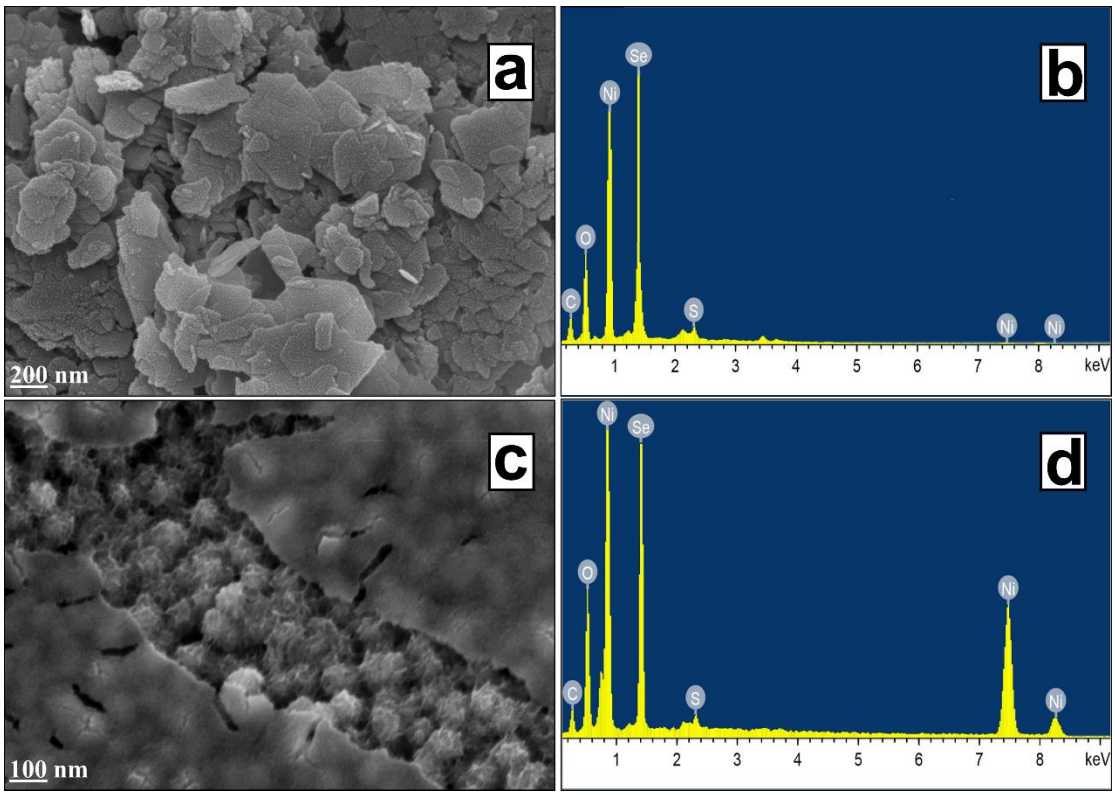

Figure 4.18 FESEM and EDS mapping of $NiSe_2$ nanosheets (a-b) and NiSe nanoflakes (c-d) after chronopotentiometric stability test for 30 h.

Table 4.7 Weight percentages of all elements in $NiSe_2$ nanosheets and NiSe nanoflakes before and after stability test.

	$NiSe_2$ nanosheets		**NiSe nanoflakes**	
Element	**Before stability test**	**After stability test**	**Before stability test**	**After stability test**
Ni	38.79	36.8	56.62	52.6
Se	53.37	49.8	25.76	22.53
O	5.63	8.65	13.9	12.44
C	2.13	2.01	3.72	11.73
S	0	2.66	0	0.70
Total	100	100	100	100

4.4 SUMMARY

$NiTe/NiTe_2$ nanosheets were hydrothermally synthesized by the successful transformation of pre-synthesized hexagonal $Ni(OH)_2$ nanosheets via anion-exchange reaction with tellurium ions. The electrocatalytic measurements were studied through linear sweep voltammetry and constant current chronopotentiometric analysis towards HER and OER, revealing their excellent electrocatalytic activities. The large current values at small overpotential and stability of electrodes suggests the promising use of this material as bifunctional electrocatalysts and for Lithium-air batteries.

$NiSe_2$ hexagonal nanosheets were also synthesized by the successful anion-exchange reaction of $Ni(OH)_2$ with Se ions. On the other hand, NiSe nanoflakes were synthesized by the selenization of the nickel foam surface. NiSe nanoflakes reveal significantly enhanced HER performance compared with $NiSe_2$ nanosheets and also complimented with the short synthesis duration of only 2 h. These interesting findings open-up opportunities for the design and developments of high performance catalytic materials.

CHAPTER 5

MOLYBDENUM CHALCOGENIDES FOR ELECTROCHEMICAL WATER-SPLITTING AND SUPERCAPACITOR ELECTRODES

In this chapter, the hydrothermal synthesis of molybdenum chalcogenide MoX_2 (X= S, Se, Te) nanostructures, W-doped $MoSe_2$ and W-$MoSe_2$/graphene hybrid nanostructures are discussed. MoX_2 (X= S, Se, Te) nanostructures are used as an electrocatalyst for the HER. Electrochemical measurements rank their performances in the following order: $MoSe_2$>MoS_2>$MoTe_2$. Further, lower onset potentials, catalytic stabilities and robustness of molybdenum chalcogenide nanostructures are complimented. On the other hand, isoelectronic tungsten (W) doping is employed to enhance the specific capacitances of molybdenum selenide ($MoSe_2$) supercapacitor electrodes. Specific capacitances as a function of W-doping indicate 2 M % of W as an optimum doping amount. Furthermore, graphene composites of these nanostructures delivered enhanced specific capacitances and superior cycle life of the supercapacitor electrodes. These electrochemical investigations on molybdenum chalcogenide nanostructures demonstrate their potential for electrochemical energy conversion and storage devices.

5.1 INTRODUCTION

Molybdenum chalcogenides have driven significant interest owing to their layered structures, electronic conductivity, thermal and chemical stabilities, low-band gap, interlayer spacing and multivalent redox states (Choi et al. 2017). All of the above features are beneficial for a variety of electrochemical investigations such as Li-ion batteries, dye-sensitized solar cells, supercapacitors and water-splitting reactions.

Considering molybdenum chalcogenides for the HER, disulfides and diselenides of molybdenum are hugely explored with numerous reports. While to the best of our knowledge, the HER activities of molybdenum ditellurides and the forthright HER performance comparisons of molybdenum dichalcogenide series are scarcely described. Among TMCs, it is well documented that as the degree of covalency in the metal-chalcogen bond increases and the declination of electronegativity from sulfur to tellurium correlates to the enhancement of metallic features in chalcogenide series (De

Silva et al. 2018). Further, band structure analysis confirm the diminution of bandgap in molybdenum dichalcogenide series from oxides to tellurides (Rasmussen and Thygesen 2015). On the other hand, some of the results elucidate the metallic feature of molybdenum tellurides (Beams et al. 2016). In this context, studying the role of different chalcogen atoms (S, Se, Te) in molybdenum chalcogenide series for HER is interesting. Further, recent reports on molybdenum dichalcogenides for the HER employ various synthesis techniques and use different substrates such as Ni foam, carbon cloth, glassy carbon, etc. The different substrate surfaces greatly influence the resulting current densities and Tafel slopes, which make the comparison among these molybdenum chalcogenide series difficult. In this regard, the following chapter describes the hydrothermal synthesis of series of molybdenum dichalcogenide nanostructures MoX_2 (X= S, Se, Te) and their use as an electrocatalyst for the HER. Herein, the electrodes for electrochemical measurements were prepared on graphite rod substrates for all the synthesized molybdenum dichalcogenide nanostructures, making the comparison among them more reasonable.

On the other hand, $MoSe_2$ is an important material for electrochemical energy storage applications, with the interlayer spacing (0.646 nm) larger than those of graphite (0.335 nm). The larger interlayer spacing decreases the diffusion energy barrier for ion intercalation and improve interlayer conductivity (Rasamani et al. 2017), which benefits energy storage devices such as Li-ion batteries and supercapacitors. In addition, although $MoSe_2$ features high theoretical capacity, the low electronic conductivity (El-Mahalawy and Evans 1977) results in low energy-storage performances. To overcome this difficult, the promising approach is to decorate with highly conductive materials by doping or by producing a composite with conductive carbon nanostructures. Recently, isoelectronic doping in molybdenum chalcogenides have gained considerable attention attributing to the ease of alloy formation, impeding the generation of dislocations and defects (Li et al. 2017). Earlier reports on isoelectronic doping in tungsten-molybdenum ternary chalcogenides have demonstrated the modulations of bandgap (Tongay et al. 2014), electrical and optical properties (Zhang et al. 2014). In this perspective, it is anticipated to observe the variation of various physiochemical parameters such as surface area, pore size and electronic conductivity, which are the key factors determining the electrochemical

applications of these materials. Further, recent literature on isoelectronic tungsten-molybdenum chalcogenides have presented the enhancement of electrochemical properties such as water-splitting and supercapacitors (Xu et al. 2016).

On the other hand, graphene is a two-dimensional carbon material composed of few-layers having high specific surface area, minimal cytotoxicity, mechanical stability and complimented with high electronic and thermal conductivity (Sreejesh et al. 2015). There are sufficient reports on graphene alone as the electrode material for supercapacitor and various synthesis methods and treatments are also employed to enhance their electrochemical activities (Worsley et al. 2010). Thus, graphene could serve as an outstanding matrix material when hybridized with certain class of materials for their electrochemical explorations. In the context, certain reports on transition metal-chalcogenides/graphene hybrids elucidate the enhancement of electrochemical properties with the addition of graphene (Ratha and Rout 2013).

With this background, we discuss the synthesis of W-doped $MoSe_2$ and also their graphene composites for their use as an active electrode materials for supercapacitors. Although there are several reports on $MoSe_2$ nanostructures as electrode materials for supercapacitors, demonstrating double layer, pseudo-capacitive and battery-like behavior based on the method of synthesis and experimental environments (Li et al. 2019; Pazhamalai et al. 2018). Nevertheless, to the best of our knowledge, the effect of the isoelectronic W-doping on $MoSe_2$ nanostructures and their graphene hybrids are not discussed. Doping concentration dependent study indicate 2 M % of tungsten as the optimum doping amount, delivering the enhanced specific capacitances to 147 F g^{-1}, in comparison to pristine $MoSe_2$ electrodes (106 F g^{-1}). Further, hybridizing with graphene enhanced the specific capacitances to 248 F g^{-1} and also complimented with excellent cyclic retention of 102 % for 20000 cycles.

5.2 SYNTHESIS

5.2.1 Synthesis of molybdenum sulfide (MoS_2) nanograins

Molybdenum sulfides (MoS_2) are prepared without the use of any reducing agent. In brief, 1.32 g (5.45 mM) of sodium molybdate dihydrate ($Na_2MoO_4 \cdot 2H_2O$) and 1.1795 g (15.7 mM) of thioacetamide (C_2H_5NS) were added to a beaker containing 80 mL of

DI water at room temperature. The as formed solution was stirred for 10 min, ensuring the complete dispersion and then transferred into a Teflon-lined stainless-steel autoclave of 120 mL capacity, sealed and placed in an oven at 200 °C for 12 h. After the autoclaves cooled down naturally, precipitates were collected by washing with excess DI water and then dried overnight at 60 °C.

5.2.2 Synthesis of molybdenum selenide ($MoSe_2$) nanoflowers

In a typical process of preparing molybdenum selenides ($MoSe_2$), a red-colored solution was formed by adding 1.32 g (5.45 mM) of sodium molybdate ($Na_2MoO_4 \cdot 2H_2O$) ,1.24 g (15.7 mM) of Selenium (Se), and 0.2 g of sodium borohydride ($NaBH_4$) in 80 mL of DI water at room temperature. The precursor solution was continued to stir for 10 min, ensuring the uniform distribution of selenium and then transferred into the Teflon-lined stainless-steel autoclave of 120 mL capacity, sealed and placed in an oven at 200 °C for 12 h. After the autoclaves cooled down naturally, precipitates were collected by washing with excess DI water and then dried overnight at 60 °C.

5.2.3 Synthesis of molybdenum telluride ($MoTe_2$) nanotubes

For the synthesis of molybdenum tellurides ($MoTe_2$), 1.4517 g (6 mM) of sodium molybdate dihydrate ($Na_2MoO_4 \cdot 2H_2O$), 1.5312 g (12 mM) of tellurium metal powder (Te), and 0.34 g (9 mM) of sodium borohydride ($NaBH_4$) were added to 80 mL of DI water at room temperature. The as formed mixture was continued to stir for 10 min, followed by transfer of mixture to the Teflon-lined stainless-steel autoclave and hydrothermal process at 200 °C for 48 h. The collected products were washed with excess of DI water and then dried overnight at 60 °C.

5.2.4 Synthesis of tungsten doped molybdenum selenide (W-$MoSe_2$) nanostructures

For the synthesis of tungsten doped molybdenum selenide nanostructures (W-$MoSe_2$), different amounts of sodium tungstate ($Na_2WO_4 \cdot 2H_2O$) (1, 2 and 3 M %) were added by replacing with equal mole percent amounts of sodium molybdate ($Na_2MoO_4 \cdot 2H_2O$), followed by the addition of required amounts of selenium (Se) and sodium borohydride

($NaBH_4$). After which, the solution was stirred for 10 min and above mentioned hydrothermal synthesis was carried out. Hereafter 1, 2 and 3 M % W-doped $MoSe_2$ nanostructures are named as W1-$MoSe_2$, W2-$MoSe_2$ and W3-$MoSe_2$, respectively.

5.2.5 Synthesis of tungsten doped molybdenum selenide/graphene (W-$MoSe_2$/G) hybrids

Graphene oxide (GO) was synthesized using the modified Hummer's method as reported elsewhere (Marcano et al. 2010). For the synthesis of tungsten doped molybdenum selenide/graphene hybrids, about ~250 mg of pre-synthesized and dried GO powder was dispersed in 50 mL of DI water through ultra-sonication for 1 h. For the preparation of W2-$MoSe_2$/G composite, after the addition of required amounts of sodium molybdate ($Na_2MoO_4 \cdot 2H_2O$), sodium tungstate ($Na_2WO_4 \cdot 2H_2O$), selenium (Se) metal powder and sodium borohydride ($NaBH_4$) in DI water, GO dispersion was added dropwise with continuous stirring, ensuring the uniform dispersion of GO in the precursor solution. The as-prepared precursor solution was then transferred into the autoclave, followed by hydrothermal process at the temperature of 200 °C for 12 h.

5.3 RESULTS AND DISCUSSIONS

5.3.1 Physiochemical analysis of molybdenum chalcogenide MoX_2 (X= S, Se, Te) nanostructures

The Figure 5.1a displays the XRD patterns of MoS_2 nanograins, indexed to their hexagonal crystal structure with lattice constants $a = b$ =3.16 Å and c = 12.29 Å, which are commensurate with JCPDS card no. 00-037-1492. Further, Figure 5.1b displays the XRD patterns of $MoSe_2$ nanoflowers indexed to its hexagonal phase with lattice constants $a = b$ =3.28 Å and c = 12.92 Å, which are in agreement with the standard JCPDS card no. 029-0914. On the other hand, XRD pattern of $MoTe_2$ nanotubes (Figure 5.1c) indicate the peaks corresponding to $MoTe_2$ and weaker Te rings, with the XRD pattern of $MoTe_2$ nanotubes indexed to their hexagonal phase with lattice constants $a = b$ =3.51 Å and c = 13.97 Å. The obtained XRD patterns are in good agreement with standard JCPDS card no. 01-073-1650 ($MoTe_2$) and 01-079-0736 (Te), respectively. It is interesting to note that, the order of crystallinity of $MoTe_2$ nanotubes are much higher

as compared with MoS_2 nanograins and $MoSe_2$ nanoflowers, which could be due to the presence of weaker Te rings acting as the nucleation centre or substrate for the formation of $MoTe_2$ nanotubes.

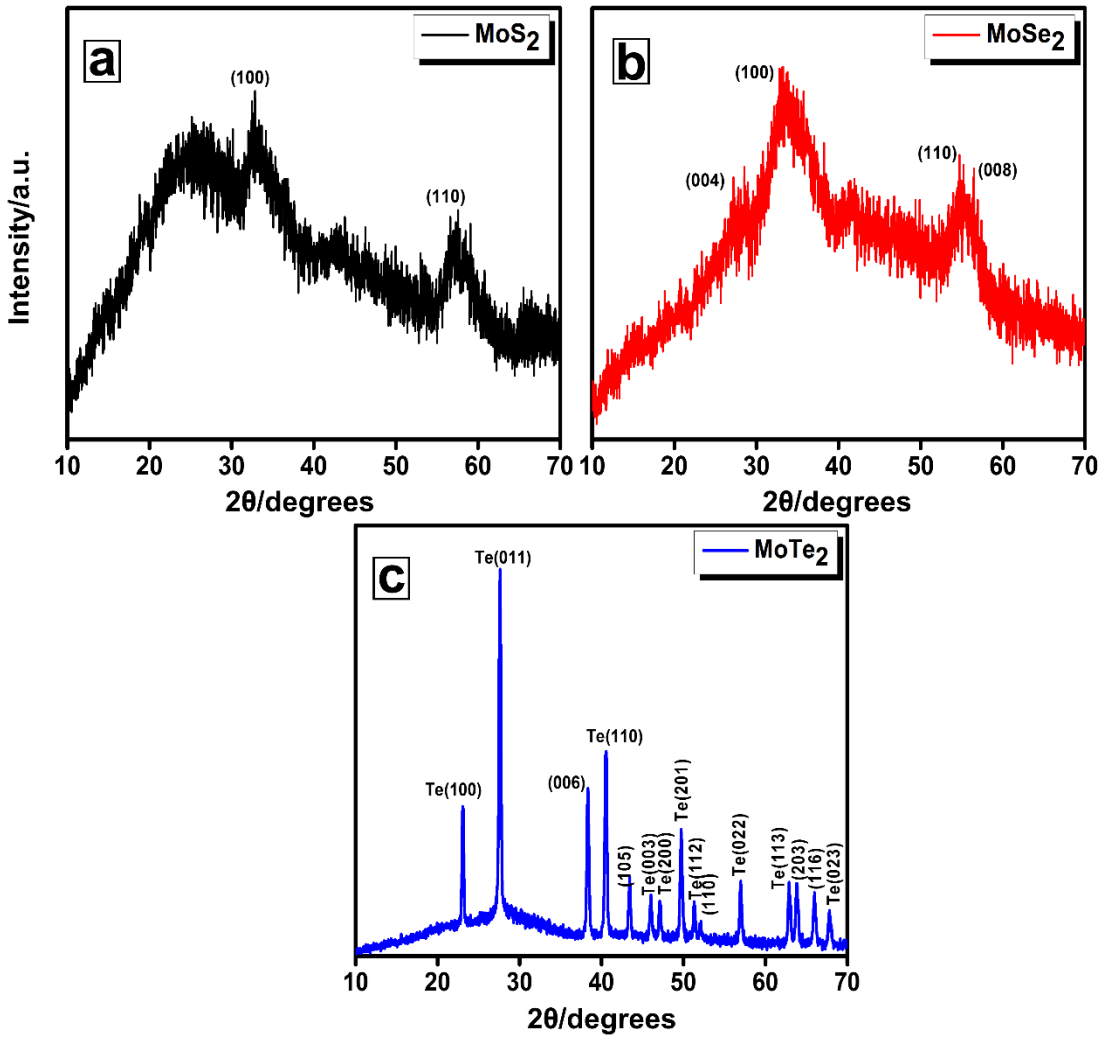

Figure 5.1 XRD patterns of (a) MoS_2 nanograins, (b) $MoSe_2$ nanoflowers and $MoTe_2$ nanotubes.

Further, FESEM and EDS measurements are employed to determine the morphology and elemental composition of the synthesized molybdenum dichalcogenide nanostructures. FESEM image of MoS_2 (Figure 5.2a) confirm the grain-like structures of estimated sizes ~16 to ~20 nm with a no ordered shape. On the other hand, FESEM image of $MoSe_2$ (Figure 5.2b) represents plenty of well-ordered two-dimensional sheet-like structures of sizes 7 ~ 10 nm, aggregated to form a bunch of nanoflowers of sizes ~100 nm. Likewise, FESEM image of $MoTe_2$ (Figure 5.2c) portrays the tube-like

structures with the estimated average length and diameter of ~500 nm and ~95 nm, respectively. Furthermore, EDS spectra's of MoS_2 nanograins, $MoSe_2$ nanoflowers and $MoTe_2$ nanotubes as shown in Figure 5.2d-e-f confirms their purity. In addition, the obtained weight percentages of elements from the EDS measurements are provided in (see APPENDIX IX) and the EDS color maps obtained from FESEM images over a large scanning area of ~100μm (see APPENDIX IX) of all the nanostructures represent the uniform distribution of elements as indicated in (see APPENDIX IX) for MoS_2 nanograins, $MoSe_2$ nanoflowers and $MoTe_2$ nanotubes, respectively. It is interesting to note that the color map of $MoTe_2$ shown Te rich patterns owing to the weaker Te rings as commensurate with XRD measurements.

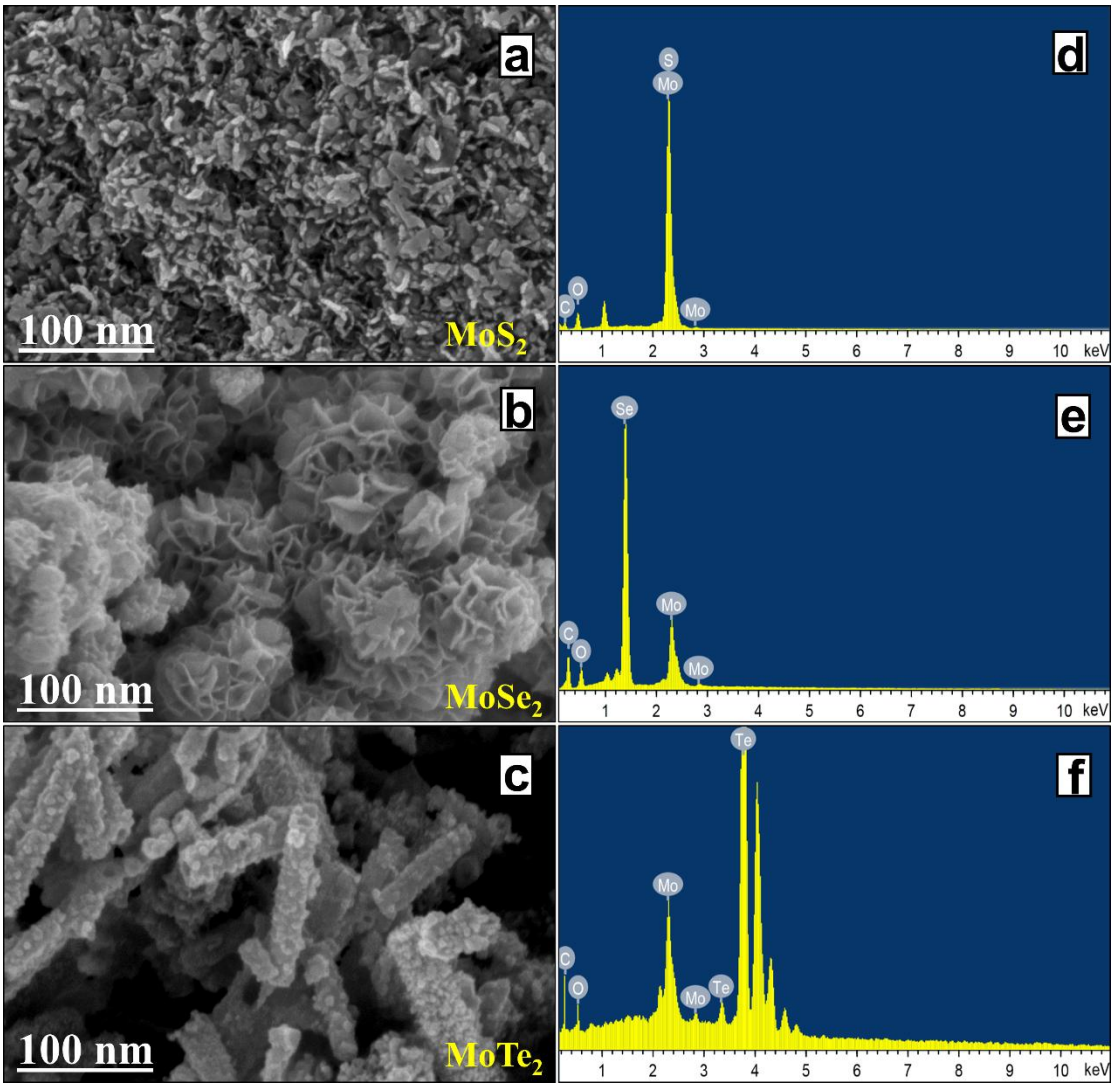

Figure 5.2 Morphological characterizations through FESEM of (a) MoS_2, (b) $MoSe_2$ and (c) $MoTe_2$ and (d), (e) and (f) represents the corresponding EDS spectra's.

5.3.2 HER performance of MoX_2 (X= S, Se, Te) nanostructures

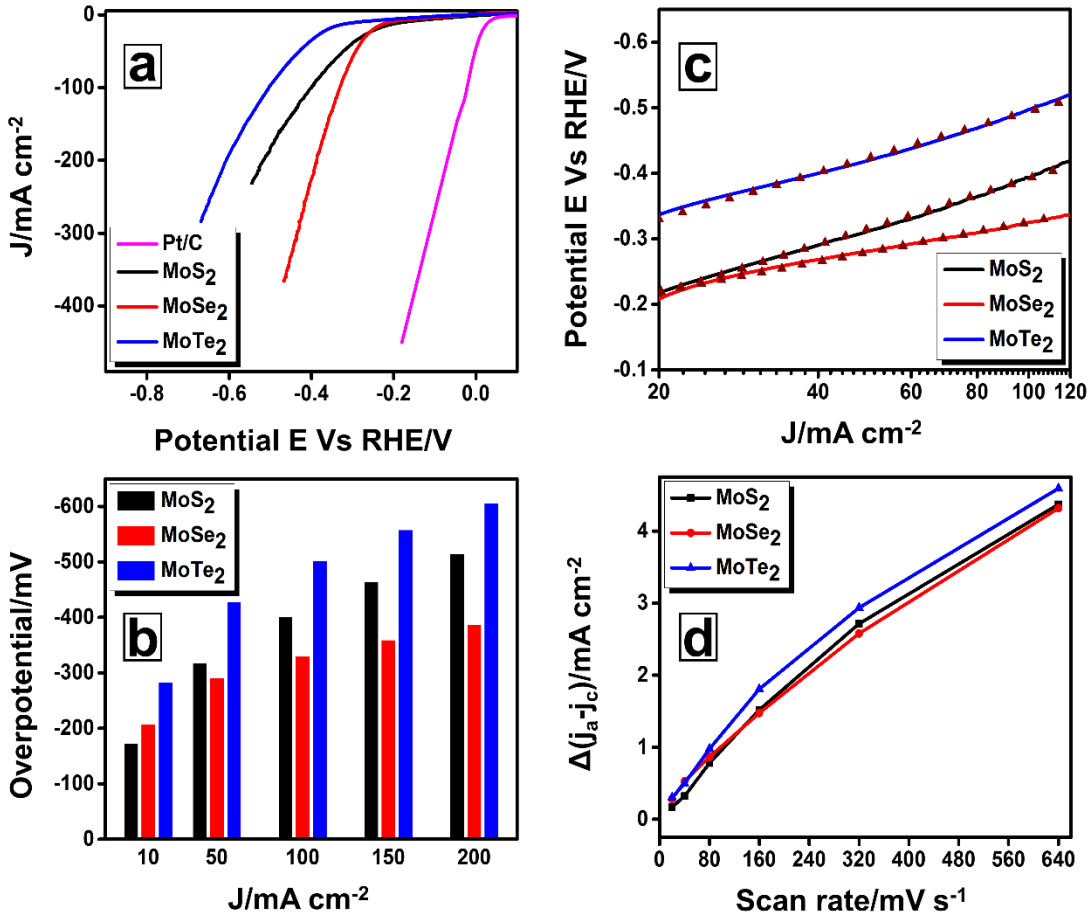

Figure 5.3 (a) iR compensated LSV curves at 5 mV s^{-1} scan rate, (b) Comparison of overpotentials required to deliver different current densities, (c) Tafel plots derived from iR compensated LSV curves, and (d) Plot of difference in double layer charging current densities Vs. scan rate of different molybdenum dichalcogenide MoX_2 (X= S, Se, Te) catalysts.

The iR compensated LSV curves of molybdenum dichalcogenide electrocatalysts (MoS_2, $MoSe_2$ and $MoTe_2$) in 0.5 M H_2SO_4 solution are displayed in Figure 5.3a. The LSV curves of MoS_2 nanograins, $MoSe_2$ nanoflowers and $MoTe_2$ nanotubes reveal the overpotentials required for the benchmark of 10 mA cm^{-2} geometric current densities as -173 mV, -208 mV and -283 mV, respectively. On the other hand, overpotentials required for 100 mA cm^{-2} current densities for MoS_2 nanograins, $MoSe_2$ nanoflowers and $MoTe_2$ nanotubes are -401 mV, -330 mV and -502 mV, respectively, while they are -515 mV, -388 mV and -607 mV for the higher current densities of 200 mA cm^{-2}. It is

worth noting that $MoSe_2$ nanoflowers could attain a very high current density of -350 mA cm^{-2} at a relatively lower overpotential of -458 mV. To summarize, overpotentials required for different current densities are pictured as a bar chart in Figure 5.3b and tabulated as Table. 5.1. Further, since Tafel slope signify the rate of electrolysis, Tafel plots derived from iR compensated LSV curves as seen in Figure 5.3c portrays the Tafel slope values of 109.81 mV dec^{-1}, 65.92 mV dec^{-1} and 102.06 mV dec^{-1} for MoS_2 nanograins, $MoSe_2$ nanoflowers and $MoTe_2$ nanotubes, respectively.

Further compare the HER performance of synthesized molybdenum dichalcogenide catalysts with state-of-the-art catalysts, 20 Wt. % Pt/C were loaded on graphite rod substrates with the same mass loading (~0.4 mg cm^{-2}) in comparison to those of molybdenum dichalcogenide electrodes. LSV curves of state-of-the art Pt/C catalyst demonstrate the onset potential of exact 0 V and ultra-low overpotential of -36 mV to deliver 10 mA cm^{-2} benchmark geometric current density. In addition, the HER performances of these molybdenum dichalcogenide catalysts are compared with earlier available reports as provided in Table 5.2.

Table 5.1. Comparison of overpotentials required to deliver different current densities for different molybdenum dichalcogenide catalysts.

Current density (mA cm^{-2})	**Overpotential (mV)**		
	MoS_2	**$MoSe_2$**	**$MoTe_2$**
10	-173	-208	-283
50	-318	-291	-428
100	-401	-330	-502
150	-464	-360	-558
200	-515	-388	-607

To gain insight into real accessible surface area for electrocatalytic reactions, ECSA was determined from double layer capacitance (C_{dl}) measurements. The CV curves of MoS_2 nanograins, $MoSe_2$ nanoflowers and $MoTe_2$ nanotubes recorded in the double-layer charging region are provided in (see APPENDIX X). The double-layer capacitance's ($2C_{dl}$) were estimated by plotting the difference in double-layer charging current densities $\Delta j = j_a - j_c$ at -0.3 V Vs. SCE for MoS_2 nanograins and $MoSe_2$ nanoflowers and at -0.35 V Vs. SCE for $MoTe_2$ nanotubes as a function of the scan rate

as displayed in Figure 5.3d. The measured $2C_{dl}$ values are 9.01 mF cm^{-2}, 8.52 mF cm^{-2} and 9.13 mF cm^{-2} for MoS_2 nanograins, $MoSe_2$ nanoflowers and $MoTe_2$ nanotubes, respectively. The obtained $2C_{dl}$ values suggest electrochemically accessible internal surface areas are roughly the same for all nanostructures (Gholamvand et al. 2016). However, the pore sizes estimated from BJH measurements (see APPENDIX X) indicate the higher pore diameter (d_P) of ~14.77 nm for $MoTe_2$ nanotubes, in comparison to MoS_2 nanograins (d_P = ~1.62 nm) and $MoSe_2$ nanoflowers (d_P = ~3.56 nm). The higher pore size of $MoTe_2$ nanotubes may be ascribed to their nanotube-like structures, which provide substantial electroactive sites (Chia and Pumera 2018) for water-splitting reactions.

Table 5.2. Comparison of catalytic activities different MoX_2 (X= S, Se, Te) nanostructures towards HER as reported in the literature.

Catalyst	Overpotential (mV)	Tafel slope	Reference
MoS_2	160 mV (Onset)	101 mV dec^{-1}	(Hu et al. 2016)
MoS_2	187 @ 10 mA cm^{-2}	43 mV dec^{-1}	(Lukowski et al. 2013)
MoS_2	120 mV (Onset)	55 mV dec^{-1}	(Xie et al. 2013)
MoS_2	130 mV (Onset)	52 mV dec^{-1}	(Wang et al. 2014)
MoS_2	550 @ 10 mA cm^{-2}	99 mV dec^{-1}	(Ambrosi et al. 2015)
$MoSe_2$	350 @ 10 mA cm^{-2}	82 mV dec^{-1}	(Ambrosi et al. 2015)
$MoSe_2$	250 @ 10 mA cm^{-2}	59.8 mV dec^{-1}	(Wang et al. 2013)
$MoSe_2$	150 mV (Onset)	101 mV dec^{-1}	(Tang et al. 2014)
$MoSe_2$	175 mV (Onset)	91 mV dec^{-1}	(Ren et al. 2018)
$MoSe_2$	231 @ 1 mA cm^{-2}	101.6 mV dec^{-1}	(Xu et al. 2018)
$MoTe_2$	356 @ 10 mA cm^{-2}	127 mV dec^{-1}	(Seok et al. 2017)
$MoTe_2$	340 @ 10 mA cm^{-2}	78 mV dec^{-1}	(McGlynn et al. 2018)
$MoTe_2$	440 @ 10 mA cm^{-2}	~100 mV dec^{-1}	(Gholamvand et al. 2016)
$MoTe_2$	530 @ 10 mA cm^{-2}	72 mV dec^{-1}	(Kosmala et al. 2018)
$MoTe_2$	481 @ 10 mA cm^{-2}	67 mV dec^{-1}	(Mc Manus et al. 2019)
MoS_2	173 @ 10 mA cm^{-2}	109 mV dec^{-1}	Present work
$MoSe_2$	208 @ 10 mA cm^{-2}	65.9 mV dec^{-1}	Present work
$MoTe_2$	283 @ 10 mA cm^{-2}	102 mV dec^{-1}	Present work

5.3.3 HER kinetics and stability of MoX_2 (X= S, Se, Te) nanostructures

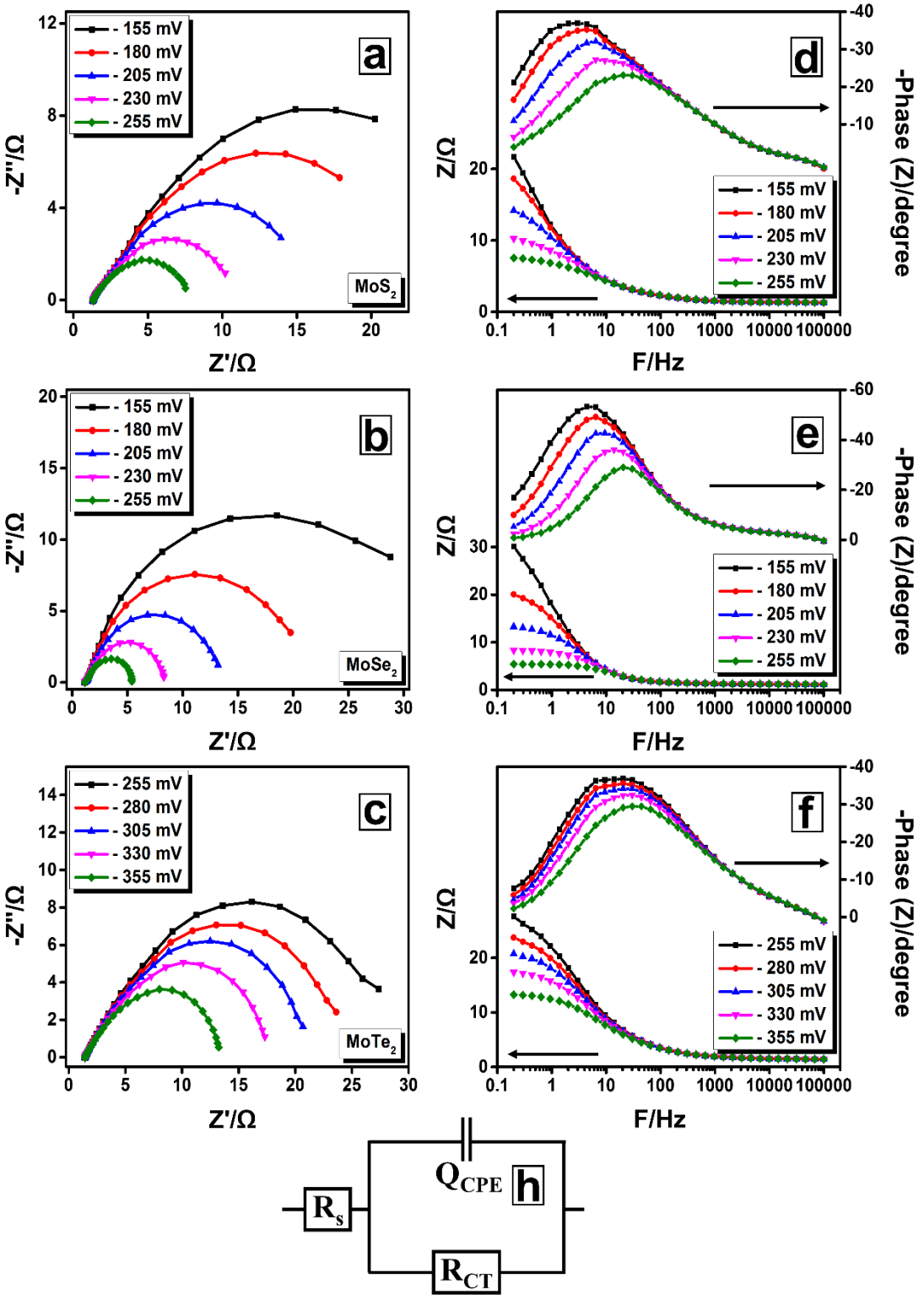

Figure 5.4 (a-b-c) Nyquist plots and corresponding Bode phase angle plots (d-e-f) of MoS_2, $MoSe_2$ and $MoTe_2$ and (h) Simulated EEC for the Nyquist plots.

The HER kinetics of the presented MoX_2 nanostructures are studied using EIS measurements. EIS measurements were conducted in the frequency range of 0.2 Hz to 100 kHz with the sinusoidal AC amplitude of $V_{AC} = 10$ mV at different bias voltages. The Nyquist plots of MoS_2 nanograins, $MoSe_2$ nanoflowers and $MoTe_2$ nanotubes at different bias voltages at the vicinity of onset potentials are represented as Figure 5.4a-b-c, respectively. The semicircular Nyquist plots represents the charge-transfer resistance and the variation of semi-circle diameter as a function of applied bias voltage indicate these semicircles are related to electrode kinetics. Further, Figure 5.4d-e-f describes the Bode phase angle plots derived from the corresponding Nyquist plots of molybdenum dichalcogenide electrodes. In addition, the total impedance and phase angle decreases at higher applied bias, indicating the enhancement of electrocatalytic activities (Ojha et al. 2017). Further, to obtain better insight on electrode kinetics, EEC were modelled for Nyquist plots of all the molybdenum dichalcogenide nanostructures. The EEC could fit into Randle's circuit as shown in Figure 5.4h consisting of solution resistance (R_S) in series with a parallel constant phase element (Q_{CPE}) and charge-transfer resistance (R_{CT}) as represented by $R_S(Q_{CPE}R_{CT})$. The EEC fitting parameters for MoS_2 nanograins, $MoSe_2$ nanoflowers and $MoTe_2$ nanotubes are tabulated in Table 5.3, Table 5.4 and Table 5.5, respectively. From EEC fitting parameters, $MoSe_2$ nanoflowers portrays the lowest solution resistance (R_S) of 1.205 Ω, indicating the better electrode-electrolyte contact. On the other hand, $MoTe_2$ nanotubes signifies the highest R_S of 1.449 Ω. Further, the R_{CT} at an applied bias of -155 mV for MoS_2 nanograins, $MoSe_2$ nanoflowers and $MoTe_2$ nanotubes are 41.38 Ω, 34.70 Ω and 56.6 Ω, respectively. While, the R_{CT} at higher bias of -255 mV are 6.97 Ω, 4.41 Ω and 30.74 Ω, respectively. It is noteworthy that, even at higher bias of -355 mV the R_{CT} of $MoTe_2$ nanotubes are still higher (13.22 Ω), demonstrating their inferior conductivity. All of these above values signify $MoSe_2$ nanoflowers has the highest electronic conductivity, which facilitates the rapid charge-transport for water-splitting reaction (Vrubel et al. 2013). In addition, although the R_S values of MoS_2 nanograins and $MoSe_2$ nanoflowers are comparable, the lowest R_{CT} of $MoSe_2$ nanoflowers compliments their superior electrocatalytic activity. While, the higher resistances (R_S and R_{CT}) of $MoTe_2$ nanotubes designate their inferior performance. The Nyquist plot of $MoTe_2$ nanotubes at -155 mV bias provided is provided as (see APPENDIX XI).

Table 5.3. EEC parameters of MoS_2 nanograins obtained by fitting the Nyquist plots.

Overpotential (mV)	R_S (Ω)	Q_{CPE1} (mF)	R_{CT1} (Ω)
-155	1.293	2.71	41.38
-180	1.299	2.56	28.96
-205	1.306	2.37	17.74
-230	1.321	2.13	10.71
-255	1.322	1.91	6.97

Table 5.4. EEC parameters of $MoSe_2$ nanoflowers obtained by fitting the Nyquist plots.

Overpotential (mV)	R_S (Ω)	Q_{CPE1} (mF)	R_{CT1} (Ω)
-155	1.205	10.42	34.70
-180	1.213	10.11	21.31
-205	1.232	9.93	13.08
-230	1.232	9.67	7.55
-255	1.235	9.38	4.41

Table 5.5. EEC parameters of $MoTe_2$ nanotubes obtained by fitting the Nyquist plots.

Overpotential (mV)	R_S (Ω)	Q_{CPE1} (mF)	R_{CT1} (Ω)
-255	1.449	7.65	30.74
-280	1.438	7.86	26.07
-305	1.443	7.91	22.41
-330	1.446	8.10	18.23
-355	1.446	8.34	13.22

The catalytic stabilities of all the molybdenum dichalcogenide electrodes were evaluated through constant current potentiometric methods. Chronopotentiometric stability tests were conducted for 12 h at higher current density of 50 mA cm^{-2}. The higher current density stability tests ensure the robustness of the electrocatalytic materials. Figure 5.5a represents the chronopotentiometric stability tests of MoS_2 nanograins, $MoSe_2$ nanoflowers and $MoTe_2$ nanotubes, respectively. Results indicate the continual evolution of hydrogen with an upward shift in the potential of +31.2 mV and +13.75 mV @ 12 h for MoS_2 nanograins and $MoSe_2$ nanoflowers, which may be

ascribed to the bleach of Sulphur/Selenium ions under long-term stability tests. On the other hand, E-t curve of $MoTe_2$ nanotubes indicate a downward shift in the potential (-13.24 mV @ 12 h) with the continuous evolution of hydrogen, owing to the activation of catalytic sites of $MoTe_2$ nanotubes. The Nyquist plots recorded after respective chronopotentiometric stability tests also validate these results. Further, Figure 5.5b-c-d represents the Nyquist plots of MoS_2 nanograins, $MoSe_2$ nanoflowers and $MoTe_2$ nanotubes after chronopotentiometric stability tests, respectively. The percentage increase in R_{CT} are about +28.5 % and +6.30 % for MoS_2 nanograins and $MoSe_2$ nanoflowers, indicating their very-less degradation. While the Nyquist plot of $MoTe_2$ nanotubes specify a decrease in R_{CT} of about -26.3 %, confirming the activation of catalytic sites and no-degradation of the electrocatalyst under long-term operations.

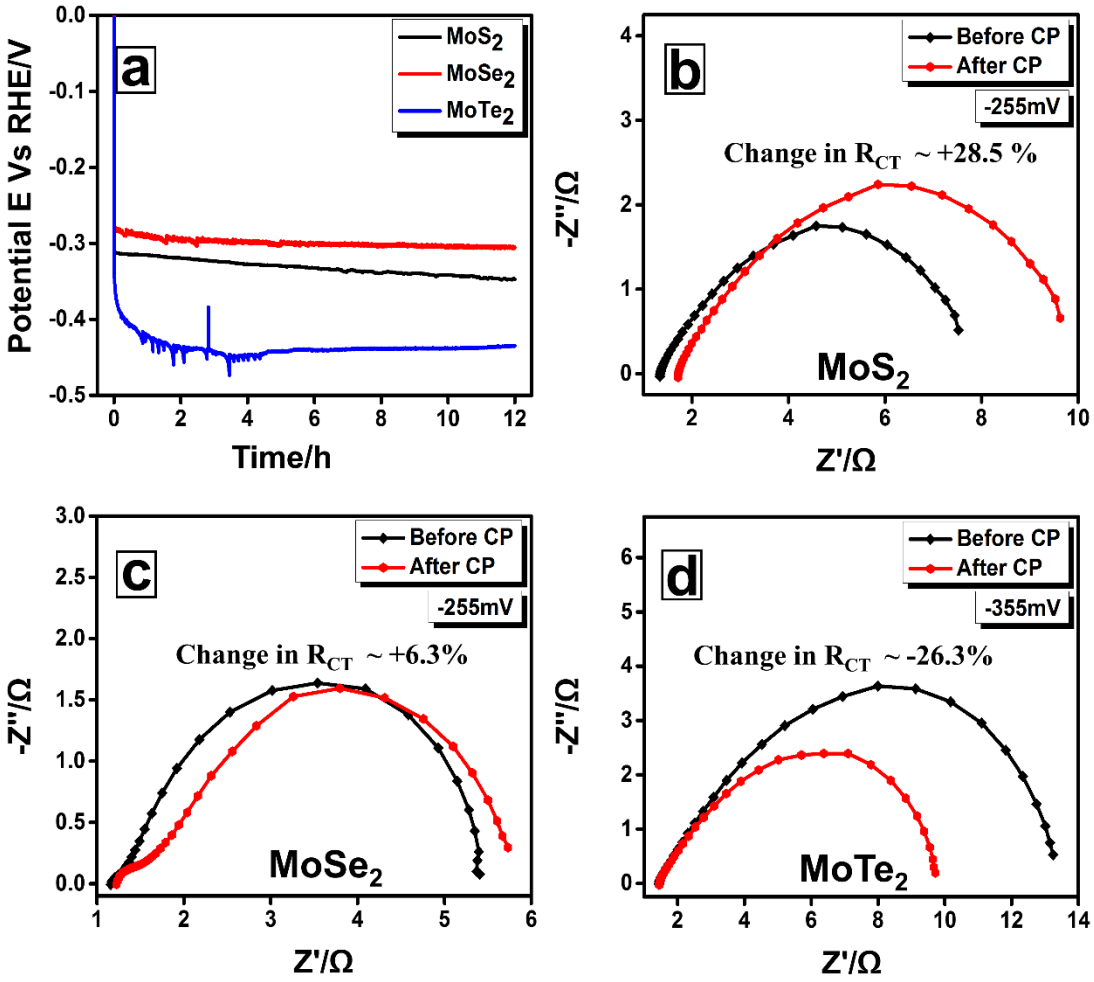

Figure 5.5 (a) Chronopotentiometric stability tests of MoS_2, $MoSe_2$ and $MoTe_2$ at an applied current density of 50 mA cm^{-2} for 12 h and Nyquist plots **(b-c-d)** recorded before and after chronopotentiometric stability tests.

5.3.4 Physiochemical analysis of pristine $MoSe_2$, W-doped $MoSe_2$ and their graphene hybrids (W-$MoSe_2$/G)

The XRD patterns of pristine $MoSe_2$, W2-$MoSe_2$ and W2-$MoSe_2$/G nanostructures are displayed in Figure 5.6a. The diffraction peaks of pristine $MoSe_2$ nanostructures are indexed to its hexagonal phase with lattice constants $a = b$ =3.28 Å and c = 12.92 Å, which is in agreement with standard JCPDS card no. 029-0914. Further, the XRD patterns W2-$MoSe_2$ and W2-$MoSe_2$/G nanostructures indicate similar peaks to those of pristine $MoSe_2$ with improved peak intensities, along with a small shift in 2θ positions towards the left. These results indicate the increase in crystallinity and successful doping of tungsten in the host lattice and also the formation of graphene composite. In addition, the XRD measurements of W2-$MoSe_2$/G nanostructures indicate a small peak at 2θ = ~24.6°, corresponding to the (002) plane of graphene (Sreejesh et al. 2015). Further, as seen from Figure 5.6b, W1-$MoSe_2$ nanostructures display the similar peaks to those of pristine $MoSe_2$ nanostructures. While, on the other hand it is interesting to note that, at higher doping amounts of tungsten (W3-$MoSe_2$) the diffraction patterns indicate the peaks corresponding to different phases of molybdenum selenides (W3-$MoSe_2$, ($) Mo_3Se_4 and (#) $Mo_{15}Se_{19}$) along with weaker Se rings (*). However, the peaks corresponding to Mo_3Se_4 and $Mo_{15}Se_{19}$ are of low intense, indicating their formations in very low quantities. Reason for the above is, beyond certain doping level tungsten (W) depolymerizes the network and facilitates the formation of random phases of molybdenum selenides and weaker Se rings. Similar depolymerization effect has been observed in tungsten-lead–germanate system as reported elsewhere (Rada et al. 2013). For a better understanding, the XRD pattern of W3-$MoSe_2$ nanostructures are compared with standard JCPDS reference patterns of Se, $MoSe_2$, Mo_3Se_4 and $Mo_{15}Se_{19}$ as provided in (see APPENDIX XII).

Raman spectrum of $MoSe_2$ nanostructures as shown in Figure 5.6c represent the prominent peaks at ~239 cm^{-1} and ~288 cm^{-1} corresponding to A_{1g} mode and in-plane E_{2g1} modes, respectively (Sekine et al. 1980). Further, Raman spectrum of W2-$MoSe_2$ nanostructures indicate a slight shift towards the right (inset of Figure 5.6c) as observed in monolayer and bilayer $Mo_{1-x}W_xSe_2$ systems (Zhang et al. 2014), confirming the successful incorporation of W in $MoSe_2$ through doping. On the other hand, Raman

spectra of W2-$MoSe_2$/G nanostructures indicate high intense bands at ~1350 cm^{-1} and ~1580 cm^{-1} in addition to characteristic A_{1g} and E_{2g1} modes of W2-$MoSe_2$ nanostructures. These bands at higher wavenumbers could be assigned to the typical D and G bands of graphene, respectively (Kaniyoor and Ramaprabhu 2012). The G band refers to the vibrational Sp^2 carbon atoms and the D band is a measure of defects and disorders of graphene oxide (Ramadoss and Kim 2013). Further, as seen from Raman spectra of W2-$MoSe_2$/G nanostructures, the I_D/I_G ratio of ~1.4 signify the formation of defects on graphene and the intensity of D band is slightly higher than those of the G band, indicate the successful reduction of graphene oxide during the hydrothermal process.

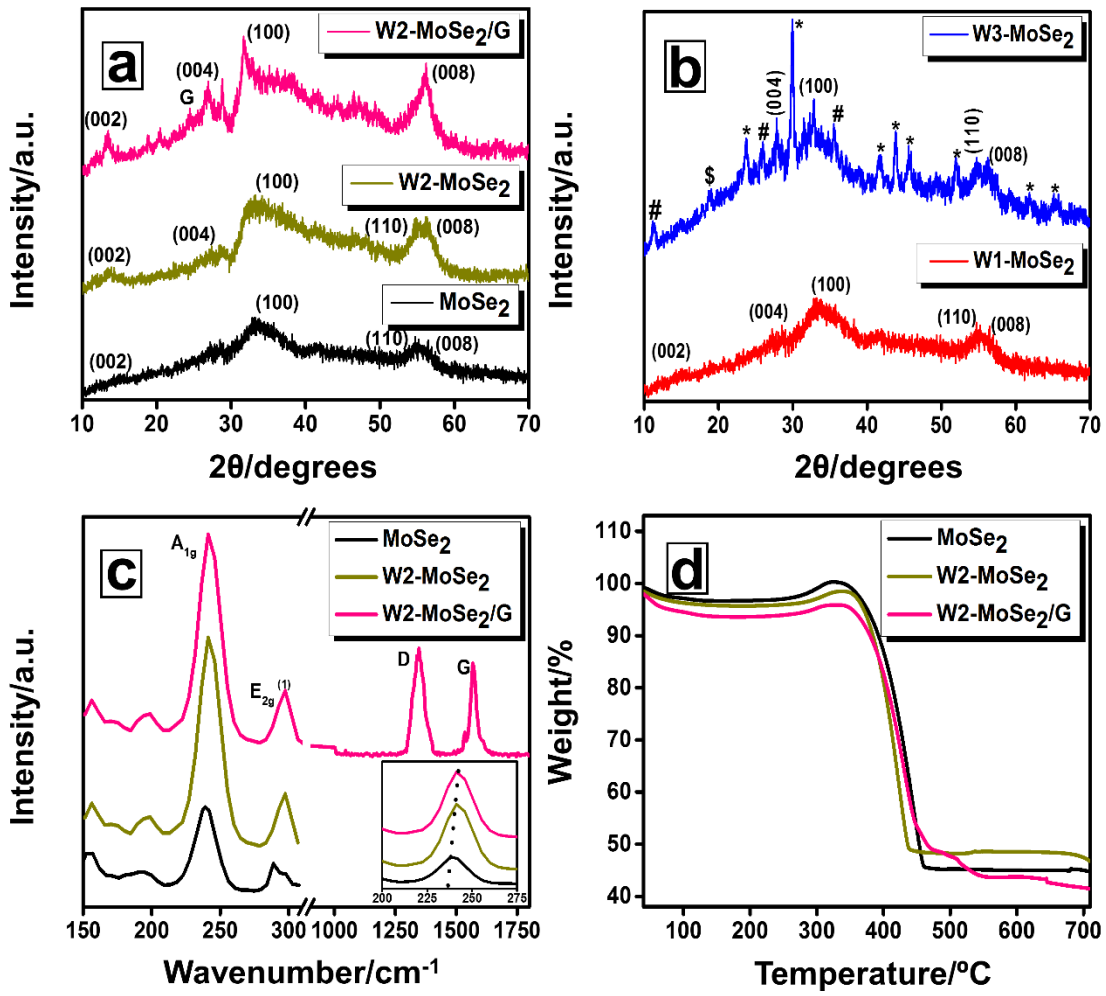

Figure 5.6 (a-b) XRD patterns of pristine, W-doped $MoSe_2$ and W-doped $MoSe_2$/G nanostructures, (c) Raman spectrums and (d) TGA curves of $MoSe_2$, W2-$MoSe_2$ and W2-$MoSe_2$/G nanostructures.

To obtain the accurate loading of W2-$MoSe_2$ in W2-$MoSe_2$/G nanostructures, TGA measurements are conducted. Figure 5.6d represents the TGA curves of pristine $MoSe_2$, W2-$MoSe_2$ and W2-$MoSe_2$/G nanostructures carried out in a temperature range of room temperature (~25°C) to 700 °C at a heating rate of 5 °C min^{-1}. $MoSe_2$ and W2-$MoSe_2$ nanostructures undergo marginal weight increment between 300 ºC to 330 ºC, which can be ascribed to the pyrolysis of $MoSe_2$ to form W/MoO_3 and SeO_2 (Zhang et al. 2015). Further, increase in the temperature volatizes SeO_2 and results in the final residue W/MoO_3. At a temperature of 700 ºC the residual weights are 45.20 % and 48.44 % for $MoSe_2$ and W2-$MoSe_2$ nanostructures, respectively. On the other hand, W2-$MoSe_2$/G nanostructures follows similar trend of W2-$MoSe_2$, followed by conversion of graphene to CO_2 (Yao et al. 2015) with the residual weight of 41.65 %. The weight loss of W2-$MoSe_2$/G nanostructures is equal to the sum of the weight loss of W2-$MoSe_2$ and carbon matrix (graphene), which could be described by the formula as given below:

$$A * 58.35\ \% = A * X * 53.05\ \% + A * (1 - X) \quad (5.1)$$

Herein, 'A' represents the mass of W2-$MoSe_2$/G nanostructures and 'X' represents the loading of W2-$MoSe_2$ in the W2-$MoSe_2$/G nanostructures. Hence, based on TGA curves the loading percentage of W2-$MoSe_2$ in graphene matrix is estimated to be 88.7 %. This pretty high loading amount is probably due to the high surface area of graphene, which provides substantial nucleation sites for the growth of W2-$MoSe_2$ nanostructures.

Further XPS measurements are employed to investigate the surface elemental composition of the synthesized W2-$MoSe_2$/G composite. The wide range XPS survey spectra as shown in Figure 5.7a indicate the presence of Mo, W, Se, C and O. The resolved binding energies of Mo 3d level as shown in Figure 5.7b are Mo 3d5/2 at 228.4 eV (M1) and Mo 3d3/2 at 231.8 eV (M2), which are about ~0.3 eV lower than the binding energies of pristine $MoSe_2$ reported elsewhere (Zhao et al. 2017). These results reveal the +4 oxidation state of Mo and the doublets (M3 and M4) at higher binding energies (232.5 eV and 235.6 eV) could be attributed to +6 oxidation state of Mo, owing to the surface oxide structure (Ren et al. 2018).

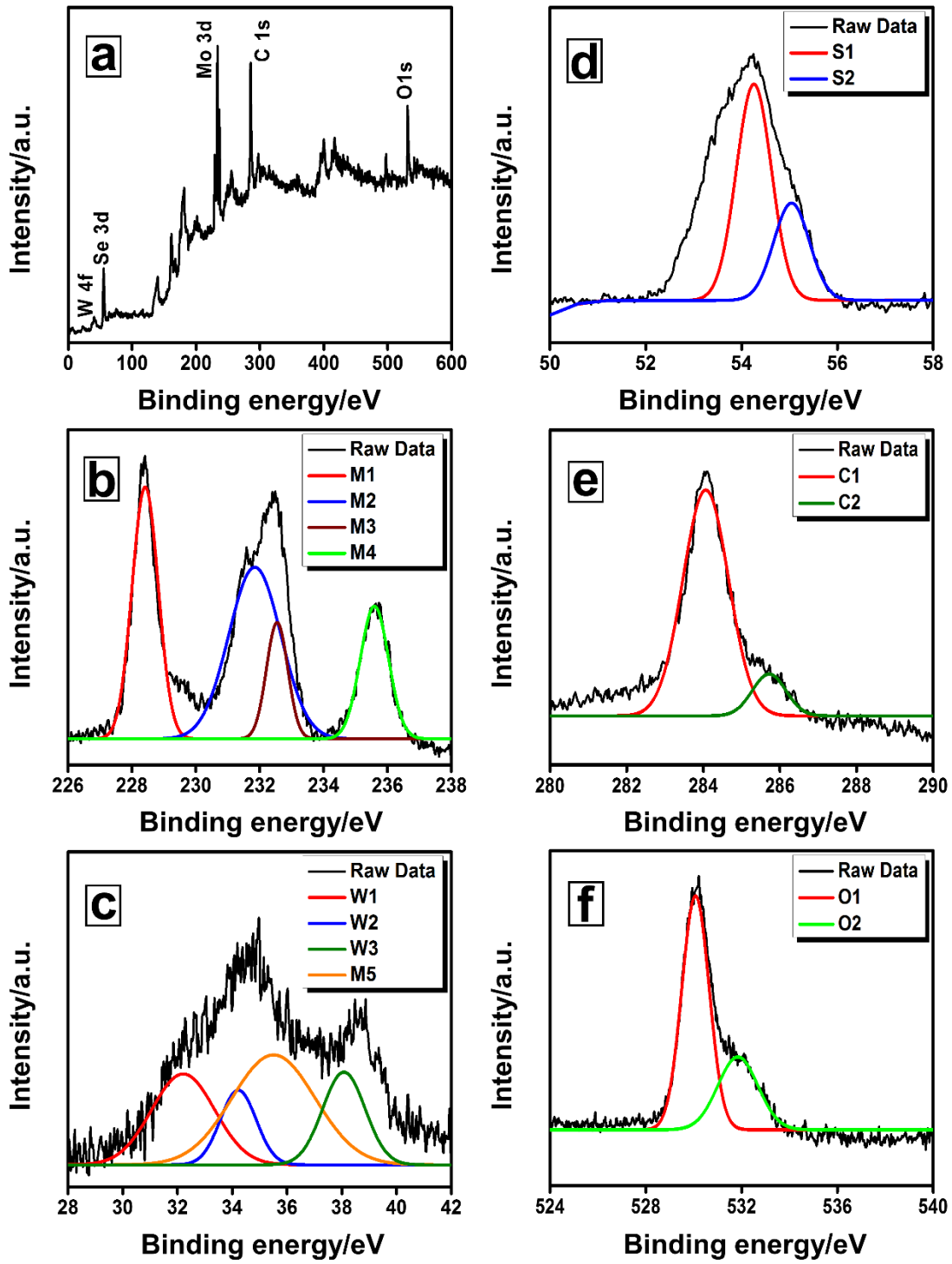

Figure 5.7 (a) XPS survey spectra and High resolution core level deconvoluted spectra's of (b) Mo 3d, (c) W 4f, (d) Se 3d, (e) C 1s and (f) O 1s components in W2-$MoSe_2$/G nanostructures.

Likewise, the W 4f level (Figure 5.7c) could be resolved into W 4f7/2 and W 4f5/2 at the binding energies of 32.1 eV and 34.2 eV (W1 and W2) respectively, corresponding to +4 oxidation state of W(Huang et al. 2015). On the other hand the peaks at higher binding energies 35.5 eV (M5) and 38 eV (W3) can be assigned to the Mo-W bond and surface tungsten oxides, respectively. Further, the 3d spectra of Se (Figure 5.7d) are resolved into two components S1 and S2, owing to the spin-orbit coupling and can be assigned to the 3d5/2 and 3d 3/2 states at 54.2 eV and 55 eV respectively (Wang et al. 2013). Next, Figure 5.7e shows the resolved C 1s spectra consisting of bands C1 and C2. The C1 band at ~284.1 eV corresponds to C-C (non-oxygenated) bond and small hump at ~ 286 eV can be assigned to the C-O (hydroxyl group) of graphene (Zhao et al. 2010) in the W2-$MoSe_2$/G composite. The resolved O 1s spectra (Figure 5.7f) indicate two bonding states (O 2f and O 3f) on the surface (Zhou et al. 2013). These results once again confirms the successful doping of W in $MoSe_2$ and in-situ reduction of GO during the hydrothermal synthesis, which are commensurate with Raman analysis.

The morphology and elemental analysis of $MoSe_2$, W2-$MoSe_2$ and W2-$MoSe_2$/G nanostructures are demonstrated using FESEM and EDS measurements as represented in Figure 5.8a-b-c and Figure 5.8d-e-f, respectively. FESEM images of all the nanostructures indicate plenty of two dimensional sheet like structures of sizes 7 ~ 10 nm, gathered to form a bunch of nanoflowers with an average diameter of ~ 200 nm. In addition, the FESEM analysis of W2-$MoSe_2$/G nanostructures describes the successful growth of W2-$MoSe_2$ nanoflowers on top of graphene sheets and the possible structures of W2-$MoSe_2$ and graphene are marked in the FESEM image (Figure 5.8c).
Further, EDS analysis of $MoSe_2$ nanostructures (Figure 5.8d) performed on the area shown in Figure 5.8a confirm their purity. On the other hand, the EDS spectra of W2-$MoSe_2$ and W2-$MoSe_2$/G nanostructures (Figure 5.8e-f) reveal the peaks corresponding to tungsten along with molybdenum, selenium and carbon. It is worth noting that, W2-$MoSe_2$/G nanostructures indicate the peaks corresponding to carbon in considerable intensities, which could be ascribed to the presence of carbon from graphene. Whereas, the presence of carbon in trace quantities in the EDS spectra of $MoSe_2$ and W2-$MoSe_2$ nanostructures could be attributed to the use of carbon tape in FESEM measurements.

The obtained weight percentages of elements from the EDS measurements are provided as insets in their respective EDS plots and the elemental color maps of W2-$MoSe_2$/G is provided in (see APPENDIX XIII), indicating the uniform distribution of elements. In addition, by comparing the weight percentages obtained through EDS, the ratio of G in W2-$MoSe_2$/G is found to be about 1:1.85.

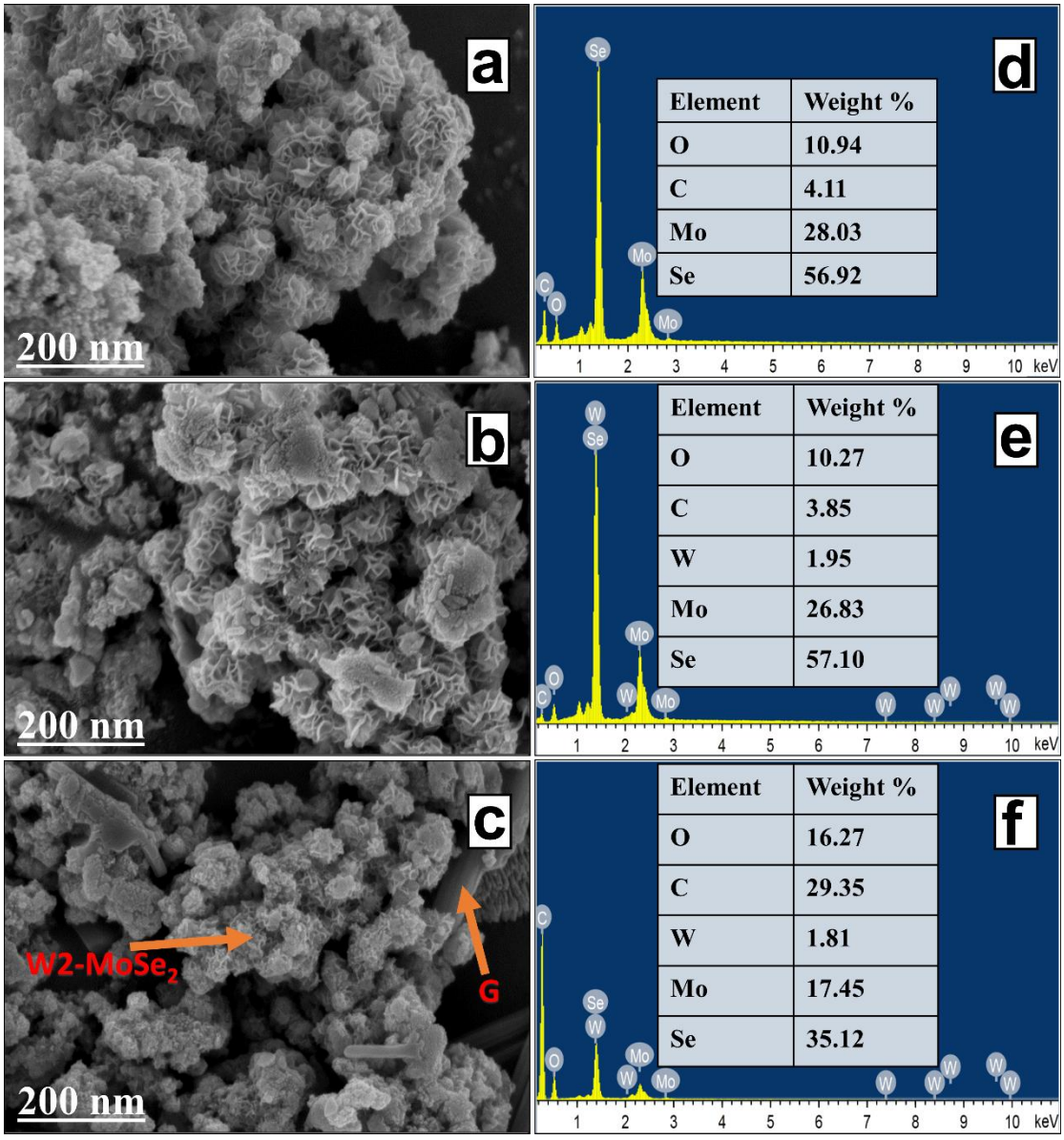

Figure 5.8 FESEM images of (a) pristine $MoSe_2$ (b), W2-$MoSe_2$ and (c) W2-$MoSe_2$ /G nanostructures, (d), (e) and (f) represent the EDS spectra's of pristine $MoSe_2$, W2-$MoSe_2$ and W2-$MoSe_2$/G nanostructures obtained from the area shown in (a), (b) and (c) respectively.

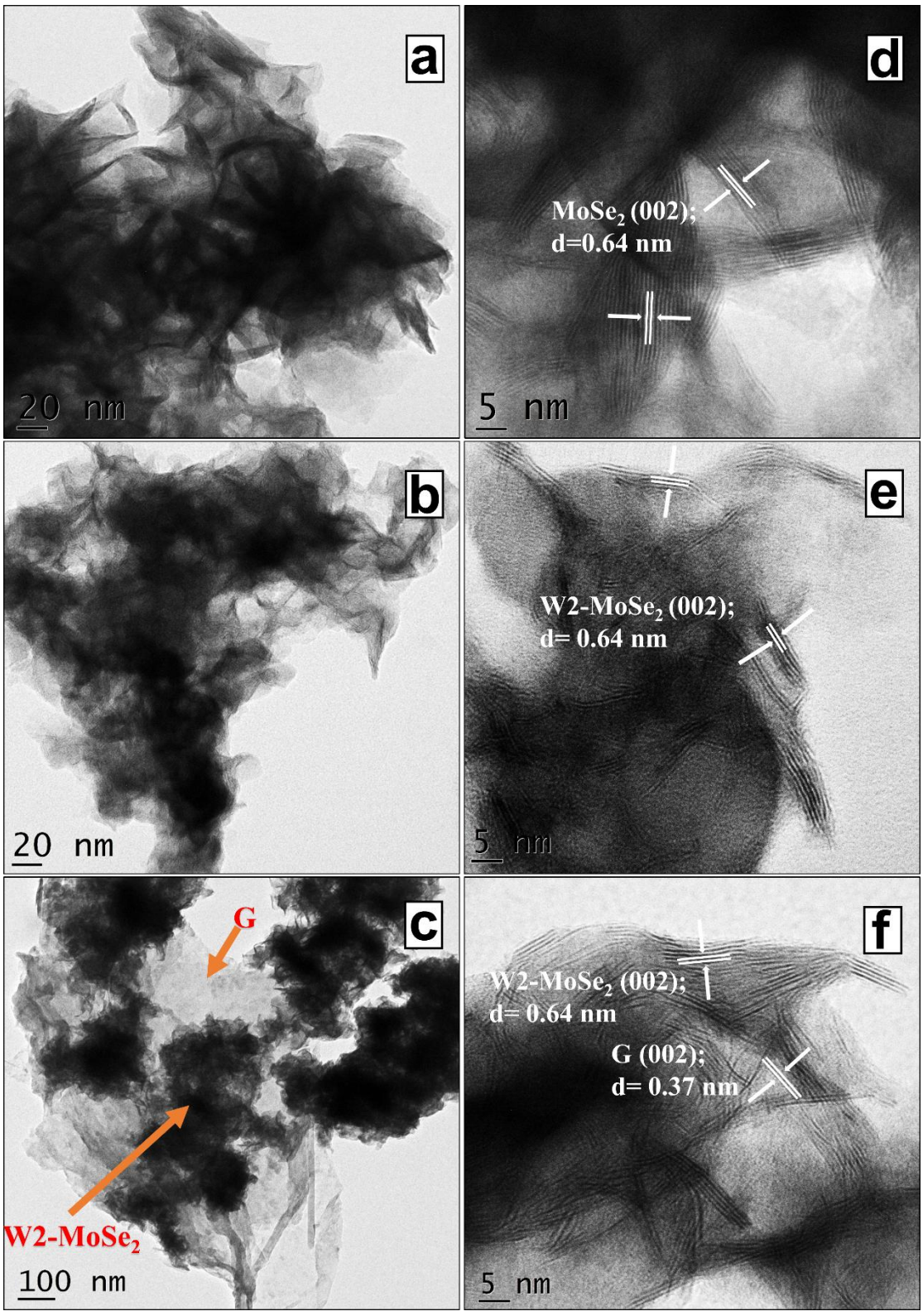

Figure 5.9 TEM and HRTEM images of (a, d) pristine $MoSe_2$, (b, e) W2-$MoSe_2$ and (c, f) W2-$MoSe_2$/G nanostructures.

TEM measurements as shown in Figure 5.9a-b-c confirms the sheets-like geometry of the synthesized $MoSe_2$, W2-$MoSe_2$ and W2-$MoSe_2$/G nanostructures and also indicate no much change in the morphology with W-doping. On the other hand, TEM image of W2-$MoSe_2$/G nanostructures confirms the successful growth of W2-$MoSe_2$ nanostructures over graphene matrix as displayed in Figure 5.9c. Further, HRTEM measurements on $MoSe_2$ and W2-$MoSe_2$ nanostructures (Figure 5.9d-e) reveal the lattice spacing value of ~0.64 nm, corresponding to the (002) basal plane of $MoSe_2$ nanostructures, commensurate with the results obtained from XRD measurements. In addition, HRTEM of W2-$MoSe_2$/G nanostructures (Figure 5.9f) also sheds light on the growth of W2-$MoSe_2$ nanostructures over graphene matrix and the obtained lattice spacing values are ~0.64 nm and ~0.37 nm, corresponding to the (002) planes of W2-$MoSe_2$ and graphene (Chen et al. 2013). The obtained results are in good agreement with XRD results and also confirms the in-situ reduction of GO to graphene during the hydrothermal process, as confirmed from XPS measurements.

The brighter SAED rings of W2-$MoSe_2$ nanostructures in contrast to those of $MoSe_2$ nanostructures (see APPENDIX XIV), indicate their improved poly-crystallinity as confirmed from XRD measurements. On the other hand, the combination of spots and ring type SAED pattern of W2-$MoSe_2$/G nanostructures (see APPENDIX XIV) confirms their polycrystalline nature, which are in agreement with the results obtained from XRD.

5.3.5 Electrochemical performance of $MoSe_2$ and W-doped $MoSe_2$ nanostructures

The electrochemical performance of pristine and W-doped $MoSe_2$ electrodes are evaluated through CV, GCD and EIS measurements. All electrochemical measurements are performed using 0.5 M H_2SO_4 as electrolyte in three-electrode configurations, consisting of working electrode, reference electrode - saturated calomel electrode and counter electrode- Pt wire. The detailed description of electrode preparations for electrochemical measurements are provided in section 2.3.5. The Figure 5.10a represents the recorded CV curves of pristine $MoSe_2$ electrodes in an voltage window range of -0.2 V to 0.5 V Vs. SCE at various scan rates (2, 5, 10, 20, 50

and 100 mV s^{-1}). The CV curves indicate the deviation from ideal rectangular response of a double-layer capacitor along with a pair of multiple redox peaks with excellent reversibility, indicating the combination of surface/non-Faradaic and redox/Faradaic reactions (Gogotsi and Penner 2018). For instance, pristine $MoSe_2$ electrodes deliver the gravimetric specific capacitance of 106 F g^{-1} at a scan rate of 2 mV s^{-1}. Next, doping is imperative to enhance the specific capacitances, which could alter the electronic conductivities and various physiochemical parameters such as nanostructure morphology, specific surface area and pore size. The large specific surface area facilitates the higher rate of adsorption of electrolyte ions and pore size accelerates diffusion of the ions for rapid charge transport. As such, CV curves of W-doped $MoSe_2$ electrodes indicate an improved current densities, suggesting enhanced electrochemical behavior of these materials as shown in Figure 5.10b-c-d respectively.

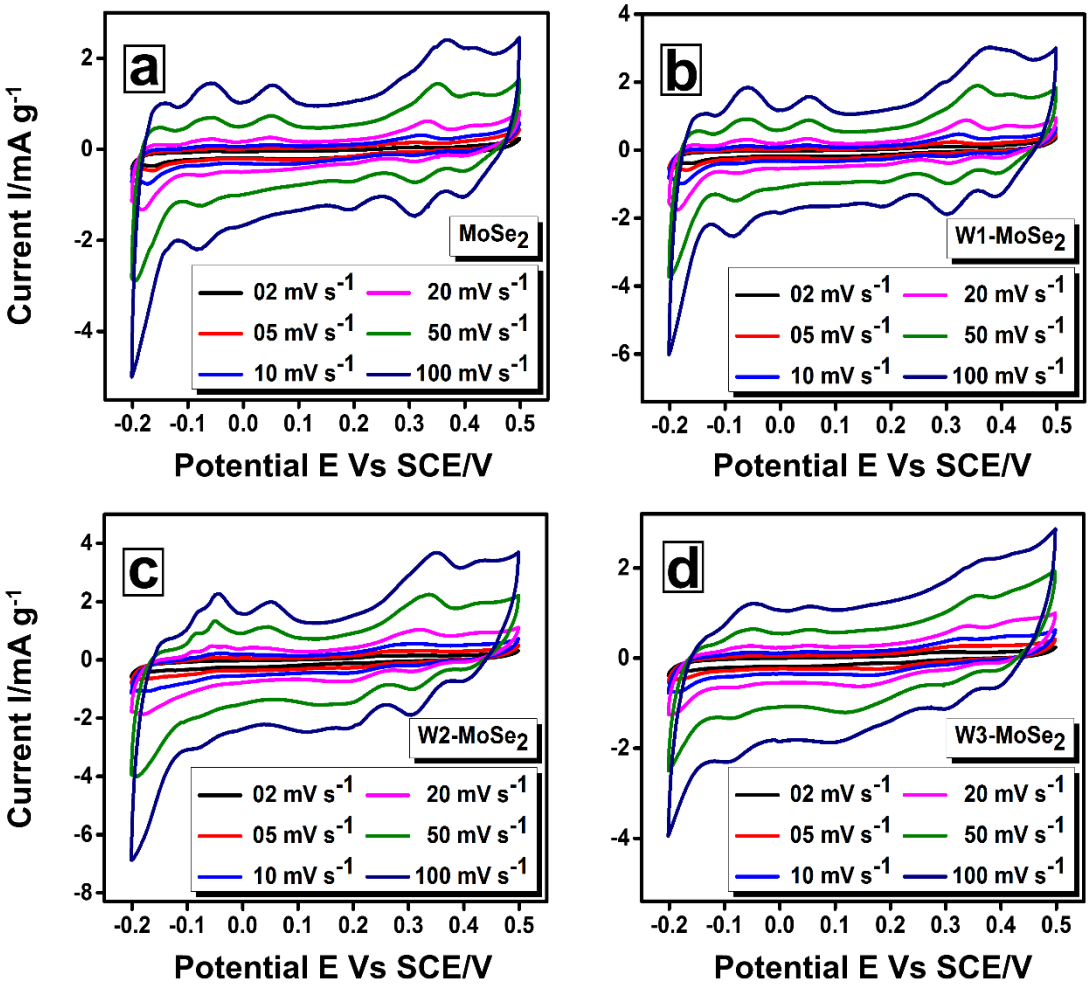

Figure 5.10 Cyclic voltammograms of (a) pristine $MoSe_2$, (b) W1-$MoSe_2$, (c) W2-$MoSe_2$ and (d) W3-$MoSe_2$ electrodes at different scan rates.

The possible Faradaic and non-Faradaic processes at the electrodes could be as represented by the reactions given below:

$$W - MoSe_2 + H^+ + e^- \rightarrow W - MoSe_2 - H^+ \quad (Surface\ process) \quad (5.2)$$

$$W - MoSe_2 + H^+ + e^- \rightarrow W - MoSe + SeH^+ \quad (redox\ process) \quad (5.3)$$

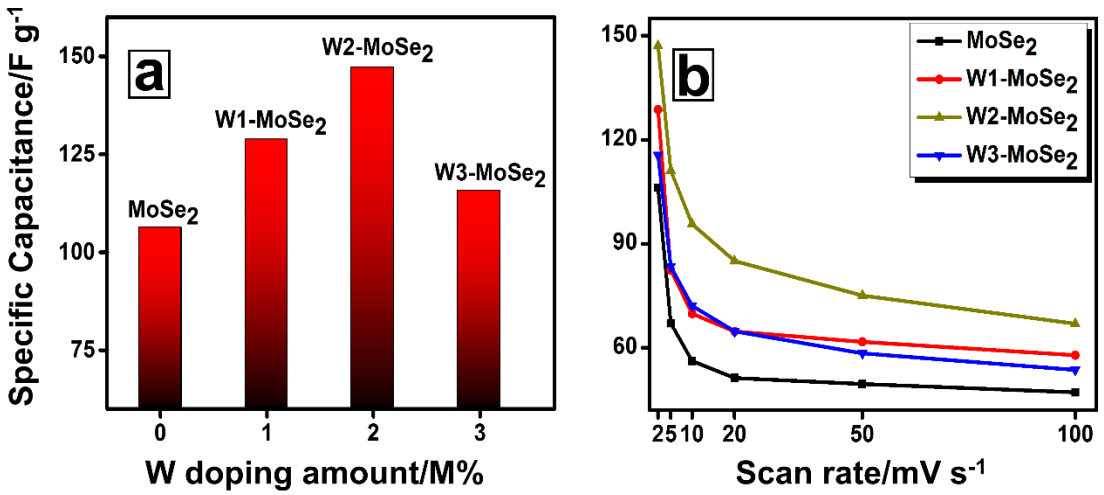

Figure 5.11 (a) Bar chart representing the effect of W-doping on specific capacitance of $MoSe_2$ nanostructures and (b) Variation of specific capacitances of $MoSe_2$, W1-$MoSe_2$, W2-$MoSe_2$ and W3-$MoSe_2$ electrodes with respect to scan rates.

The doping with 1 M % tungsten (W1-$MoSe_2$) increased the specific capacitance to 128 F g^{-1} (~21% increment) and for 2 M % tungsten (W2-$MoSe_2$), the specific capacitance further increased to 147 F g^{-1} (~39 % increment). Whereas, the increase in doping amount to 3 M % tungsten (W3-$MoSe_2$) portrayed only a marginal increase in the specific capacitances (115.53 F g^{-1}) from pristine $MoSe_2$ electrodes and a decrement in specific capacitance by ~ 22 % with respect to W2-$MoSe_2$ electrodes. The decrement in the specific capacitances with higher doping amount (3 M%, W3-$MoSe_2$) may be attributed to the phase separation as confirmed from XRD measurements (Figure 5.6b). Further, the bar chart as shown in Figure 5.11a represents the effect of W-doping amounts on specific capacitances and hence suggests 2 M % as an optimum W-doping amount for $MoSe_2$ nanostructures.

The enhancement in specific capacitances could be attributed to various physiochemical aspects such as enhanced electronic conductivity and specific surface

area. The large specific surface area of W2-$MoSe_2$ nanostructures (S_{BET}=17.695 m^2/g) in comparison to pristine $MoSe_2$ nanostructures (S_{BET}=5.931 m^2/g) revealed from N_2 adsorption-desorption isotherms (see APPENDIX XV) evidence their superior electrochemical performance. On the other hand, BJH measurements (see APPENDIX XV) indicate no substantial change in the pore sizes with the average diameter of ~3.563 nm and ~3.115 nm for $MoSe_2$ and W2-$MoSe_2$ nanostructures, respectively. Thus, these results indicate surface processes are dominant in enhancing the specific capacitances of these materials. Further with an increase in scan rates, gradual decrease in the specific capacitances could be attributed to the mass-transport limitation of H^+ ions at the electrode-electrolyte interface. Figure 5.11b represents the variation of specific capacitances with respect to scan rates and the values of specific capacitances of $MoSe_2$, W1-$MoSe_2$, W2-$MoSe_2$ and W3-$MoSe_2$ electrodes calculated using equation 2.5 at different scan rates are provided in Table 5.6.

Table 5.6. Comparison of specific capacitances (F g^{-1}) of $MoSe_2$, W1-$MoSe_2$, W2-$MoSe_2$ and W3-$MoSe_2$ electrodes with respect to scan rates (mV s^{-1}).

Scan rate/mV s^{-1}	Specific capacitances/F g^{-1}			
	$MoSe_2$	**W1-$MoSe_2$**	**W2-$MoSe_2$**	**W3-$MoSe_2$**
2	106.13	128.70	147.08	115.53
5	67.11	82.40	111.12	83.43
10	56.20	69.84	95.67	72.13
20	51.28	64.69	85.03	64.72
50	49.53	61.69	75.07	58.39
100	47.14	57.85	66.95	53.60

The electrochemical behavior of the electrodes are also studied with the help of GCD measurements. Figure 5.12a-b-c-d represents the GCD measurements of pristine $MoSe_2$, W1-$MoSe_2$, W2-$MoSe_2$ and W3-$MoSe_2$ electrodes performed in the voltage window range of -0.2 to 0.5 V Vs. SCE at different applied current densities (0.4, 0.6, 0.8 and 1 A g^{-1}). The GCD curves of all the pristine and W-doped $MoSe_2$ electrodes indicate the deviation from an ideal charge-discharge profile of a capacitor, suggesting the combination of Faradaic and non-Faradaic processes as confirmed from CV

measurements. Also, the charging and discharging times of all the electrodes are almost equal, representing 100% coulomb efficiencies. Further, the charge-discharge times are in the order of $MoSe_2$<W3-$MoSe_2$<W1-$MoSe_2$<W2-$MoSe_2$, confirming the higher values of specific capacitances of W2-$MoSe_2$ electrodes as obtained from CV measurements**.** In addition, the observed trend in the specific capacitances Vs. W-doping amounts are similar to those obtained from CV measurements. To get better insight on the electrochemical performance, CV and GCD curves of all the pristine and W-doped $MoSe_2$ electrodes are compared at a fixed scan rate of 20 mV s^{-1} and 0.4 A g^{-1} constant current density as shown in Figure 5.13a-b**,** respectively.

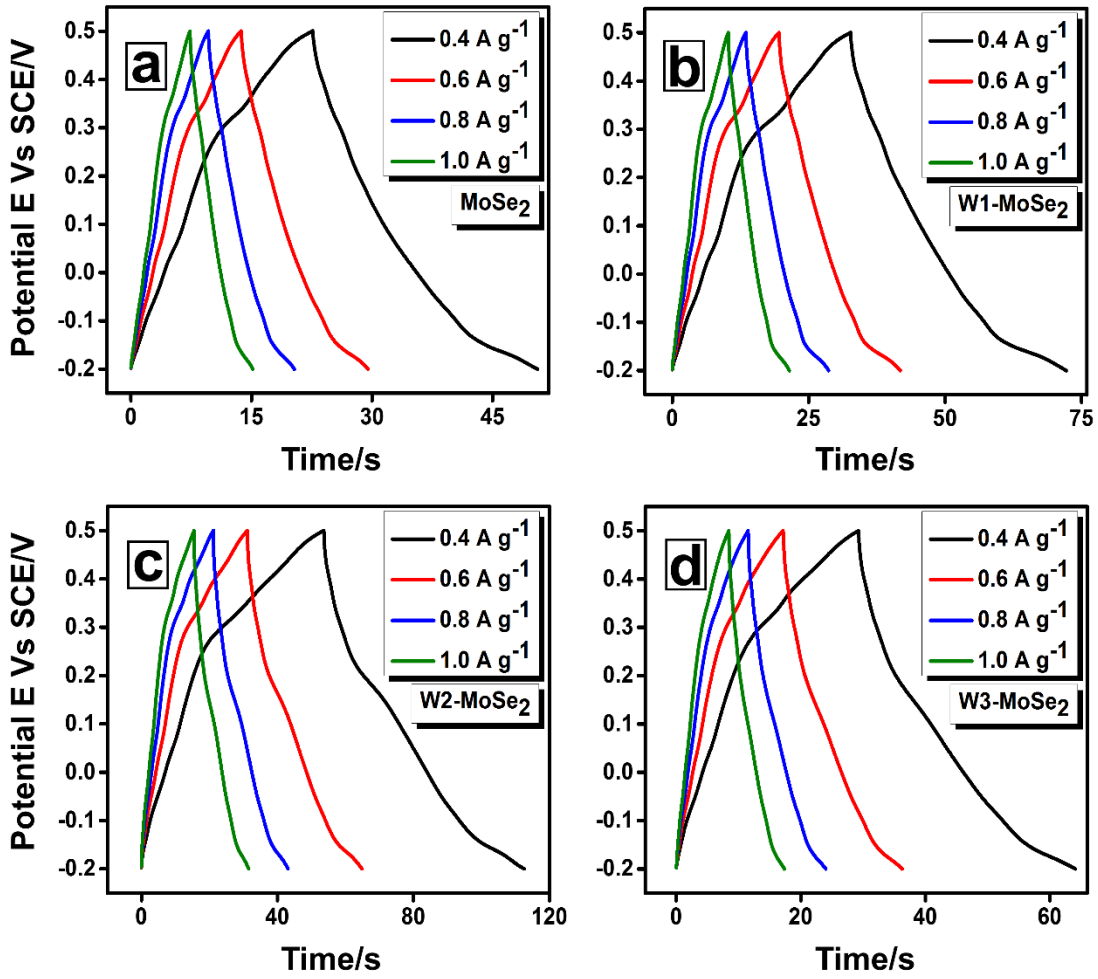

Figure 5.12 Galvanostatic charge-discharge curves of (a) pristine $MoSe_2$, (b) W1-$MoSe_2$, (c) W2-$MoSe_2$ and (d) W3-$MoSe_2$ electrodes at different applied current densities.

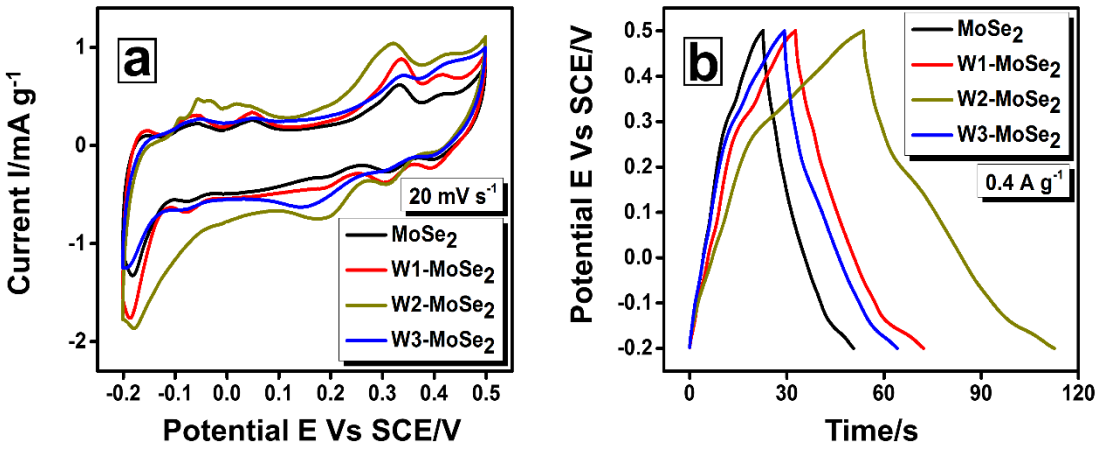

Figure 5.13 (a) Comparison of cyclic voltammograms at 20 mV s^{-1} scan rate and (b) charge-discharge curves at 0.4 A g^{-1} current density of $MoSe_2$, W1-$MoSe_2$, W2-$MoSe_2$ and W3-$MoSe_2$ electrodes.

The interface behavior of the electrodes are characterized using EIS measurements in the frequency range of 0.2 Hz to 100 kHz with the AC amplitude of V_{AC}=10 mV. The Nyquist plots as the function of frequency for pristine and W-doped $MoSe_2$ electrodes are presented in Figure 5.14a. Also for a clear understanding, the magnified portions of the Nyquist plots are pictured as Figure 5.14b, while Figure 5.14c represents the Bode Phase angle plot. Further Figure 5.14d represents EEC, indicating a pair of charge-transfer resistances (R_{CT1} and R_{CT2}) and capacitances (Q_1 and Q_2), followed by solution resistance (R_S). The simulated EEC could be represented as $R_S(R_{CT1}Q_1)(R_{CT2}Q_2)$ and the EEC fitting parameters are tabulated in Table 5.7.

As a function of W-doping, the first $Q_{CPE1}R_{CT1}$ component is relatively W-doping independent and associated with porosity of the electrodes (Candy et al. 1981). Whereas, the second $Q_{CPE2}R_{CT2}$ component varies largely as a function of W-doping, indicating the variation of total resistances (Day et al. 2015). As evident from the Nyquist plots (Inset of Figure 5.14a) and EEC fitting parameters (Table 5.7), W2-$MoSe_2$ electrodes displays the lowest solution resistance (R_S) of 0.557 Ω, indicating better electrode-electrolyte contact. Further, the higher R_{CT1} values of W2-$MoSe_2$ may be due to the formation of defects through doping (Gong et al. 2015) or due to the marginal decrease in pore size as confirmed from BJH measurements (see APPENDIX

XV). It is worth noting that, W2-$MoSe_2$ electrodes displays four-fold decrease in charge transfer resistance (R_{CT2}) in comparison with pristine $MoSe_2$ electrodes. In addition, the effective values of capacitances (Q_1 and Q_2) are higher for W2-$MoSe_2$ electrodes further validates their superior electrochemical performance. Bode phase angle is the important parameter for the fabrication of low-leakage supercapacitors. Figure 5.14c represents the Bode phase angle plots of pristine and W-doped $MoSe_2$ electrodes. Pristine $MoSe_2$ and W1-$MoSe_2$ electrodes shown the phase angle of -79º, whereas W2-$MoSe_2$ and W3-$MoSe_2$ electrodes specifies the phase angle of -77º and -73.65º, respectively.

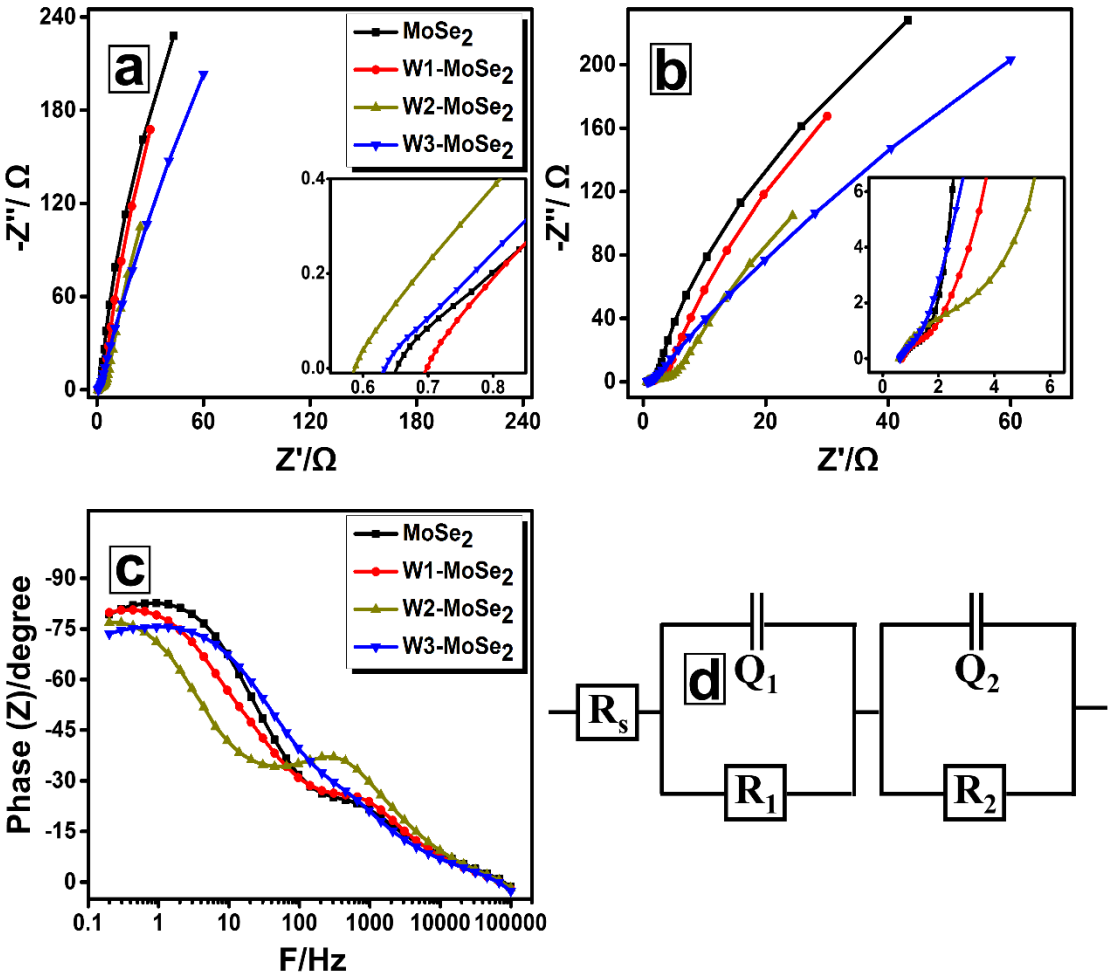

Figure 5.14 (a) Nyquist plots of $MoSe_2$, W1-$MoSe_2$, W2-$MoSe_2$ and W3-$MoSe_2$ electrodes, (b) magnified Nyquist plots clearly representing the variation in charge-transfer resistances (R_{CT1} and R_{CT2}) with doping, (c) Bode phase angle plots derived from the Nyquist plots and (d) Simulated EEC for the Nyquist plots.

Table 5.7. EEC parameters derived by fitting the Nyquist plots of $MoSe_2$, W1-$MoSe_2$, W2-$MoSe_2$ and W3-$MoSe_2$ electrodes.

	R_s (Ω)	Q_1 (mF)	R_{CT1} (Ω)	Q_2 (mF)	R_{CT2} (Ω)
$MoSe_2$	0.642	6.27	1.44	3.38	2314
W1-$MoSe_2$	0.682	5.47	2.16	4.60	855.1
W2-$MoSe_2$	0.557	6.20	6.34	6.74	519.8
W3-$MoSe_2$	0.629	9.01	1.02	3.76	2581

Long cycle life is one of the important parameter of supercapacitor performance evaluation. Pristine and W-doped $MoSe_2$ electrodes were subjected to stability test for 10000 GCD cycles at an higher current density of 5 A g^{-1} as represented in Figure 5.15. Results indicate the sharp decrease in the specific capacitances of all the pristine and W-doped $MoSe_2$ electrodes up to 1000 cycles, which could be attributed to the saturation of active sites on surface of the electrodes during repeated charge–discharge process (Cao et al. 2013), after which the loss was comparatively minimal. Pristine $MoSe_2$ electrodes retained ~68 % of the initial specific capacitance, while the W-doped counterparts viz., W1-$MoSe_2$, W2-$MoSe_2$ and W3-$MoSe_2$ electrodes could retain ~66 %, ~58 % and ~74 % of the initial specific capacitances over 10000 cycles, indicating their promising stabilities.

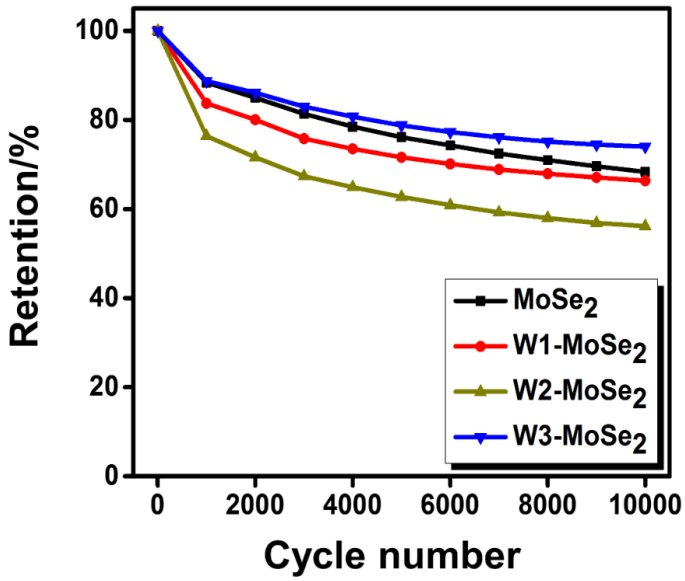

Figure 5.15 Cycle life of pristine $MoSe_2$, W1-$MoSe_2$, W2-$MoSe_2$ and W3-$MoSe_2$ electrodes for 10000 GCD cycles.

In brief, W-doping enhanced the specific capacitance of $MoSe_2$ electrodes with 2 M % of tungsten as an optimum doping amount. On the other hand, the cyclic stability was reduced by ~10 % for W2-$MoSe_2$ electrodes in comparison with pristine $MoSe_2$ electrodes. It is also interesting to note that W3-$MoSe_2$ electrodes displayed enhanced capacitance retention of 74 % for 10000 cycles, which may be attributed to their better reversibility and the lower charge-transfer resistance (R_{CT1}) (Wang et al. 2017) as obtained from EIS measurements. In order to justify the effect of W-doping on $MoSe_2$, composite was synthesized with graphene and the results are discussed in the subsequent section.

5.3.6 Electrochemical performance of W-$MoSe_2$/G hybrid electrodes

Since W2-$MoSe_2$ electrodes delivered the higher specific capacitances as compared with pristine $MoSe_2$ and other W-doped counterparts, a hybrid with graphene for W2-$MoSe_2$ nanostructures were synthesized to further enhance the electrochemical performance. The synthesis of W2-$MoSe_2$/G hybrids are discussed in section 5.2.5.

As seen from Figure 5.16a, the CV curves of W2-$MoSe_2$/G electrodes indicate the prominent adsorption-desorption and enhanced redox peaks, signifying their higher specific capacitances as compared with pristine $MoSe_2$ and W2-$MoSe_2$ electrodes. For an analogy, Figure 5.16b represents the CV curves of pristine $MoSe_2$, W2-$MoSe_2$ and W2-$MoSe_2$/G electrodes at a scan rate of 20 mV s^{-1}. Using equation 2.5, the calculated values of specific capacitance at 2 mV s^{-1} scan rate is 248 F g^{-1}, which is about ~2.4 and ~1.4 times higher in comparison to pristine $MoSe_2$ and W2-$MoSe_2$ electrodes, respectively. Further, Figure 5.17 represent the effect of scan rates on W2-$MoSe_2$ electrodes. Even at higher scan rates such as 50 and 100 mV s^{-1}, the electrodes could retain specific capacitances of 103.6 F g^{-1} and 97 F g^{-1} respectively, indicating their promising rate-capability. The large increment in the specific capacitances can be attributed to their various physical and structural features such as: (i) formation of hybrid nanostructures on highly conductive graphene framework, (ii) effective contribution for charge storage via Faradaic and non-Faradaic interactions and (iii) physiochemical aspects such as enhanced electronic conductivity for fast charge transport, specific surface area and pore size for higher rate of electrolyte adsorption and intercalation of ions.

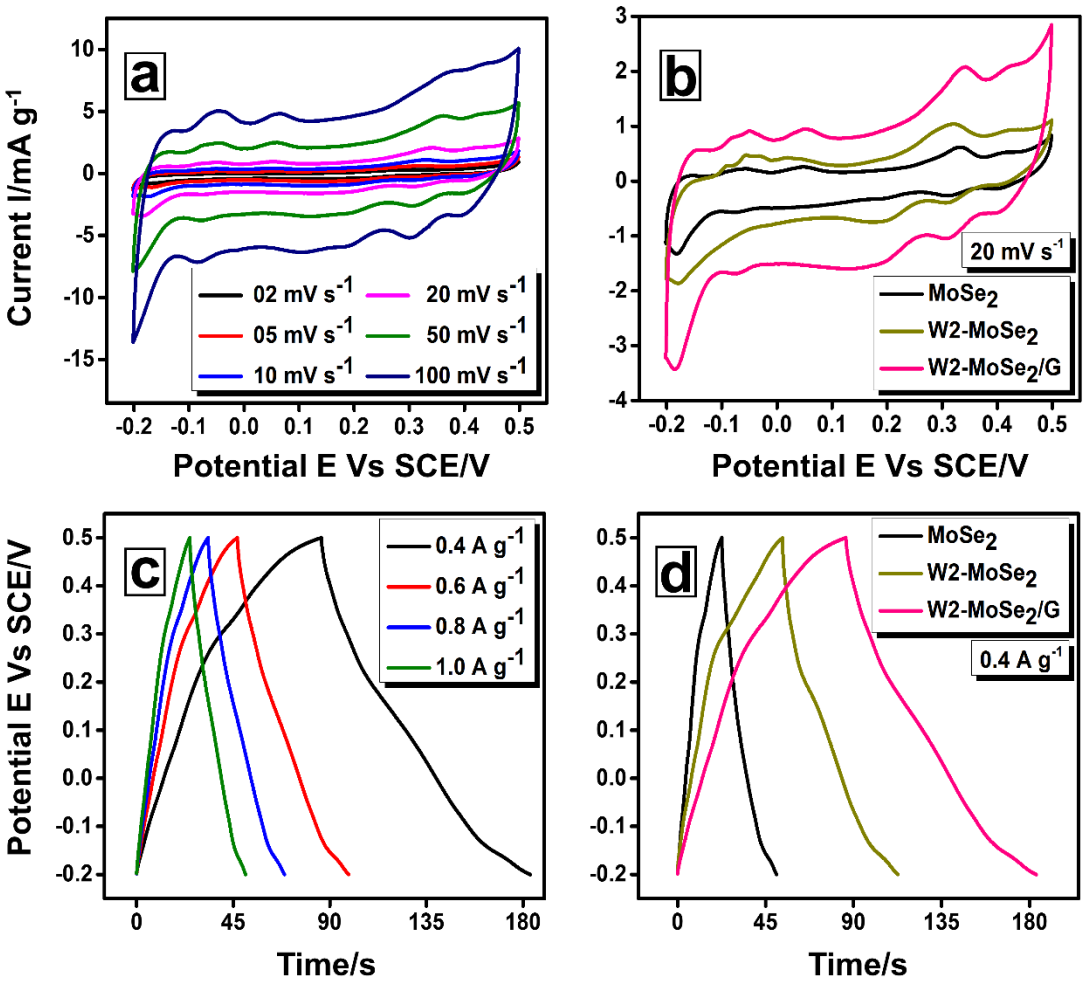

Figure 5.16 (a) Cyclic voltammograms of W2-$MoSe_2$/G electrodes, (b) comparison of cyclic voltammograms of W2-$MoSe_2$/G electrodes with pristine $MoSe_2$ and W2-$MoSe_2$ electrodes, (c) Galvanostatic charge-discharge curves of W2-$MoSe_2$/G electrodes and (d) comparison of charge-discharge curves of W2-$MoSe_2$/G electrodes with pristine $MoSe_2$ and W2-$MoSe_2$ electrodes at 0.4 A g^{-1} current density.

Additionally, the non-linear GCD curves as portrayed in Figure 5.16c confirm the hybrid charge-storage mechanism of W2-$MoSe_2$/G electrodes. As seen from Figure 5.16d, the higher charge-discharge time at a constant current density of 0.4 A g^{-1} for W2-$MoSe_2$/G electrodes in comparison to pristine $MoSe_2$ and W2-$MoSe_2$ electrodes are consistent with the larger values of specific capacitances obtained through CV and GCD measurements. The estimated values of specific capacitances using equation 2.6 of W2-$MoSe_2$/G electrodes from the GCD curves, in comparison with pristine $MoSe_2$ and other W-doped counterparts are provided in Table 5.8. The higher specific surface

area S_{BET} = 215.960 m^2/g and pore diameter (~5.517 nm) revealed through N_2 adsorption-desorption isotherms and BJH measurements (see APPENDIX XV) evidence the superior electrochemical performances of W2-$MoSe_2$/G electrodes.

Table 5.8. Comparison of specific capacitances (F g^{-1}) of $MoSe_2$, W1-$MoSe_2$, W2-$MoSe_2$, W3-$MoSe_2$ W2-$MoSe_2$/G electrodes at different applied current densities.

Current density A g^{-1}	**Specific capacitances/F g^{-1}**				
	$MoSe_2$	**W1-$MoSe_2$**	**W2-$MoSe_2$**	**W3-$MoSe_2$**	**W2-$MoSe_2$/G**
0.4	14.93	22.63	31.10	20.93	52.39
0.6	12.52	19.10	26.57	17.35	42.31
0.8	11.60	17.33	23.35	14.98	38.76
1.0	10.54	15.99	21.36	13.41	36.23

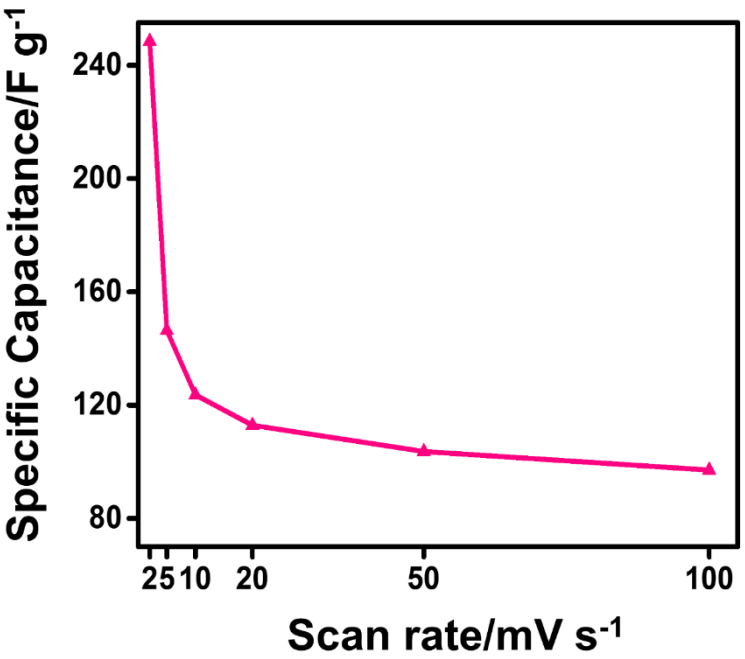

Figure 5.17 Variation of specific capacitances of W2-$MoSe_2$/G hybrid electrodes with respect to scan rates.

The interface behavior of W2-$MoSe_2$/G electrodes are characterized using EIS measurements as described earlier. Nyquist plot as seen in Figure 5.18a indicate nearly vertical straight line with a Bode phase angle of -79° (Figure 5.18b), confirming the

hybrid charge-storage mechanism of W2-$MoSe_2$/G electrodes. The simulated EEC (as pictured in Figure 5.14d) indicate a very small solution resistance R_S = 0.419 Ω, charge-transfer resistances of R_{CT1} = 1.41 Ω and R_{CT2} = 665.9 Ω and effective capacitances of Q_1 = 10.1 mF and Q_2 = 38.6 mF. All these values further indorse the higher values of specific capacitances of W2-$MoSe_2$/G electrodes as validated through CV and GCD measurements.

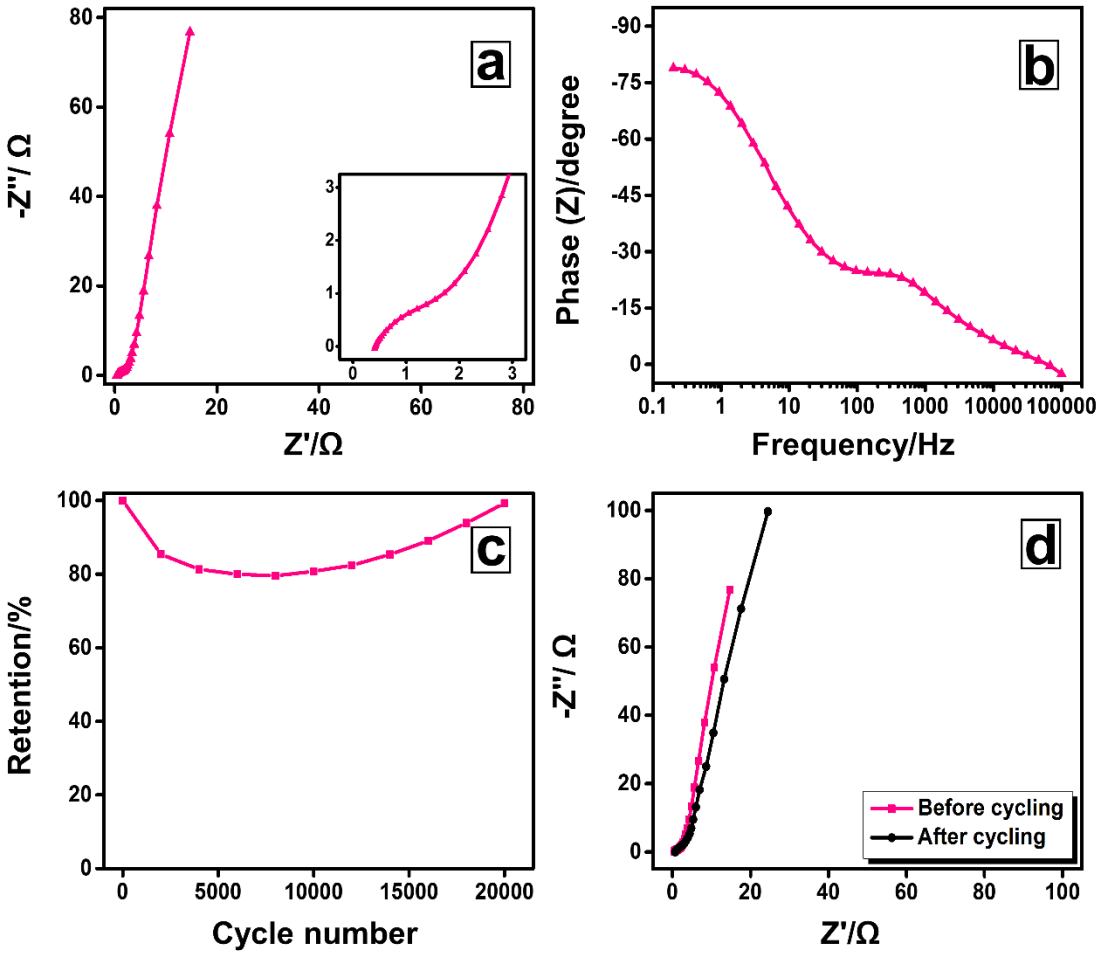

Figure 5.18 (a) Nyquist plot of W2-$MoSe_2$/G electrodes and the corresponding Bode phase angle plot (b), (c) cycle life of W2-$MoSe_2$/G electrodes for 20000 cycles and (d) comparison of Nyquist plots of W2-$MoSe_2$/G electrodes before and after cycling.

Further, Figure 5.18c the represents cyclic stability plot of W2-$MoSe_2$/G electrodes recorded at a constant current density of 5 A g^{-1} for 20000 cycles. We observed the steady decrease in specific capacitances up to ~8000 cycles, which can be attributed to

the dissociation of few nanosheets under repeated cycling process (Balasingam et al. 2016). Interestingly, after 10000 cycles the electrodes could regain its specific capacitances and finally achieving the capacitance retention of 102 % at 20000 cycles. This could be attributed to the following factors such as setting up of nanostructures, re-exfoliation of graphene sheets via continuous intercalation/de-intercalation and also the further reduction of some unreduced GO to form graphene. This similar trend in enhancement of specific capacitances under cycling process are also observed in other graphene based composites as reported by others (Bissett et al. 2015). Furthermore, the Nyquist plot recorded after 20000 cycles as shown in Figure 5.18d indicate no much deviation from the initial Nyquist plot, demonstrating very less degradation of the W2-$MoSe_2$/G electrodes under cycling process. The comparison of performances of $MoSe_2$, W2-$MoSe_2$, and W2-$MoSe_2$/G electrodes over other $MoSe_2$ based materials as reported in literature are provided in (see APPENDIX XVI).

5.3.7 Charge storage mechanism of electrodes

The electrochemical charge storage mechanism of pristine $MoSe_2$ and W-doped $MoSe_2$ electrodes are validated via Dunn's method (Wang et al. 2007). The current response (*i*) at a fixed potential (V) can be described as the combination of two separate mechanisms, namely capacitive ($k_1 v$) and diffusive contribution ($k_2 v^{\frac{1}{2}}$) where 'v' is the scan rate and 'k_1' and 'k_2' are constants. Assuming that the current (*i*) obeys a power-law relationship $i = av^b$; where '*a'* and '*b'* are adjustable parameters, with *b*-values determined from the slope of the linear plot of log *i* vs log *v* (Figure 5.19a). The slope *b*=1 is indicative of ideal capacitive response, while *b*=0.5 is representative of a battery-type/diffusion controlled behavior (Kirubasankar et al. 2019). The obtained *b*-values at V = 0.3 V are 0.69, 0.73, 0.77, 0.64 and 0.74 for pristine $MoSe_2$, W1-$MoSe_2$, W2-$MoSe_2$, W3-$MoSe_2$ and W2-$MoSe_2$/G electrodes, respectively. These values suggest the charge-storage mechanism is of hybrid type (Both capacitive and diffusive response). In addition, the higher *b*-value of W2-$MoSe_2$ and W2-$MoSe_2$/G electrodes confirms the large amount of capacitive contribution than the diffusion controlled process.

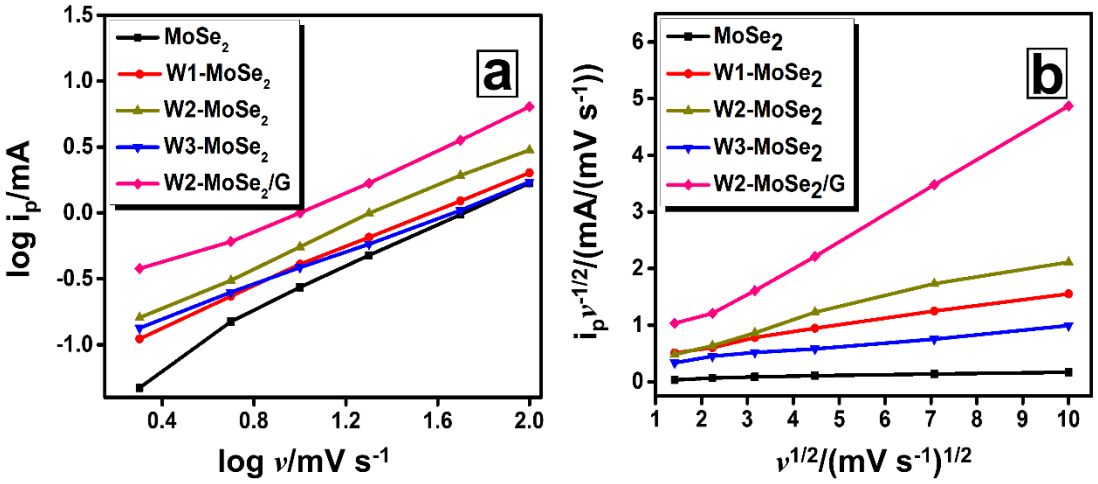

Figure 5.19 (a) Plots of log *v* (scan rate) vs log i_p (peak current at 0.3 V) for the estimation of *b*-values of all the electrodes and (b) plots of $v^{\frac{1}{2}}$ Vs $i(V)v^{\frac{-1}{2}}$ to calculate constants k_1 and k_2 and to determine the capacitive and redox contributions.

Further, the percentage of capacitive and diffusive contributions to the total stored charge are evaluated using the equation $i(V)v^{\frac{-1}{2}} = k_1 v + k_2 v^{\frac{1}{2}}$. Where $k_1 v$ and $k_2 v^{\frac{1}{2}}$ correspond to the current contribution from capacitive controlled process and diffusion/redox processes (Ajay et al. 2015), respectively. Thus, by determining 'k_1' and 'k_2' from the plots of $v^{\frac{1}{2}}$ Vs $i(V)v^{\frac{-1}{2}}$ (Figure. 5.20b) the percentage contributions from these mechanisms are evaluated.

At a slow scan-rate of 2 mV s^{-1}, the capacitive contributions of pristine $MoSe_2$, W1-$MoSe_2$, W2-$MoSe_2$, W3-$MoSe_2$ and W2-$MoSe_2$/G electrodes are 41%, 32.5%, 52%, 28% and 74%, respectively. These values indicate involving of diffusive processes owing to the sufficient diffusion time for protons into the internal structure of active electrode materials (Chen et al. 2019). Whereas, at a higher scan rate of 50 mV s^{-1}, the capacitive contributions was the dominant process with the calculated values of 77%, 71%, 85% 66% and 93% for pristine $MoSe_2$, W1-$MoSe_2$, W2-$MoSe_2$, W3-$MoSe_2$ and W2-$MoSe_2$/G electrodes, respectively. The plot of capacitive and diffusive contributions to the total stored charge at different scan rates for pristine $MoSe_2$, W-doped $MoSe_2$ and W2-$MoSe_2$/G electrodes are provided in Figure 5.20.

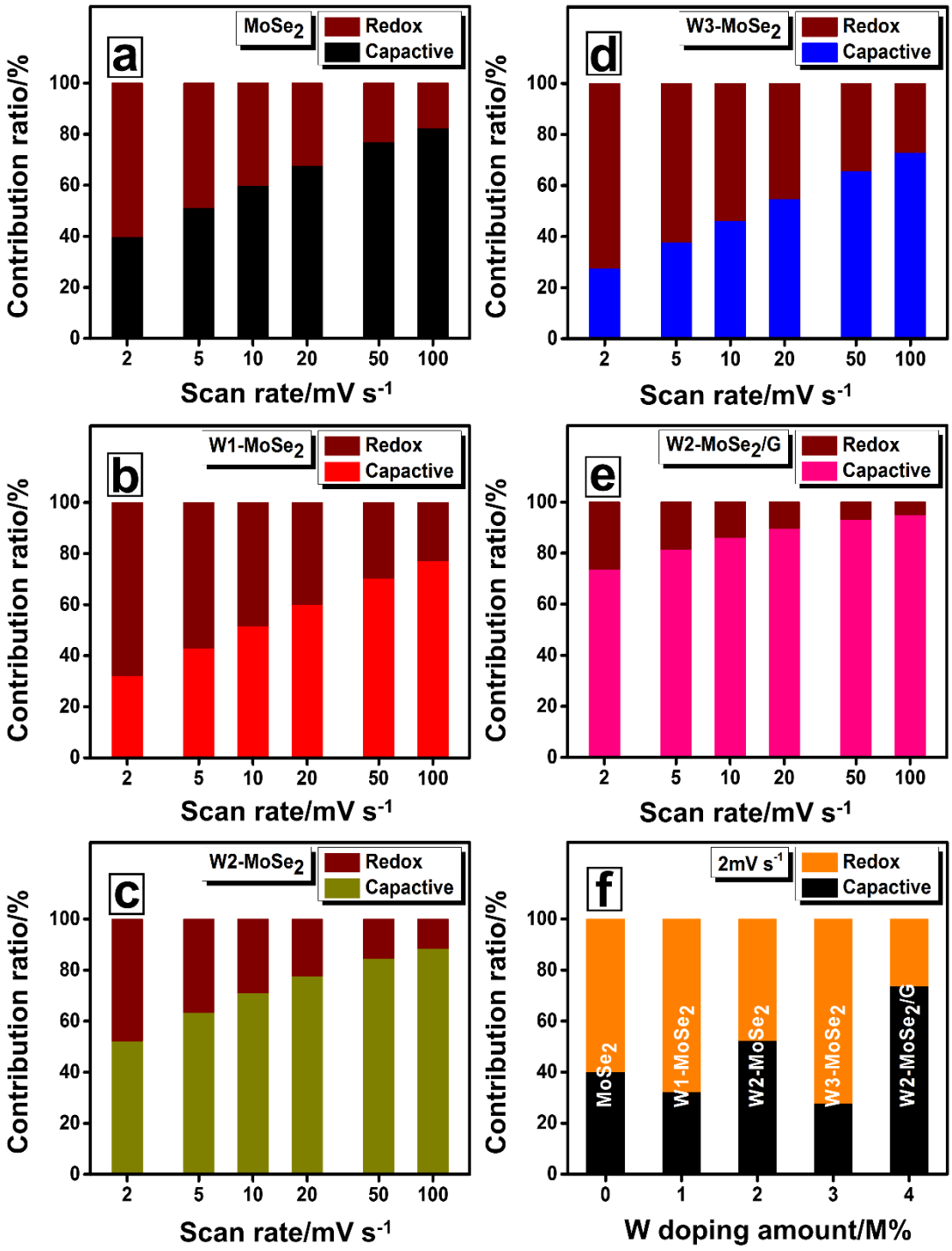

Figure 5.20 Capacitive and redox contributions to total charge stored for (a) $MoSe_2$, (b) W1-$MoSe_2$, (c) W2-$MoSe_2$, (d) W3-$MoSe_2$, (e) W2-$MoSe_2$/G electrodes at different of scan rates and (f) represents the comparison of capacitive and redox contributions at 2 mV s^{-1} scan rate as the function of W-doping and graphene hybrids.

5.4 SUMMARY

Series of molybdenum dichalcogenide nanostructures MoX_2 (X = S, Se, Te), W-doped $MoSe_2$ and W-$MoSe_2$/graphene hybrid nanostructures were successfully prepared employing hydrothermal method. Further, MoX_2 (X= S, Se, Te) nanostructures as an electrocatalyst for the HER rank these catalysts in the order $MoSe_2$>MoS_2>$MoTe_2$. Besides other factors influencing HER, the best performance of $MoSe_2$ was attributed to their predominant electronic conductivity. Further, all MoX_2 catalysts exhibit prominent stability and robustness, as evident from chronopotentiometric measurements. These imperative findings shed light on HER activities of non-noble catalysts and open-up opportunities for the advancements of high-performance electrocatalysts.

On the other hand, W-doping on $MoSe_2$ nanostructures demonstrate the variation of specific capacitances with 2 M % of tungsten (W) as an optimum doping amount. Further, addition of graphene oxide during the hydrothermal synthesis of W2-$MoSe_2$ indicated the formation of W2-$MoSe_2$/G nanostructures and in-situ reduction of graphene oxide. Physiochemical investigations indicate the successful growth of W2-$MoSe_2$ nanostructures over a graphene matrix, which facilitate rapid transport of electrolyte ions. In addition, synergistic factors such as high specific surface area, porosity and electronic conductivity enabled W2-$MoSe_2$/G electrodes to deliver the specific capacitance of 248 F g^{-1}, which is about ~2.4 and ~1.4 times higher in comparison to pristine $MoSe_2$ and W2-$MoSe_2$ electrodes. The higher values of specific capacitances are complimented with excellent capacitance retention of 102 % for 20000 cycles.

CHAPTER 6

COPPER CHALCOGENIDES FOR ELECTROCHEMICAL WATER-SPLITTING

In this chapter, the synthesis of copper sulfide (Cu_2S) micro-hexagons and the synthesis of copper sulfide-nickel sulfide (Cu_2S-Ni_3S_2) arrays supported by three-dimensional conducting nickel foam (NF) as a substrate are presented. Cu_2S micro-hexagons could catalyze the HER in both basic (1 M KOH) and acidic solutions (0.5 M H_2SO_4), corresponding to the extreme pH values of 14 and 0, respectively. The lower overpotentials was complemented with the prominent long-term stability as evident from chronopotentiometric analysis. On the other hand, Cu_2S enhanced the water-splitting characteristics of nickel sulfide (Ni_3S_2) in alkaline solution (1 M KOH), requiring the overpotential of -149 mV and 329 mV to drive the catalytic current density of 10 mA cm^{-2} for the HER and OER, respectively. Furthermore, overall-water splitting in symmetrical configurations required the cell-voltage of 1.77 V to deliver 10 mA cm^{-2}, complimented with an ultra-long term stability for 100 h. Therefore Cu_2S and Cu_2S-Ni_3S_2/NF could be a promising and effective electrocatalyst for water-splitting reactions.

6.1 INTRODUCTION

Electrochemical water-splitting has been an effective technique to generate hydrogen (H_2) and molecular oxygen (O_2), owing to their eco-friendly characteristics and high energy density (Roger et al. 2017). Although noble metal compounds (Pt, RuO_2 and IrO_2) and their derivatives are regarded as state-of-the-art catalysts for the HER and the OER, while, their high cost, low abundance and poor long-term durability (Pu et al. 2017) impede commercial applications. In addition, the overall water splitting efficiency depends upon the HER and OER kinetics, parity of two-electrodes, electrolyte solution and catalytic stability of the individual electrodes. Thus significant efforts have been made to develop highly efficient HER and OER catalyst in the same electrolyte to demonstrate the overall water splitting characteristics, which is highly demanding and challenging (Wang et al. 2019). Copper possess important and attractive properties such as high earth-abundance, multiple oxidation states, fast redox kinetics

and rich coordination chemistry (Kosman 2010). However, metallic copper (Cu) demonstrate poor HER activity owing to its weak hydrogen adsorption-desorption at the Cu sites (Fan et al. 2016). Therefore it is required to optimize hydrogen adsorption properties of Cu for the efficient HER. Among numerous successful attempts, tuning the coordination environment of Cu catalytic sites by different electronegative elements such as P, O and N was effective in improving the hydrogen adsorption of Cu, which in turn enhanced the HER (Zhang et al. 2015). Herein, the electron density drift from Cu metal atoms to anions may lead to positively-charged Cu atoms and the negatively-charged anions; which might function as hydride and proton acceptors, respectively, which facilitate the HER (Zhang et al. 2014). Based on this hypothesis, several Cu based HER electrocatalysts such as Cu_3P, Cu_3N, Cu_2O, etc. was reported. With this background, it is anticipated to observe the HER performance of Cu atoms coordinated with chalcogen atoms, since it is believed that the increase in covalency and declination of electronegativity favors the superior HER (De Silva et al. 2018).

Copper chalcogenides as electrocatalyst was prepared using anion-exchange (He et al. 2018), hydrothermal (Fan et al. 2016), chemical vapor deposition and electrodeposition methods (Masud et al. 2018), among which some of the processes are relatively expensive and complex. Therefore a simple and cost-effective technique is necessary for the synthesis of copper chalcogenides. Considering the HER of synthesized copper sulfides, the performances are measured in different electrolytes such as acidic, alkaline and neutral solutions. However, no effort has been put up to compare the intrinsic catalytic activity of synthesized copper sulfides at extreme pH conditions. In this regard, we propose the synthesis of Cu_2S with a unique morphology of micro-hexagons, which could catalyze HER in both basic and acidic solutions. The lower overpotentials of Cu_2S micro-hexagons are complimented with their long-term stability as evident from chronopotentiometric measurements.

On the other hand, considering nickel chalcogenides, although there are plentiful reports on the individual HER and OER performances of sulfides, selenides, and tellurides, the number of reports on overall water-splitting characteristics is still scarce. Considering nickel sulfides, several reports employ hydrothermal method for the synthesis (Luo et al. 2017), and the electrocatalytic performances are evaluated over a wide pH electrolytes. However, the performances are reasonably poor as compared with

other transition metal dichalcogenide systems, which may be ascribed to the more electronegativity of sulfur (~2.58) in addition to their poor electronic conductivity (Barthelemy et al. 1973). Very recently, there are reports on heterostructure TMCs and their use as an electrocatalyst for water-splitting reactions, wherein the integration of two different TMCs greatly enhanced the electrocatalytic performance (Lei et al. 2017; Xu et al. 2019). Among the few reports on nickel sulfide (Ni_3S_2) heterostructure, Ni_3S_2 is integrated with MoS_X, (Zhang et al. 2019a) and amorphous CoS_X (Shit et al. 2018), etc. Herein, it is believed that the charge-transfer within the electrocatalyst via S-bridge and chemisorption of hydrogen and oxygen-containing intermediates improved synergistically, which in turn accelerated the electrocatalytic performance. Since copper (Cu^{2+}) possess good redox kinetics (Tran et al. 2012), high electronic conductivity and the electronegativity of copper (~1.90) is very close to that of nickel (~1.91), it may also be envisioned that the integration of copper sulfide (Cu_2S) and nickel sulfide (Ni_3S_2) could be promising for water-splitting reactions.

Furthermore, the in-situ synthesis of electrocatalysts on highly conductive metallic foam current collector substrates has proven advantageous such as exposing more surface area, improved catalyst-electrolyte contact, mechanical stability and also providing a pathway for evolved gas bubbles without damaging the electrode surface (Sivanantham and Shanmugam 2017). In this background, we report the synthesis of copper sulfide-nickel sulfide (Cu_2S-Ni_3S_2) arrays on nickel foam (NF) substrate via a one-step hydrothermal process. The synthesized Cu_2S-Ni_3S_2/NF presented exceptional performance as an electrocatalyst for the HER and OER, complimented with promising long-term durability in alkaline solution. Furthermore, overall water-splitting characteristics were demonstrated by assembling two identical Cu_2S-Ni_3S_2/NF electrodes in symmetrical configurations, delivering superior performance even at high current densities.

6.2 SYNTHESIS

6.2.1 Synthesis of copper sulfide (Cu_2S) micro-hexagons

Copper sulfide (Cu_2S) micro-hexagons were synthesized employing a one-pot hydrothermal method. About 1 mM (250 mg) of copper sulfate pentahydrate

($CuSO_4.5H_2O$) was added to a beaker containing 30 mL of DI water at room temperature under continuous stirring. On the other hand, 0.5 mM (16 mg) of sulfur powder (S) was added to a vial containing 5 mL of hydrazine hydrate ($NH_2NH_2.H_2O$), followed by ultra-sonication for a short interval of ~2-3 min. After this, the as-formed solution was added dropwise to a beaker containing 30 mL of $CuSO_4.5H_2O$ solution, resulting in an immediate color change from green to dark brown and then black.

The final black colored solution was then transferred into a 50 mL Teflon-lined stainless steel autoclave, followed by the hydrothermal process at a temperature of 180 °C for 12 h. After the reaction, the autoclaves were allowed to cool down naturally, and the collected precipitates were washed in excess of DI water and dried in vacuum at 60 °C. The successful formation of Cu_2S-micro-hexagons may be as given below:

$$S + N_2H_4.H_2O \rightarrow H_2S\,(aq) + 4H^+(aq) + N_2\,(g) \quad (6.1)$$

$$2CuSO_4.5H_2O + 2H_2S \rightarrow 2Cu_2S + +2H_2SO_4 + 5H_2O \quad (6.2)$$

6.2.2 Synthesis of copper sulfide-nickel sulfide (Cu_2S-Ni_3S_2) arrays on nickel foam (NF)

Copper sulfide-nickel sulfide (Cu_2S-Ni_3S_2) arrays were directly grown on three-dimensional nickel foam (NF) via a hydrothermal method. In brief, 1 mM (250 mg) copper sulphate pentahydrate ($CuSO_4.5H_2O$) were added to a beaker containing 30 mL of DI water at room temperature under continuous stirring. On the other hand, 0.5 mM (16 mg) of sulphur powder (S) were added to a vial containing 5 mL of hydrazine hydrate ($NH_2NH_2.H_2O$), followed by ultra-sonication for a short interval of 2-3 min. After which, the sonicated solution was added dropwise to a beaker containing 30 mL of prepared copper sulphate solution, resulting in an immediate color change from green to dark brown and then black. The final black colored solution was then transferred into a 50 mL Teflon-lined stainless steel autoclave, to which two pieces of pre-cleaned NF of dimensions (1 cm × 1 cm) was introduced. The autoclave was sealed and the hydrothermal reaction was carried out at a temperature of 180 °C for 12 h. After the reaction, the autoclaves were allowed to cool down naturally, the collected Cu_2S-Ni_3S_2/NF samples were washed in excess of DI water and dried in vacuum at 60 °C.

With the above synthesis conditions, the successful formation of Cu_2S-Ni_3S_2 arrays on NF could be as given below:

$$4S + 2N_2H_4.H_2O \rightarrow 4H_2S\,(aq) + 2H^+(aq) + 2N_2\,(g) \quad (6.3)$$

$$4CuSO_4.5H_2O + 3Ni\,(s) + 4H_2S \rightarrow 2Cu_2S + Ni_3S_2 + 4H_2SO_4 + 10H_2O \quad (6.4)$$

In the present experiment, NF is used as a substrate as well as nickel source for the formation of Ni_3S_2. On the other hand $NH_2NH_2.H_2O$ plays the dual-role: (a) For the formation of Cu_2S via replacement reaction and (b) sulfidization of the NF to form Ni_3S_2.

The mass loading of Cu_2S-Ni_3S_2 on NF was determined by the weight difference before and after hydrothermal reaction. The estimated mass loading was about ~1.3 mg cm^{-2}.

For comparisons, pristine Ni_3S_2/NF were also synthesized without the addition of $CuSO_4.5H_2O$ by following the same hydrothermal synthesis conditions.

The formation of Ni_3S_2/NF may follow the reactions below:

$$2S + N_2H_4.H_2O \rightarrow 2H_2S\,(aq) + 4H^+(aq) + N_2\,(g) \quad (6.5)$$

$$2H_2S\,(aq) + 3\,Ni\,(s) \rightarrow Ni_3S_2 + 4H\,(aq) \quad (6.6)$$

6.3 RESULTS AND DISCUSSIONS

6.3.1 Physiochemical analysis of Cu_2S micro-hexagons

The Figure 6.1 represents the various physiochemical analysis employed for the as-synthesized Cu_2S micro-hexagons. Structural characterization using XRD measurements recorded in the 2θ range of 15-50º as seen in Figure 6.1a indicate the indexed multiple diffraction peaks, which are commensurate with standardized JCPDS reference pattern number #033-0490. The recorded XRD pattern of Cu_2S is indexed into their monoclinic phase, with lattice constants a = 15.23 Å, b =11.88 Å and c = 13.49 Å of P21/c space group. Further, EDS measurements are employed to determine elemental composition and phase purity of the synthesized Cu_2S micro-hexagons. As displayed in Figure 6.1b, EDS spectra indicate the elemental peaks corresponding to Cu and S along with low intense peaks of C and O. The representative SEM image wherein EDS measurements are performed are provided in (see APPENDIX XVII). The existence of C and O peaks could be ascribed to the use of carbon tape during EDS

measurements and surface oxygen moieties of Cu or S, respectively. Furthermore, the calculated atomic ratio of Cu to S is 2.06:1, which is close to the stoichiometric ratio of Cu_2S. In addition, the weight and atomic percentages of all the visualized elements are provided as a bar diagram in the inset of Figure 6.1b and tabulated in (see APPENDIX XVII). FESEM images confirm the morphology of synthesized Cu_2S micro-hexagons. FESEM images (Figure 6.1c-d) at two different magnifications demonstrate the uniformly structured Cu_2S of hexagonal shape with obvious thickness at a micron level. The average width and thickness of hexagons are about ~1.32 µm and ~0.65 µm, respectively. Furthermore, BET and BJH measurements (see APPENDIX XVIII) based on N_2 adsorption-desorption isotherms indicate the superior surface area of ~33.97 $m^2 g^{-1}$ and an average pore size of ~2.02 nm, respectively.

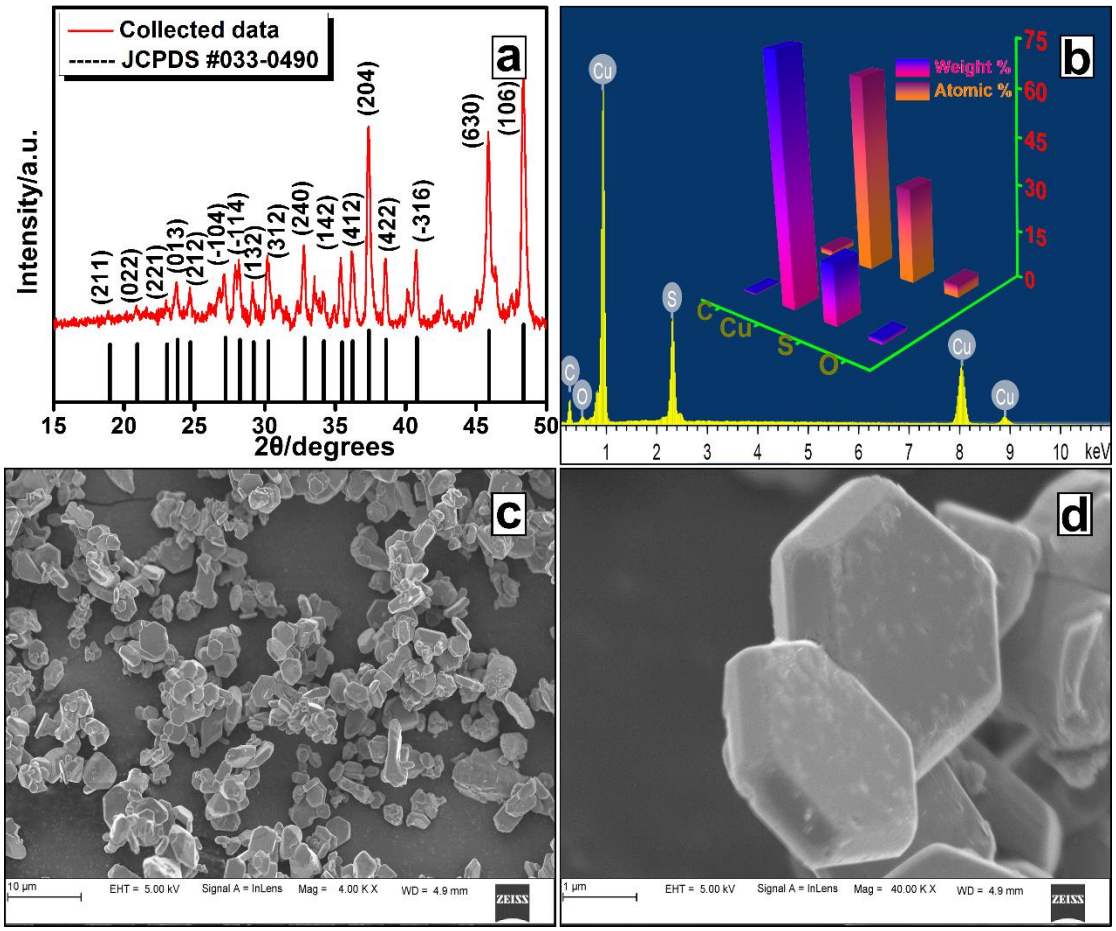

Figure 6.1 Physiochemical characterization of Copper sulfide micro-hexagons: (a) XRD pattern, (b) EDS spectra and (c-d) FESEM images at two different magnifications.

6.3.2 HER performance of Cu_2S micro-hexagons at extreme pH conditions

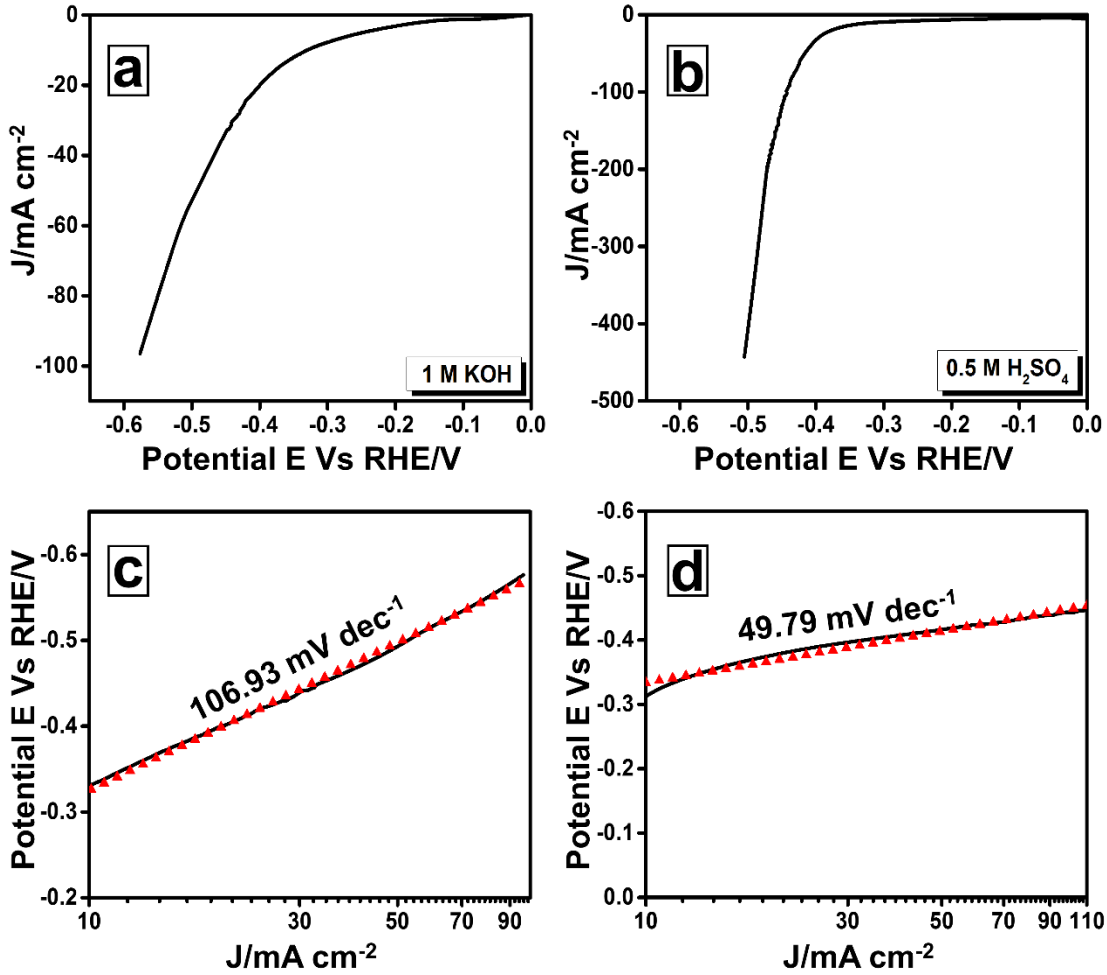

Figure 6.2 (a-b) iR compensated LSV curves of Cu_2S micro-hexagons in 1 M KOH and 0.5 M H_2SO_4 corresponding to pH values of 14 and 0, respectively and (c-d) Tafel plots derived from polarization curves.

The electrochemical measurements of Cu_2S micro-hexagons towards the HER was evaluated with three-electrode configurations. Since the as-synthesized nanostructures was in the powder form, they were assembled on graphite rod substrates as described in section 2.3.7 for successful electrochemical measurements. The three-electrode setup consisted of a working electrode, saturated calomel electrode (SCE) as reference electrode and platinum (Pt) wire as a counter electrode. The HER performance of the synthesized Cu_2S micro-hexagons was evaluated in two different solutions namely 1 M KOH (basic) and 0.5 M H_2SO_4 (acidic), corresponding to extreme pH values of 14 and

0, respectively. Further, the resulting data is calibrated to reversible hydrogen electrode (RHE) standards, using the relation of E Vs. RHE = E Vs. SCE + (0.059* pH) +0.244 V. The LSV curves were recorded at a scan rate of 5 mV s^{-1}. Further, iR compensation was applied to remove resistive and background losses. As such, Figure 6.2a-b demonstrate the LSV curves of Cu_2S micro-hexagons in basic and acidic solutions, respectively. As evident from the LSV curve in a basic solution (Figure 6.2a), Cu_2S micro-hexagons require the overpotentials of -330 mV, -399 mV, -492 mV and -596 mV to deliver benchmark catalytic current densities 10, 20, 50 and 100 mA cm^{-2}, respectively. Whereas, in acidic solution (Figure 6.2b), the overpotentials were -312 mV, -376 mV, -416 mV and -443 mV to deliver the same benchmark current densities 10, 20, 50 and 100 mA cm^{-2}, respectively. It is also worth noting that Cu_2S micro-hexagons could deliver a relatively high current density of ~440 mA cm^{-2} at a moderate overpotential of -505 mV in acidic solution. Furthermore, Tafel plots (Figure 6.2c-d) obtained by redrawing the polarization curves signify the rate of electrolysis, demonstrate the Tafel slope values of 106.93 mV dec^{-1} and 49.79 mV dec^{-1} in basic and acidic solutions, respectively. These results suggest that Cu_2S micro-hexagons has better kinetic HER interfaces in acidic solution than in alkaline solution.

6.3.3 HER Kinetics and stability of Cu_2S micro-hexagons

The Nyquist plots were recorded in the frequency range of 0.2 Hz – 100 kHz at different applied bias. Figure 6.3a-b and Figure 6.3c-d represents the Nyquist plots and Bode phase angle plots of Cu_2S micro-hexagons in basic and acidic solutions, respectively. The Nyquist plots of Cu_2S micro-hexagons in both basic and acidic solutions are semicircles, representing charge-transfer resistance (Chen and Lasia 1991). The declination of resistive semicircle diameter with respect to applied bias demonstrates these semicircles are related to HER kinetics (Elias and Hegde 2016). In addition, the downfall of phase angle and shift towards higher frequencies at higher applied bias demonstrate faster kinetics (Ojha et al. 2017). Furthermore, the recorded Nyquist plots of Cu_2S micro-hexagons in both basic and acidic solutions are fit into the Randle's electrochemical equivalent circuit (EEC) represented by $R_S(Q_{CPE}R_{CT})$ (Figure 6.3e), wherein R_S, R_{CT} and Q_{CPE} portrays the solution resistance, charge-transfer resistance and constant phase element/pseudocapacitive element, respectively.

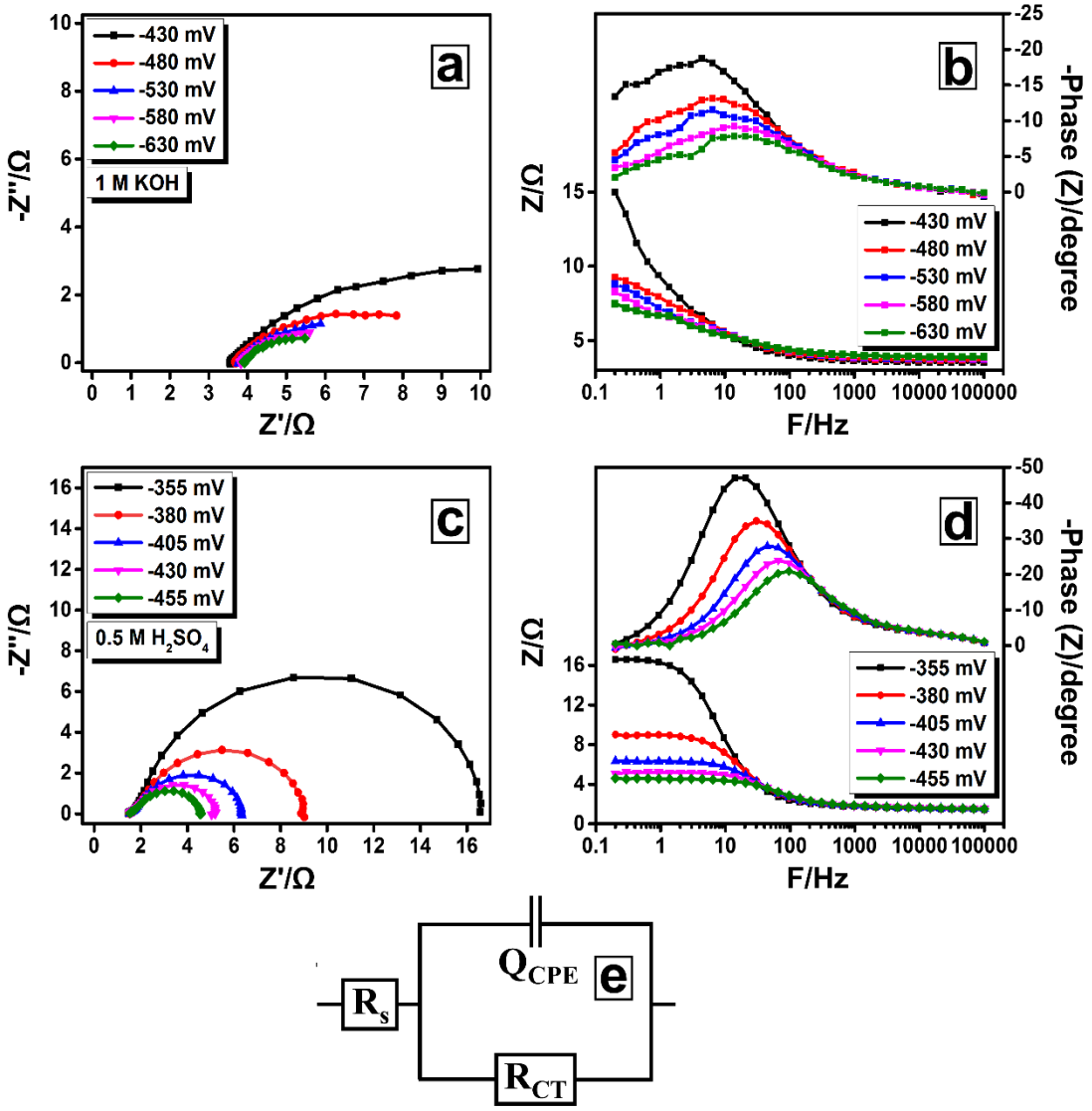

Figure 6.3 (a-b) Nyquist plot and corresponding Bode phase angle plot in a basic solution (1 M KOH), (c-d) Nyquist plot and corresponding Bode phase angle plot in acidic solution (0.5 M H_2SO_4) and (e) Simulated electrochemical equivalent circuit (EEC) for the Nyquist plots.

As evident from EEC fitting parameters, at an applied bias of -430 mV, Cu_2S micro-hexagons reveal the resistance values R_S and R_{CT} of ~3.9 Ω and ~16.5 Ω in basic solution, which are reasonably higher than the resistance values in acidic solution (R_S = ~1.6 Ω and R_{CT} = ~3.74 Ω). In addition, other EEC fitting parameters extracted by fitting the recorded Nyquist plots in basic and acidic solutions are tabulated in Table 6.1 and Table 6.2, respectively. All of these values compliments and supports the

superior HER performance of Cu_2S micro-hexagons in acidic solution. On the other hand, these results also indicate the high R_S and R_{CT} values of Cu_2S micro-hexagons could be disparaging for the HER in alkaline solution.

Moreover, these results are further supported by ECSA measurements, which indicate effective surface area available for the HER. The ECSA is determined in the double layer chagrining region of the voltammetry curve, wherein no Faradaic reaction takes place (Hu et al. 2017). The CV curves of Cu_2S micro-hexagons in basic (1 M KOH) and acidic (0.5 M H_2SO_4) solutions in the non-Faradaic region as provided in (see APPENDIX XIX). The ECSA values are estimated by plotting the difference in double-layer charging current densities $\Delta j = j_a - j_c$ Vs. scan rates as displayed in Figure 6.4. The difference in double-layer charging current densities were estimated at a potential of −0.55 V Vs. SCE and at −0.3 V Vs. SCE in basic and acidic solutions, respectively. As awaited, Cu_2S micro-hexagons demonstrate the greater ECSA of 5.83 mF cm^{-2} in acidic solution than in basic solution (3.89 mF cm^{-2}). These results further supports the superior HER in an acidic solution than in basic solution as confirmed from Tafel plots and HER kinetic analysis.

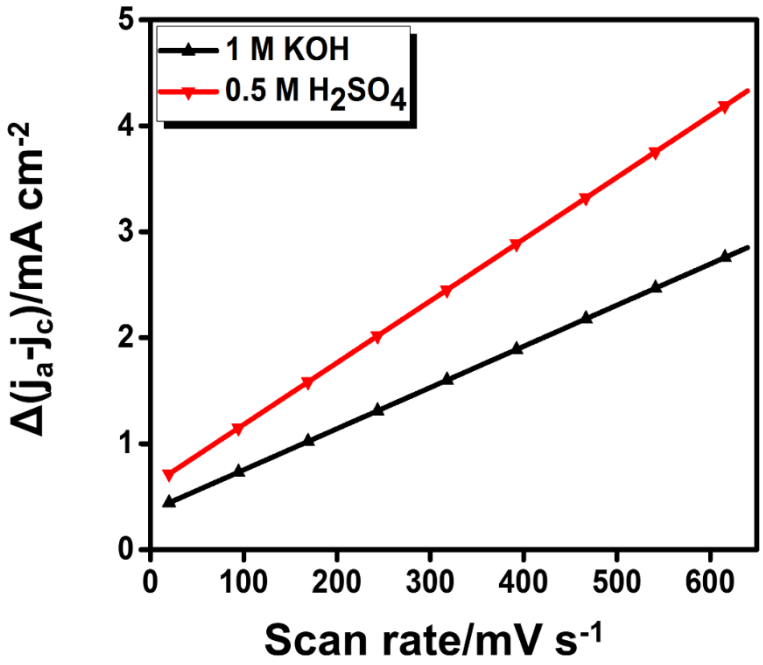

Figure 6.4 Plot of difference in double-layer charging current densities vs. scan rate for the estimation of ECSA.

Table 6.1. EEC parameters of Cu_2S micro-hexagons in basic solution (1 M KOH).

Overpotential/mV	R_S/Ω	Q_{CPE1}/mF	R_{CT1}/Ω
-430	3.507	3.194	15.79
-480	3.643	3.550	7.70
-530	3.723	3.774	5.11
-580	3.774	3.681	3.73
-630	3.850	3.644	3.05

Table 6.2. EEC parameters of Cu_2S micro-hexagons in acidic solution (0.5 M H_2SO_4).

Overpotential/mV	R_S/Ω	Q_{CPE1}/mF	R_{CT1}/Ω
-355	1.606	39.7	16.5
-380	1.617	31.9	5.91
-405	1.609	44.2	5.84
-430	1.603	38.4	3.74
-455	1.604	50.5	3.37

Further, chronopotentiometry measurements of Cu_2S micro-hexagons are recorded at an applied current density of -35 mA cm^{-2} for 24 h, as pictured in Figure 6.5a and Figure 6.5d for basic and acidic solution, respectively. Results demonstrate the vigorous evolution of hydrogen, with no obvious drift in the overpotential for chronopotentiometry in basic solution. Furthermore, the polarization curve (Figure 6.5b) and Nyquist plot (at -580 mV bias) (Figure 6.5c) recorded after chronopotentiometry measurements could retrace the initial curve, confirming their promising stability. As evident from the Nyquist plot, a small increment in R_S of ~3.7 Ω to ~ 4.27 Ω may be noted. While, the R_{CT} remained the same before the after chronopotentiometry measurements, which further endorse the promising stability in basic solution. On the other hand, a small downward shift is observed for chronopotentiometry in acidic solution, which can be necessarily attributed to the enhanced wettability and/or activation of electroactive sites under long-term operations. Also, the polarization curve recorded after chronopotentiometry (Figure 6.5e) represents an enhanced overall current density of about ~13 %. In addition, the Nyquist plot recorded at -455 mV bias (Figure 6.5f), specify the decrease in R_{CT} by ~ 40 %.

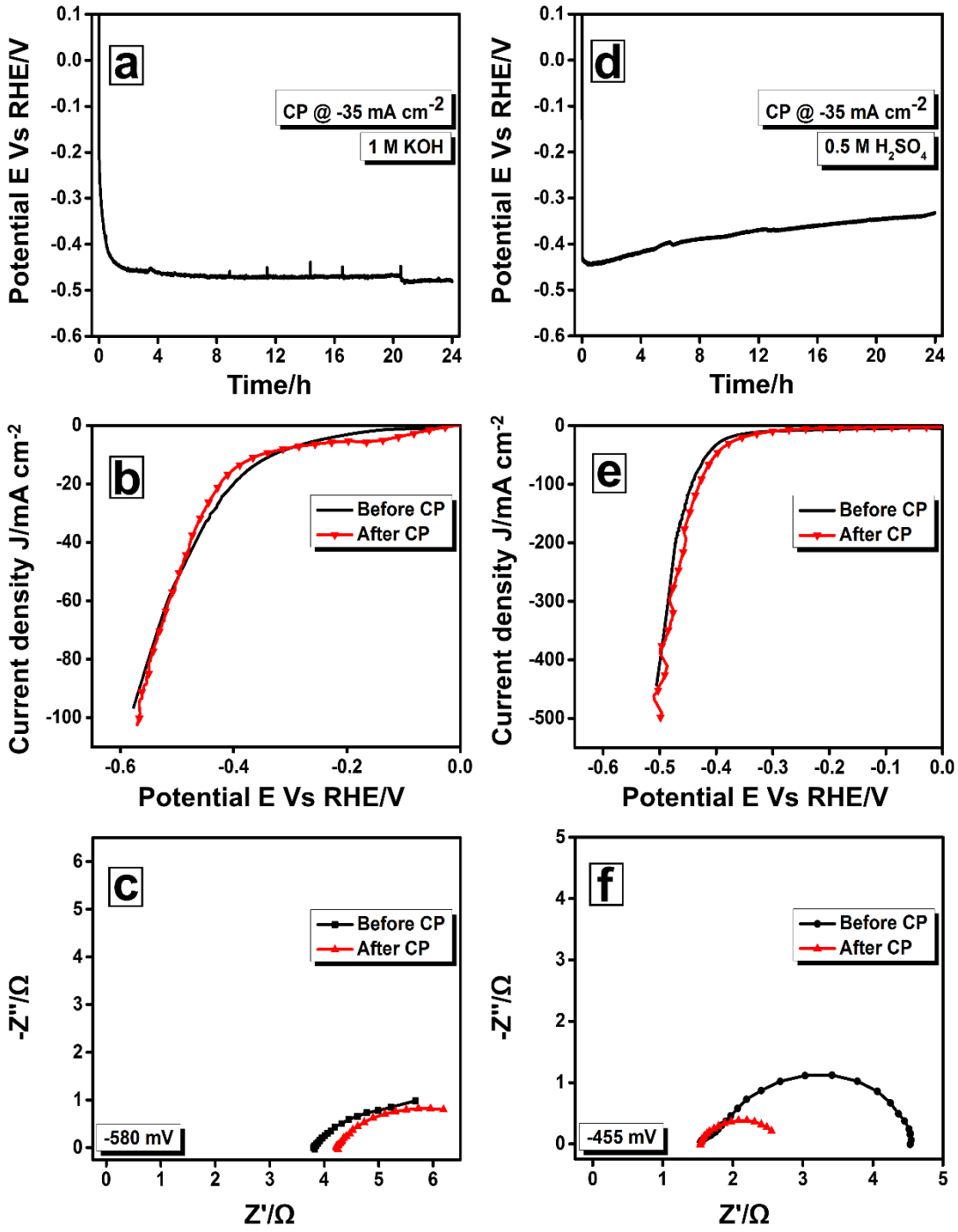

Figure 6.5 (a) Chronopotentiometric stability tests of Cu_2S micro-hexagons in 1 M KOH, (b) LSV curve and (c) Nyquist plot recorded before and after stability tests. (d) Chronopotentiometric stability tests of Cu_2S micro-hexagons in 0.5 M H_2SO_4, (e) LSV curve and (f) Nyquist plot recorded before and after chronopotentiometric stability test.

6.3.4 Physiochemical analysis of Cu_2S-Ni_3S_2/NF arrays

The XRD patterns of synthesized Cu_2S-Ni_3S_2/NF is analyzed and indexed as displayed in Figure 6.6a, which was recorded in the 2θ range of 10-80º. The diffraction pattern indicate the predominant peaks corresponding to Cu_2S, Ni_3S_2 and metallic nickel foam (NF), represented by different symbols: an asterisk (*) – Cu_2S, dollar ($) – Ni_3S_2 and spade (♠) – metallic nickel foam (NF), respectively. The diffraction peaks of Cu_2S could be successfully indexed to their cubic phase, with lattice constants $a = b = c = 5.735$ Å, which are in good agreement with the JCPDS reference number 012-0175. On the other hand, Ni_3S_2 represents the rhombohedral phase with lattice constants $a = b = 5.74$ Å and $c = 7.13$ Å, which are commensurate with JCPDS reference number 030-0863. Interestingly, peak emanating at ~44º could be indexed to the NF as well as Cu_2S, which demonstrates the preferential growth of Cu_2S over NF during the hydrothermal process. For comparisons, XRD patterns of Cu_2S-Ni_3S_2/NF, Ni_3S_2/NF and bare NF are provided in Figure 6.6b. Herein the vertically stacked XRD pattern confirms the preferential growth of Cu_2S over NF. On the other hand, XRD pattern of pristine Ni_3S_2/NF is also indexed to their rhombohedral phase, with the overall intensities lower than those of Cu_2S-Ni_3S_2/NF.

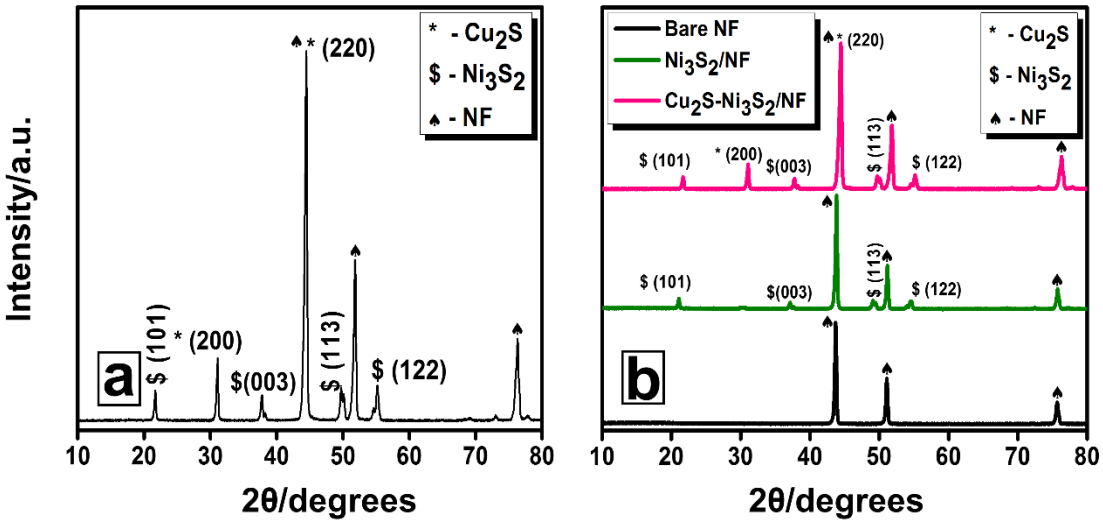

Figure 6.6 (a) XRD pattern of Cu_2S-Ni_3S_2/NF and (b) comparison of XRD patterns of Cu_2S-Ni_3S_2/NF, Ni_3S_2/NF and bare NF in the 2θ range of 10-80º at a scan rate of 1º min^{-1}.

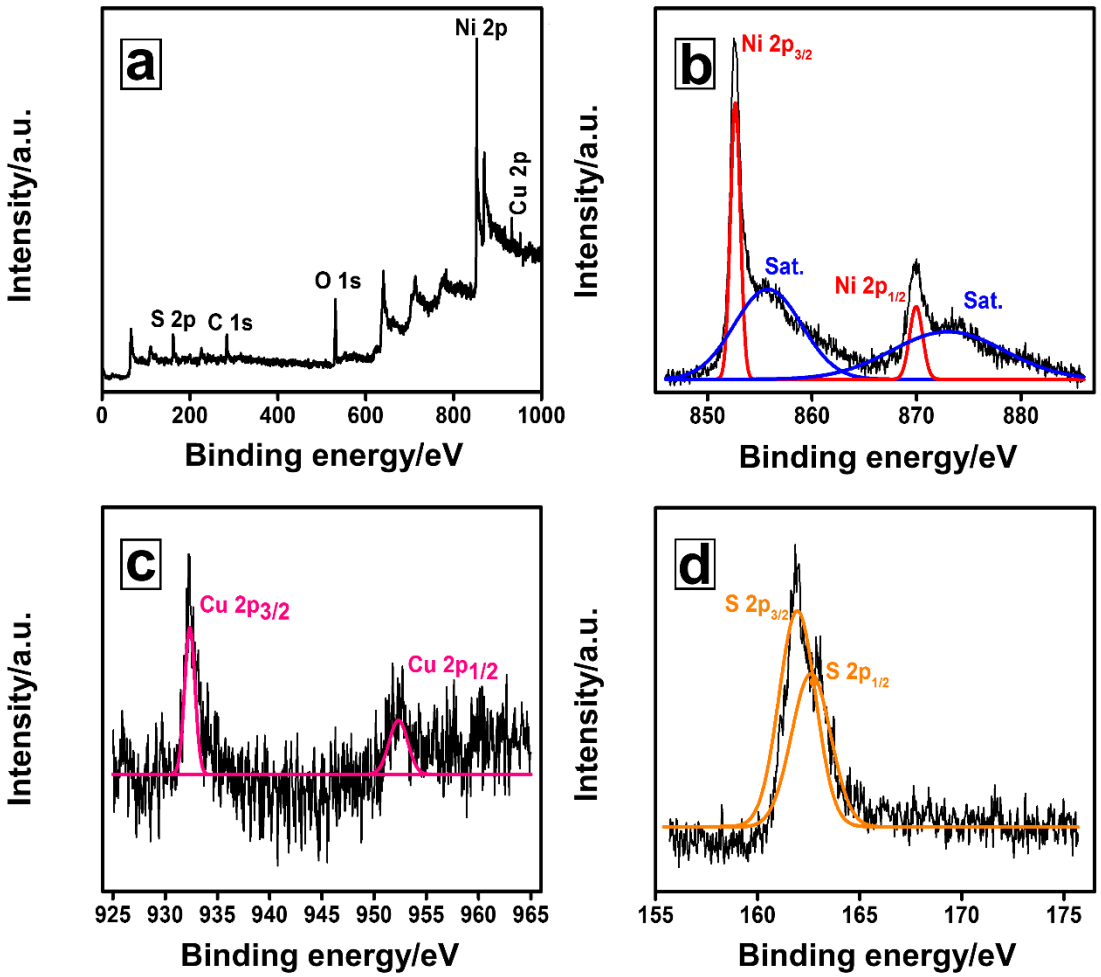

Figure 6.7 (a) XPS survey spectra of Cu_2S-Ni_3S_2/NF, high-resolution core-level spectra of Ni 2p (b), Cu 2p (c) and S 2p (d).

The formation of Cu_2S-Ni_3S_2/NF was also confirmed through X-ray photoelectron spectroscopy (XPS) measurements. Figure 6.7a shows the XPS survey spectra indicating the presence of C, O, Ni, Cu and S elements in Cu_2S-Ni_3S_2/NF. The existence of C and O is generally attributed to the use of elemental carbon as reference and surface oxide structures of non-oxide materials, respectively. The resolved spectra of Ni 2p as seen in Figure 6.7b indicate two doublets $2p_{3/2}$ and $2p_{1/2}$, owing to the spin-orbit interaction. The two doublets appeared due to the presence of Ni^{2+} and Ni^{3+} states of Ni in Ni_3S_2 (Zhang et al. 2017). In addition, an earlier report (Jiang et al. 2016) also suggests the peak emanating at ~ 853 eV is a characteristic signature of Ni_3S_2 and the satellite peaks at higher binding energies are ascribed to the surface oxides of nickel. On the other hand, resolved spectra of Cu 2p (Figure 6.7c) also indicate the two-

doublets at 932.3 eV and ~952.2 eV belonging to Cu $2p_{3/2}$ and Cu $2p_{1/2}$ (Kuo et al. 2011), respectively. Also, the resolved spectra of S 2p (Figure 6.7d) indicate the binding energy peaks at ~ 161.7 eV and ~162.8 eV indexing to the S $2p_{3/2}$ and S $2p_{1/2}$ (Fan et al. 2016), respectively.

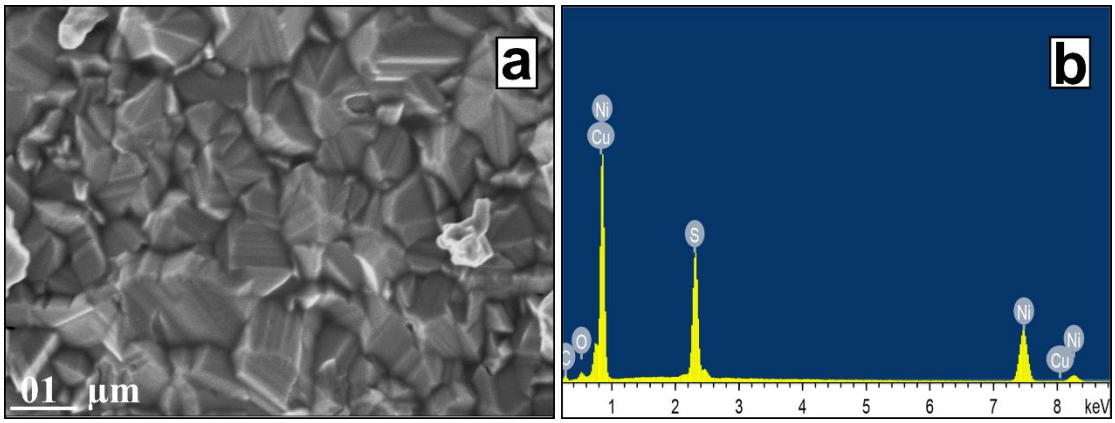

Figure 6.8 FESEM micrograph (a) and (b) EDS spectra of Cu_2S-Ni_3S_2/NF.

FESEM analysis shed light on the growth of copper-nickel sulfides on the surface of NF. Figure 6.8a represents the FESEM micrograph reveal the highly-ordered, interlocked and three-dimensional cube-like arrays at the submicron level. It can also be noted that FESEM morphology indicates the complete and uniform coverage of Cu_2S-Ni_3S_2 over NF. Earlier reports (Wu et al. 2016) demonstrate these structures are favorable for water-splitting reactions, owing to the high surface area and rapid charge-transfer kinetics. EDS measurements (Figure 6.8b) performed on the area as shown in Figure 6.8a, indicate the presence of O, C, Cu, Ni and S. The existence of O moieties could be ascribed to the surface oxides of Cu, Ni or S, while the occurrence of C may be attributed to the use of carbon tape during FESEM measurements. Furthermore elemental smart maps of O, Cu, Ni and S as presented in Figure 6.9, indicate the uniform distribution of elements. For better accuracy, a larger area of the sample as seen in Figure 6.9a is probed for mapping analysis. The elemental maps of the individual elements are indicated in different colors: O (orange), Cu (red), Ni (blue) and S (green) as represented in Figure 6.9b-c-d-e, respectively. Furthermore the elemental maps of Cu, Ni and S are merged and presented as a single image Figure 6.9f, describing the homogeneous distribution of elements throughout the area of the sample under investigation.

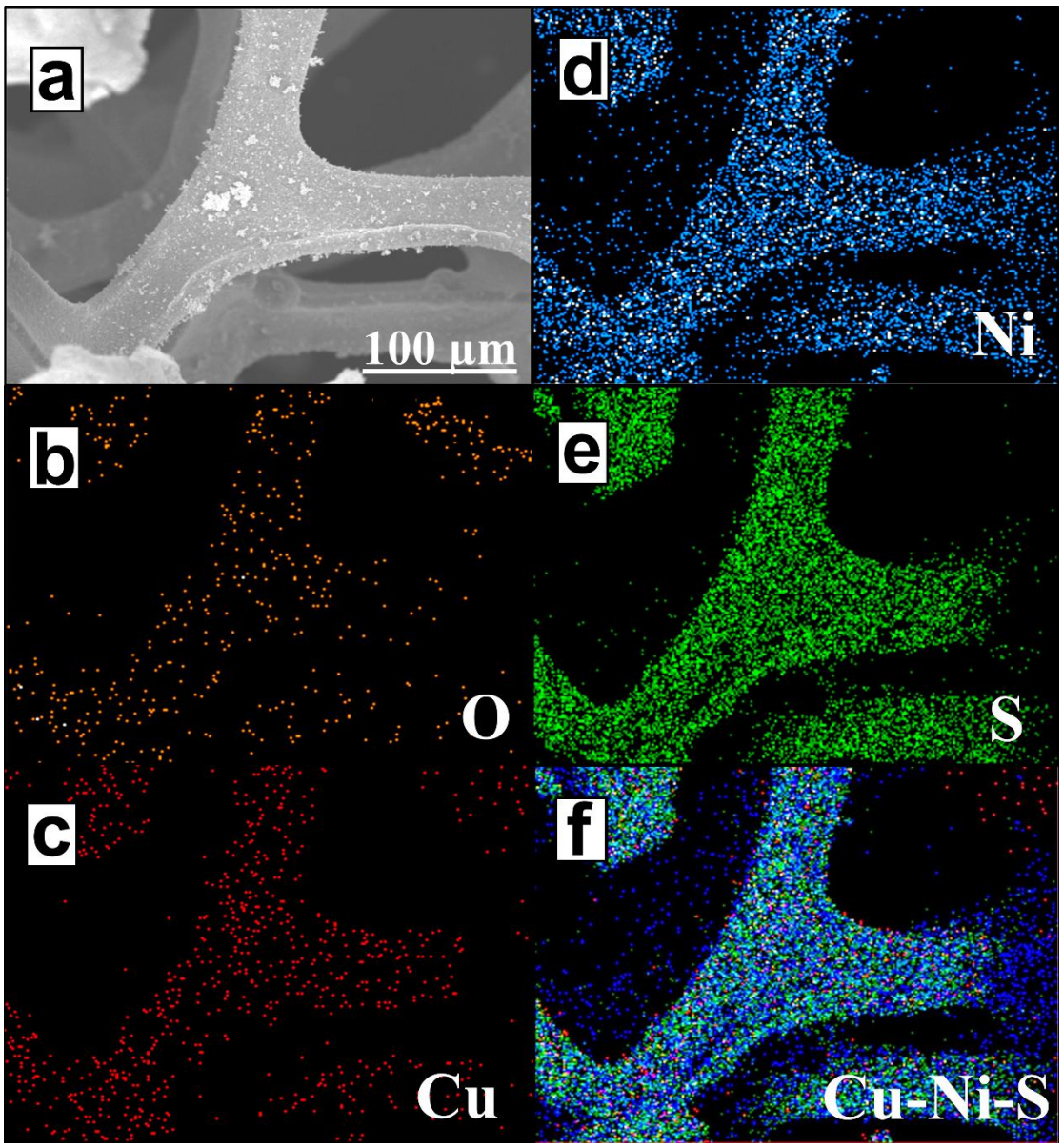

Figure 6.9 Elemental mapping images of Cu_2S-Ni_3S_2/NF: (a) SEM image wherein elemental mapping are conducted, (b) O (orange), (c) Cu (red), (d) Ni (blue), (e) S (green) and (f) merged mapping of Cu, Ni and S.

The structural features of Cu_2S-Ni3S_2/NF are also envisioned through HRTEM measurements. The high magnification TEM image Figure 6.10a indicate two-sets of planes, confirm the formation of Cu_2S-Ni_3S_2 heterostructure. The measured lattice spacing values was ~ 0.20 nm and ~0.28 nm, corresponding to the (220) and (110) planes of Cu_2S and Ni_3S_2, respectively. Additionally, the corresponding SAED pattern (Figure 6.10b) contains few bright spots, suggesting their polycrystallinity.

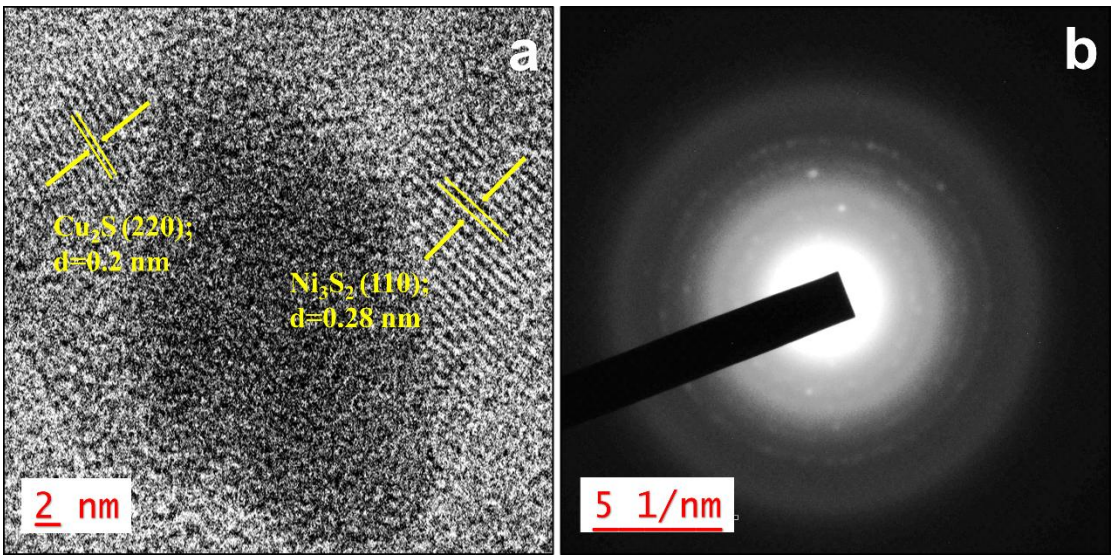

Figure 6.10 (a) HRTEM image and (b) SAED pattern of Cu_2S-Ni_3S_2/NF.

Additionally, Ni_3S_2/NF also shown similar morphology to those of Cu_2S-Ni_3S_2/NF as provided in (Figure 6.11a) and the EDS measurements (Figure 6.11b) of Ni_3S_2/NF indicate the presence of O, C, Ni and S. While the elemental maps (see APPENDIX XX) describe the homogeneous distribution of elements. Furthermore, weight percentages of all the elements present in Ni_3S_2/NF is tabulated in (see APPENDIX XX).

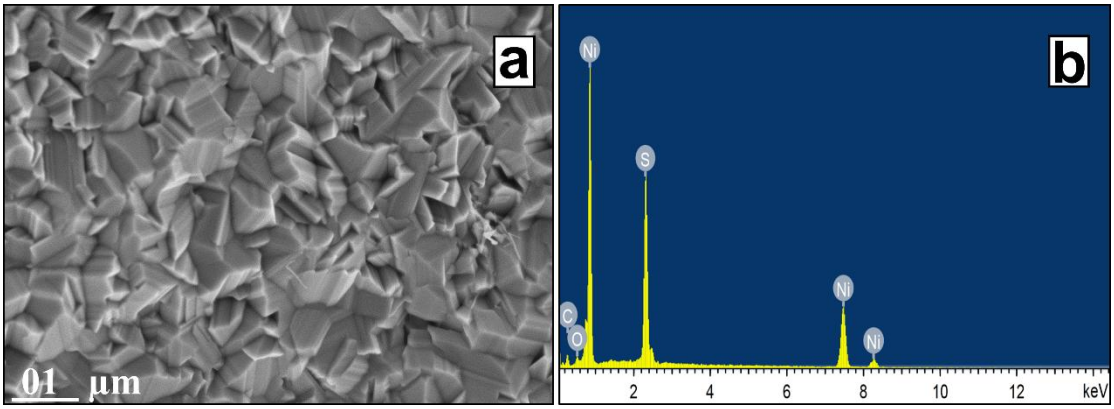

Figure 6.11 (a) FESEM micrograph and (b) EDS spectra of Ni_3S_2/NF.

6.3.5 Electrochemical measurements of Cu_2S-Ni_3S_2/NF arrays

6.3.5.1 Hydrogen evolution reaction (HER)

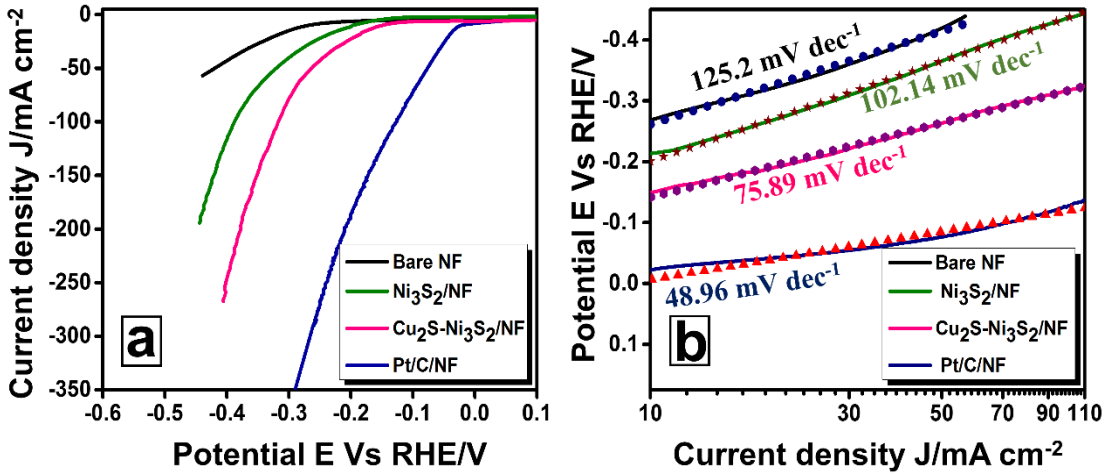

Figure 6.12 (a) iR compensated LSV curves at 5 mV s^{-1} scan rate and (b) Corresponding Tafel plot of bare NF, Ni_3S_2/NF, Cu_2S-Ni_3S_2/NF and Pt/C/NF towards the HER.

The electrocatalytic performance of the synthesized Cu_2S-Ni_3S_2/NF towards the HER was measured in 1 M KOH solution. The LSV curves are recorded at a scan rate of 5 mV s^{-1} and the Tafel plots are obtained by replotting the iR compensated LSV curve as a plot of log *J* Vs. Overpotential (η) and fit into the equation: $\eta = a + b\ log\ j$. Figure 6.12a-b displays iR-corrected LSV curves and the corresponding Tafel plots of bare NF, Ni_3S_2/NF, Cu_2S-Ni_3S_2/NF and Pt/C/NF, respectively. As anticipated, Cu_2S-Ni_3S_2/NF demonstrates the overpotential of -149 mV to drive the catalytic current density of 10 mA cm^{-2} (η_{10}). In addition, Cu_2S-Ni_3S_2/NF also required the overpotentials of -317 mV (η_{100}) and -377 mV (η_{200}) to deliver high catalytic current density of 100 and 200 mA cm^{-2}, respectively. On the other hand, Pt/C/NF showed a superior HER activity requiring a very-low overpotential of -22 mV to drive a catalytic current density of 10 mA cm^{-2}. In contrast, Ni_3S_2/NF and bare NF shown rationally poor HER performance with the need of –198 mV and -268 mV, respectively, to approach the same current density. Furthermore, the obtained Tafel slope value is 75.89 mV dec^{-1} for Cu_2S-Ni_3S_2/NF, which is quite less than those of Ni_3S_2/NF (102.14 mV dec^{-1}), bare NF (125.2 mV dec^{-1}) and slightly higher than state-of-the-art Pt/C/NF catalyst (48.96

mV dec^{-1}). Furthermore, the HER parameters of Cu_2S-Ni_3S_2/NF are compared with recently reported sulfide-based HER electrocatalysts as provided in Table 6.3. The lower overpotential and Tafel slope value of the presented Cu_2S-Ni_3S_2/NF suggest more favorable HER kinetics.

Table 6.3. Comparison of the alkaline HER activities of Cu_2S-Ni_3S_2/NF over other nickel and copper sulfides as reported in the literature.

Catalyst	Overpotential/mV	Tafel slope	Reference
NiS_2	474 @ 10 mA cm^{-2}	128 mV dec^{-1}	(Jiang et al. 2016)
Cu_2S@CF	316 @ 10 mA cm^{-2}	55 mV dec^{-1}	(Ma et al. 2019)
$Cu_{1-x}Ni_xS$/NF	189 @ 10 mA cm^{-2}	127.2 mV dec^{-1}	(Li et al. 2019)
CoSx/Ni_3S_2@NF	204 @ 10 mA cm^{-2}	133.32 mV dec^{-1}	(Shit et al. 2018)
Ni/NiS	230 @ 10 mA cm^{-2}	123.3 mV dec^{-1}	(Chen et al. 2016)
Ni_3S_2/NF	200 @ 10 mA cm^{-2}	107 mV dec^{-1}	(Ouyang et al. 2015)
Cu_2S-Ni_3S_2/NF	149 @ 10 mA cm^{-2}	75.89 mV dec^{-1}	Present work

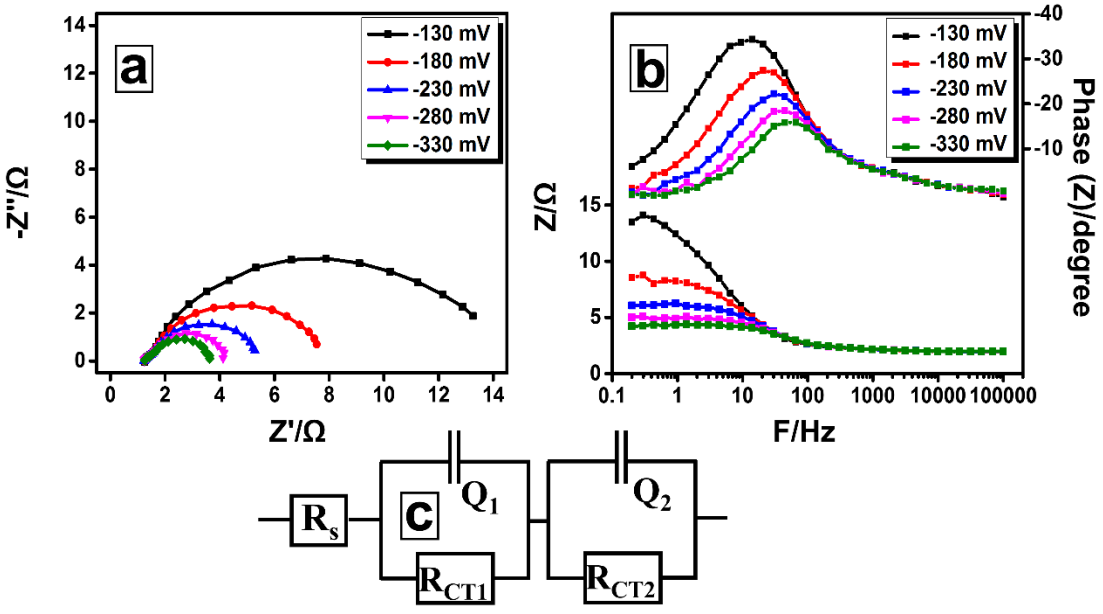

Figure 6.13 (a) Nyquist plot and the corresponding Bode phase angle plot (b) of Cu_2S-Ni_3S_2/NF towards the HER and (c) simulated EEC for the Nyquist plot.

To get a better insight into the HER kinetics EIS measurements are conducted in potentiostatic mode. Figure 6.13a-b portrays the recorded Nyquist plots and

corresponding Bode phase angle plots in the frequency range of 0.2 Hz to 100 kHz at different applied bias voltages Vs. RHE. The Nyquist plots of Cu_2S-Ni_3S_2/NF are two capacitive semicircles, of which the former being overpotential independent and associated with porosity of the electrodes. In addition, the declination of capacitive semicircular diameter with a variation of bias indicates the electrocatalytic processes are characterized by a single time constant, which validate HER as controlled charge-transfer process (Yang et al. 2016). Further, the Nyquist data are fit into EEC represented by $R_S(Q_1R_{CT1})(Q_2R_{CT2})$ (Figure 6.13c) and the EEC fitting parameters are tabulated in Table 6.4. The different EEC components include solution resistance (R_S), pseudocapacitances (Q_1, Q_2) and charge-transfer resistances (R_{CT1}, R_{CT2}). As evident from EEC fitting parameters, Cu_2S-Ni_3S_2/NF indicates the low R_S value of ~1.22 Ω, which is comparatively lower than Ni_3S_2/NF (~2.48 Ω) and bare NF (~3 Ω) (see APPENDIX XXI). On the other hand at the applied bias of -130 mV, Cu_2S-Ni_3S_2/NF demonstrates the charge-transfer resistance (R_{CT2}) of ~12.35 Ω, which is fairly lower than Ni_3S_2/NF (~17.3 Ω) and four-times lower than bare NF (~ 46 Ω). Furthermore, at higher bias (-330 mV), the charge-transfer resistance R_{CT2} of Cu_2S-Ni_3S_2/NF are as low as ~1.76 Ω, which is also comparatively lower than other recently reported electrocatalysts (Ma et al. 2019; Pan et al. 2015). In addition, the declination of total impedance and Bode phase angle (Figure 6.13b) at higher bias also indorse the superior HER. It may be anticipated that the in-situ formation of Cu_2S-Ni_3S_2 on NF favors rapid charge transport during the HER in alkaline environment. In addition, the value of Q_1 and R_{CT1} remain constant with the variation of bias, which is in accordance with the hypothesis of single time constant controlled electrocatalysis process.

Table 6.4. EEC fitting parameters of Cu_2S-Ni_3S_2/NF towards the HER.

Overpotential/mV	R_S/Ω	R_1/Ω	Q_1/mF	R_2/Ω	Q_2/mF
-130	1.234	0.102	0.432	12.35	7.902
-180	1.241	0.218	1.101	6.414	6.296
-230	1.228	0.330	5.351	3.893	4.841
-280	1.235	0.361	5.497	2.655	3.933
-330	1.241	0.511	6.399	1.768	2.643

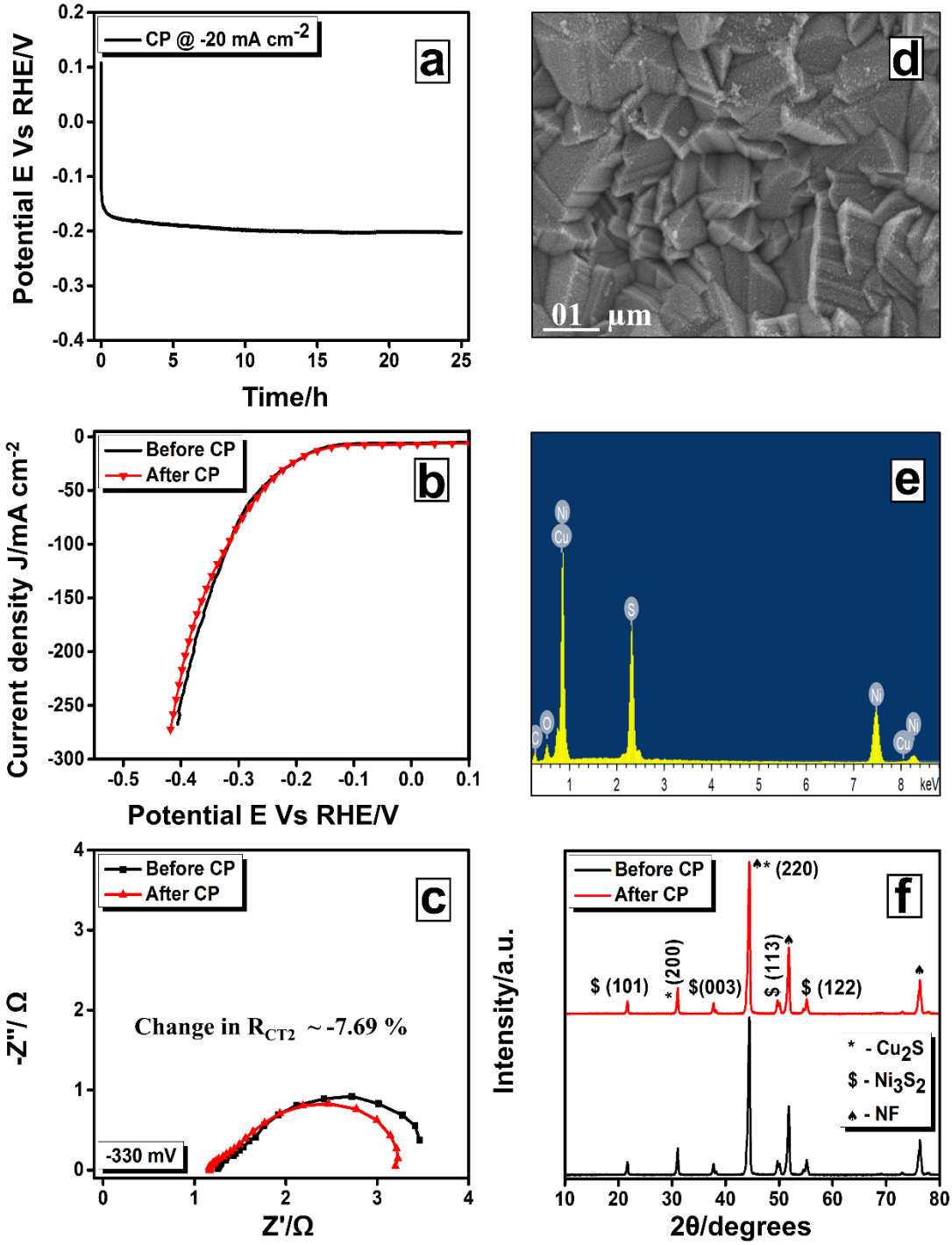

Figure 6.14 (a) Chronopotentiometric stability test of Cu_2S-Ni_3S_2/NF towards the HER at an applied current density of +20 mA cm^{-2} for 25 h, (b-c) LSV curves at a scan rate of 5 mV s^{-1} and Nyquist plot at an applied bias of 340 mV before and after chronopotentiometric stability test, (d) SEM micrograph, (e) EDS spectra and (f) comparison of XRD patterns of Cu_2S-Ni_3S_2/NF after chronopotentiometry.

The HER stability of Cu_2S-Ni_3S_2/NF was investigated through constant current chronopotentiometry. Figure 6.14a shows the chronopotentiometric curve at an applied current density of -20 mA cm^{-2} for 25 h. It is noteworthy that the overpotential achieved by Cu_2S-Ni_3S_2/NF for an applied current density 20 mA cm^{-2} remained almost constant, implying prominent stability and robustness. Moreover, the LSV curve after chronopotentiometry (Figure 6.14b) was very close to the initial one, without any noticeable difference in the overpotential or the current density. The Nyquist plot (at -330 mV) recorded after chronopotentiometry (Figure 6.14c) portrays the decrease in R_{CT2} by ~7.68 %, represents no-degradation in the HER after stability test. Furthermore, morphological, elemental and compositional analysis of Cu_2S-Ni_3S_2/NF were also conducted through FESEM, EDS and XRD post chronopotentiometric stability test. Morphology of Cu_2S-Ni_3S_2/NF as seen in Figure 6.14d portrays exact initial features, demonstrating excellent morphological stability under long-term operations. EDS measurements (Figure 6.14e) confirm the presence of only initial elements, while no other extra elements were detected. For a better understanding, weight percentages of Cu_2S-Ni_3S_2/NF before and after chronopotentiometric stability tests are provided in (Table 6.5) and the EDS color maps represent the homogeneous distribution of elements (see APPENDIX XXII). Furthermore, XRD pattern after chronopotentiometry (Figure 6.14f) also represents the initial peaks corresponding to Cu_2S-Ni_3S_2/NF with prominent retention of the phase and no loss of overall peak intensities, which further provisions Cu_2S-Ni_3S_2/NF are structurally stable enough in highly alkaline conditions for the HER.

Table 6.5. Weight percentages of all elements before and after stability test towards the HER.

Element	Before stability test	After stability test
O	2.08	3.65
C	1.37	1.52
Ni	76.2	76
Cu	2.16	2.13
S	18.19	16.7
Total	100	100

6.3.5.2 Oxygen evolution reaction (OER)

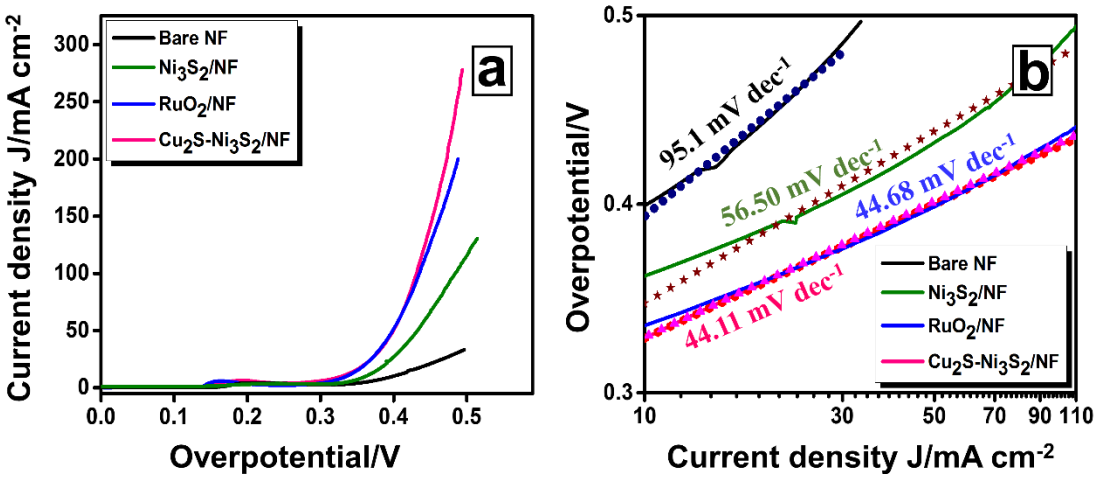

Figure 6.15 (a) iR compensated LSV curves at 5 mV s^{-1} scan rate and (b) Corresponding Tafel plot of bare NF, Ni_3S_2/NF, Cu_2S-Ni_3S_2/NF and RuO_2/NF towards the OER.

The electrocatalytic performance of the synthesized Cu_2S-Ni_3S_2/NF and Ni_3S_2/NF towards the OER was also measured in 1 M KOH solution. Figure 6.15a-b portrays the iR compensated LSV curves (at 5 mV s^{-1} scan rate) and the corresponding Tafel plots of Cu_2S-Ni_3S_2/NF, Ni_3S_2/NF, RuO_2/NF and bare NF, respectively. As expected, Cu_2S-Ni_3S_2/NF demonstrates the overpotential of 329 mV to drive the catalytic current density of 10 mA cm^{-2} (η_{10}). In addition, Cu_2S-Ni_3S_2/NF required the overpotentials of 431 mV and 473 mV to deliver a higher catalytic current density of 100 and 200 mA cm^{-2} (η_{100} and η_{200}), respectively. In contrast, RuO_2/NF displayed similar catalytic activity to deliver the catalytic current density of 10 mA cm^{-2}, while it required overpotential of 435 mV and 488 mV to deliver the higher catalytic current density of 100 and 200 mA cm^{-2} (η_{100} and η_{200}), respectively, demonstrating marginally inferior performance at higher overpotentials.

On the other hand, Ni_3S_2/NF and bare NF shown poor OER performance with a need of 362 mV and 399 mV, respectively, to approach the same benchmark current density of 10 mA cm^{-2}. These observations establish the fact that Cu_2S-Ni_3S_2/NF outperforms state-of-the-art RuO_2 electrocatalyst at high overpotentials. Furthermore the Tafel plots of Cu_2S-Ni_3S_2/NF and RuO_2/NF obtained by replotting the iR-corrected LSV curve overlap each other, signifying the comparable Tafel slope values of 44.11 mV dec^{-1} of

44.68 mV dec^{-1}, respectively. While, Ni_3S_2/NF and bare NF indicated the higher Tafel slope values of 56.50 mV dec^{-1} and 95.1 mV dec^{-1}, respectively. The lower slope values of Cu_2S-Ni_3S_2/NF suggest faster electron transfer kinetics, which is favorable for the OER. In addition, the OER parameters of Cu_2S-Ni_3S_2/NF are compared with recently reported sulfide-based OER electrocatalysts as provided in Table 6.6.

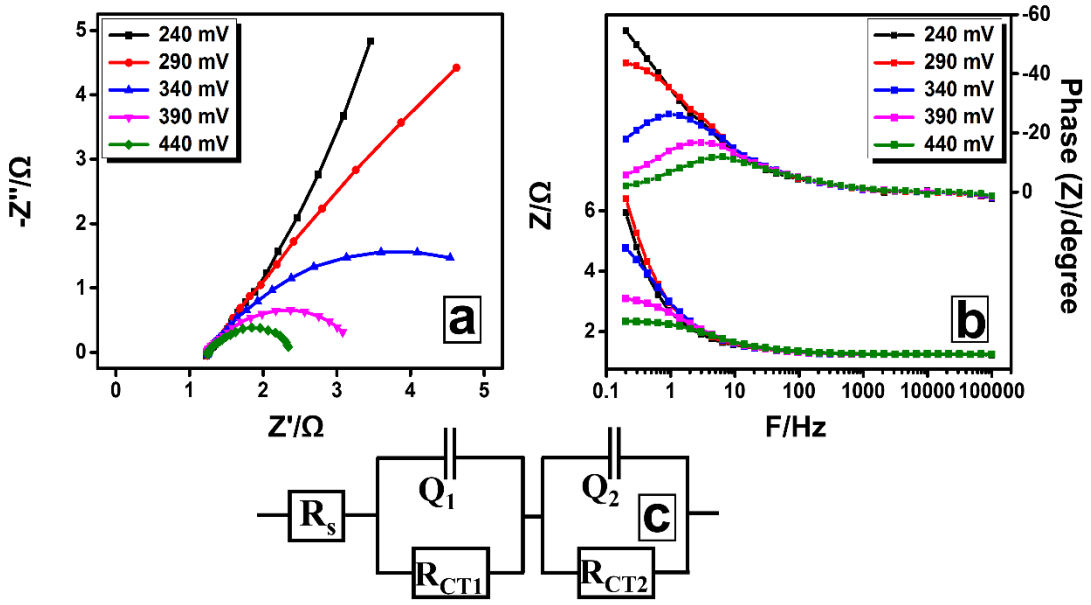

Figure 6.16 (a) Nyquist plots and the corresponding Bode phase angle plots (b) of Cu_2S-Ni_3S_2/NF towards the OER and (c) simulated EEC for the Nyquist plot.

Further, EIS measurements were performed on Cu_2S-Ni_3S_2/NF towards the OER in a same way as discussed for the HER. Figure 6.16a-b represents the recorded Nyquist plots and corresponding Bode phase angle plots in the frequency range of 0.2 Hz to 100 kHz at different applied bias voltages.

The Nyquist plots could fit into EEC represented as $R_S(Q_1R_{CT1})(Q_2R_{CT2})$ (Figure 6.16c) and the EEC fitting parameters are tabulated in Table 6.7. At an applied bias of 240 mV, Cu_2 S/NF portrays the R_S of ~1.23 Ω and R_{CT2} of ~25.86 Ω, which is about ~5 times lower than Ni_3S_2/NF (R_S = ~ 2.24 Ω, R_{CT2} = ~ 122.7 Ω) and about ~14 times lower than bare NF (R_S = ~3 Ω, R_{CT2} = ~350 Ω) (see APPENDIX XXI) at the same bias. In addition at the higher bias of 440 mV, Cu_2S-Ni_3S_2/NF demonstrates the very-low charge-transfer resistance R_{CT2} of ~0.99 Ω, which further provisions the superior OER than recently reported electrocatalysts (Yuan et al. 2017; Zhang et al. 2019b). In

addition, the phase angle shift towards higher frequencies at the higher applied bias demonstrates faster kinetics (Ojha et al. 2017).

Table 6.6. Comparison of the alkaline OER activities of Cu_2S-Ni_3S_2/NF over other nickel and copper sulfides as reported in the literature.

Catalyst	Overpotential/mV	Tafel slope	Reference
$Cu_{1-x}Ni_xS$/NF	350 @ 20 mA cm^{-2}	132.1 mV dec^{-1}	(Li et al. 2019)
Cu_2S@CF	345 @ 20 mA cm^{-2}	80 mV dec^{-1}	(Ma et al. 2019)
MoS_2/Ni_3S_2	218 @ 10 mA cm^{-2}	88 mV dec^{-1}	(Zhang et al. 2016)
$CoSx/Ni_3S_2$@NF	280 @ 20 mA cm^{-2}	105.4 mV dec^{-1}	(Shit et al. 2018)
Fe-Ni_3S_2	253 @ 100 mA cm^{-2}	65.5 mV dec^{-1}	(Cheng et al. 2015)
Cu_2S-Ni_3S_2/NF	329 @ 10 mA cm^{-2}	44.11 mV dec^{-1}	Present work

Table 6.7. EEC fitting parameters of Cu_2S-Ni_3S_2/NF towards the OER.

Overpotential/mV	R_S/Ω	R_1/Ω	Q_1/F	R_2/Ω	Q_2/F
240	1.236	0.028	0.289	25.86	0.263
290	1.242	0.051	0.067	43.37	0.144
340	1.245	0.091	0.068	4.944	0.133
390	1.247	0.101	0.045	1.94	0.093
440	1.254	0.143	0.041	0.99	0.078

Chronopotentiometric stability curve of Cu_2S-Ni_3S_2/NF is recorded at an applied current density of +20 mA cm^{-2} for 25 h. As evident from Figure 6.17a, the continuous evolution of oxygen with a small deviation in potential (~ +3.49 mV @ 25 h) was observed, demonstrating the promising stability. Furthermore, LSV curve recorded after the chronopotentiometry could retrace the initial LSV curve as represented in Figure 6.17b, while the overall catalytic current density was decreased by about ~19.4 %. The Nyquist plot (Figure 6.17c) recorded (at 340 mV) after the chronopotentiometry specify a marginal increment in the R_S from ~1.25 Ω to ~1.62 Ω, while the R_{CT2} remained unchanged.

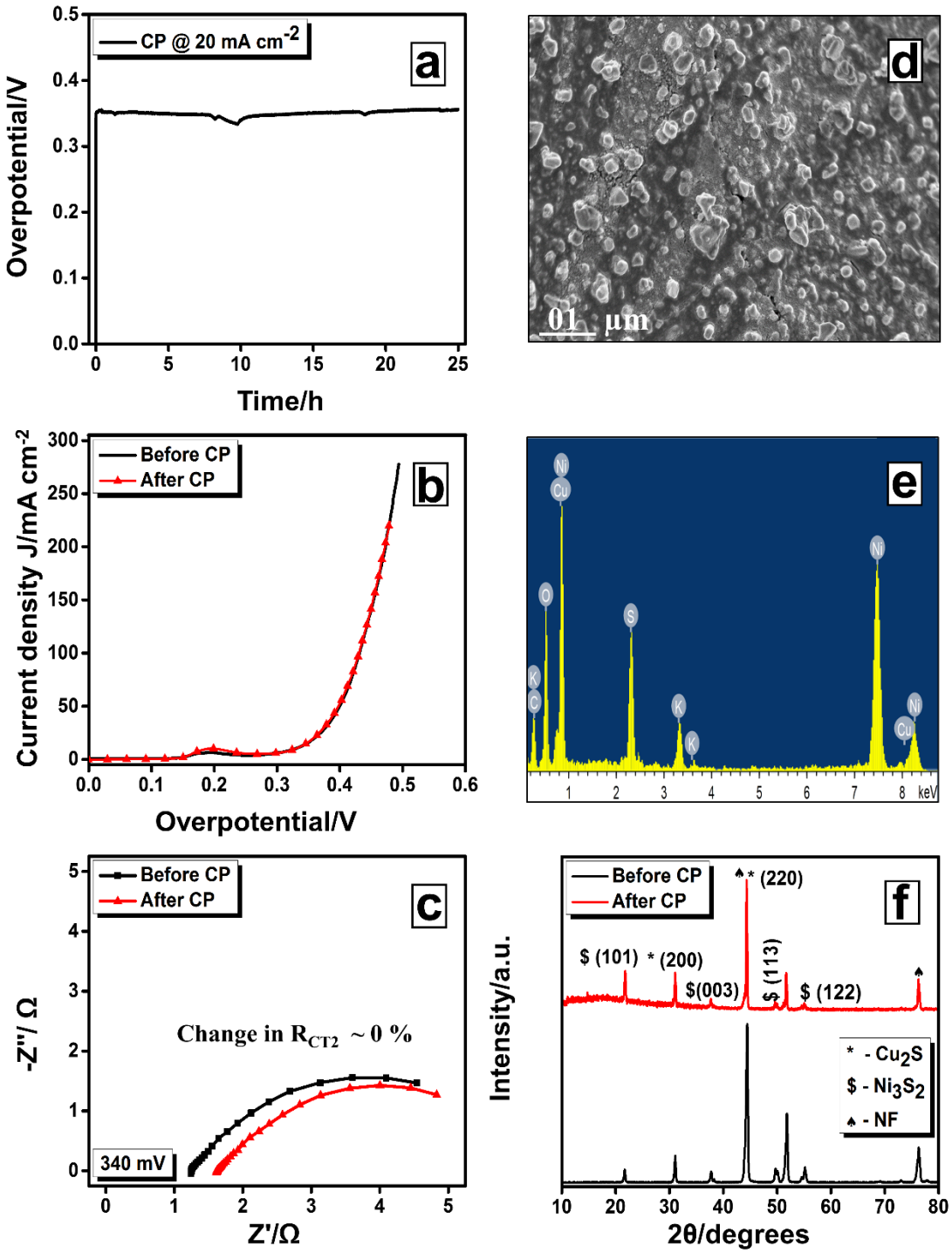

Figure 6.17 (a) Chronopotentiometric stability test of Cu_2S-Ni_3S_2/NF towards the OER at an applied current density of +20 mA cm^{-2} for 25 h, (b-c) LSV curves at a scan rate of 5 mV s^{-1} and Nyquist plot at an applied bias of 340 mV before and after chronopotentiometric stability test, (d) SEM micrograph, (e) EDS spectra and (f) comparison of XRD patterns of Cu_2S-Ni_3S_2/NF after chronopotentiometry.

The increment in the catalyst/electrolyte resistance was further investigated through morphological, elemental and compositional analysis using FESEM, EDS and XRD measurements. Surprisingly, FESEM surface morphology after chronopotentiometry as seen in Figure 6.17d reveal the formation of micro granule-like structures, which may be possibly attributed to the incorporation/doping of potassium (K ions) as inspected from EDS measurements (Figure 6.17e). The presence of potassium moieties could be due to the prolonged chronopotentiometry performed in potassium hydroxide solution. In addition, weight percentages of Cu_2S-Ni_3S_2/NF before and after chronopotentiometric stability test are provided in (Table 6.8) and the EDS color maps represent the homogeneous distribution of elements (see APPENDIX XXIII). In addition, XRD pattern after the chronopotentiometry (Figure 6.17f) also indicate the initial peaks with a minimal loss of overall intensities, suggesting the marginal degradation of the Cu_2S-Ni_3S_2/NF catalyst under long-term operations.

Table 6.8. Weight percentages of all elements before and after stability test towards the OER.

Element	Before stability test	After stability test
O	1.97	6.1
C	1.35	1.36
K	0	4.8
Ni	75.9	71.17
Cu	2.15	1.97
S	18.63	14.6
Total	100	100

Furthermore, to better understand the catalytic performances, it is necessary to evaluate the ECSA by measuring their double-layer capacitances (C_{dl}) values. The CV curves at different scan rates (10, 20, 40, 80, 160, 320 and 640 mV s^{-1}) were recorded in the potential window range of -0.1 – +0.2 V Vs. SCE as displayed in (see APPENDIX XXIV). Herein, the current response is obviously due to the charging of the double-layer and no Faradaic reaction takes place. Further the plot of difference in double-layer

charging current densities ($\Delta j = j_a - j_c$) Vs. scan rate (Figure 6.18) derives the $2C_{dl}$ value, which is related to the ECSA by definition. The measured $2C_{dl}$ values are 1.88 mF cm^{-2}, 4.36 mF cm^{-2} and 7.29 mF cm^{-2} for bare NF, Ni_3S_2/NF and Cu_2S-Ni_3S_2/NF, respectively. These results indicate the greater active sites and much higher surface roughness of Cu_2S-Ni_3S_2/NF, which further comprehends their superior catalytic activity.

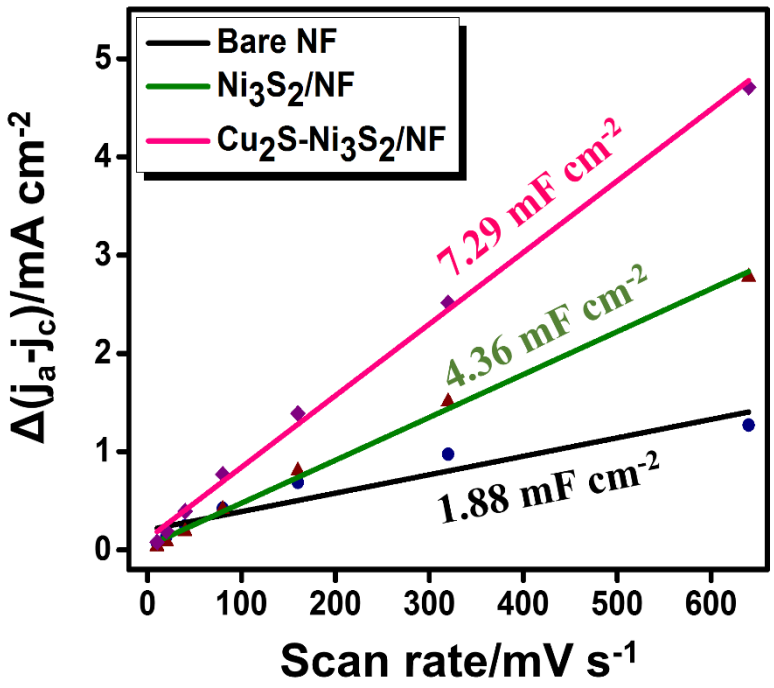

Figure 6.18 Plot of the difference in double-layer charging current densities ($\Delta j = j_a - j_c$) Vs. scan rate of bare NF, Ni_3S_2/NF, Cu_2S-Ni_3S_2/NF for the estimation of ECSA.

6.3.5.3 Symmetrical overall water-splitting

Considering the excellent electrochemical performances of Cu_2S-Ni_3S_2/NF towards the HER and OER, it is essential to study the overall water-splitting characteristics, which is close to the real-scale commercial applications. Two identical samples of Cu_2S-Ni_3S_2/NF were directly used as cathode and anode (in symmetrical configuration) using 1 M KOH as an electrolyte for overall water-splitting measurements. Figure 6.19a demonstrate the non-iR compensated LSV curves at a scan rate of 5 mV s^{-1}, recorded in the voltage range of 0 to 2.5 V. The LSV curve of Cu_2S-Ni_3S_2/NF || Cu_2S-Ni_3S_2/NF electrodes indicate the cell-voltage of ~1.77 V to deliver the catalytic current density of

10 mA cm^{-2}, which was significantly lower than Ni_3S_2/NF || Ni_3S_2/NF (1.85 V) and bare NF || bare NF (1.93 V). On the other hand, Cu_2S-Ni_3S_2/NF || Cu_2S-Ni_3S_2/NF symmetrical cell required the cell-voltages of 1.87 V, 2.08 V and 2.32 V to deliver the higher catalytic current density of 20, 50 and 100 mA cm^{-2}, respectively. Further, chronopotentiometric stability test was carried out for the same set of electrodes at an applied current density of 20 mA cm^{-2} for 100 h. As evident from Figure 6.19b, Cu_2S-Ni_3S_2/NF || Cu_2S-Ni_3S_2/NF electrodes could retain the cell-voltage of 1.87 V without major fluctuations over the duration of stability test. In addition, the LSV curve (inset of Figure 6.19b) after the stability test of 100 h is very close to the initial LSV curve, further promotes their promising stability. In addition, the overall water-splitting parameters of Cu_2S-Ni_3S_2/NF are compared with recently reported overall water-splitting electrocatalysts as provided in Table 6.9.

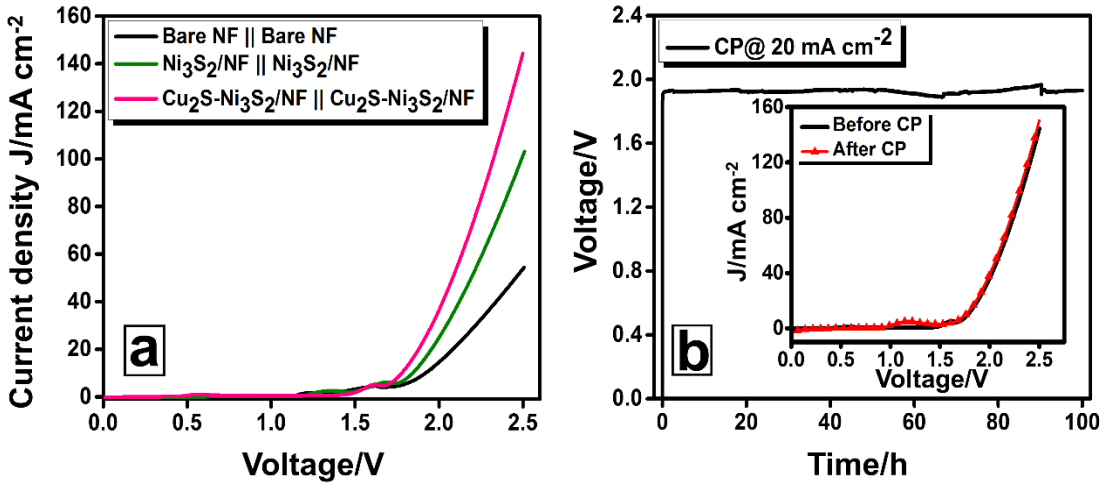

Figure 6.19 (a) non-iR compensated LSV curves at 5 mV s^{-1} scan rate of bare NF || bare NF, Ni_3S_2/NF || Ni_3S_2/NF and Cu_2S-Ni_3S_2/NF || Cu_2S-Ni_3S_2/NF symmetrical electrodes towards overall water-splitting, (b) chronopotentiometric stability test of Cu_2S-Ni_3S_2/NF || Cu_2S-Ni_3S_2/NF electrodes at an applied current density of +20 mA cm^{-2} for 100 h and the inset of (b) represents the non-iR corrected LSV curve of Cu_2S-Ni_3S_2/NF || Cu_2S-Ni_3S_2/NF electrodes before and after stability test.

Table 6.9. Comparison of catalytic activities of Cu_2S-Ni_3S_2/NF towards overall water-splitting.

Material	Potential/V	Stability	Reference
NiS/Ni foam	1.64 @ 10 mA cm^{-2}	~ 35 h	(Zhu et al. 2016)
Ni_3S_2/NF	1.68 @ 10 mA cm^{-2}	~ 14 h	(Ren et al. 2018)
Cu_2S@Cu	1.84 @ 10 mA cm^{-2}	> 25 h	(Ma et al. 2019)
CoS_x/Ni_3S_2@NF	1.572 @ 10 mA cm^{-2}	~ 30 h	(Shit et al. 2018)
$Ni(OH)_2$/NF	1.82 @ 10 mA cm^{-2}	-	(Luo et al. 2014)
Ni_5P_4	1.7 @ 10 mA cm^{-2}	-	(Ledendecker et al. 2015)
NiO-Ni_3S_2	1.57 @ 10 mA cm^{-2}	50 h	(Peng et al. 2019)
Ni_3S_2	2 @ 10 mA cm^{-2}	200 h	(Ho et al. 2018)
Cu_2S-Ni_3S_2/NF	1.77 @ 10 mA cm^{-2}	100 h	Present work

6.4 SUMMARY

In summary, Cu_2S micro-hexagons were successfully synthesized via a hydrothermal method and used as an electrocatalyst for the HER in both basic and acidic solutions, corresponding to the extreme pH values of 14 and 0, respectively. In addition, the Cu_2S micro-hexagons are also complimented with their long-term stability of 24 h as evident from chronopotentiometric measurements. Therefore, Cu_2S micro-hexagons could be a promising and effective electrocatalyst for water-splitting applications.

On the other hand, a new strategy to fabricate Cu_2S-Ni_3S_2/NF electrodes via a hydrothermal method was demonstrated. The as-prepared Cu_2S-Ni_3S_2/NF demonstrate promising electrocatalytic activity for both HER and OER and also complemented with persistent stability in alkaline medium. Moreover, Cu_2S-Ni_3S_2/NF symmetrical electrodes for overall water-splitting required the cell voltage of 1.77 V to deliver 10 mA cm^{-2}, demonstrating excellent durability under long-term operations. Synergistic factors such as rational design, binder-free approach, improved electronic conductivity and material hybridization favored the bifunctional and overall water-splitting performances of Cu_2S-Ni_3S_2/NF electrodes. These imperious findings open up new possibilities for the synthesis and demonstration of earth-abundant electrocatalysts for the production of sustainable energy.

CHAPTER 7

CONCLUSIONS AND FUTURE DIRECTIONS

7.1 SUMMARY AND CONCLUSIONS

In the present thesis work, hydrothermal method was employed for the synthesis of different transition metal chalcogenide nanostructures. The synthesis parameters influenced the physiochemical and electrochemical performance of transition metal chalcogenides.

- Anion-exchange reaction of $Co(OH)_2$ nanosheets with Te/Se resulted in the formation of $CoTe_2$ and $CoSe_2$ nanostructures, respectively. Of which, $CoSe_2$ exactly replicated the nanostructure morphology of precursor hydroxide. While, $CoTe_2$ indicated their formation in mixed morphologies mainly consisting of nanorods along with some nanoparticles. Synergistic factors such as 2D nanoporous layer formation, good electronic conductivity and shorter diffusion paths for ion exchange enabled the $CoSe_2$ electrode to exhibit an excellent specific capacitance value of 951 F g^{-1}, which was three times higher in comparison to $CoTe_2$ electrode (360 F g^{-1}).
- Anion-exchange reaction of $Ni(OH)_2$ nanosheets with Te/Se resulted in the formation of mixed phase $NiTe/NiTe_2$ and pure phase $NiSe_2$ nanosheets, respectively. Electrocatalytic measurements of $NiTe/NiTe_2$ towards the HER and OER revealed their promising electrocatalytic activities.
- NiSe nanoflakes were obtained by the direct selenization of nickel surface. HER performance was comparable to state-of-the-art Pt/C catalyst. The superior performance of NiSe nanoflakes is attributed to the morphological evolution of NiSe as vertically aligned nanoflakes on conductive Ni foam framework, which expose more edge active sites for the HER.
- Series of molybdenum dichalcogenide nanostructures MoX_2 (X = S, Se, Te) were prepared employing hydrothermal method. FESEM investigations indicate nanograins, nanoflowers and nanotubes morphology of MoS_2, $MoSe_2$ and $MoTe_2$, respectively. Further, electrocatalytic HER measurements rank these catalysts in the order $MoSe_2$>MoS_2>$MoTe_2$. Besides other factors influencing the HER, best performance of $MoSe_2$ is attributed to their predominant electronic conductivity.

- Tungsten (W)-doping was employed to enhance the specific capacitance of $MoSe_2$ nanostructures. Doping concentration dependent analysis indicate 2 M % of tungsten (W) as an optimum doping amount. Further, addition of graphene oxide during the hydrothermal synthesis of W2-$MoSe_2$ indicated the formation of W2-$MoSe_2$/G nanostructures and in-situ reduction of graphene oxide. Synergistic factors such as high specific surface area, porosity and electronic conductivity enabled W2-$MoSe_2$/G electrodes to deliver the specific capacitance of 248 F g^{-1}, which is about ~2.4 and ~1.4 times higher in comparison to pristine $MoSe_2$ and W2-$MoSe_2$ electrodes. The higher values of specific capacitances are complimented with an excellent capacitance retention of 102 % for 20000 cycles.
- Cu_2S micro-hexagons were successfully synthesized via a hydrothermal method and used as an electrocatalyst for the HER in both basic and acidic solutions, corresponding to the extreme pH values of 14 and 0, respectively. In addition, the Cu_2S micro-hexagons are complimented with their long-term stability of 24 h as evident from chronopotentiometric measurements.
- A new synthesis strategy to fabricate copper sulfide-nickel sulfide (Cu_2S-Ni_3S_2) arrays on three-dimensional nickel foam was demonstrated. The as-prepared Cu_2S-Ni_3S_2/NF revealed promising electrocatalytic activity for the both HER and OER. Moreover, Cu_2S-Ni_3S_2/NF symmetrical electrodes for overall water-splitting required the cell voltage of 1.77 V to deliver 10 mA cm^{-2} current density and demonstrating excellent durability (100 hours) under long-term operations. Synergistic factors such as rational design, binder-free approach, improved electronic conductivity and material hybridization favored the bifunctional and overall water-splitting performance of Cu_2S-Ni_3S_2/NF electrodes.

7.2 SCOPE FOR THE FUTURE WORK

The investigations of the present research work can be extended further in the following directions:

- Systematic investigations of both theory and experiments are required to optimize the design of nanostructured TMCs. Computational calculations such as density function theory (DFT) are necessary for the design and synthesis/fabrication of the electrodes. In addition, it may also be required to play with different control

parameters such as, choice of substrate, reaction temperature, the concentration of precursors and reducing agents, use of different capping agents/stabilizers, etc., which define the electrochemical performance of the prepared nanostructures.

- The supercapacitor performance parameters such as, specific capacitance and cycle-life may be improved by the incorporation of different carbonaceous material such as, activated carbons, carbon nanostructures and conducting polymers. Further, electrochemical performance of the electrodes could be measured by using them as anode and cathode in two-electrode (symmetric or asymmetric) configurations, instead of conventional three-electrode measurements.
- Research efforts may also be focussed on optimization of the active sites of electrocatalysts by various measures such as, compositing with carbon-based materials, doping, etc. Heteroatom doped carbonaceous materials feature unique properties, demonstrate the promising potential for water-splitting reactions owing to their abundant active sites, strong tolerance to acid/alkaline conditions and controllable molecular structures. Finally, as solar energy is an abundant and renewable energy resource, it would be of great interest to integrate overall water-splitting cells with solar energy devices for sustainable hydrogen production.

.

APPENDIX

APPENDIX I: SAED patterns of $Co(OH)_2$, $CoTe_2$ and $CoSe_2$ nanostructures.

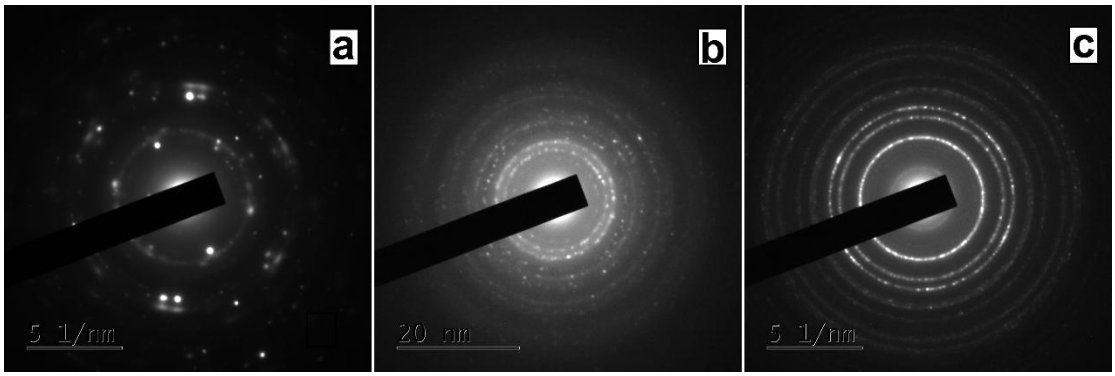

Figure I SAED patterns of $Co(OH)_2$, $CoTe_2$ and $CoSe_2$ nanostructures

APPENDIX II: BJH pore size measurements of $CoTe_2$ and $CoSe_2$ nanostructures.

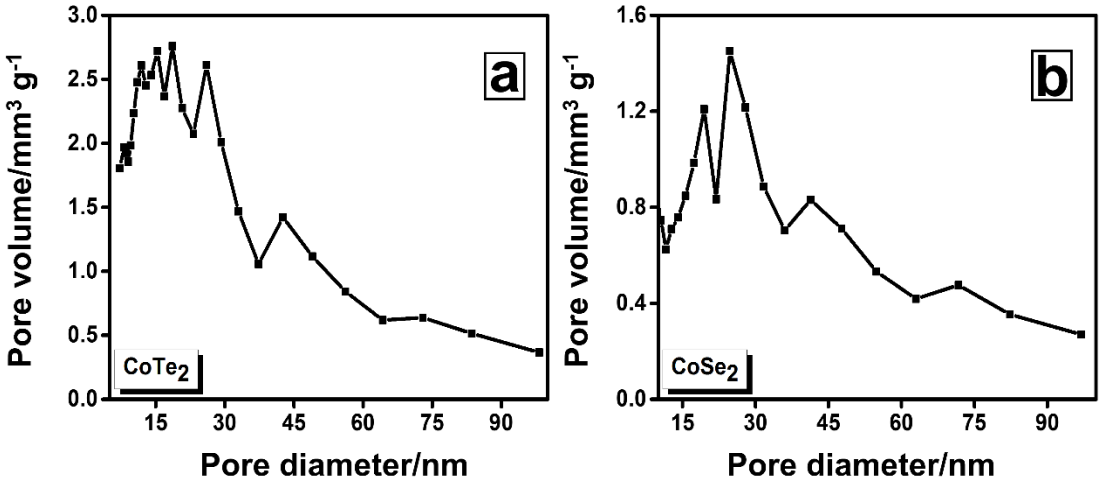

Figure II BJH pore size measurements of (a) $CoTe_2$ and (b) $CoSe_2$ nanostructures.

APPENDIX III: CV curves and cycle life of $Co(OH)_2$ electrodes.

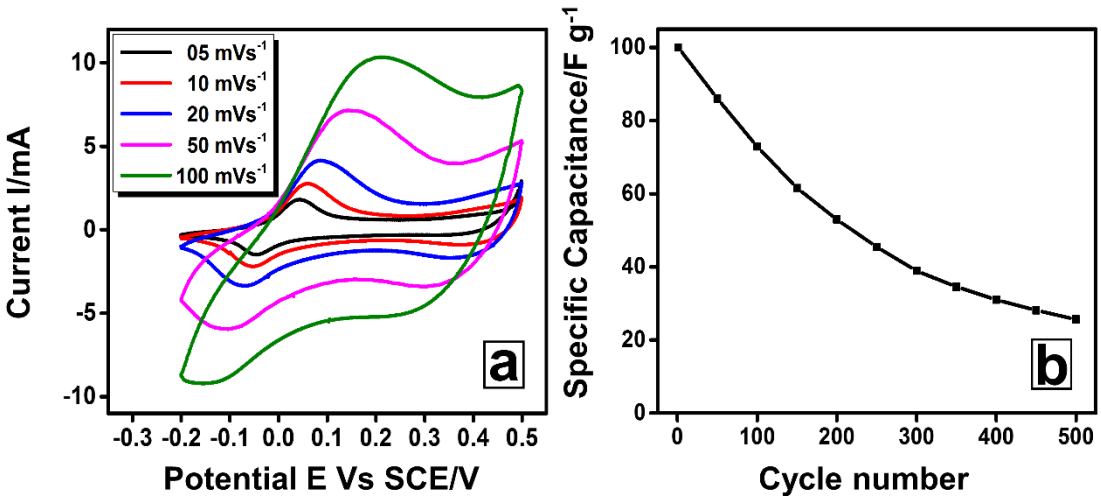

Figure III (a) Cyclic voltammograms of $Co(OH)_2$ electrode at different scan rates and (b) Cyclic stability of the electrode fabricated using $Co(OH)_2$ nanosheets at a scan rate of 50 mVs^{-1} for 500 CV cycles.

APPENDIX IV: SAED patterns of $Ni(OH)_2$, $NiTe/Te_2$, $NiSe_2$ and NiSe nanostructures.

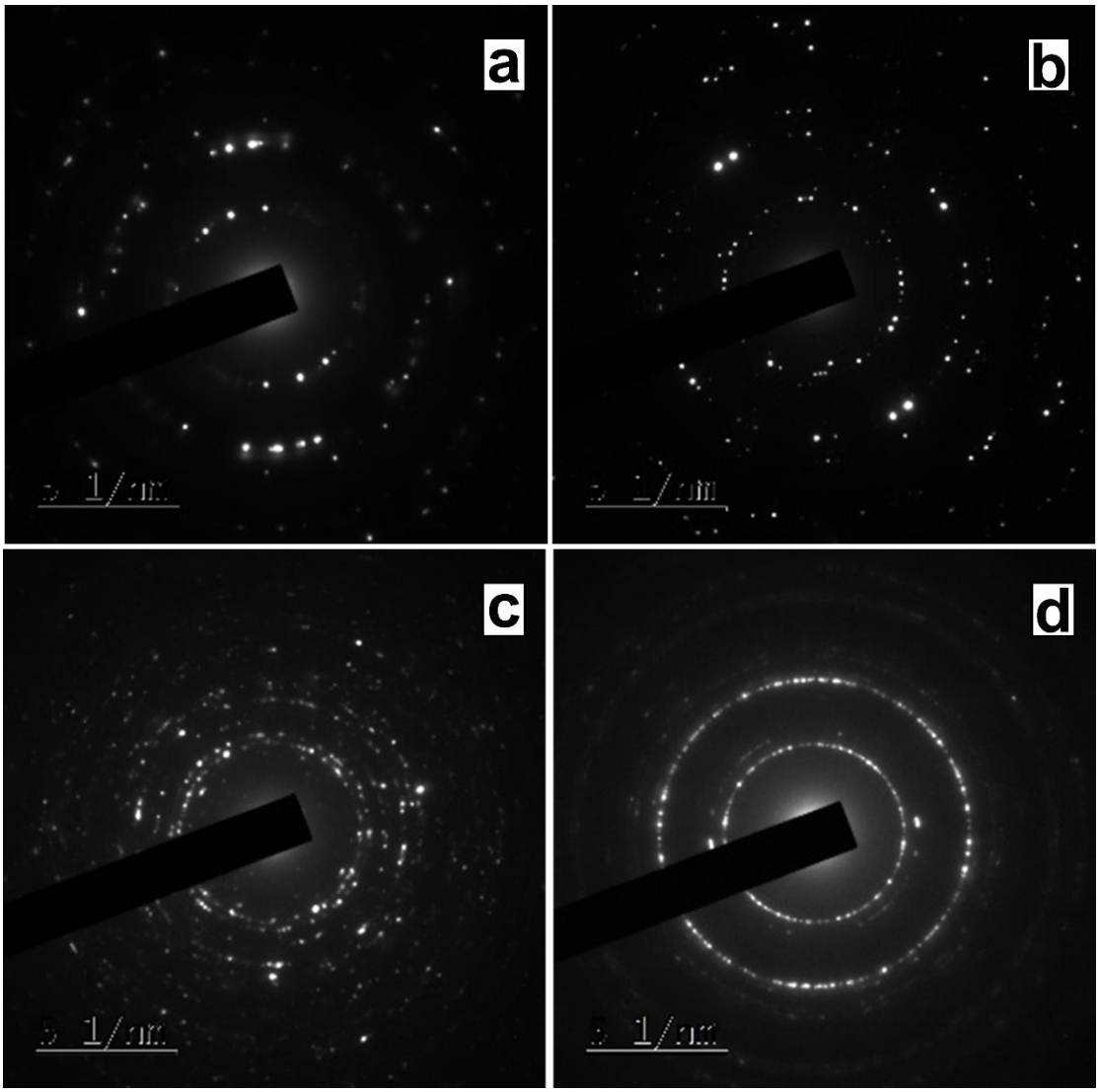

Figure IV SAED patterns of (a) $Ni(OH)_2$ nanosheets, (b) $NiTe/Te_2$ nanosheets, (c) $NiSe_2$ nanosheets and (d) NiSe nanoflakes, respectively.

APPENDIX V: BJH pore size and BET surface area of $NiTe/NiTe_2$ nanosheets.

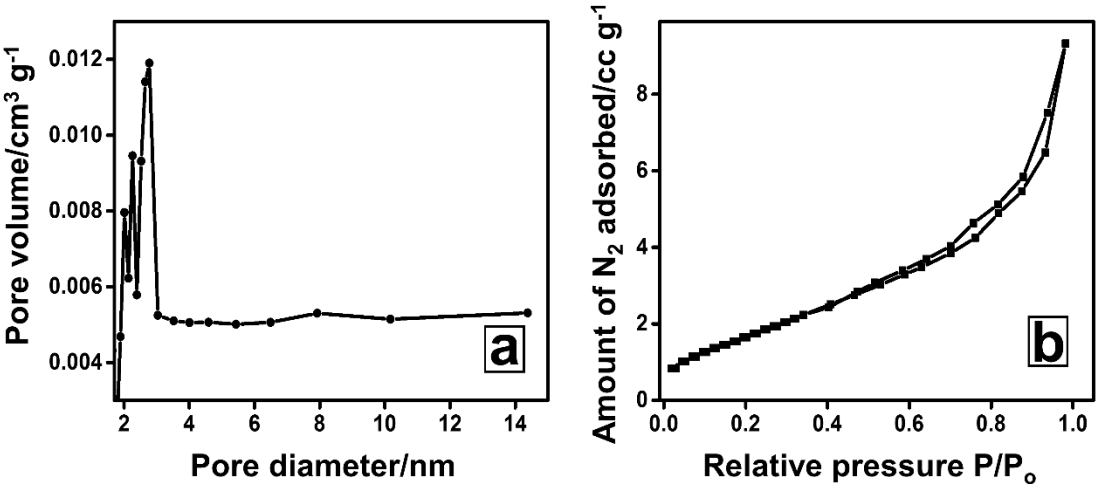

Figure V (a) BJH pore size measurements and N_2 adsorption desorption isotherm of $NiTe/NiTe_2$ nanosheets.

APPENDIX VI: Comparison of LSV curves with substrates.

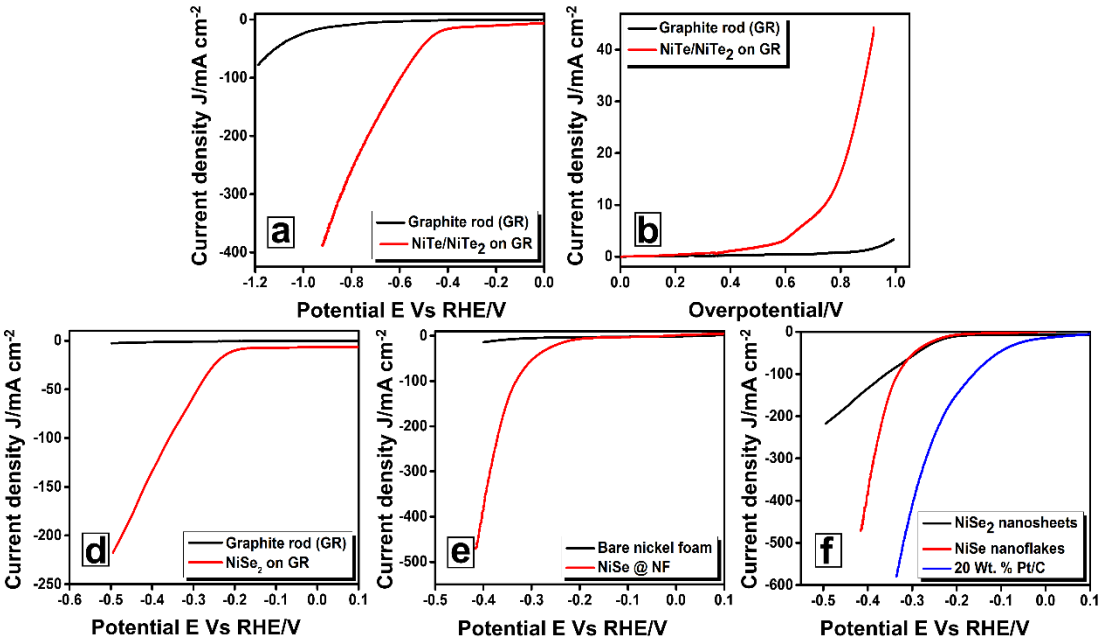

Figure VI. Comparison of iR compensated LSV curves of $NiTe/NiTe_2$ nanosheets and graphite rod substrate towards the HER (a) and OER (b), comparison of iR compensated LSV curves of (c) $NiSe_2$ nanosheets and (d) NiSe nanoflakes with substrates graphite rod and bare NF, respectively and (e) comparison of iR compensated LSV curves of $NiSe_2$ nanosheets and NiSe nanoflakes with state-of-the-art Pt/C catalyst at 5 mV s^{-1} scan rate.

APPENDIX VII: Comparison of HER performance of $NiSe_2$ nanosheets and NiSe nanoflakes.

Table A1. Comparison of catalytic activities different nickel selenides towards the HER in contrast to hydrothermal synthesis time as available in the literature.

Catalyst	Potential (mV)	Synthesis time	Tafel slope	Reference
$NiSe_2$	156 @ 10 mA cm^{-2}	16 h	54 mV dec^{-1}	(Ge et al. 2017)
Ni_3Se_2	203 @ 10 mA cm^{-2}	5 h	118 mV dec^{-1}	(Xu et al. 2016)
$NiSe_2$ NW	145 @ 10 mA cm^{-2}	12 h	41 mV dec^{-1}	(Tang et al. 2016)
$NiSe_2$	200 @ 40 mA cm^{-2}	24 h	29.4 mV dec^{-1}	(Yu et al. 2017)
$NiSe_2$ NS	198 @ 10 mA cm^{-2}	15 h	72.1 mV dec^{-1}	This work
NiSe NF	217 @ 10 mA cm^{-2}	2 h	28.6 mV dec^{-1}	This work

APPENDIX VIII: Estimation of ECSA from CV curves of $NiSe_2$ nanosheets and NiSe nanoflakes.

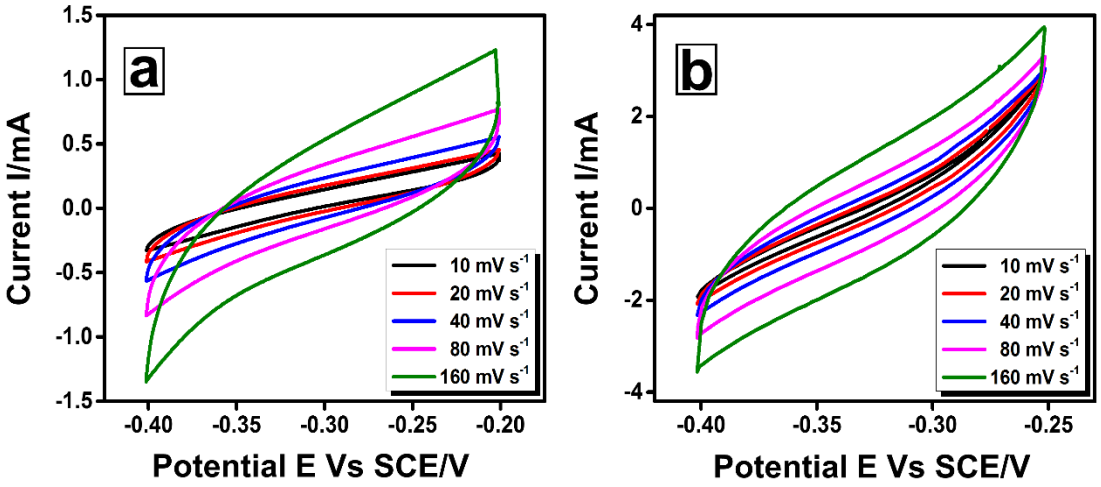

Figure VIII. CV curves (a) $NiSe_2$ nanosheets and (b) NiSe nanoflakes at different scan rates of in the double layer charging region for the estimation of ECSA.

APPENDIX IX: SEM images of MoX_2 nanostructures for EDS measurements and their elemental maps and the weight percentages estimated form EDS.

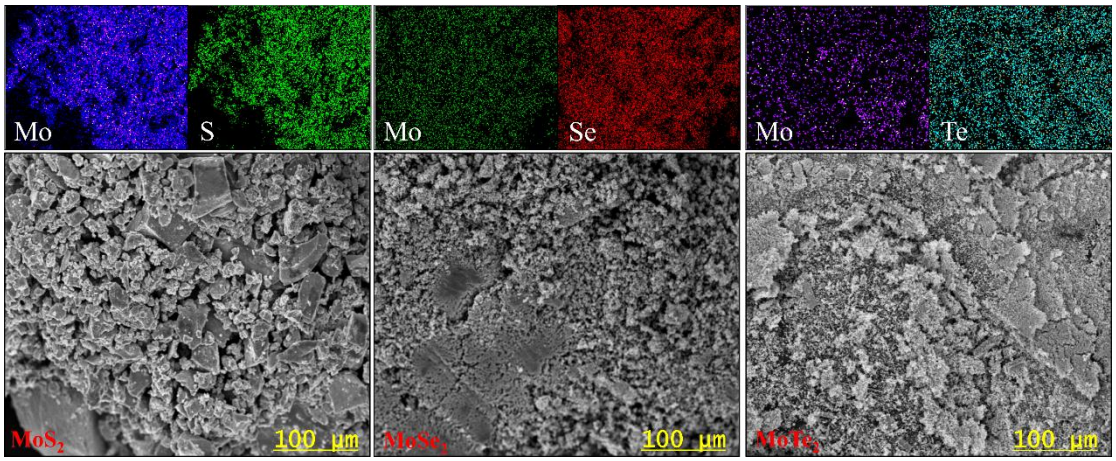

Figure IX. Elemental maps and SEM images wherein EDS measurements are performed for MoS_2 nanograins, $MoSe_2$ nanoflowers and $MoTe_2$ nanotubes.

Table A2. Weight percentages of all the elements in MoS_2 nanograins, $MoSe_2$ nanoflowers and $MoTe_2$ nanotubes.

MoS_2 nanograins		**$MoSe_2$ nanoflowers**		**$MoTe_2$ nanotubes**	
Element	**Weight percentage/%**	**Element**	**Weight percentage/%**	**Element**	**Weight percentage/%**
O	12.47	O	10.94	O	10.82
C	5.29	C	4.11	C	4.06
Mo	27.40	Mo	28.03	Mo	18.46
S	54.84	Se	56.92	Te	66.66

APPENDIX X: Estimation of ECSA from CV curves and BJH plots for MoX_2 nanostructures.

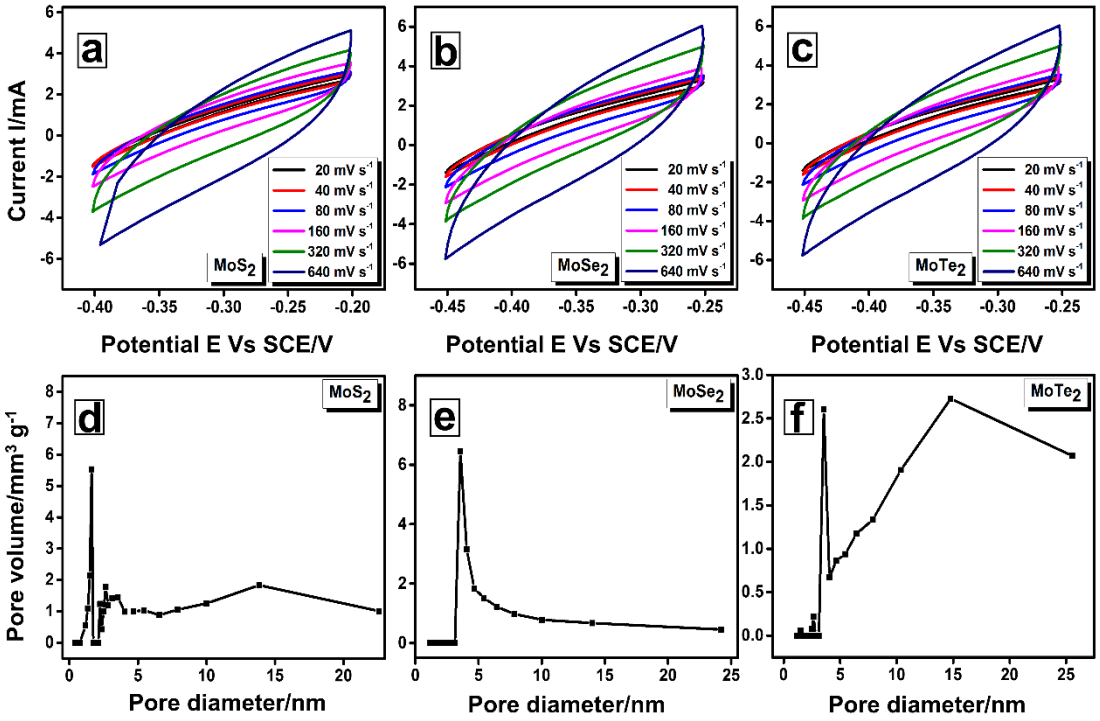

Figure X. CV curves at different scan rates of in the double layer charging region for the estimation of ECSA and BJH pore size measurement plots of MoS_2 nanograins (a, d), $MoSe_2$ nanoflowers (b, e) and $MoTe_2$ nanotubes (c, f), respectively.

APPENDIX XI: Nyquist plot of $MoTe_2$ nanotubes at lower bias.

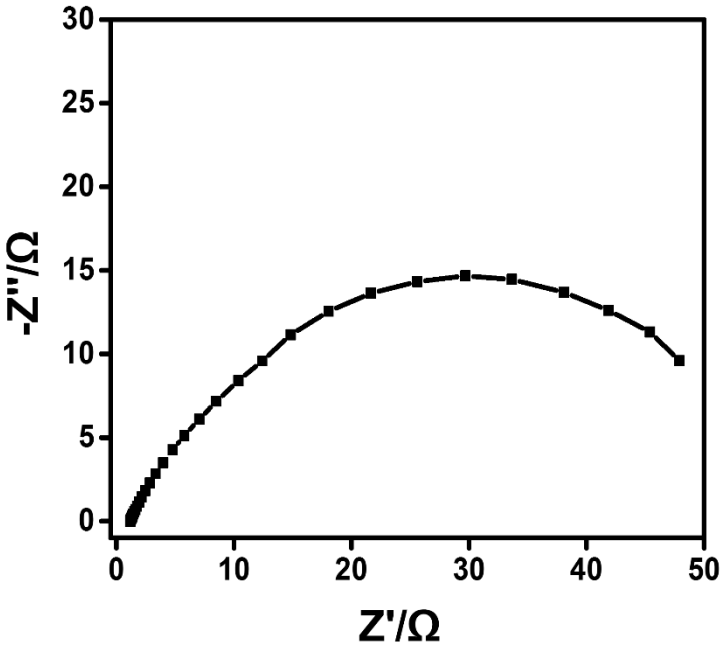

Figure XI. Nyquist plot of $MoTe_2$ nanotubes at -155 mV bias.

APPENDIX XII: XRD plot and EDS measurements of W3-$MoSe_2$ nanostructures.

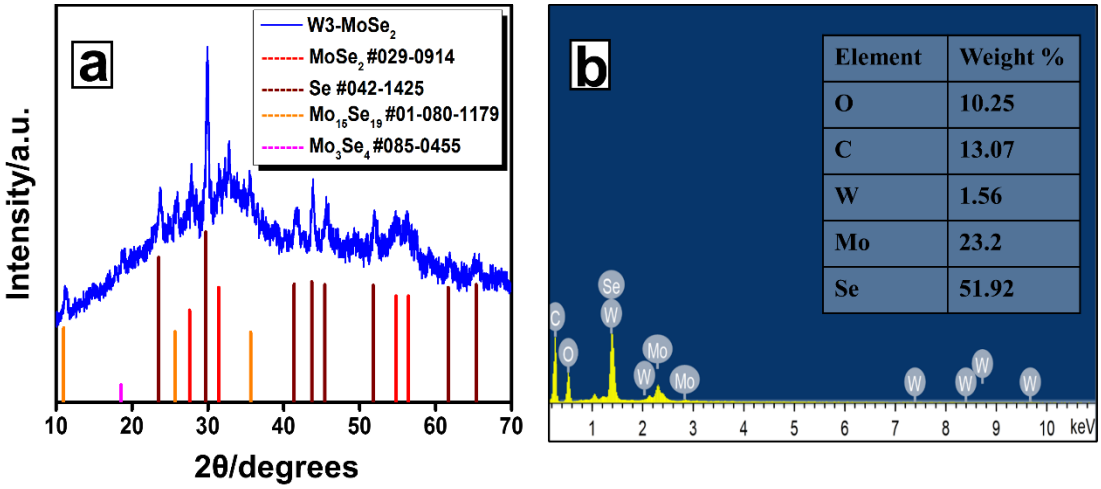

Figure XII. (a) XRD plot of W3-$MoSe_2$ nanostructures in comparison with standard JCPDS cards and (b) EDS spectra of W3-$MoSe_2$ nanostructures and their weight percentages.

APPENDIX XIII: Elemental color maps of W2-$MoSe_2$/G nanostructures.

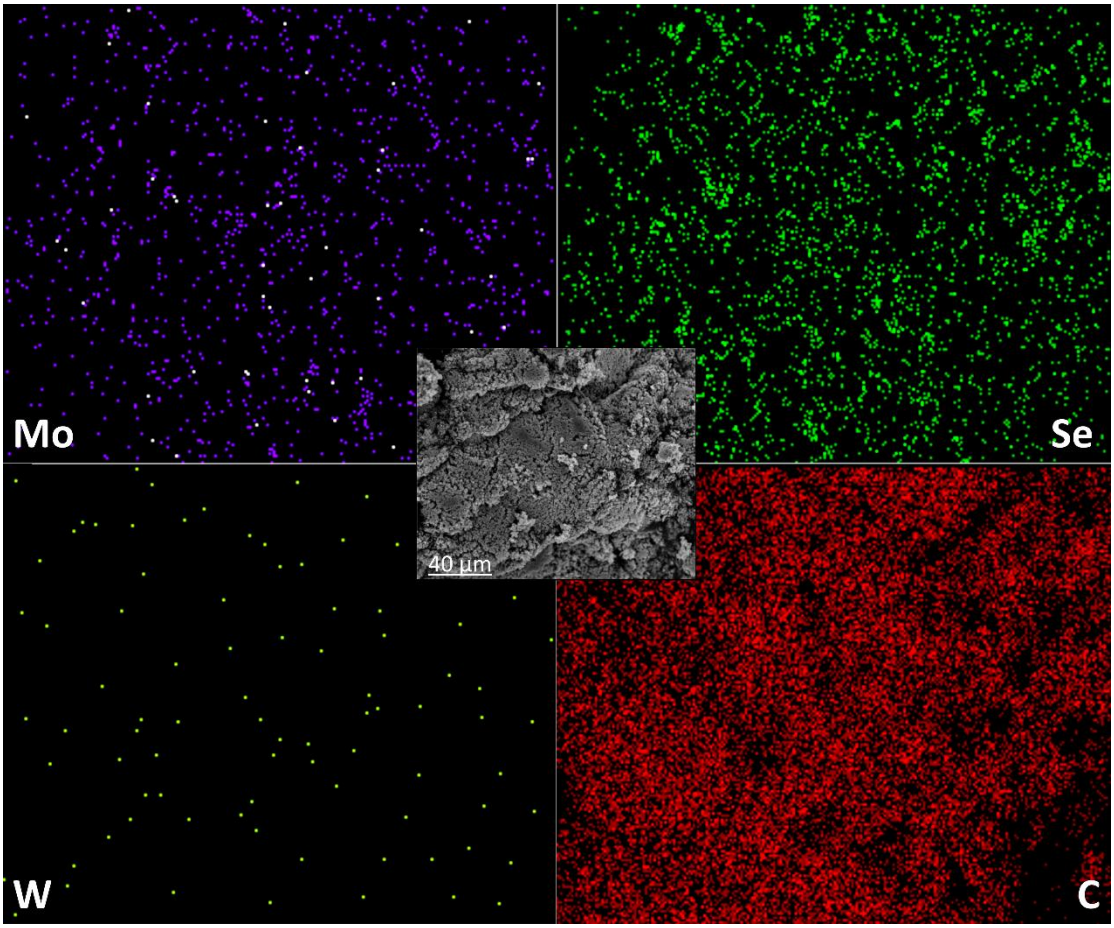

Figure XIII. Elemental maps of Mo, Se, W and C in W2-$MoSe_2$/G nanostructures, Inset represents the SEM image for the corresponding elemental map.

APPENDIX XIV: SAED patterns of $MoSe_2$, W2-$MoSe_2$ and W2-$MoSe_2$/G nanostructures.

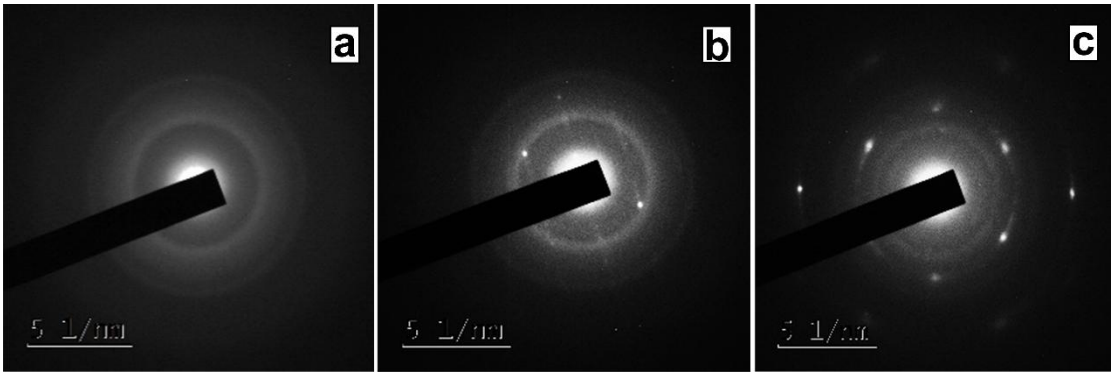

Figure XIV. SAED patterns of (a) $MoSe_2$, (b) W2-$MoSe_2$ and (c) W2-$MoSe_2$/G nanostructures.

APPENDIX XV: BET surface area and BJH pore size plots of $MoSe_2$, W2-$MoSe_2$ and W2-$MoSe_2$/G nanostructures.

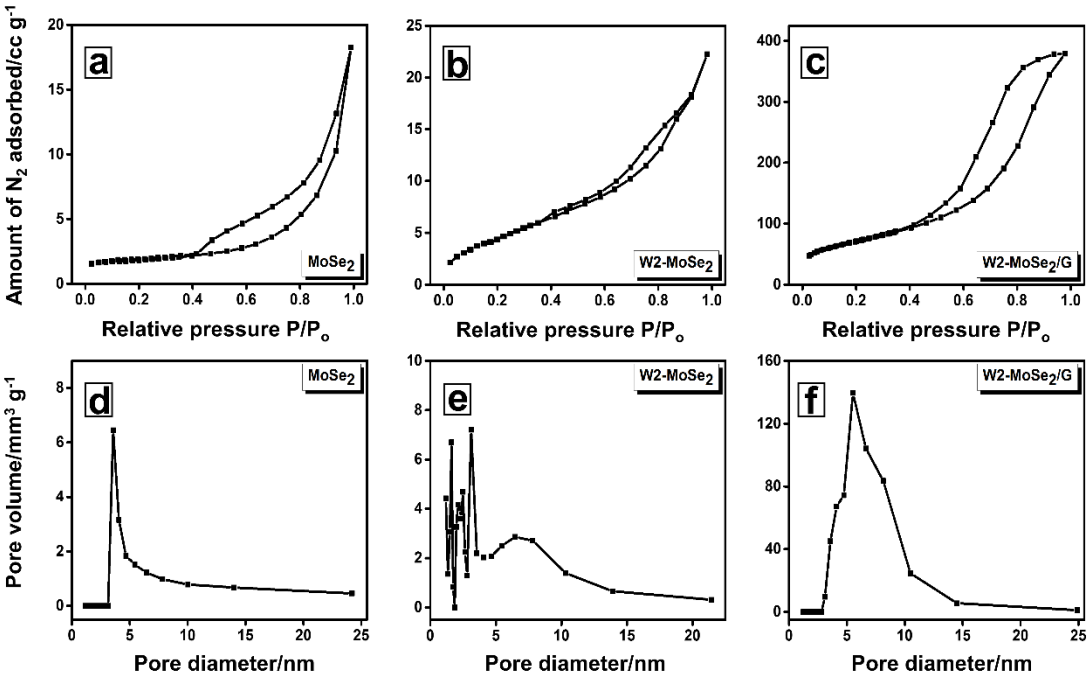

Figure XV. BET N_2 adsorption-desorption isotherms of as-synthesized (a) $MoSe_2$, (b) W2-$MoSe_2$ and (c) W2-$MoSe_2$/G nanostructures and their corresponding BJH plots (d),(e) and (f).

APPENDIX XVI: Comparison of specific capacitances of $MoSe_2$ with earlier reports.

Table A3. Comparison of specific capacitances (F g^{-1}) and other parameters of $MoSe_2$, W2-$MoSe_2$, and W2-$MoSe_2$/G electrodes with earlier reports.

Material	Specific capacitance	Scan rate / Current density	Cyclic retention	Reference
$MoSe_2$-CNT	228 F g^{-1}	5 mV s^{-1}	93 % @ 1k	(Karade and Sankapal 2017)
$MoSe_2$	49.7 F g^{-1}	2 mV s^{-1}	75 % @ 10k	(Balasingam et al. 2015)
$MoSe_2$/rGO	211 F g^{-1}	5 mV s^{-1}	180 % @ 10k	(Balasingam et al. 2016)
$MoSe_2$–CA	775.3 C g^{-1}	1.0 A g^{-1}	98 % @ 1.5k	(He 2017)
$MoSe_2$	243 F g^{-1}	0.5 A g^{-1}	90.3 % @ 1k	(Gao et al. 2017)
$MoSe_2$	25.31 F g^{-1}	5 mV s^{-1}	87 % @ 10k	(Pazhamalai et al. 2019)
$MoSe_2$	106.13 F g^{-1}	2 mV s^{-1}	68 % @ 10k	This work
W2-$MoSe_2$	147.08 F g^{-1}	2 mV s^{-1}	58 % @ 10k	This work
W2-$MoSe_2$/G	248.01 F g^{-1}	2 mV s^{-1}	102 % @ 20k	This work

APPENDIX XVII: SEM image of Cu_2S micro-hexagons for EDS measurements.

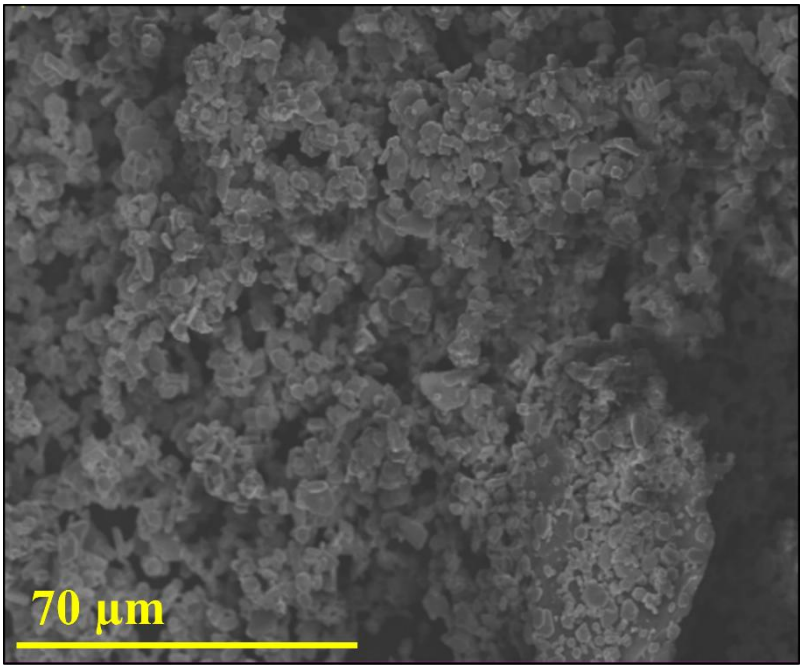

Figure XVII. SEM image wherein EDS measurements are performed for Cu_2S micro-hexagons.

Table A4. Weight and atomic percentages of all the elements in Cu_2S micro-hexagons as obtained from EDS measurements.

Element	Weight percentage/%	Atomic percentage/%
Cu	78.98	63.32
S	19.27	30.62
C	0.47	2.02
O	1.26	4.04
Total	100	100

APPENDIX XVIII: BET surface area and BJH pore size plots of Cu_2S micro-hexagons.

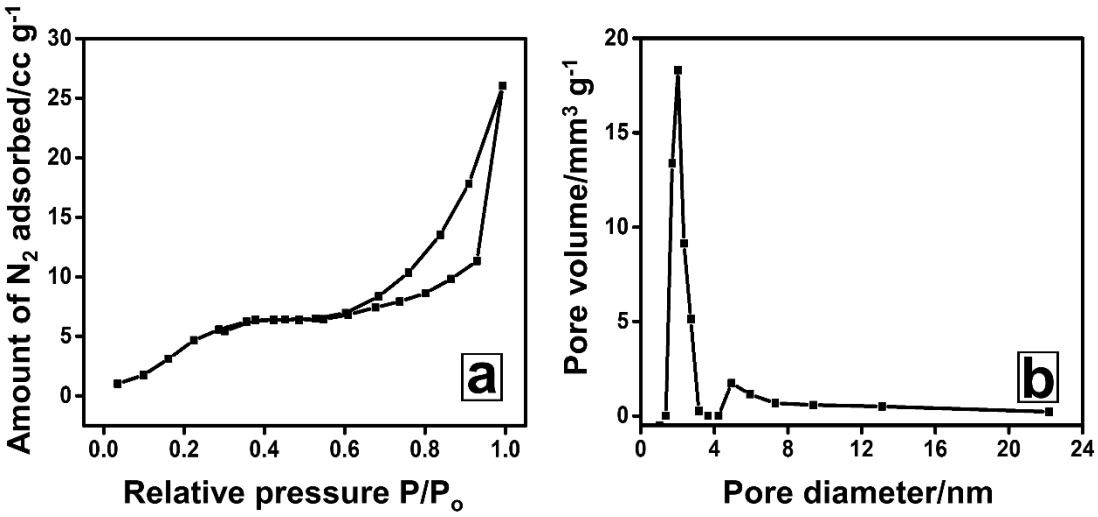

Figure XVIII. BET N_2 adsorption-desorption isotherms of Cu_2S micro-hexagons and (b) BJH pore size distribution plots.

APPENDIX XIX: Estimation of ECSA from CV curves of Cu_2S micro-hexagons at extreme pH solutions.

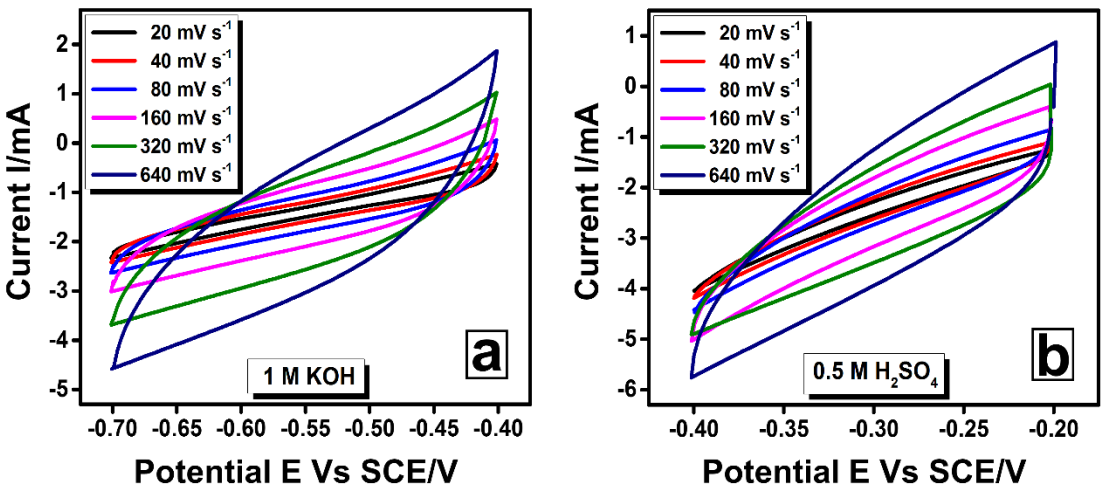

Figure XIX. CV curves of Cu_2S micro-hexagons in double layer charging region for the estimation of ECSA.

APPENDIX XX: Elemental mapping images of Ni_3S_2/NF.

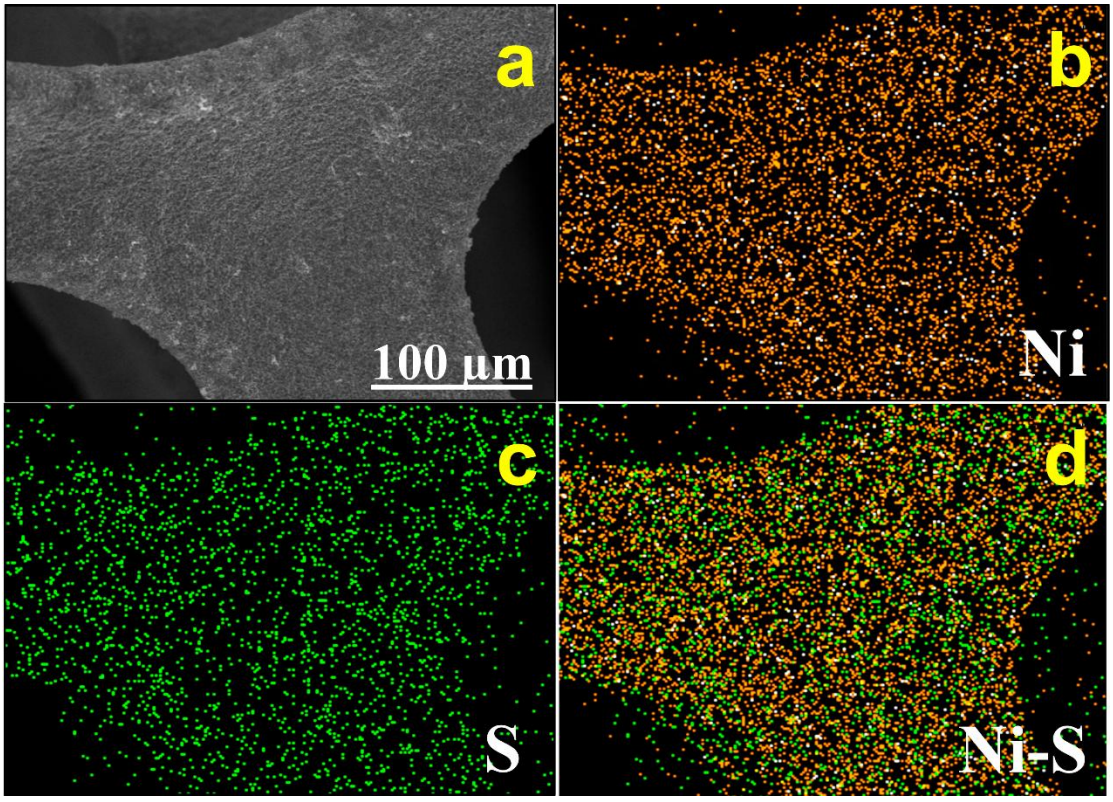

Figure XV. Elemental mapping images of Ni_3S_2/NF: (a) SEM image wherein elemental mapping are conducted, (b) Ni (orange), (c) S (green) and (f) merged mapping of Ni and S.

Table A5. Weight percentages of all elements of Ni_3S_2/NF.

Element	Weight percent
O	1.589
C	0.589
Ni	71.53
S	26.32
Total	100

APPENDIX XXI: Nyquist plots comparisons of Cu_2S-Ni_3S_2/NF, Ni_3S_2/NF and bare NF.

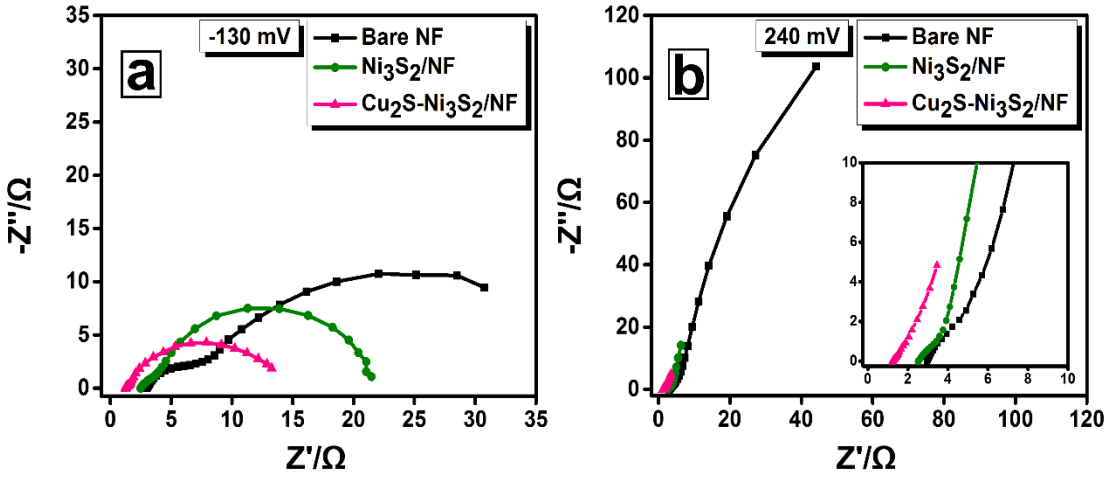

Figure XXI. Nyquist plots comparisons of Cu_2S-Ni_3S_2/NF, Ni_3S_2/NF and bare NF at an applied bias of -130 mV (towards the HER) (a) and (b) at an applied bias of 240 mV (towards the OER).

APPENDIX XXII: Elemental mapping images of Cu_2S-Ni_3S_2/NF after chronopotentiometric stability test towards the HER.

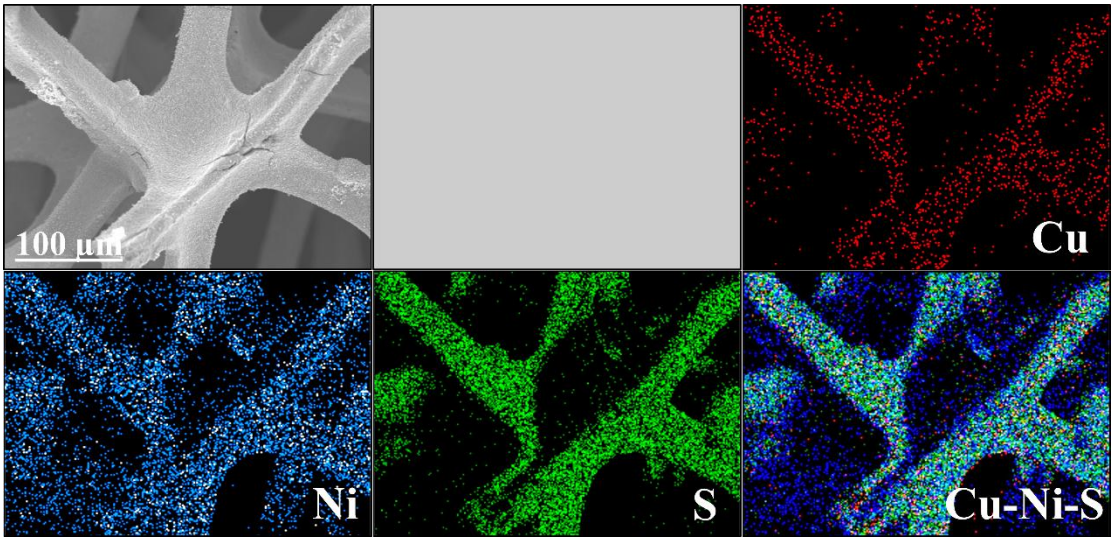

Figure XXII. Elemental mapping images of Cu_2S-Ni_3S_2/NF after chronopotentiometric stability test towards the HER.

APPENDIX XXIII: Elemental mapping images of Cu_2S-Ni_3S_2/NF after chronopotentiometric stability test towards the OER.

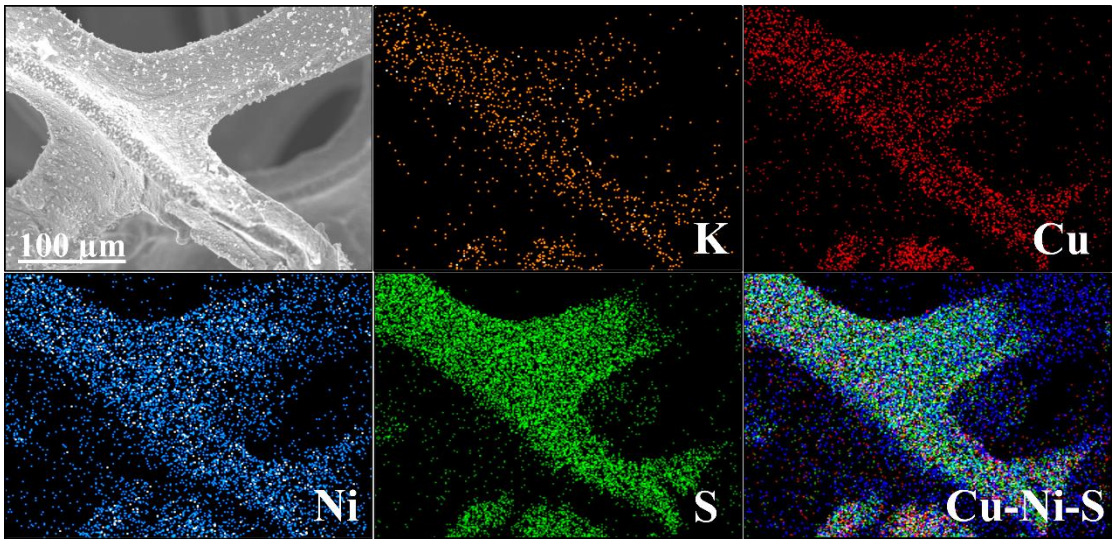

Figure XXIII. Elemental mapping images of Cu_2S-Ni_3S_2/NF after chronopotentiometric stability test towards the OER.

APPENDIX XXIV: Estimation of ECSA from CV curves of bare NF, Ni_3S_2/NF and Cu_2S- Ni_3S_2/NF.

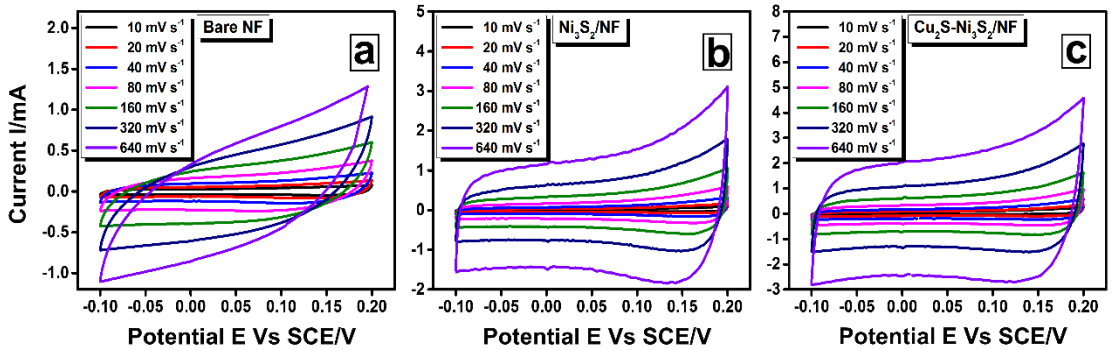

Figure XXIV. CV curves of (a) bare NF, (b) Ni_3S_2/NF and (c) Cu_2S- Ni_3S_2/NF for the estimation of ECSA.

REFERENCES

Aikens, D. A. (1983). “Electrochemical methods, fundamentals and applications.” *J. Chem. Educ.*, 60(1), A25.

Ajay, A., Paravannoor, A., Joseph, J., V, A., SS, A., Nair, S. V., and Balakrishnan, A. (2015). “2 D amorphous frameworks of NiMoO4 for supercapacitors: defining the role of surface and bulk controlled diffusion processes.” *Appl. Surf. Sci.*, 326, 39–47.

Ambrosi, A., Sofer, Z., and Pumera, M. (2015). “2H → 1T phase transition and hydrogen evolution activity of MoS2, MoSe2, WS2 and WSe2 strongly depends on the MX2 composition.” *Chem. Commun.*, 51(40), 8450–8453.

Anantharaj, S., Karthick, K., and Kundu, S. (2018). “NiTe2 Nanowire Outperforms Pt/C in High-Rate Hydrogen Evolution at Extreme pH Conditions.” *Inorg. Chem.*, 57(6), 3082–3096.

Arul, N. S., and Han, J. I. (2016). “Facile hydrothermal synthesis of hexapod-like two dimensional dichalcogenide NiSe2 for supercapacitor.” *Mater. Lett.*, 181, 345–349.

Arul, N. S., and Han, J. I. (2019). “Enhanced pseudocapacitance of NiSe2/Ni(OH)2 nanocomposites for supercapacitor electrode.” *Mater. Lett.*, 234, 87–91.

Balasingam, S. K., Lee, J. S., and Jun, Y. (2015). “Few-layered MoSe2 nanosheets as an advanced electrode material for supercapacitors.” *Dalton Trans.*, 44(35), 15491–15498.

Balasingam, S. K., Lee, J. S., and Jun, Y. (2016). “Molybdenum diselenide/reduced graphene oxide based hybrid nanosheets for supercapacitor applications.” *Dalton Trans.*, 45(23), 9646–9653.

Barreto, L., Makihira, A., and Riahi, K. (2003). “The hydrogen economy in the 21st century: a sustainable development scenario.” *Int. J. Hydrog. Energy*, 28(3), 267–284.

Barthelemy, E., Gorochov, O., and McKinzie, H. (1973). “The electrical and magnetic properties of the transition in nickel sulfide.” *Mater. Res. Bull.*, 8(12), 1401–1412.

Beams, R., Cançado, L. G., Krylyuk, S., Kalish, I., Kalanyan, B., Singh, A. K., Choudhary, K., Bruma, A., Vora, P. M., Tavazza, F., Davydov, A. V., and Stranick, S. J. (2016). “Characterization of Few-Layer 1T′ MoTe2 by Polarization-Resolved Second Harmonic Generation and Raman Scattering.” *ACS Nano*, 10(10), 9626–9636.

Birry, L., and Lasia, A. (2004). “Studies of the Hydrogen Evolution Reaction on Raney Nickel—Molybdenum Electrodes.” *J. Appl. Electrochem.*, 34(7), 735–749.

Bissett, M. A., Kinloch, I. A., and Dryfe, R. A. W. (2015). “Characterization of MoS2–Graphene Composites for High-Performance Coin Cell Supercapacitors.” *ACS Appl. Mater. Interfaces*, 7(31), 17388–17398.

Bissett, M. A., Worrall, S. D., Kinloch, I. A., and Dryfe, R. A. W. (2016). “Comparison of Two-Dimensional Transition Metal Dichalcogenides for Electrochemical Supercapacitors.” *Electrochimica Acta*, 201, 30–37.

Biswal, M., Banerjee, A., Deo, M., and Ogale, S. (2013). “From dead leaves to high energy density supercapacitors.” *Energy Environ. Sci.*, 6(4), 1249–1259.

Bu, I. Y. Y., and Huang, R. (2015). “One-pot synthesis of ZnO/reduced graphene oxide nanocomposite for supercapacitor applications.” *Mater. Sci. Semicond. Process.*, 31, 131–138.

Candy, J.-P., Fouilloux, P., Keddam, M., and Takenouti, H. (1981). “The characterization of porous electrodes by impedance measurements.” *Electrochimica Acta*, 26(8), 1029–1034.

Cao, L., Yang, S., Gao, W., Liu, Z., Gong, Y., Ma, L., Shi, G., Lei, S., Zhang, Y., Zhang, S., Vajtai, R., and Ajayan, P. M. (2013). “Direct Laser-Patterned Micro-Supercapacitors from Paintable MoS2 Films.” *Small*, 9(17), 2905–2910.

Chakravarty, D., Kumar, P., Ugale, V. S., and Late, D. J. (2015). “Microwave-Assisted Synthesis of Few-Layered TaTe2 and Its Application as Supercapacitor.” *Eur. J. Inorg. Chem.*, 2015(9).

Chen, D., Wang, G.-S., He, S., Liu, J., Guo, L., and Cao, M.-S. (2013). “Controllable fabrication of mono-dispersed RGO–hematite nanocomposites and their enhanced wave absorption properties.” *J. Mater. Chem. A*, 1(19), 5996–6003.

Chen, G.-F., Ma, T. Y., Liu, Z.-Q., Li, N., Su, Y.-Z., Davey, K., and Qiao, S.-Z. (2016). “Efficient and Stable Bifunctional Electrocatalysts Ni/NixMy (M = P, S) for Overall Water Splitting.” *Adv. Funct. Mater.*, 26(19), 3314–3323.

Chen, L., and Lasia, A. (1991). “Study of the Kinetics of Hydrogen Evolution Reaction on Nickel-Zinc Alloy Electrodes.” *J. Electrochem. Soc.*, 138(11), 3321–3328.

Chen, W., Yu, X., Zhao, Z., Ji, S., and Feng, L. (2019). “Hierarchical architecture of coupling graphene and 2D WS2 for high-performance supercapacitor.” *Electrochimica Acta*, 298, 313–320.

Chen, X., and Mao, S. S. (2007). “Titanium Dioxide Nanomaterials: Synthesis,

Properties, Modifications, and Applications." *Chem. Rev.*, 107(7), 2891–2959.

Cheng, N., Liu, Q., Tian, J., Xue, Y., Asiri, A. M., Jiang, H., He, Y., and Sun, X. (2015). "Acidically oxidized carbon cloth: a novel metal-free oxygen evolution electrode with high catalytic activity." *Chem. Commun.*, 51(9), 1616–1619.

Chia, X., Eng, A. Y. S., Ambrosi, A., Tan, S. M., and Pumera, M. (2015). "Electrochemistry of Nanostructured Layered Transition-Metal Dichalcogenides." *Chem. Rev.*, 115(21), 11941–11966.

Chia, X., and Pumera, M. (2018). "Inverse Opal-like Porous MoSex Films for Hydrogen Evolution Catalysis: Overpotential-Pore Size Dependence." *ACS Appl. Mater. Interfaces*, 10(5), 4937–4945.

Chia, X., Sofer, Z., Luxa, J., and Pumera, M. (2017). "Unconventionally Layered CoTe2 and NiTe2 as Electrocatalysts for Hydrogen Evolution." *Chem. – Eur. J.*, 23(48), 11719–11726.

Choi, W., Choudhary, N., Han, G. H., Park, J., Akinwande, D., and Lee, Y. H. (2017). "Recent development of two-dimensional transition metal dichalcogenides and their applications." *Mater. Today*, 20(3), 116–130.

Conway, B. E. (1991). "Transition from 'supercapacitor' to 'battery' behavior in electrochemical energy storage." *J. Electrochem. Soc.*, 138(6), 1539–1548.

Day, N. U., Walter, M. G., and Wamser, C. C. (2015). "Preparations and Electrochemical Characterizations of Conductive Porphyrin Polymers." *J. Phys. Chem. C*, 119(30), 17378–17388.

De Silva, U., Masud, J., Zhang, N., Hong, Y., Liyanage, W. P. R., Asle Zaeem, M., and Nath, M. (2018). "Nickel telluride as a bifunctional electrocatalyst for efficient water splitting in alkaline medium." *J. Mater. Chem. A*, 6(17), 7608–7622.

Deng, C., Xie, J., Xue, Y., He, M., Wei, X., and Yan, Y.-M. (2016). "Synthesis of MoP decorated carbon cloth as a binder-free electrode for hydrogen evolution." *RSC Adv.*, 6(73), 68568–68573.

Devaraju, M. K., and Honma, I. (2012). "Hydrothermal and Solvothermal Process Towards Development of LiMPO4 (M = Fe, Mn) Nanomaterials for Lithium-Ion Batteries." *Adv. Energy Mater.*, 2(3), 284–297.

Dickinson, R. G., and Pauling, L. (1923). "THE CRYSTAL STRUCTURE OF MOLYBDENITE." *J. Am. Chem. Soc.*, 45(6), 1466–1471.

Dubal, D. P., Ayyad, O., Ruiz, V., and Gómez-Romero, P. (2015). "Hybrid energy storage: the merging of battery and supercapacitor chemistries." *Chem. Soc. Rev.*, 44(7), 1777–1790.

Edwards, P. P., Kuznetsov, V. L., David, W. I. F., and Brandon, N. P. (2008). "Hydrogen and fuel cells: Towards a sustainable energy future." *Energy Policy*, Foresight Sustainable Energy Management and the Built Environment Project, 36(12), 4356–4362.

Elias, L., and Hegde, A. C. (2016). "Synthesis and characterization of Ni-P-Ag composite coating as efficient electrocatalyst for alkaline hydrogen evolution reaction." *Electrochimica Acta*, 219, 377–385.

El-Mahalawy, S. H., and Evans, B. L. (1977). "Temperature dependence of the electrical conductivity and hall coefficient in 2H-MoS2, MoSe2, WSe2, and MoTe2." *Phys. Status Solidi B*, 79(2), 713–722.

Fan, M., Gao, R., Zou, Y.-C., Wang, D., Bai, N., Li, G.-D., and Zou, X. (2016). "An efficient nanostructured copper(I) sulfide-based hydrogen evolution electrocatalyst at neutral pH." *Electrochimica Acta*, 215, 366–373.

Fournier, J., Miousse, D., and Legoux, J.-G. (1999). "Wire-arc sprayed nickel based coating for hydrogen evolution reaction in alkaline solutions." *Int. J. Hydrog. Energy*, 24(6), 519–528.

Frindt, R. F. (1966). "Single Crystals of MoS2 Several Molecular Layers Thick." *J. Appl. Phys.*, 37(4), 1928–1929.

Gao, M.-R., Xu, Y.-F., Jiang, J., and Yu, S.-H. (2013). "Nanostructured metal chalcogenides: synthesis, modification, and applications in energy conversion and storage devices." *Chem. Soc. Rev.*, 42(7), 2986–3017.

Gao, Y.-P., Huang, K.-J., Shuai, H.-L., and Liu, L. (2017). "Synthesis of sphere-feature molybdenum selenide with enhanced electrochemical performance for supercapacitor." *Mater. Lett.*, 209, 319–322.

Ge, Y., Gao, S.-P., Dong, P., Baines, R., Ajayan, P. M., Ye, M., and Shen, J. (2017). "Insight into the hydrogen evolution reaction of nickel dichalcogenide nanosheets: activities related to non-metal ligands." *Nanoscale*, 9(17), 5538–5544.

George, G., Elias, L., Hegde, A. C., and Anandhan, S. (2015). "Morphological and structural characterisation of sol–gel electrospun Co3O4 nanofibres and their electro-

catalytic behaviour." *RSC Adv.*, 5(51), 40940–40949.

Gholamvand, Z., McAteer, D., Backes, C., McEvoy, N., Harvey, A., Berner, N. C., Hanlon, D., Bradley, C., Godwin, I., Rovetta, A., Lyons, M. E. G., Duesberg, G. S., and Coleman, J. N. (2016). "Comparison of liquid exfoliated transition metal dichalcogenides reveals MoSe2 to be the most effective hydrogen evolution catalyst." *Nanoscale*, 8(10), 5737–5749.

Gogotsi, Y., and Penner, R. M. (2018). "Energy Storage in Nanomaterials – Capacitive, Pseudocapacitive, or Battery-like?" *ACS Nano*, 12(3), 2081–2083.

Gomez, R., Fernandez-Vega, A., Feliu, J. M., and Aldaz, A. (1993). "Hydrogen evolution on platinum single crystal surfaces: effects of irreversibly adsorbed bismuth and antimony on hydrogen adsorption and evolution on platinum (100)." *J. Phys. Chem.*, 97(18), 4769–4776.

Gómez-Aguilar, J. F., Escalante-Martínez, J. E., Calderón-Ramón, C., Morales-Mendoza, L. J., Benavidez-Cruz, M., and Gonzalez-Lee, M. (2016). "Equivalent Circuits Applied in Electrochemical Impedance Spectroscopy and Fractional Derivatives with and without Singular Kernel." *Adv. Math. Phys.*, <https://www.hindawi.com/journals/amp/2016/9720181/> (Mar. 11, 2019).

Gong, Y., Li, D., Fu, Q., and Pan, C. (2015). "Influence of graphene microstructures on electrochemical performance for supercapacitors." *Prog. Nat. Sci. Mater. Int.*, 25(5), 379–385.

Grosvenor, A. P., Biesinger, M. C., Smart, R. St. C., and McIntyre, N. S. (2006). "New interpretations of XPS spectra of nickel metal and oxides." *Surf. Sci.*, 600(9), 1771–1779.

Gustavsson, F., Svahn, F., Bexell, U., and Jacobson, S. (2013). "Nanoparticle based and sputtered WS2 low-friction coatings — Differences and similarities with respect to friction mechanisms and tribofilm formation." *Surf. Coat. Technol.*, 232, 616–626.

He, B. (2017). "Molybdenum diselenide nanosheets wraping carbon aerogel nanospheres as an advanced material for supercapacitor and electrochemical sensing." *Electrochimica Acta*, 257, 301–310.

He, C., Wu, X., and He, Z. (2014). "Amorphous Nickel-Based Thin Film As a Janus Electrocatalyst for Water Splitting." *J. Phys. Chem. C*, 118(9), 4578–4584.

He, L., Zhou, D., Lin, Y., Ge, R., Hou, X., Sun, X., and Zheng, C. (2018). "Ultrarapid

in Situ Synthesis of Cu2S Nanosheet Arrays on Copper Foam with Room-Temperature-Active Iodine Plasma for Efficient and Cost-Effective Oxygen Evolution." *ACS Catal.*, 8(5), 3859–3864.

Ho, T. A., Bae, C., Nam, H., Kim, E., Lee, S. Y., Park, J. H., and Shin, H. (2018). "Metallic Ni3S2 Films Grown by Atomic Layer Deposition as an Efficient and Stable Electrocatalyst for Overall Water Splitting." *ACS Appl. Mater. Interfaces*, 10(15), 12807–12815.

Hu, C., Zhang, L., Zhao, Z.-J., Luo, J., Shi, J., Huang, Z., and Gong, J. (2017). "Edge Sites with Unsaturated Coordination on Core–Shell Mn3O4@MnxCo3−xO4 Nanostructures for Electrocatalytic Water Oxidation." *Adv. Mater.*, 29(36), 1701820.

Hu, W.-H., Han, G.-Q., Dai, F.-N., Liu, Y.-R., Shang, X., Dong, B., Chai, Y.-M., Liu, Y.-Q., and Liu, C.-G. (2016). "Effect of pH on the growth of MoS2 (002) plane and electrocatalytic activity for HER." *Int. J. Hydrog. Energy*, 41(1), 294–299.

Huang, J., Yang, L., Liu, D., Chen, J., Fu, Q., Xiong, Y., Lin, F., and Xiang, B. (2015a). "Large-area synthesis of monolayer WSe2 on a SiO2/Si substrate and its device applications." *Nanoscale*, 7(9), 4193–4198.

Huang, K.-J., Wang, L., Liu, Y.-J., Wang, H.-B., Liu, Y.-M., and Wang, L.-L. (2013). "Synthesis of polyaniline/2-dimensional graphene analog MoS2 composites for high-performance supercapacitor." *Electrochimica Acta*, 109, 587–594.

Huang, K.-J., Zhang, J.-Z., and Fan, Y. (2015b). "One-step solvothermal synthesis of different morphologies CuS nanosheets compared as supercapacitor electrode materials." *J. Alloys Compd.*, 625, 158–163.

Jayalakshmi, M., Mohan Rao, M., and Choudary, B. M. (2004). "Identifying nano SnS as a new electrode material for electrochemical capacitors in aqueous solutions." *Electrochem. Commun.*, 6(11), 1119–1122.

Jiang, N., Tang, Q., Sheng, M., You, B., Jiang, D., and Sun, Y. (2016). "Nickel sulfides for electrocatalytic hydrogen evolution under alkaline conditions: a case study of crystalline NiS, NiS2, and Ni3S2 nanoparticles." *Catal. Sci. Technol.*, 6(4), 1077–1084.

Jung, H.-G., Venugopal, N., Scrosati, B., and Sun, Y.-K. (2013). "A high energy and power density hybrid supercapacitor based on an advanced carbon-coated Li4Ti5O12 electrode." *J. Power Sources*, 221, 266–271.

Kaniyoor, A., and Ramaprabhu, S. (2012). "A Raman spectroscopic investigation of

graphite oxide derived graphene." *AIP Adv.*, 2(3), 032183.

Karade, S. S., and Sankapal, B. R. (2017). "Two dimensional cryptomelane like growth of MoSe2 over MWCNTs: Symmetric all-solid-state supercapacitor." *J. Electroanal. Chem.*, 802, 131–138.

Kellenberger, A., Vaszilcsin, N., Brandl, W., and Duteanu, N. (2007). "Kinetics of hydrogen evolution reaction on skeleton nickel and nickel–titanium electrodes obtained by thermal arc spraying technique." *Int. Symp. Sol.-Hydrog.-Fuel Cells 2005*, 32(15), 3258–3265.

Kibsgaard, J., Jaramillo, T. F., and Besenbacher, F. (2014). "Building an appropriate active-site motif into a hydrogen-evolution catalyst with thiomolybdate [Mo3S13]2− clusters." *Nat. Chem.*, 6, 248.

Kiran, V., Mukherjee, D., Jenjeti, R. N., and Sampath, S. (2014). "Active guests in the MoS2/MoSe2 host lattice: efficient hydrogen evolution using few-layer alloys of MoS2(1−x)Se2x." *Nanoscale*, 6(21), 12856–12863.

Kirubasankar, B., Palanisamy, P., Arunachalam, S., Murugadoss, V., and Angaiah, S. (2019). "2D MoSe2-Ni(OH)2 nanohybrid as an efficient electrode material with high rate capability for asymmetric supercapacitor applications." *Chem. Eng. J.*, 355, 881–890.

Kosmala, T., Diaz, H. C., Komsa, H.-P., Ma, Y., Krasheninnikov, A. V., Batzill, M., and Agnoli, S. (2018). "Metallic Twin Boundaries Boost the Hydrogen Evolution Reaction on the Basal Plane of Molybdenum Selenotellurides." *Adv. Energy Mater.*, 8(20), 1800031.

Kosman, D. J. (2010). "Multicopper oxidases: a workshop on copper coordination chemistry, electron transfer, and metallophysiology." *JBIC J. Biol. Inorg. Chem.*, 15(1), 15–28.

Kötz, R., Hahn, M., and Gallay, R. (2006). "Temperature behavior and impedance fundamentals of supercapacitors." *Sel. Pap. Ninth Ulm Electrochem. Days*, 154(2), 550–555.

Kukunuri, S., Krishnan, M. R., and Sampath, S. (2015). "The effect of structural dimensionality on the electrocatalytic properties of the nickel selenide phase." *Phys. Chem. Chem. Phys.*, 17(36), 23448–23459.

Kumar, K. S., Choudhary, N., Jung, Y., and Thomas, J. (2018). "Recent advances in

two-dimensional nanomaterials for supercapacitor electrode applications." *ACS Energy Lett.*, 3(2), 482–495.

Kumbhar, V. S., Lokhande, A. C., Gaikwad, N. S., and Lokhande, C. D. (2016). "One-step chemical synthesis of samarium telluride thin films and their supercapacitive properties." *Chem. Phys. Lett.*, 645, 112–117.

Kuo, C.-H., Chu, Y.-T., Song, Y.-F., and Huang, M. H. (2011). "Cu2O Nanocrystal-Templated Growth of Cu2S Nanocages with Encapsulated Au Nanoparticles and In-Situ Transmission X-ray Microscopy Study." *Adv. Funct. Mater.*, 21(4), 792–797.

Ledendecker, M., Krick Calderón, S., Papp, C., Steinrück, H.-P., Antonietti, M., and Shalom, M. (2015). "The Synthesis of Nanostructured Ni5P4 Films and their Use as a Non-Noble Bifunctional Electrocatalyst for Full Water Splitting." *Angew. Chem. Int. Ed.*, 54(42), 12361–12365.

Lee, Y., Suntivich, J., May, K. J., Perry, E. E., and Shao-Horn, Y. (2012). "Synthesis and Activities of Rutile IrO2 and RuO2 Nanoparticles for Oxygen Evolution in Acid and Alkaline Solutions." *J. Phys. Chem. Lett.*, 3(3), 399–404.

Lei, Y., Pakhira, S., Fujisawa, K., Wang, X., Iyiola, O. O., Perea López, N., Laura Elías, A., Pulickal Rajukumar, L., Zhou, C., Kabius, B., Alem, N., Endo, M., Lv, R., Mendoza-Cortes, J. L., and Terrones, M. (2017). "Low-temperature Synthesis of Heterostructures of Transition Metal Dichalcogenide Alloys (WxMo1–xS2) and Graphene with Superior Catalytic Performance for Hydrogen Evolution." *ACS Nano*, 11(5), 5103–5112.

Levesanos, N., Liyanage, W. P. R., Ferentinos, E., Raptopoulos, G., Paraskevopoulou, P., Sanakis, Y., Choudhury, A., Stavropoulos, P., Nath, M., and Kyritsis, P. (2017). "Investigating the Structural, Spectroscopic, and Electrochemical Properties of [Fe{(EPiPr2)2N}2] (E = S, Se) and the Formation of Iron Selenides by Chemical Vapor Deposition." *Eur. J. Inorg. Chem.*, 2017(5), 988–988.

Li, R., Luo, Z., and Papadimitrakopoulos, F. (2006). "Redox-Assisted Asymmetric Ostwald Ripening of CdSe Dots to Rods." *J. Am. Chem. Soc.*, 128(19), 6280–6281.

Li, S., Zang, W., Liu, X., Pennycook, S. J., Kou, Z., Yang, C., Guan, C., and Wang, J. (2019a). "Heterojunction engineering of MoSe2/MoS2 with electronic modulation towards synergetic hydrogen evolution reaction and supercapacitance performance." *Chem. Eng. J.*, 359, 1419–1426.

Li, X., Hao, X., Abudula, A., and Guan, G. (2016). “Nanostructured catalysts for electrochemical water splitting: current state and prospects.” *J. Mater. Chem. A*, 4(31), 11973–12000.

Li, X., Puretzky, A. A., Sang, X., KC, S., Tian, M., Ceballos, F., Mahjouri-Samani, M., Wang, K., Unocic, R. R., Zhao, H., Duscher, G., Cooper, V. R., Rouleau, C. M., Geohegan, D. B., and Xiao, K. (2017). “Suppression of Defects and Deep Levels Using Isoelectronic Tungsten Substitution in Monolayer MoSe2.” *Adv. Funct. Mater.*, 27(19), 1603850.

Li, Y., Su, H., Fu, J., and Du, X. (2019b). “The 3D ultra-thin Cu1-xNixS/NF nanosheet as a highly efficient and stable electrocatalyst for overall water splitting.” *Int. J. Hydrog. Energy*, 44(23), 11744–11753.

Liang, H.-W., Guan, Q.-F., Chen, L.-F., Zhu, Z., Zhang, W.-J., and Yu, S.-H. (2012). “Macroscopic-Scale Template Synthesis of Robust Carbonaceous Nanofiber Hydrogels and Aerogels and Their Applications.” *Angew. Chem. Int. Ed.*, 51(21), 5101–5105.

Liang, Z., Ahn, H. S., and Bard, A. J. (2017). “A Study of the Mechanism of the Hydrogen Evolution Reaction on Nickel by Surface Interrogation Scanning Electrochemical Microscopy.” *J. Am. Chem. Soc.*, 139(13), 4854–4858.

Lu, A.-H., Salabas, E. L., and Schüth, F. (2007). “Magnetic Nanoparticles: Synthesis, Protection, Functionalization, and Application.” *Angew. Chem. Int. Ed.*, 46(8), 1222–1244.

Lukowski, M. A., Daniel, A. S., Meng, F., Forticaux, A., Li, L., and Jin, S. (2013). “Enhanced Hydrogen Evolution Catalysis from Chemically Exfoliated Metallic MoS2 Nanosheets.” *J. Am. Chem. Soc.*, 135(28), 10274–10277.

Luo, J., Im, J.-H., Mayer, M. T., Schreier, M., Nazeeruddin, M. K., Park, N.-G., Tilley, S. D., Fan, H. J., and Grätzel, M. (2014). “Water photolysis at 12.3% efficiency via perovskite photovoltaics and Earth-abundant catalysts.” *Science*, 345(6204), 1593.

Luo, P., Zhang, H., Liu, L., Zhang, Y., Deng, J., Xu, C., Hu, N., and Wang, Y. (2017). “Targeted Synthesis of Unique Nickel Sulfide (NiS, NiS2) Microarchitectures and the Applications for the Enhanced Water Splitting System.” *ACS Appl. Mater. Interfaces*, 9(3), 2500–2508.

Lv, R., Robinson, J. A., Schaak, R. E., Sun, D., Sun, Y., Mallouk, T. E., and Terrones, M. (2015). “Transition Metal Dichalcogenides and Beyond: Synthesis, Properties, and

Applications of Single- and Few-Layer Nanosheets.” *Acc. Chem. Res.*, 48(1), 56–64.

Ma, B., Yang, Z., Yuan, Z., and Chen, Y. (2019). “Effective surface roughening of three-dimensional copper foam via sulfurization treatment as a bifunctional electrocatalyst for water splitting.” *Int. J. Hydrog. Energy*, 44(3), 1620–1626.

Mak, K. F., Lee, C., Hone, J., Shan, J., and Heinz, T. F. (2010). “Atomically Thin ${\mathrm{MoS}}_{2}$: A New Direct-Gap Semiconductor.” *Phys. Rev. Lett.*, 105(13), 136805.

Man, I. C., Su, H.-Y., Calle-Vallejo, F., Hansen, H. A., Martínez, J. I., Inoglu, N. G., Kitchin, J., Jaramillo, T. F., Nørskov, J. K., and Rossmeisl, J. (2011). “Universality in Oxygen Evolution Electrocatalysis on Oxide Surfaces.” *ChemCatChem*, 3(7), 1159–1165.

Mandale, A. B., Badrinarayanan, S., Date, S. K., and Sinha, A. P. B. (1984). “Photoelectron-spectroscopic study of nickel, manganese and cobalt selenides.” *J. Electron Spectrosc. Relat. Phenom.*, 33(1), 61–72.

Manos, M. J., Malliakas, C. D., and Kanatzidis, M. G. (2007). “Heavy-metal-ion capture, ion-exchange, and exceptional acid stability of the open-framework chalcogenide (NH(4))(4)In(12)Se(20).” *Chem. Weinh. Bergstr. Ger.*, 13(1), 51–58.

Mao, H., Yu, J., Li, J., Zheng, T., Cen, J., and Ye, Y. (2019). “A high-performance supercapacitor electrode based on nanoflower-shaped CoTe2.” *Ceram. Int.*

Marcano, D. C., Kosynkin, D. V., Berlin, J. M., Sinitskii, A., Sun, Z., Slesarev, A., Alemany, L. B., Lu, W., and Tour, J. M. (2010). “Improved Synthesis of Graphene Oxide.” *ACS Nano*, 4(8), 4806–4814.

Masud, J., Ioannou, P.-C., Levesanos, N., Kyritsis, P., and Nath, M. (2016). “A Molecular Ni-complex Containing Tetrahedral Nickel Selenide Core as Highly Efficient Electrocatalyst for Water Oxidation.” *ChemSusChem*, 9(22), 3128–3132.

Masud, J., Liyanage, W. P. R., Cao, X., Saxena, A., and Nath, M. (2018). “Copper Selenides as High-Efficiency Electrocatalysts for Oxygen Evolution Reaction.” *ACS Appl. Energy Mater.*, 1(8), 4075–4083.

Mc Manus, J. B., Cunningham, G., McEvoy, N., Cullen, C. P., Gity, F., Schmidt, M., McAteer, D., Mullarkey, D., Shvets, I. V., Hurley, P. K., Hallam, T., and Duesberg, G. S. (2019). “Growth of 1T′ MoTe2 by Thermally Assisted Conversion of Electrodeposited Tellurium Films.” *ACS Appl. Energy Mater.*, 2(1), 521–530.

McGlynn, J. C., Cascallana-Matías, I., Fraser, J. P., Roger, I., McAllister, J., Miras, H. N., Symes, M. D., and Ganin, A. Y. (2018). "Molybdenum Ditelluride Rendered into an Efficient and Stable Electrocatalyst for the Hydrogen Evolution Reaction by Polymorphic Control." *Energy Technol.*, 6(2), 345–350.

Ming, F., Liang, H., Shi, H., Xu, X., Mei, G., and Wang, Z. (2016). "MOF-derived Co-doped nickel selenide/C electrocatalysts supported on Ni foam for overall water splitting." *J. Mater. Chem. A*, 4(39), 15148–15155.

Miousse, D., Lasia, A., and Borck, V. (1995). "Hydrogen evolution reaction on Ni-Al-Mo and Ni-Al electrodes prepared by low pressure plasma spraying." *J. Appl. Electrochem.*, 25(6), 592–602.

Mu, C. H., Qi, H. X., Song, Y. Q., Liu, Z. P., Ji, L. X., Deng, J. G., Liao, Y. B., and Scarpa, F. (2016). "One-pot synthesis of nanosheet-assembled hierarchical MoSe2/CoSe2 microcages for the enhanced performance of electrocatalytic hydrogen evolution." *RSC Adv.*, 6(1), 23–30.

Najafi Sayar, P., and Bahrololoom, M. E. (2009). "Comparison of anodic dissolution, surface brightness and surface roughness of nanocrystalline nickel coatings with conventional decorative chromium coatings." *J. Appl. Electrochem.*, 39(12), 2489.

Nicolosi, V., Chhowalla, M., Kanatzidis, M. G., Strano, M. S., and Coleman, J. N. (2013). "Liquid Exfoliation of Layered Materials." *Science*, 340(6139), 1226419.

Ohsaka, T., Izumi, F., and Fujiki, Y. (1978). "Raman spectrum of anatase, TiO2." *J. Raman Spectrosc.*, 7(6), 321–324.

Ojha, K., Saha, S., Banerjee, S., and Ganguli, A. K. (2017). "Efficient Electrocatalytic Hydrogen Evolution from MoS2-Functionalized Mo2N Nanostructures." *ACS Appl. Mater. Interfaces*, 9(23), 19455–19461.

Ouyang, C., Wang, X., Wang, C., Zhang, X., Wu, J., Ma, Z., Dou, S., and Wang, S. (2015). "Hierarchically Porous Ni3S2 Nanorod Array Foam as Highly Efficient Electrocatalyst for Hydrogen Evolution Reaction and Oxygen Evolution Reaction." *Electrochimica Acta*, 174, 297–301.

Pan, Y., Chen, Y., Li, X., Liu, Y., and Liu, C. (2015). "Nanostructured nickel sulfides: phase evolution, characterization and electrocatalytic properties for the hydrogen evolution reaction." *RSC Adv.*, 5(127), 104740–104749.

Patil, S. J., Kumbhar, V. S., Patil, B. H., Bulakhe, R. N., and Lokhande, C. D. (2014).

"Chemical synthesis of α-La2S3 thin film as an advanced electrode material for supercapacitor application." *J. Alloys Compd.*, 611, 191–196.

Patil, S. J., Lokhande, A. C., Lee, D.-W., Kim, J. H., and Lokhande, C. D. (2017). "Chemical synthesis and supercapacitive properties of lanthanum telluride thin film." *J. Colloid Interface Sci.*, 490, 147–153.

Patil, S. J., Lokhande, V. C., Chodankar, N. R., and Lokhande, C. D. (2016). "Chemically prepared La2Se3 nanocubes thin film for supercapacitor application." *J. Colloid Interface Sci.*, 469, 318–324.

Pazhamalai, P., Krishnamoorthy, K., Mariappan, V. K., Sahoo, S., Manoharan, S., and Kim, S.-J. (2018). "A High Efficacy Self-Charging MoSe2 Solid-State Supercapacitor Using Electrospun Nanofibrous Piezoelectric Separator with Ionogel Electrolyte." *Adv. Mater. Interfaces*, 5(12), 1800055.

Pazhamalai, P., Krishnamoorthy, K., Sahoo, S., and Kim, S.-J. (2019). "Two-dimensional molybdenum diselenide nanosheets as a novel electrode material for symmetric supercapacitors using organic electrolyte." *Electrochimica Acta*, 295, 591–598.

Peng, L., Shen, J., Zheng, X., Xiang, R., Deng, M., Mao, Z., Feng, Z., Zhang, L., Li, L., and Wei, Z. (2019). "Rationally design of monometallic NiO-Ni3S2/NF heteronanosheets as bifunctional electrocatalysts for overall water splitting." *J. Catal.*, 369, 345–351.

Perera, S. D., Ding, X., Bhargava, A., Hovden, R., Nelson, A., Kourkoutis, L. F., and Robinson, R. D. (2015). "Enhanced Supercapacitor Performance for Equal Co–Mn Stoichiometry in Colloidal Co3-xMnxO4 Nanoparticles, in Additive-Free Electrodes." *Chem. Mater.*, 27(23), 7861–7873.

Pu, Z., Amiinu, I. S., Kou, Z., Li, W., and Mu, S. (2017). "RuP2-Based Catalysts with Platinum-like Activity and Higher Durability for the Hydrogen Evolution Reaction at All pH Values." *Angew. Chem. Int. Ed.*, 56(38), 11559–11564.

Pumera, M., Sofer, Z., and Ambrosi, A. (2014). "Layered transition metal dichalcogenides for electrochemical energy generation and storage." *J. Mater. Chem. A*, 2(24), 8981–8987.

Rada, S., Chelcea, R., Rada, M., Bot, A., Aldea, N., Rednic, V., and Culea, E. (2013). "Electrochemical characterization and structure of tungsten–lead–germanate glasses

and glass ceramics." *Electrochimica Acta*, 109, 82–88.

Ramadoss, A., and Kim, S. J. (2013). "Improved activity of a graphene–TiO2 hybrid electrode in an electrochemical supercapacitor." *Carbon*, 63, 434–445.

Ranganatha, S., Kumar, S., Penki, T. R., Kishore, B., and Munichandraiah, N. (2017). "Co2(OH)3Cl xerogels with 3D interconnected mesoporous structures as a novel high-performance supercapacitor material." *J. Solid State Electrochem.*, 21(1), 133–143.

Rasamani, K. D., Alimohammadi, F., and Sun, Y. (2017). "Interlayer-expanded MoS2." *Mater. Today*, 20(2), 83–91.

Rasmussen, F. A., and Thygesen, K. S. (2015). "Computational 2D Materials Database: Electronic Structure of Transition-Metal Dichalcogenides and Oxides." *J. Phys. Chem. C*, 119(23), 13169–13183.

Ratha, S., and Rout, C. S. (2013). "Supercapacitor electrodes based on layered tungsten disulfide-reduced graphene oxide hybrids synthesized by a facile hydrothermal method." *ACS Appl Mater Interfaces*, 5(21), 11427–33.

Ren, G., Hao, Q., Mao, J., Liang, L., Liu, H., Liu, C., and Zhang, J. (2018a). "Ultrafast fabrication of nickel sulfide film on Ni foam for efficient overall water splitting." *Nanoscale*, 10(36), 17347–17353.

Ren, X., Ma, Q., Ren, P., and Wang, Y. (2018b). "Synthesis of nitrogen-doped MoSe2 nanosheets with enhanced electrocatalytic activity for hydrogen evolution reaction." *Int. J. Hydrog. Energy*, 43(32), 15275–15280.

Roger, I., Shipman, M. A., and Symes, M. D. (2017). "Earth-abundant catalysts for electrochemical and photoelectrochemical water splitting." *Nat. Rev. Chem.*, 1(1), 0003.

Sankar, K. V., Kalpana, D., and Selvan, R. K. (2012). "Electrochemical properties of microwave-assisted reflux-synthesized Mn3O4 nanoparticles in different electrolytes for supercapacitor applications." *J. Appl. Electrochem.*, 42(7), 463–470.

Sekine, T., Izumi, M., Nakashizu, T., Uchinokura, K., and Matsuura, E. (1980). "Raman Scattering and Infrared Reflectance in 2H-MoSe2." *J. Phys. Soc. Jpn.*, 49(3), 1069–1077.

Seok, J., Lee, J.-H., Cho, S., Ji, B., Kim, H. W., Kwon, M., Kim, D., Kim, Y.-M., Oh, S. H., Kim, S. W., Lee, Y. H., Son, Y.-W., and Yang, H. (2017). "Active hydrogen evolution through lattice distortion in metallic MoTe2." *2D Mater.*, 4(2), 025061.

Shang, X., Dong, B., Chai, Y.-M., and Liu, C.-G. (2018). “In-situ electrochemical activation designed hybrid electrocatalysts for water electrolysis.” *Sci. Bull.*, 63(13), 853–876.

Sharma, P., and Bhatti, T. S. (2010). “A review on electrochemical double-layer capacitors.” *Energy Convers. Manag.*, 51(12), 2901–2912.

Shen, J., Ji, J., Dong, P., Baines, R., Zhang, Z., Ajayan, P. M., and Ye, M. (2016). “Novel FeNi2S4/TMD-based ternary composites for supercapacitor applications.” *J. Mater. Chem. A*, 4(22), 8844–8850.

Shenasa, M., Sainkar, S., and Lichtman, D. (1986). “XPS study of some selected selenium compounds.” *J. Electron Spectrosc. Relat. Phenom.*, 40(4), 329–337.

Shibli, S. M. A., and Sebeelamol, J. N. (2013). “Development of Fe2O3–TiO2 mixed oxide incorporated Ni–P coating for electrocatalytic hydrogen evolution reaction.” *Int. J. Hydrog. Energy*, 38(5), 2271–2282.

Shit, S., Chhetri, S., Jang, W., Murmu, N. C., Koo, H., Samanta, P., and Kuila, T. (2018). “Cobalt Sulfide/Nickel Sulfide Heterostructure Directly Grown on Nickel Foam: An Efficient and Durable Electrocatalyst for Overall Water Splitting Application.” *ACS Appl. Mater. Interfaces*, 10(33), 27712–27722.

Silva, L. A. da, Alves, V. A., Silva, M. A. P. da, Trasatti, S., and Boodts, J. F. C. (1996). “ELectrochemical impedance, SEM, EDX and voltammetric study of oxygen evolution on Ir + Ti + Pt ternary-oxide electrodes in alkaline solution.” *Electrochem. Impendance Spectrosc.*, 41(7), 1279–1285.

Silva, U. D., Masud, J., Zhang, N., Hong, Y., Liyanage, W. P. R., Zaeem, M. A., and Nath, M. (2018). “Nickel telluride as a bifunctional electrocatalyst for efficient water splitting in alkaline medium.” *J. Mater. Chem. A*, 6(17), 7608–7622.

Sivanantham, A., and Shanmugam, S. (2017). “Nickel selenide supported on nickel foam as an efficient and durable non-precious electrocatalyst for the alkaline water electrolysis.” *Appl. Catal. B Environ.*, 203, 485–493.

Soon, J. M., and Loh, K. P. (2007). “Electrochemical double-layer capacitance of MoS2 nanowall films.” *Electrochem. Solid-State Lett.*, 10(11), A250–A254.

Sreejesh, M., Huang, N. M., and Nagaraja, H. S. (2015). “Solar Exfoliated Graphene and its Application in Supercapacitors and Electrochemical H2O2 Sensing.” *Electrochimica Acta*, 160, 94–99.

Sun, H., Liang, Z., Shen, K., Luo, M., Hu, J., Huang, H., Zhu, Z., Li, Z., Jiang, Z., and Song, F. (2018). “Fabrication of NiSe2 by direct selenylation of a nickel surface.” *Appl. Surf. Sci.*, 428, 623–629.

Tang, C., Cheng, N., Pu, Z., Xing, W., and Sun, X. (2015). “NiSe Nanowire Film Supported on Nickel Foam: An Efficient and Stable 3D Bifunctional Electrode for Full Water Splitting.” *Angew. Chem. Int. Ed.*, 54(32), 9351–9355.

Tang, C., Xie, L., Sun, X., Asiri, A. M., and He, Y. (2016). “Highly efficient electrochemical hydrogen evolution based on nickel diselenide nanowall film.” *Nanotechnology*, 27(20), 20LT02.

Tang, H., Dou, K., Kaun, C.-C., Kuang, Q., and Yang, S. (2014). “MoSe2 nanosheets and their graphene hybrids: synthesis, characterization and hydrogen evolution reaction studies.” *J. Mater. Chem. A*, 2(2), 360–364.

Tongay, S., Narang, D. S., Kang, J., Fan, W., Ko, C., Luce, A. V., Wang, K. X., Suh, J., Patel, K. D., Pathak, V. M., Li, J., and Wu, J. (2014). “Two-dimensional semiconductor alloys: Monolayer Mo1−xWxSe2.” *Appl. Phys. Lett.*, 104(1), 012101.

Tran, P. D., Nguyen, M., Pramana, S. S., Bhattacharjee, A., Chiam, S. Y., Fize, J., Field, M. J., Artero, V., Wong, L. H., Loo, J., and Barber, J. (2012). “Copper molybdenum sulfide: a new efficient electrocatalyst for hydrogen production from water.” *Energy Environ. Sci.*, 5(10), 8912–8916.

Vrubel, H., Moehl, T., Grätzel, M., and Hu, X. (2013). “Revealing and accelerating slow electron transport in amorphous molybdenum sulphide particles for hydrogen evolution reaction.” *Chem. Commun.*, 49(79), 8985–8987.

Walter, M. G., Warren, E. L., McKone, J. R., Boettcher, S. W., Mi, Q., Santori, E. A., and Lewis, N. S. (2010). “Solar Water Splitting Cells.” *Chem. Rev.*, 110(11), 6446–6473.

Wang, D., Pan, Z., Wu, Z., Wang, Z., and Liu, Z. (2014a). “Hydrothermal synthesis of MoS2 nanoflowers as highly efficient hydrogen evolution reaction catalysts.” *J. Power Sources*, 264, 229–234.

Wang, F., Shifa, T. A., Zhan, X., Huang, Y., Liu, K., Cheng, Z., Jiang, C., and He, J. (2015). “Recent advances in transition-metal dichalcogenide based nanomaterials for water splitting.” *Nanoscale*, 7(47), 19764–19788.

Wang, H., Feng, H., and Li, J. (2014b). “Graphene and Graphene-like Layered

Transition Metal Dichalcogenides in Energy Conversion and Storage." *Small*, 10(11), 2165–2181.

Wang, H., Kong, D., Johanes, P., Cha, J. J., Zheng, G., Yan, K., Liu, N., and Cui, Y. (2013a). "MoSe2 and WSe2 Nanofilms with Vertically Aligned Molecular Layers on Curved and Rough Surfaces." *Nano Lett.*, 13(7), 3426–3433.

Wang, J., Polleux, J., Lim, J., and Dunn, B. (2007). "Pseudocapacitive Contributions to Electrochemical Energy Storage in TiO2 (Anatase) Nanoparticles." *J. Phys. Chem. C*, 111(40), 14925–14931.

Wang, Q., Jiao, L., Du, H., Si, Y., Wang, Y., and Yuan, H. (2012). "Co3S4 hollow nanospheres grown on graphene as advanced electrode materials for supercapacitors." *J. Mater. Chem.*, 22(40), 21387–21391.

Wang, Q., Zhao, H., Li, F., She, W., Wang, X., Xu, L., and Jiao, H. (2019). "Mo-doped Ni2P hollow nanostructures: highly efficient and durable bifunctional electrocatalysts for alkaline water splitting." *J. Mater. Chem. A*, 7(13), 7636–7643.

Wang, X., Li, W., Wang, X., Zhang, J., Sun, L., Gao, C., Shang, J., Hu, Y., and Zhu, Q. (2017). "Electrochemical properties of NiCoO2 synthesized by hydrothermal method." *RSC Adv.*, 7(80), 50753–50759.

Wang, X., Liu, B., Wang, Q., Song, W., Hou, X., Chen, D., Cheng, Y., and Shen, G. (2013b). "Three-Dimensional Hierarchical GeSe2 Nanostructures for High Performance Flexible All-Solid-State Supercapacitors." *Adv. Mater.*, 25(10), 1479–1486.

Wang, Y., Guo, C. X., Liu, J., Chen, T., Yang, H., and Li, C. M. (2011). "CeO2 nanoparticles/graphene nanocomposite-based high performance supercapacitor." *Dalton Trans.*, 40(24), 6388–6391.

Wang, Z., Sha, Q., Zhang, F., Pu, J., and Zhang, W. (2013c). "Synthesis of polycrystalline cobalt selenide nanotubes and their catalytic and capacitive behaviors." *CrystEngComm*, 15(29), 5928–5934.

Wang, Z., and Zhang, L. (2018a). "In situ growth of NiTe nanosheet film on nickel foam as electrocatalyst for oxygen evolution reaction." *Electrochem. Commun.*, 88, 29–33.

Wang, Z., and Zhang, L. (2018b). "Nickel Ditelluride Nanosheet Arrays: A Highly Efficient Electrocatalyst for the Oxygen Evolution Reaction." *ChemElectroChem*, 5(8),

1153–1158.

Wolfart, F., Dubal, D. P., Vidotti, M., Holze, R., and Gómez-Romero, P. (2016). "Electrochemical supercapacitive properties of polypyrrole thin films: influence of the electropolymerization methods." *J. Solid State Electrochem.*, 20(4), 901–910.

Worsley, M. A., Pauzauskie, P. J., Olson, T. Y., Biener, J., Satcher, J. H., and Baumann, T. F. (2010). "Synthesis of Graphene Aerogel with High Electrical Conductivity." *J. Am. Chem. Soc.*, 132(40), 14067–14069.

Wu, Y., Li, G.-D., Liu, Y., Yang, L., Lian, X., Asefa, T., and Zou, X. (2016). "Overall Water Splitting Catalyzed Efficiently by an Ultrathin Nanosheet-Built, Hollow Ni3S2-Based Electrocatalyst." *Adv. Funct. Mater.*, 26(27), 4839–4847.

Xie, J., Zhang, J., Li, S., Grote, F., Zhang, X., Zhang, H., Wang, R., Lei, Y., Pan, B., and Xie, Y. (2013). "Controllable Disorder Engineering in Oxygen-Incorporated MoS2 Ultrathin Nanosheets for Efficient Hydrogen Evolution." *J. Am. Chem. Soc.*, 135(47), 17881–17888.

Xu, J., Dong, L., Li, C., and Tang, H. (2016a). "Facile synthesis of Mo0.91W0.09S2 ultrathin nanosheets/amorphous carbon composites for high-performance supercapacitor." *Mater. Lett.*, 162, 126–130.

Xu, J., Yin, Y., Xiong, H., Du, X., Jiang, Y., Guo, W., Wang, Z., Xie, Z., Qu, D., Tang, H., Deng, Q., and Li, J. (2019a). "Improving catalytic activity of metal telluride by hybridization: An efficient Ni3Te2-CoTe composite electrocatalyst for oxygen evolution reaction." *Appl. Surf. Sci.*, 490, 516–521.

Xu, J., Yin, Y., Xiong, H., Du, X., Jiang, Y., Guo, W., Wang, Z., Xie, Z., Qu, D., Tang, H., Deng, Q., and Li, J. (2019b). "Improving catalytic activity of metal telluride by hybridization: An efficient Ni3Te2-CoTe composite electrocatalyst for oxygen evolution reaction." *Appl. Surf. Sci.*, 490, 516–521.

Xu, L., Ma, L., Zhou, X., Liu, Z., Luo, D., Xu, X., and Zhang, L. (2018). "Boosting electrocatalytic activity of ultrathin MoSe2/C composites for hydrogen evolution via a surfactant assisted hydrothermal method." *Int. J. Hydrog. Energy*, 43(33), 15749–15761.

Xu, R., Wu, R., Shi, Y., Zhang, J., and Zhang, B. (2016b). "Ni3Se2 nanoforest/Ni foam as a hydrophilic, metallic, and self-supported bifunctional electrocatalyst for both H2 and O2 generations." *Nano Energy*, 24, 103–110.

Xu, Y., Wu, R., Zhang, J., Shi, Y., and Zhang, B. (2013). “Anion-exchange synthesis of nanoporous FeP nanosheets as electrocatalysts for hydrogen evolution reaction.” *Chem. Commun.*, 49(59), 6656–6658.

Yang, L., Zhu, X., Xiong, S., Wu, X., Shan, Y., and Chu, P. (2016). “Synergistic WO3•2H2O Nanoplates/WS2 Hybrid Catalysts for High-Efficiency Hydrogen Evolution.” *ACS Appl. Mater. Interfaces*, 8.

Yao, J., Liu, B., Ozden, S., Wu, J., Yang, S., Rodrigues, M.-T. F., Kalaga, K., Dong, P., Xiao, P., Zhang, Y., Vajtai, R., and Ajayan, P. M. (2015). “3D Nanostructured Molybdenum Diselenide/Graphene Foam as Anodes for Long-Cycle Life Lithium-ion Batteries.” *Electrochimica Acta*, 176, 103–111.

Yin, Y., Rioux, R. M., Erdonmez, C. K., Hughes, S., Somorjai, G. A., and Alivisatos, A. P. (2004). “Formation of Hollow Nanocrystals Through the Nanoscale Kirkendall Effect.” *Science*, 304(5671), 711–714.

Young, A. P., Colbow, V., Harvey, D., Rogers, E., and Wessel, S. (2013). “A Semi-Empirical Two Step Carbon Corrosion Reaction Model in PEM Fuel Cells.” *J. Electrochem. Soc.*, 160(4), F381–F388.

Yu, B., Wang, X., Qi, F., Zheng, B., He, J., Lin, J., Zhang, W., Li, Y., and Chen, Y. (2017). “Self-Assembled Coral-like Hierarchical Architecture Constructed by NiSe2 Nanocrystals with Comparable Hydrogen-Evolution Performance of Precious Platinum Catalyst.” *ACS Appl. Mater. Interfaces*, 9(8), 7154–7159.

Yu, F., Yao, H., Wang, B., Zhang, K., Zhang, Z., Xie, L., Hao, J., Mao, B., Shen, H., and Shi, W. (2018). “Nickel foam derived nitrogen doped nickel sulfide nanowires as an efficient electrocatalyst for the hydrogen evolution reaction.” *Dalton Trans.*, 47(29), 9871–9876.

Yuan, C.-Z., Sun, Z.-T., Jiang, Y.-F., Yang, Z.-K., Jiang, N., Zhao, Z.-W., Qazi, U. Y., Zhang, W.-H., and Xu, A.-W. (2017). “One-Step In Situ Growth of Iron–Nickel Sulfide Nanosheets on FeNi Alloy Foils: High-Performance and Self-Supported Electrodes for Water Oxidation.” *Small*, 13(18), 1604161.

Yuan, D., Chen, J., Tan, S., Xia, N., and Liu, Y. (2009). “Worm-like mesoporous carbon synthesized from metal–organic coordination polymers for supercapacitors.” *Electrochem. Commun.*, 11(6), 1191–1194.

Zeng, Z., Sun, T., Zhu, J., Huang, X., Yin, Z., Lu, G., Fan, Z., Yan, Q., Hng, H. H., and

Zhang, H. (2012). “An Effective Method for the Fabrication of Few-Layer-Thick Inorganic Nanosheets.” *Angew. Chem. Int. Ed.*, 51(36), 9052–9056.

Zhang, D., Jiang, L., Liu, Y., Qiu, L., Zhang, J., and Yuan, D. (2019a). “Ni3S2-MoSx nanorods grown on Ni foam as high-efficient electrocatalysts for overall water splitting.” *Int. J. Hydrog. Energy*, 44(33), 17900–17908.

Zhang, H., Jiang, H., Hu, Y., Li, Y., Xu, Q., Petr, S., and Li, C. (2019b). “Tailorable surface sulfur chemistry of mesoporous Ni3S2 particles for efficient oxygen evolution.” *J. Mater. Chem. A*, 7(13), 7548–7552.

Zhang, J., Wang, T., Pohl, D., Rellinghaus, B., Dong, R., Liu, S., Zhuang, X., and Feng, X. (2016). “Interface Engineering of MoS2/Ni3S2 Heterostructures for Highly Enhanced Electrochemical Overall-Water-Splitting Activity.” *Angew. Chem. Int. Ed.*, 55(23), 6702–6707.

Zhang, L. L., Zhou, R., and Zhao, X. S. (2010). “Graphene-based materials as supercapacitor electrodes.” *J. Mater. Chem.*, 20(29), 5983–5992.

Zhang, L., Wang, J., Zhu, J., Zhang, X., San Hui, K., and Hui, K. N. (2013). “3D porous layered double hydroxides grown on graphene as advanced electrochemical pseudocapacitor materials.” *J. Mater. Chem. A*, 1(32), 9046–9053.

Zhang, M., Wu, J., Zhu, Y., Dumcenco, D. O., Hong, J., Mao, N., Deng, S., Chen, Y., Yang, Y., Jin, C., Chaki, S. H., Huang, Y.-S., Zhang, J., and Xie, L. (2014a). “Two-Dimensional Molybdenum Tungsten Diselenide Alloys: Photoluminescence, Raman Scattering, and Electrical Transport.” *ACS Nano*, 8(7), 7130–7137.

Zhang, N., Lei, J., Xie, J., Huang, H., and Yu, Y. (2017a). “MoS2/Ni3S2 nanorod arrays well-aligned on Ni foam: a 3D hierarchical efficient bifunctional catalytic electrode for overall water splitting.” *RSC Adv.*, 7(73), 46286–46296.

Zhang, P., Wang, M., Yang, Y., Yao, T., and Sun, L. (2014b). “A Molecular Copper Catalyst for Electrochemical Water Reduction with a Large Hydrogen-Generation Rate Constant in Aqueous Solution.” *Angew. Chem. Int. Ed.*, 53(50), 13803–13807.

Zhang, P., Yang, X., Jiang, P., Yin, J., Gong, Y., and Lin, J. (2015a). “Cu(i) complex based on 6H-indolo[2,3-b]quinoxaline: structure and electrocatalytic properties for hydrogen evolution reaction from water.” *RSC Adv.*, 5(43), 34058–34064.

Zhang, S., and Pan, N. (2015). “Supercapacitors Performance Evaluation.” *Adv. Energy Mater.*, 5(6), 1401401.

Zhang, Y., Yan, C., Wang, F., and Li, W. (2005). “Electrochemical behavior of anodized Mg alloy AZ91D in chloride containing aqueous solution.” *Corros. Sci.*, 47(11), 2816–2831.

Zhang, Y., Zhou, Q., Zhu, J., Yan, Q., Dou, S. X., and Sun, W. (2017b). “Nanostructured metal chalcogenides for energy storage and electrocatalysis.” *Adv. Funct. Mater.*, 27(35), 1702317.

Zhang, Z., Yang, X., Fu, Y., and Du, K. (2015b). “Ultrathin molybdenum diselenide nanosheets anchored on multi-walled carbon nanotubes as anode composites for high performance sodium-ion batteries.” *J. Power Sources*, 296, 2–9.

Zhao, J., Pei, S., Ren, W., Gao, L., and Cheng, H.-M. (2010). “Efficient Preparation of Large-Area Graphene Oxide Sheets for Transparent Conductive Films.” *ACS Nano*, 4(9), 5245–5252.

Zhao, W., Zhang, C., Geng, F., Zhuo, S., and Zhang, B. (2014). “Nanoporous Hollow Transition Metal Chalcogenide Nanosheets Synthesized via the Anion-Exchange Reaction of Metal Hydroxides with Chalcogenide Ions.” *ACS Nano*, 8(10), 10909–10919.

Zhao, Y., Lee, H., Choi, W., Fei, W., and Lee, C. J. (2017). “Large-area synthesis of monolayer MoSe2 films on SiO2/Si substrates by atmospheric pressure chemical vapor deposition.” *RSC Adv.*, 7(45), 27969–27973.

Zhong, L., Bao, Y., Yu, X., and Feng, L. (2019). “An Fe-doped NiTe bulk crystal as a robust catalyst for the electrochemical oxygen evolution reaction.” *Chem. Commun.*

Zhou, H., Shi, Y., Wang, L., Zhang, H., Zhao, C., Hagfeldt, A., and Ma, T. (2013). “Notable catalytic activity of oxygen-vacancy-rich WO2.72 nanorod bundles as counter electrodes for dye-sensitized solar cells.” *Chem. Commun.*, 49(69), 7626–7628.

Zhu, W., Yue, X., Zhang, W., Yu, S., Zhang, Y., Wang, J., and Wang, J. (2016). “Nickel sulfide microsphere film on Ni foam as an efficient bifunctional electrocatalyst for overall water splitting.” *Chem. Commun.*, 52(7), 1486–1489.

LIST OF PUBLICATIONS AND CONFERENCES

PEER-REVIEWED PUBLICATIONS

1. **Karthik S Bhat**, Sulakshana Shenoy, H S Nagaraja and Kishore Sridharan *"Porous cobalt chalcogenide nanostructures as high performance pseudo-capacitor electrodes"* ***Electrochimica Acta*** 248 *(2017)* 188-196. *DOI link: https://doi.org/10.1016/j.electacta.2017.07.137*

2. **Karthik S Bhat**, Harish C Barshilia and H S Nagaraja *"Porous nickel telluride nanostructures as bifunctional electrocatalyst towards hydrogen and oxygen evolution reaction"* ***International Journal of Hydrogen Energy*** 42, 39 *(2017)* 24645-24655. *DOI link: https://doi.org/10.1016/j.ijhydene.2017.08.098*

3. **Karthik S Bhat** and H S Nagaraja *"Nickel selenide nanostructures as an electrocatalyst for hydrogen evolution reaction"* ***International Journal of Hydrogen Energy*** 43, 43 *(2018)* 19851-19863. *DOI link: https://doi.org/10.1016/j.ijhydene.2018.09.018*

4. **Karthik S Bhat** and H S Nagaraja *"Effect of isoelectronic tungsten doping on molybdenum selenide nanostructures and their graphene hybrids for supercapacitors"* ***Electrochimica Acta*** 302 *(2019)* 459-471. *DOI link: https://doi.org/10.1016/j.electacta.2019.02.059*

5. **Karthik S Bhat** and H S Nagaraja *"Performance evaluation of molybdenum dichalcogenide (MoX_2; X= S, Se, Te) nanostructures for hydrogen evolution reaction"* ***International Journal of Hydrogen Energy*** 44, 33 *(2019)* 17878-17886. *DOI link: https://doi.org/10.1016/j.ijhydene.2019.05.179*

6. **Karthik S Bhat** and H S Nagaraja *"Recent Trends and Insights in Nickel chalcogenide Nanostructures for Water-splitting reactions"* ***Materials Research Innovations*** **(Accepted manuscript)**. *DOI link: https://doi.org/10.1080/14328917.2019.1703523*

7. **Karthik S Bhat** and H S Nagaraja *"In-situ synthesis of copper sulfide-nickel sulfide arrays on three-dimensional nickel foam for overall water-splitting"* ***ChemistrySelect*** 5, 8 *(2020)* 2455-2464. *DOI link: https://doi.org/10.1002/slct.202000026*

8. **Karthik S Bhat** and H S Nagaraja *"Hydrogen evolution reaction at extreme pH conditions of copper sulfide micro-hexagons". Journal of Science: Advanced Materials and Devices 5 (2020)* 361-367. *DOI link: https://doi.org/10.1016/j.jsamd.2020.06.004*

PEER-REVIEWED PUBLICATIONS IN RELATED WORK:

9. **Karthik S Bhat** and H S Nagaraja "Two-dimensional nickel hydroxide nanosheets as high performance pseudo-capacitor electrodes" ***AIP Conference Proceedings*** 1943, 1 (2017) 020057. *DOI link: https://doi.org/10.1063/1.5029633*

10. **Karthik S Bhat** and H S Nagaraja *"Effect of oxygen substitution and phase on nickel selenide nanostructures for supercapacitor applications"* ***Materials Research Express*** 5, 10 *(2018)* 105504. *DOI link: https://doi.org/10.1088/2053-1591/aadac2*

11. **Karthik S Bhat** and H S Nagaraja *"Morphology Dependent Electrochemical Performances of Nickel Hydroxide Nanostructures"* ***Bulletin of Materials Science*** 42:265 *(2019). DOI link: https://doi.org/10.1007/s12034-019-1951-9*

12. K Mahendra, **Karthik S Bhat,** H S Nagaraja and N.K. Udayashankar *"Modulations of physio-chemical and electronic properties of metalorganic KHO single crystals through $Co(OH)_2$ nanoparticles doping",* ***Journal of Materials Science: Materials in Electronics*** 30, 13 *(2019)* 12566-12576. *DOI link: https://doi.org/10.1007/s10854-019-01617-1*

13. **Karthik S Bhat,** Basavaraj R Huvinahalli and H S Nagaraja *"Two-dimensional cadmium hydroxide nanosheets for electrochemical capacitors under high-*

operating-voltage", ***Journal of Electronic Materials*** 49, 2 *(2020)* 995-1001**.** *DOI link: https://doi.org/10.1007/s11664-019-07860-w*

14. **Karthik S Bhat** and H S Nagaraja *"Electrochemical hydrogen-storage performance of copper sulfide micro-hexagons"* **(Under Revision)**.

CONFERENCE PRESENTATIONS

1. **Karthik S Bhat** and H S Nagaraja "*Cobalt hydroxide nanosheets as high performance pseudo-capacitor electrodes*" ICN3i – 2017, IIT Roorkee, India.

2. **Karthik S Bhat** and H S Nagaraja "*Two-dimensional Nickel Hydroxide Nanosheets As High Performance Pseudo-capacitor Electrodes*" ICDEM-2018, NITK Surathkal, India.

3. **Karthik S Bhat** and H S Nagaraja "*Morphology Dependent Electrochemical Performances of Nickel Hydroxide Nanostructures*" MTECS-2018, BARC Mumbai, India.

4. **Karthik S Bhat** and H S Nagaraja "*Nickel sulphide nanostructures as bifunctional electrocatalyst for hydrogen and oxygen evolution reaction*" ICME-2018, SS Jain Subodh PG college, Jaipur, India.

5. **Karthik S Bhat** and H S Nagaraja "*Enhancing the hydrogen evolution reaction activity of cobalt selenide nanostructures by nickel substitution*" ICSM-2018, MNIT Jaipur, India. (**Best paper award**).

CURRICULUM VITAE

Karthik S Bhat
Research Scholar
Department of Physics
National Institute of Technology Karnataka, Surathkal
Mangalore – 575 025, India.
Mobile: +91-8880831899
E-mail: kasubhat@gmail.com

Scopus ID: 56926173400
Google Scholar: https://scholar.google.co.in/citations?user=58fIEyoAAAAJ&hl=en

---

Education qualification:

- **Ph.D. Physics** (*2015-Present*), National Institute of Technology Karnataka (NITK), Surathkal, India.
- **M.Sc Physics**, *2014*, Mangalore University, India.
- **B.Sc Physics, Chemistry and Mathematics**, *2012*, Mangalore University, India.